*Author:*
**Nikonovas, Arkadijus**

*Title:*
**Taylor Spatial Frame: Kinematics, Mechanical Properties and Automation**

# Taylor Spatial Frame: Kinematics, Mechanical Properties and Automation

Arkadijus Nikonovas

A dissertation submitted to the University of Bristol in accordance with the requirements of the degree of PhD in the Faculty of Engineering.

Department of Mechanical Engineering, October, 2005

Word Count: 36628

# ABSTRACT

The Taylor Spatial Frame (TSF) is a recently introduced form of a circular external orthopaedic fixator for long bone fracture reduction and deformity correction. The TSF is constructed from two circular rings interconnected with six variable-length struts. Its kinematics are based on the Stewart-Gough platform. The TSF is attached to the patient's anatomy using fine wires and half-pins.

In this thesis, three aspects of the TSF are analysed. First, the solution to non-trivial forward and inverse kinematics has been addressed. Second, the mechanical properties of the TSF fixator are investigated. Individual component stiffness is assessed separately and then the complete fixator is modelled. Simple stiffness models of fine wires and half-pins are derived. Considerations for the use of the TSF for the peri-articular fractures are investigated and potential modifications are proposed. The effect of backlash in the frame components on the accuracy of the fixator has been analysed. Finally, in order to validate the kinematics solution, to provide a training aid for surgeons and to demonstrate the concept of accurately controlled interfragmentary motion, a prototype of an active TSF was designed and built.

Computationally efficient algorithms for solving the forward and inverse kinematics have been developed that require little numerical processing overhead and can be implemented on a mobile computing device. It was found that the TSF fixator has similar axial stiffness to the circular Ilizarov ring fixator, since wires and half-pins are significantly less stiff than the frames. Furthermore, the TSF exhibits more uniform stiffness for a range of off-axis loads and is significantly stiffer for torsional loads than the Ilizarov fixator. Slack, in the form of a backlash, can lead to severe strains in the unloaded frames and therefore fractures, and hence precautions are recommended. Finally, considerations and prototype for the automated TSF are presented that can be utilised for demonstration purposes and surgeon training.

**Keywords**: Taylor Spatial Frame, fine wire, half-pin, peri-articular fracture, active fixator, kinematics, orthopaedics, Stewart-Gough platform.

To My Father and Mother

Liudas - Milicijus Nikonovas & Dalia Nikonova

# ACKNOWLEDGEMENTS

The author would like to express his sincere thanks to:

- Dr. Andrew Harrison for guidance and supervision.

- Mr. Roger Atkins for clinical advice and financial support of the projects.

- Mr. Chris Butcher for assisting in planning and performing mechanical testing.

- Workshop technicians for manufacturing parts.

- Overseas Research Students Awards Scheme for funding tuition fees

- University of Bristol for scholarship and facilities.

- John Giles and Richard Bovey for proofreading the thesis.

## AUTHOR'S DECLARATION

I declare that the work in this dissertation was carried out in accordance with the Regulations of the University of Bristol. The work is original except where indicated by special reference in the text and no part of the dissertation has been submitted for any other degree.

Any views expressed in the dissertation are those of the author and in no way represent those of the University of Bristol.

The dissertation has not been presented to any other University for examination either in the United Kingdom or overseas.

SIGNED: .....

DATE: 5/5/2006 .....

# LIST OF CONTENTS

# LIST OF FIGURES

# LIST OF TABLES

# LIST OF ABBREVIATIONS

AP – anterior-posterior (font-back)

AX – axial

C# – type of C programming language for the .NET environment

*e.g.* – exempli gratia (for example)

IFM – interfragmentary motion

ILF – Ilizarov frame

ILH – Ilizarov hinged frame

IMN – intramedullary nail

*i.e.* – id est (that is)

ML – medial lateral (inside-outside)

PCD – pitch circle diameter

PID – proportional plus integral plus derivative

SGP – Stewart Gough Platform

S&N – Smith and Nephew (company)

TSF – Taylor Spatial Frame

UIFM – uncontrolled interfragmentary motion

# LIST OF NOTATIONS

| Symbol | Description, units |
|---|---|
| $a$ | Distance between wire clamp and bone, m |
| $\alpha$ | Angle of rotation around $x$ axis, rad |
| $A$ | Cross sectional area, $m^2$ |
| $\beta$ | Angle of rotation around y axis, rad |
| **b** | Matrix of a base local connection points coordinates, m |
| **B** | Matrix of a base global connection points coordinates, m |
| $\varepsilon$ | Strain in a fine wire |
| $E$ | Young's modulus of material, $N/m^2$ |
| $\boldsymbol{E}$ | Link length error vector, m |
| $d$ | Diameter of a half-pin or a fine wire, m |
| $\varphi$ | Angle of rotation about central bone axis, rad |
| $\theta$ | Angle between a tension vector $T$ and its tangential component $T_\varphi$, rad |
| $F$ | Axial force, N |
| $\gamma$ | Angle of rotation around $z$ axis, rad |
| $h$ | Improvement to a solution used in the 2D Newton-Raphson algorithm |
| $I$ | Second moment of area, $m^4$ |
| $k$ | Stiffness, N/mm or N·m/deg |
| $k_p$ | Proportional gain of a PID controller |
| $k_i$ | Integral gain of a PID controller |
| $k_d$ | Derivative gain of a PID controller |
| $l$ | Length of a wire or a half-pin, m |
| $\boldsymbol{l}$ | Link length vector, m |
| **L** | Link vector matrix, m |
| $M$ | Axial moment around bone's long axis, N·m |
| $N$ | Number of transfixing components per bone segment |
| **p** | Matrix of a platform local connection points coordinates, m |
| **P** | Matrix of a platform global connection points coordinates, m |
| $R$ | Equivalent radius of a bone, m |

| | |
|---|---|
| $\sigma$ | Stress in the material, $N/m^2$ |
| $\boldsymbol{t}$ | Vector defining a set of transformations, [ $\alpha$ $\beta$ $\gamma$ $x$ $y$ $z$ ] |
| $\boldsymbol{T}$ | Tension in a fine wire, N |
| **T** | Transformation matrix |
| $x$ | Translation along $x$ axis, m |
| $y$ | Translation along $y$ axis, m |
| $z$ | Translation along $z$ axis, m |

**Notation Formatting**

1. Symbols for physical quantities are represented in italic (sloping) type set, including vectors aligned along a single principal axis of the space, *e.g. F, T, y etc.*

2. Physical quantities, mathematical operators, constants, and symbols for units are represented in roman (upright) type set, *e.g.* kg, m/s, sin, log, $\pi$ *etc.*

3. Vectors, not aligned with principal axes of the space, are represented in bold italic type set. Optional subscripts in square brackets represent an element involved in the mathematical operation, *e.g.* $\boldsymbol{L}_{[2]}$ - a second element of the $\boldsymbol{L}$ vector.

4. Matrices are represented in bold upright type set. Subscript values in square brackets indicate either matrix size, or set of elements used from the matrix, *e.g.* $\mathbf{p}_{[6x4]}$ - a matrix **p** contains six rows and four columns; $\mathbf{p}_{[2,3]}$ - an element from the matrix **p** from the second row and third column; $\mathbf{p}_{[2,:]}$ - a vector containing all second row elements of the matrix **p**.

# CHAPTER 1 : INTRODUCTION

The principal aim of this thesis is the exploration of the Taylor Spatial Frame (TSF) based ring orthopaedic fixator. The following areas were therefore addressed: kinematics, mechanical properties and automation possibilities. A new solution to the kinematics of the TSF has been derived. Simple but effective models of the mechanical properties have been developed. Strategies for automation of motion of the frame have been developed and implemented. The principal benefits are seen as the delivery of a practical guide for surgeons and therefore better outcomes for patients presented with complex fractures and deformities in the long leg bones.

The musculoskeletal system is responsible for mobility, protection and support of the human anatomy. Long bones are part of the skeleton and are found in the arms and legs. They are responsible for motion and manipulation. The long bones transmit amongst the highest loads in the skeletal system. If these bones are overloaded or subjected to a high-energy impact, a fracture is formed and has to be treated.

A fracture union/healing is a sequence of biological transformations that unites separated segments of the broken bone. Four types of healing begin simultaneously. However, only one of them dominates, depending on the mechanical environment between the fracture surfaces. The fastest healing types producing strong bone material are known as primary callus formation and external callus bridging, and often are preferred among surgeons. To promote such types of healing, a small controlled interfragmentary motion, IFM, between the surfaces of the fractured bone in the direction of the longest bone axis is required. Shear forces and consequent lateral movements must be totally abolished in order to prevent breaking or weakening of the newly-laid blood vessels and minerals.

The mechanical environment of the fracture can be controlled with the aid of an orthopaedic fixation device, also known as an orthopaedic fixator. The huge range of such available devices is discussed in Chapter 2. The simplest examples of

orthopaedic fixators are the splint, cast and plaster, which are also non-invasive fixators. These devices are most suited to simple fractures that are not subjected to high loads or accidental impacts throughout the treatment period. They do not provide direct connection between the fractured bone and the fixator itself, and thus act more like guides for a fracture stabilisation. Non-invasive fixators provide little control over the positioning of the segments of the fractured bone and can result in a misaligned union or sometimes failure to unite. This is not favourable in the case of long bones, as this would affect mobility, dexterity and the strength of the union. In addition, misalignment can inflict severe pains and might lead to late union failure, requiring further treatment or amputation. The late union failure appears typically post-treatment in the form of a re-fracture.

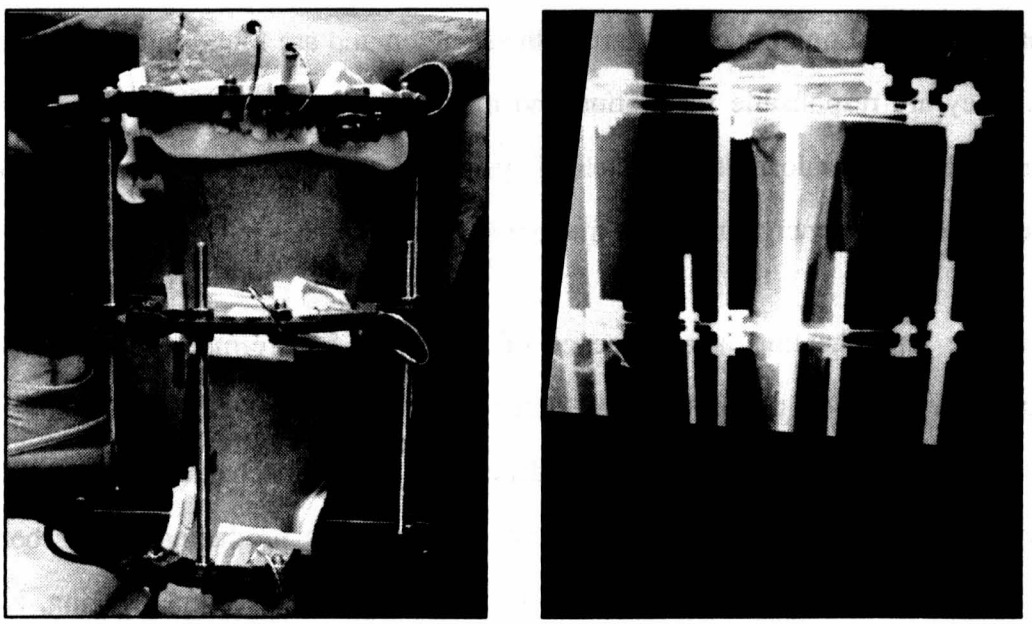

(a) (b)

**Figure 1. A fractured tibia bone stabilised with an Ilizarov ring fixator. a) – photographic isometric view; b) – X-Ray frontal (AP) view. Bone-transfixing components: fine wires.**

Fixators such as intramedullary nails and plates are completely implantable and provide precise control over the position of the segments during surgery. In addition, they reduce the load and strain on the fracture surfaces by transmitting part of the load through their own structure. However, it is very hard or impossible to adjust these fixators post-operatively and normally further surgery is required.

In between non-invasive and completely implantable fixators are external invasive fixators. The major structural body of such a fixator is located outside the anatomy, and the interface between the bone and the fixator is established via fine wires (Figure 1) and/or half-pins (Figure 2). Such fixators offer numerous advantages, such as minimal intrusion into human anatomy and an ability to adjust geometry post-operatively. Post-operative adjustments are important because a satisfactory fracture reduction obtained at the time of surgery is often not maintained due to the settling of the newly-laid bone tissue, the effect of weight bearing and sub-optimal imaging during the surgery [1-5]. In addition, the property of the post-operative adjustment of the fixator enables bone lengthening / shortening and bone transport to be performed for complex traumas.

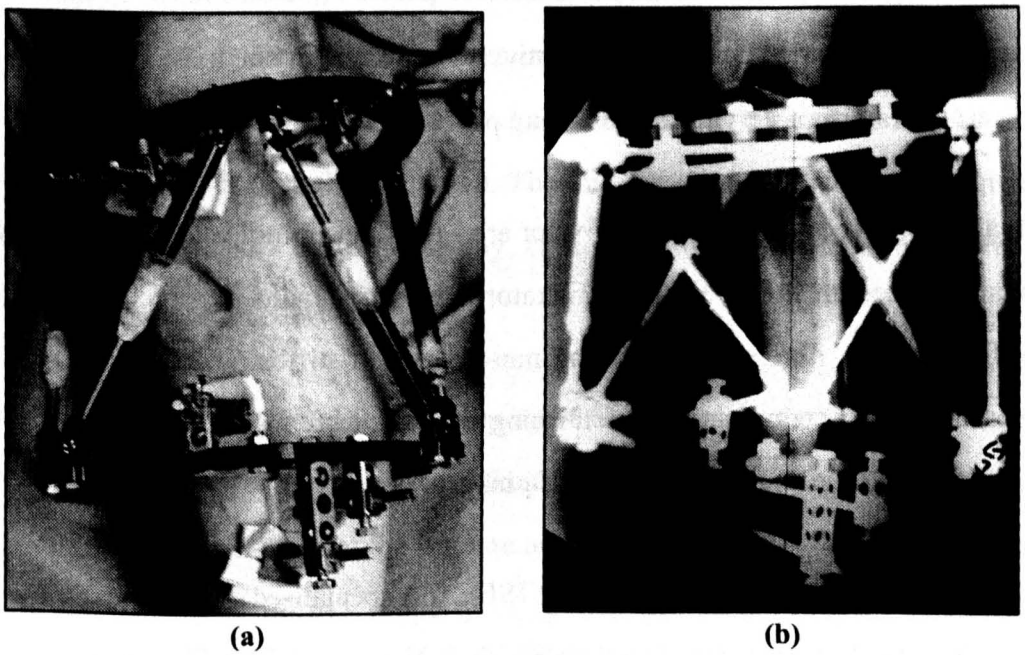

(a) (b)

**Figure 2. A fractured tibia bone stabilised with a Taylor Spatial Frame based fixator. a) – photographic frontal view; b) – X-Ray frontal (AP) view. Bone-transfixing components: half-pins.**

One of the most commonly used invasive external fixator is a circular (ring) fixator. The Ilizarov fixator is one well-established example of such a device, Figure 1. It allows the surgeon considerable freedom in the choice and the direction of fixation points with resultant improved healing. This type of fixator is increasingly popular, especially for the treatment of complex deformities or highly displaced fractures and

has been used to treat over one million cases worldwide during the last 20 years. It has a simple structure consisting of rings, connecting rods, and fine wires and/or half-pins. The standard configuration is of four concentrically-aligned rings, four struts and eight wires. The rings are made of aluminium alloy, steel or more recently composite material: carbon fibre. There is a wide range of connecting struts available. The most simple and commonly-used one is a threaded rod.

A hinge can be added to the Ilizarov fixator in the sub-acute period of treatment for correction of multi-planar angulation. Other components can be added when translational or rotational adjustments are required. However, additional components severely complicate the kinematics of the Ilizarov fixator and it becomes problematic to correct a deformity in more than two axes or planes simultaneously. In addition, the correction of the deformity post-operatively in more than one axis or plane using the Ilizarov fixator is a very time consuming process.

The main advantages of the Ilizarov fixator are - relatively simple structure, intuitive kinematics, freedom in rod positions, fixator symmetry, radio translucent rings (if made from carbon fibre composite) and non-linear self-stiffening behaviour [6, 7]. Disadvantages are complications performing multiplane deformity corrections and risk of infection (due to wounds from half-pins and wires).

More recently, a Taylor Spatial Frame (TSF), the specialised form of a Stewart-Gough platform, has been introduced by Smith & Nephew (S&N), Tennessee, USA, Figure 2. It is a parallel manipulator consisting of at least two rings interconnected with six variable-length struts, which are connected at the manufacturer's predefined locations. The application of such a device is very similar to an Ilizarov frame with the interface between the fractured bone and the fixator established via half-pins and/or fine wires. The Stewart-Gough platform, and therefore the TSF, offer simple manipulation of the position and orientation of the fractured bone surfaces in the full six degrees of freedom. By varying the strut lengths, the fractured bone ends can be

moved in the 3D workspace ($x$, $y$, $z$) as well as rotated about all three spatial axes ($x$, $y$, $z$), without the introduction of any additional frame components. However, the geometry of the TSF is insufficiently generalised, so that the choice of half-pin and fine wire anchorage sites available to the surgeon is restricted, especially for the treatment of peri-articular fractures, and this renders the fixator inadequate for some cases.

The forward and inverse kinematics are the key to the successful operation and manipulation of the TSF. Their solutions are non-intuitive. A computerised solver is required to calculate and control the frame geometry and this is internet dependent currently. The internet kinematics solver limits ring-interconnecting strut positioning, thus preventing potential modification of the frame and application to peri-articular fracture treatment. Furthermore, the manufacturer's solution requires significant numerical processing overhead and specialised computers, and hence is not suitable for 'stand alone' distribution. The internet service for solving kinematics can be slow during peak times of the day, causing increased cost and time spent by both the patient and the surgeon.

There is very little published information available regarding the TSF's mechanical properties. It is important to understand fixator mechanics as these influence directly the mechanical environment of the fracture and therefore healing. The TSF possesses the Stewart-Gough platform's property of having the full six degrees of freedom, giving it a huge advantage over the Ilizarov frame. The author expects that increased use of Stewart-Gough platform based fixators would reduce surgery and outpatients' clinical time and could improve patients' outcomes.

Half-pins and wires are used to establish the connection between the external ring fixator and the anatomy. They are inserted in anatomically safe corridors in order to prevent severe damage to nerves, muscles, and blood vessels. The number of wires and half-pins used per fixator is determined by the surgeon. A standard configuration

involves two wires or half-pins per ring, crossing at an angle of 60 to 90 degrees. Typical wire diameters are 1.6 mm and 1.8 mm. Wires allow IFM at the fracture site by bending, at the same time restricting high amplitude motion by self-stiffening. The fine wire is pretensioned in order to increase its axial stiffness. It is clamped on the ring at its two ends using slotted or cannulated bolts. Half-pins require only a single anchoring point and offer similar stiffness to that of a fine wire. Half-pins are made from high strength stainless steel or titanium alloy rods of typical diameter from 4 mm to 6 mm. It is important to choose the correct wire/half-pin combination in order to achieve the desired healing and therefore simple yet accurate mathematical models are required for this purpose.

During the application of the external fixator, patients are encouraged to load the injured limb in order to create mechanical loads on the fracture – this is believed to stimulate the healing process [8-18]. In the case of leg long bones, this is accomplished by partial or full weight bearing on the injured limb. The loads generate the IFM at the fracture site, which is believed to be controlled by the mechanical properties of the fixator. It was noted during frame clinics at the Bristol Royal Infirmary (BRI) that some uncontrolled and unrestricted motion was present in the TSF for some patients. This was observed in the unloaded frames, and in frames that during application reversed load direction. The patients experiencing such phenomenon reported severe pain. The reason for this occurrence is the slack in the frame components, which leads to uncontrolled shear and axial strains at the fracture site, thus possibly delaying the union and damaging the newly-laid bone tissue. To the author's knowledge, the effects of slack have not been reported for either the TSF or the Ilizarov frame.

During the course of healing, the patient's limb is often subjected to unfavourable impacts, which in turn cause undesirable displacements between the bone segments and therefore the fracture surfaces. It would be attractive to mechanise the fixator to prevent such unplanned impacts by monitoring and controlling continuously the

strain levels at the fracture site. The mechanised fixator could be utilised to generate a controlled IFM stimulus while the patient is at rest in order to improve healing. Furthermore, it could be utilised for demonstration purposes and surgeon training.

The aim of this thesis is to investigate and better understand the properties of the TSF fixator in order to improve healing of severely fractured limbs, to reduce operating theatre and outpatients' waiting times, and to aid surgeons in training and fixation planning. It is desired to increase the understanding of the true role of the external circular fixator and its true effect on the IFM. The following problems / questions are tackled in order to achieve the aim:

1. Is there a fast general solution to the forward and inverse kinematics of the most general TSF that could be implemented on an ordinary and/or hand held computer device?

2. What are the mechanical properties of the TSF fixator?

    a. How do the mechanical properties of the TSF compare to the 'gold standard' Ilizarov frame?

    b. Is it possible to modify the TSF to make it more suitable for the peri-articular fractures?

    c. What effects do bone-transfixing components (wires and half-pins) pose to overall fixator stiffness?

    d. How accurate is the TSF? Is the uncontrolled movement due to slack in the TSF components significant in fracture healing? If it is, what can be done to minimise it?

3. Is it feasible to automate the TSF in order to improve control of the mechanical environment of the fracture and to generate mechanical stimulus for rapid healing?

Background information on the bone structure, healing, and fixation devices is provided in Chapter 2. Advantages and disadvantages of different types of healing and fixation methods are investigated. Definitions to the anatomy and the TSF are presented.

The problems and the challenges set out above are addressed and possible solutions are proposed in the next six chapters. The chapters are structured to state the question, to justify the question by reviewing the state of the art, to discuss why it is worth analysing and finally to suggest the solution or the answer. The author has developed an algorithm allowing a rapid solution of the forward and inverse kinematics of the general TSF that can be deployed on a hand-held computing device. The solution and details of implementation are provided in Chapter 3. The assessment of the mechanical stiffness of the TSF is presented in Chapter 4. The stiffness results of the TSF are compared to the stiffness of the Ilizarov frame. In addition, new configurations, suitable for the peri-articular fractures, are investigated. Simple models for a fine wire and half-pin stiffness assessment have been developed by the author, and are presented in Chapter 5. Effects of use of multiple wires and half-pins have been investigated. The load capacities of the transfixing components have been addressed. A stiffness model of the TSF based fixator has been presented in Chapter 6. The effect of fine wires on the overall stiffness of the fixator is investigated. The slack analysis of the TSF is performed in Chapter 7. The results are then used to analyse the strain at the fracture site and the accuracy of the TSF. In addition, the correlation between slack and the TSF configuration together with slack minimisation techniques are investigated. The feasibility of automation of the Stewart-Gough platform based fixators is presented in Chapter 8. The author has designed and built a prototype of an active TSF that can be used for surgeon training and to demonstrate the idea of the controlled mechanical stimulus. Design considerations and calculations for the active strut and electronics are provided. Considerations for the *in vivo* design are discussed.

A general discussion of the work, including implications to the orthopaedic field, is provided in Chapter 9. Finally, conclusions to the thesis, a summary of contributions to the field of work and further research suggestions are presented in Chapter 10.

# CHAPTER 2 : FRACTURES AND FRACTURE MANAGEMENT

The aim of this chapter is to provide the background information on the anatomy, fracture and healing of the long bone. The basic concepts of the skeletal fixation are overviewed, with reference to circular fixation devices.

## 2.1 Anatomy of Long Bones

Our skeletal system consists of bones, Figure 3. Bone is partly organic (cells and matrix) and partly inorganic (mineralised component). There are four types of bones: long, short, flat and irregular. In this research, the author has concentrated on long bones only, especially the femur and tibia, since they are subjected to most of the load during daily activities and they are crucial for skeletal mobility.

Long bones have four main functions. The first function is structural. Bones provide the shape for our bodies and host vital organs. Body locomotion is the second function of the bone. The complicated kinematic skeletal system enables movement, using muscles that control bone positions and orientations. Bones transmit loads and act as levers. Joints are the fulcrums about which bones move. Therefore, the prime qualities of bones are strength and rigidity [19]. Once the load exceeds the capacity of the bone, the fracture occurs. The body then initiates bone repair and the reconstruction process in order to restore bone functional properties. Details of the healing types and stages are described in the next section of this chapter. The third function of the bone is blood cell formation. Blood cell precursor cells, hemocytoblasts, are found in red marrow. The red marrow is simply a loose connective tissue that contains these blood cell precursors and the cells that they are making. The fourth function of the bone is inorganic salt regulation and storage of calcium, phosphate, sodium and potassium.

Bone structure can be described based on its overall macroscopic shape and microscopic composition. The end region of the bone is called the epiphysis and the

middle region is called the diaphysis or bone shaft, Figure 3. The region between is called the metaphysis. Between the metaphysis and epiphysis is the epiphyseal disk or plate, which is responsible for longitudinal bone growth in childhood. It is at the epiphysis where one bone contacts another in a joint to allow for movement. Each epiphysis is coated with an articular cartilage. The articular cartilage is simply a coating of hyaline cartilage, which reduces friction and absorbs shocks at freely moveable joints.

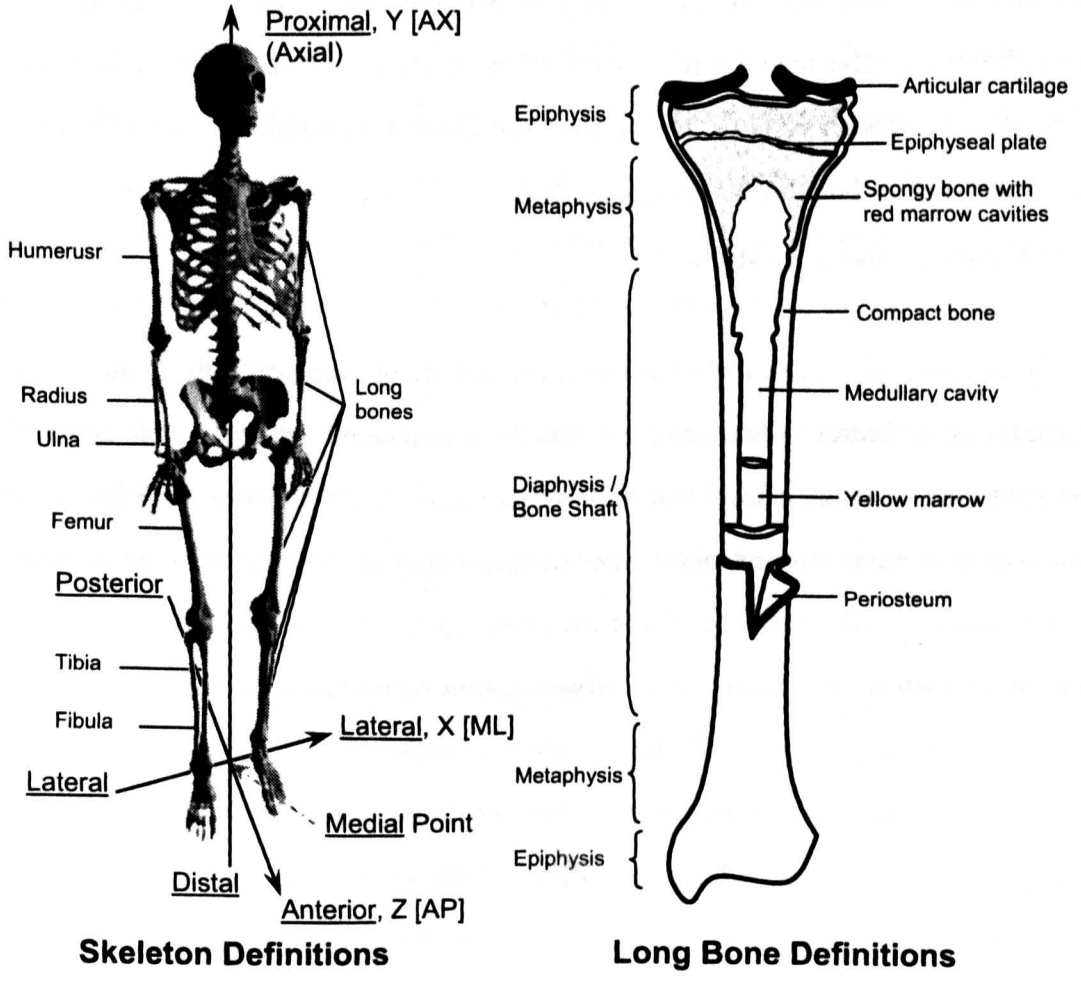


**Figure 3. Skeleton and long bone definitions.**

All bones are covered by a thin membrane called a periosteum. The periosteum is made of two layers of a dense connective tissue. The outer fibrous layer consists of fibroblasts and collagen fibres. The inside, or osteogenic, layer contains

osteoprogenitor cells. Long bones have a hollow region called the medullary cavity in the middle of the diaphysis. The perimeter of the medullary cavity is covered with an endosteum. The cavity itself is filled with marrow. Marrow can be either red or yellow depending on its function and composition. Red marrow is responsible for generation of blood cells and yellow marrow stores fat.

There are two types of bone tissue: spongy and compact, also known as dense. Spongy bone makes up most of the tissue of epiphyses. It consists of lamellae arranged in an irregular latticework of thin plates of bone called trabeculae. The spaces between trabeculae are filled with red bone marrow. Compact bone structure is based on Haversian systems. Haversian systems are located in the diaphysis. They also cover spongy bone in the epiphyses. The functions of Haversian systems are to protect, support, and resist stress.

On the microscopic level, the long bone has five main types of cells found in the skeletal tissue matrix. Osteoprogenitor cells are located in the inner layer of periosteum, endosteum, central and perforating canals. Their function is to divide by mitosis and develop into osteoblasts cells. Osteoblasts are the second type of cells. They spread over the surfaces of bones. Their function is to form bone tissue by secreting a matrix of collagen plus other organic compounds. Mature bone cells, known as osteocytes, are the third type of cells. They are responsible for maintenance of the bone matrix and are located throughout the bone tissue in each lacuna. The last type of cells is the osteoclasts. They are formed by the fusion of 2 to 50 monocytes, a type of white blood cell. Their function is destruction of bone matrix leaving tiny unfilled spaces behind for the osteoblasts, also known as resorption. Resorption allows for the repair and optimisation of the geometry and strength of the bone [20].

## 2.2 Forces Transmitted Through Long Leg Bones

The human skeletal system is a complicated kinematic chain. Loads are transmitted via bones and bone positions and orientations are controlled by muscles. The largest loads in our body can be found in the lower extremity of the skeletal system, namely long leg bones. The total load combines body weight and both external and dynamic loadings.

The investigation and quantification of force distributions in individual muscles and bones during various activities is complicated. The main reason, to the author's knowledge, is a deficiency of non-operative (non-invasive) and remote data acquisition systems that would enable the accurate measurement of forces inside the human anatomy. Therefore, many investigators have adopted mathematical modelling and simulation to tackle this problem. The results obtained using such models commonly overestimate the magnitudes of forces and bending moments [21]. However, these models can be refined by injecting experimentally-obtained data for muscle and bone properties, and loads. The experimental data available are very limited. Most experimental data come from measurements on animals and in some cases on human anatomy post-mortem. The other source of data is orthopaedic fixators, instrumented with data acquisition systems. Such fixators monitor and measure load patterns and displacements during the patient's daily activities. However, data obtained using this approach are limited and only indicate the partial capacity of the limb. Heller *et al* [22] have measured forces in the hip and found the peak force is more than 300 % of body weight for both walking and stair climbing. Their mathematical model was confirmed by *in vivo* testing and data obtained from hip implants. Duda *et al* [23], have modelled load distribution throughout a healthy femur. Their results indicate that the femur transmits loads of more than 230 % of body weight and bending moments of up to 20 % of body-weight-metres during walking activity. Schneider *et al* [24] have implanted a telemetrized intramedullary nail into the femur with a midshaft fracture in a 33 year old patient. The maximum

measured load in axial bone direction was 120 % of the body-weight and maximum axial moment of 1.3 % body-weight-metres for a single stance. Anterior-Posterior and Medial-Lateral loads were of the order of 8 % of body-weight and moments of up to 5 % of body-weight-metres (data derived from graphs based on body-weight of 750 N). It can be speculated that loads in the tibia are of the same magnitude or higher, based on the geometry and structure of the bone, and direction of gravity.

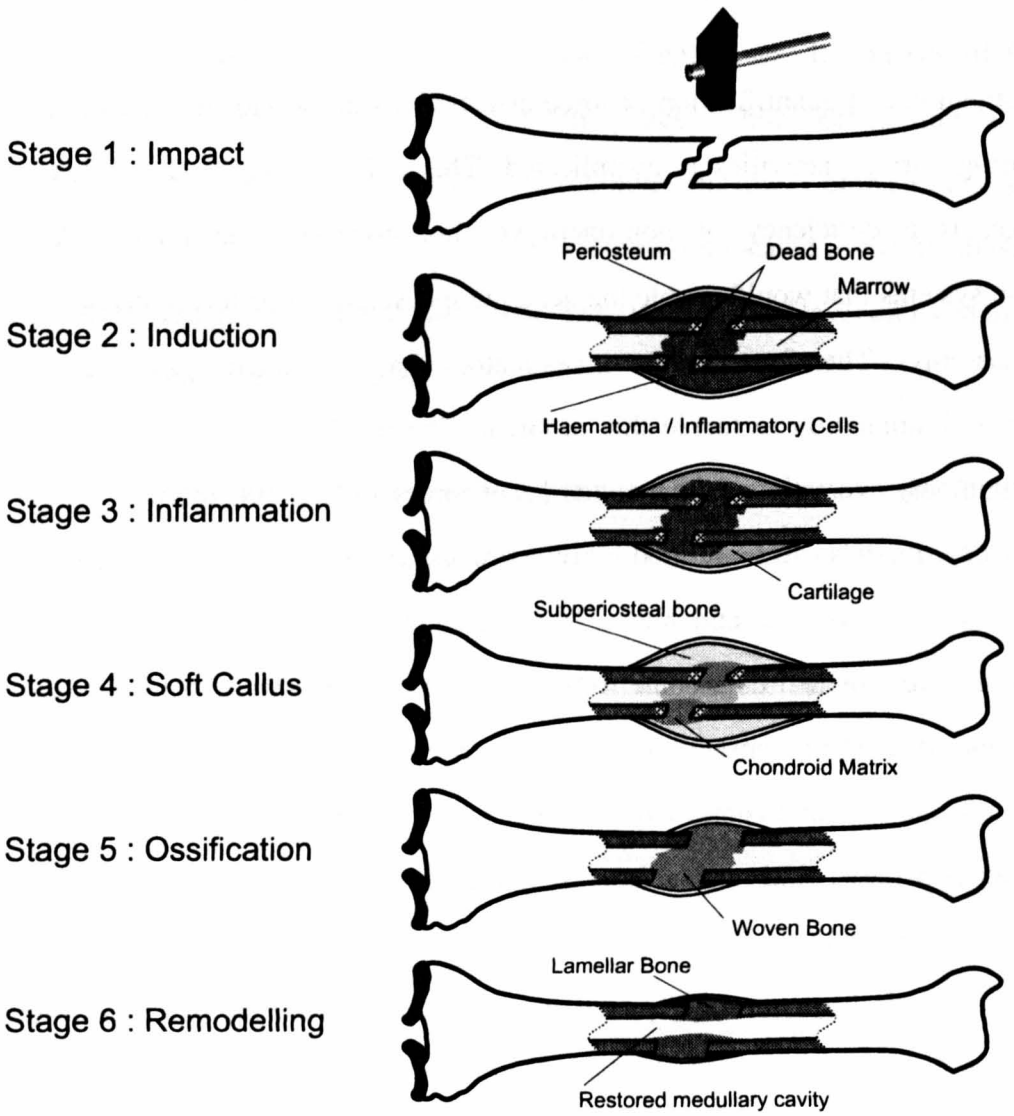


**Figure 4. Stages of long bone healing.**

## 2.3 Fractures and Healing

The remarkable property of bone healing is that the fracture is united, sometimes without a scar, and the bone is reconstructed [25]. Kenneth and Koval [26] outlined

the following six stages of bone fracture healing, Figure 4. The first stage is the impact when the bone absorbs enough energy for a bone tissue failure to be introduced. The energy level required to induce the bone failure is related to the volume of the bone and the rate of loading. The fractures formed can be classified based on the location and the pattern, Figure 5. Peri-articular fractures are located at the metaphysis or epiphysis of the bone. Those fractures are known as complex to stabilise due to restricted space available for fixation at bone ends. Fractures at the diaphysis are referred to as midshaft fractures. Based on pattern, fractures can be classified into transverse, oblique, spiral, comminuted and segmental.

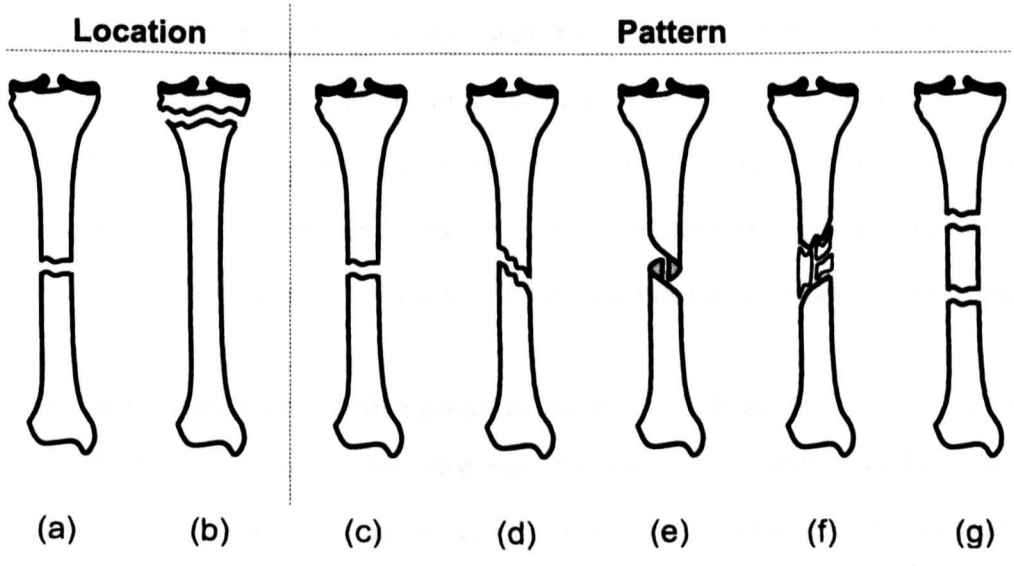


**Figure 5. Types of long bone fractures based on fracture location and pattern. a) midshaft, b) peri-articular, c) transverse, d) oblique, e) spiral, f) comminuted, g) segmental.**

Induction is the second stage of the healing process. It starts with the formation of a fracture haematoma and ends with the appearance of inflammatory cells approximately 48 hours from the impact. The third stage is inflammation. It begins with the influx of inflammatory cells and ends with the appearance of the bone and cartilage production. Stage four is known as the soft callus stage. It is characterised by the development of cartilage and bone tissue and is completed with a cessation of appreciable fracture motion. Stage five involves the conversion of the soft, largely chondroid, callus into woven bone via endochondral ossification. At the completion of this stage, the fracture is considered healed both clinically and radio-graphically.

The fracture strength is regarded as directly proportional to the amount of the new bone produced. Bone remodelling, the final stage, is a conversion of the woven bone to the lamellar bone. Unwanted bone is removed, and both the medullary cavity and the bone geometry are restored.

The fracture healing process itself is very complicated. Although it all starts with stage one and two, the way it progresses through stages three to five depends on a variety of factors which influence different types of healing. McKibbin [25] in his review on biology of fracture healing in long bones identified four healing processes.

Primary callus response is the first and fastest type of healing. It is initiated in the majority of fractures. Large amounts of callus beneath the periosteum are produced, trying to bridge the bone ends of the fracture. This type of healing is very tolerant of interfragmentary movement and total rigidity. However if the bone gap is not bridged within two weeks, primary callus response is likely to fail.

The second type of healing is the external bridging callus. It is initiated often with the primary callus response. This type of healing is also known as the 'natural' one [27], where callus is formed on the outside of the bone. Its major function is to join and immobilise the moving fragments of the bone. Healing by external bridging callus is tolerant of slight fracture motion, which can be achieved using external skeletal fixation. However, total rigidity at the fracture may lead to suppression of this type of healing. The success is highly dependent on the blood supply from surrounding tissues, as oxygen supply to the fracture site is one of the primary factors influencing successful union of the bone. External bridging callus, like primary callus formation, will not continue indefinitely unless the fracture is bridged. Once satisfactory bridging is achieved, the remodelling of the bone, stage 6, is initiated. Unwanted bone is removed and the geometry of the bone is restored to best effect.

Under conditions of higher stability, late medullary callus formation, the third type of healing, can be initiated. It is a slow process principally but not exclusively initiated from the intermediary cavity of the bone. In some cases, it follows failure of the external bridging callus formation. The unique properties of this type of healing are relative independence from mechanical influences and ability to replace fibrous tissues with new bone tissues.

In the case of extreme mechanical rigidity at the fracture site, primary cortical healing takes place. It is the slowest healing process of all four. During this type of healing, bone union is achieved by direct osteonal penetration. Normally, this healing process is supported by the medullary callus activity.

Since each fracture environment can differ significantly and undergo various mechanical stabilities, more than one type of healing may occur simultaneously or in sequence. The next section describes factors influencing the success and speed of bone fraction treatment.

## 2.4 Factors Influencing the Success of Fracture Healing

Once a bone is damaged or a fracture takes place, the new cells have to be laid out so that bone segments can unite, and the fracture can be bridged and repaired. The rate of fracture healing is dependant on a wide range of factors. They can be grouped into two main groups: systematic and local. Systematic factors relate to the overall condition of the patient's body systems. Such factors might be patient age, nutrition status, tobacco use, activity level, nerve function, hormones and drugs. The oxygen supply to the fracture site is of prime importance to the healing process and therefore properly-functioning oxygen intake and delivery systems of human anatomy are advantageous.

Local factors relate to conditions at the injury site. They would reflect the severity of the injury, *i.e.* soft tissue damage, bone loss, infection, local damage to vascular and

nerve tissue, local pathological conditions and the mechanical environment at the fracture site. Drugs can be used to promote and accelerate healing activities. One of the most important factors in the fracture healing is the controlled immobilisation and the bridging of ends of broken bone segments. This needs a correct mechanical environment at the fracture site and to some degree dictates, which healing process takes place. It is common practice to employ orthopaedic fixators for this purpose, and to align the bones correctly. The range of such fixators, their advantages, disadvantages and suitability are discussed below.

In addition to fixation of the fracture, additional mechanical or electrical stimulation can be applied in order to promote healing. To the author's knowledge, no statistically conclusive research has been done into electrical stimulation and therefore it is not possible to draw conclusions from this method. Nevertheless, experiments on animals suggest that electrical stimulation applied correctly can increase healing rates.

| Tissue | Young's modulus, MPa | Ultimate tensile strength, MPa | Ultimate tensile strain, % |
|---|---|---|---|
| Lamellar bone | 19620 | 127.53 | +2% |
| Cartilage | 490.5 | 14.715 | +10% |
| Granulated Tissue | 0.049 | 0.0981 | +100% |

**Table 1. Properties of human bone tissues**

On the other hand, mechanical stimulation, also know as dynamisation of the fracture anatomy, involves forced controlled relative motion between the ends of the fractured bone segments, also known as interfragmentary motion (IFM). It is specifically applicable to the external bridging callus type of healing as the IFM can stimulate callus formation. There have been many attempts to quantify the optimum magnitude of the IFM but so far no statistical conclusion can be drawn. Studies performed are very subjective and therefore it is hard to generalise the results. Motion in the axial direction of the bone is believed to help bone cell formation [9-

14, 16-18, 28]. Shear between bone interfaces is believed to be a destructive influence as it leads to formation of the fibro cartilage and possibly pseudarthrosis [10, 28-30]. Torsion and bending are more complicated to analyse as they involve both axial and shear displacements.

It was shown by Kenwright *et al* [31] that imposed interfragmentary motion has different effects at different stages of healing. Early fracture IFM (first 4-6 weeks) promotes high amounts of callus formation and helps healing [14]. However, once weight-bearing period starts, such IFM can delay fracture union [32] and therefore the fixation could be stiffened up. From the literature available to date, based on animals, clinical experience and modelling it can be concluded that the tolerable axial IFM for long bone ranges from 0.2 mm – 2 mm. In most cases displacements greater than 2 mm led to delayed union or non-union [32]. McKellop *et al* [27] have shown that during natural healing of tibia fractures, the elastic IFM ranges from 0.5 mm - 1.9 mm and also angulations or rotations from 0.7 to 1.2 degrees. Wolf *et al* [12] have found the optimum IFM of 0.5 mm for fractures with a gap size of 3 mm in their study on sheep diaphysal osteotomies. Claes *et al* [14] have shown that the size of the fracture gap plays an important role in determining optimum amplitude of axial displacement. Therefore, an interfragmentary strain (IFS) could be a better quantifying measure. Perren *et al* [33] have defined IFS as the IFM divided by the gap size. The reduction of the IFS from 45 % to 5 % during normal healing process was observed by Claes *et al* and Gardner *et al* [14, 15]. Claes *et al* [14] have explained such observation by splitting the healing into three stages based on the composition and the amount of callus formed. It was observed that as the bone healed, callus strength was increasing and the tolerance to strain was decreasing. Those results agree with bony tissue mechanical properties [19, 34, 35], presented in Table 1. These data suggest that granulated tissue, which forms in the early stage of healing, can tolerate high rates of strain of up to 100 %. However once fibrous tissues, tendon and cartilage surround the fracture, strain tolerance significantly decreases to 10 %, and once the lamellar bone is formed, the maximum strain

tolerance further decreases to 2 %. In addition, Claes *et al* [14] have looked into the quality of the newly laid bone and concluded that despite larger IFM-promoted higher rates of callus formation, tissue quality suffered.

## 2.5 Fracture Fixation

The bone fracture healing method, time, quality and geometry of union are highly dependent on fracture stabilization. An incorrect mechanical environment at the fracture site can lead to a deformity, delayed healing or a bone loss. Selection of the method of stabilization depends on a range of factors, such as the severity and complexity of damage to soft tissues and the bone, anatomical access restrictions and the perception of the patient.

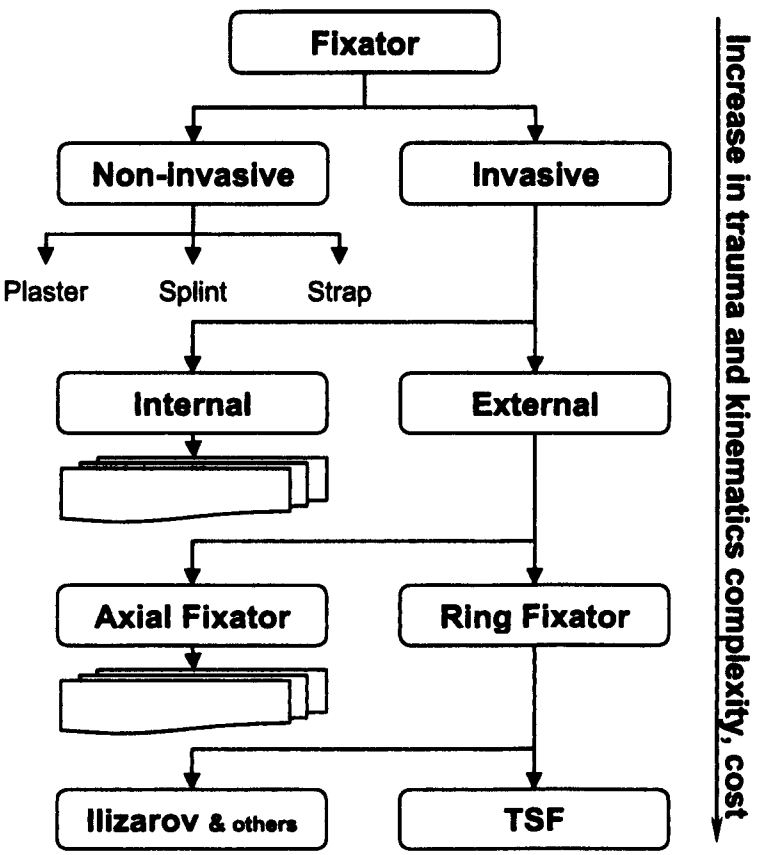


**Figure 6. Types of orthopaedic fixation.**

There is a wide range of commercially available orthopaedic fixators in the market today and each has its advantages and disadvantages. Figure 6 presents a flow chart

for the types of fixation used to date. As one progresses down the chart the cost of treatment, complexity of kinematics of fixation and severity of the injury increases.

First, all fixation methods can be classified into two groups: invasive and non-invasive. Non-invasive stabilization methods are suitable for treating relatively simple bone fractures. They provide the least control over the mechanical environment of the fracture, because they have no direct contact with the skeletal system. Positional control of the broken bone segments is performed via surrounding tissues and therefore is neither very accurate nor versatile. Non-invasive stabilization was one of the first methods used in medicine. Original methods included the use of a wooden bar/splint attached along the side of the anatomy using flexible ties. This type of method was not very effective because the wooden component did not follow the bone geometry and as a result, often badly-aligned union was achieved. A more advanced version of this type of stabilization has replaced the wooden component by a plaster cast. The plaster cast more successfully mimicked the shape of the bones and its surrounding tissues. If a long plaster cast was used it was possible to avoid unwanted angulations, however, there was very poor control over the length of the bone, axial rotation and position of the fractured bone segments. The advantage of non-invasive fixators is that they do not cause any direct damage to the anatomy; they are easy to assemble and use. They also avoid infection. However, there is a limit to control of the fracture due to the soft tissue properties and presence. The common type of healing for fractures stabilised with non-invasive fixation devices is external bridging callus.

Unlike to non-invasive fixators, invasive fixators penetrate the anatomy in order to establish direct connection with the skeletal system. They can be grouped into: internal and external, Figure 7.

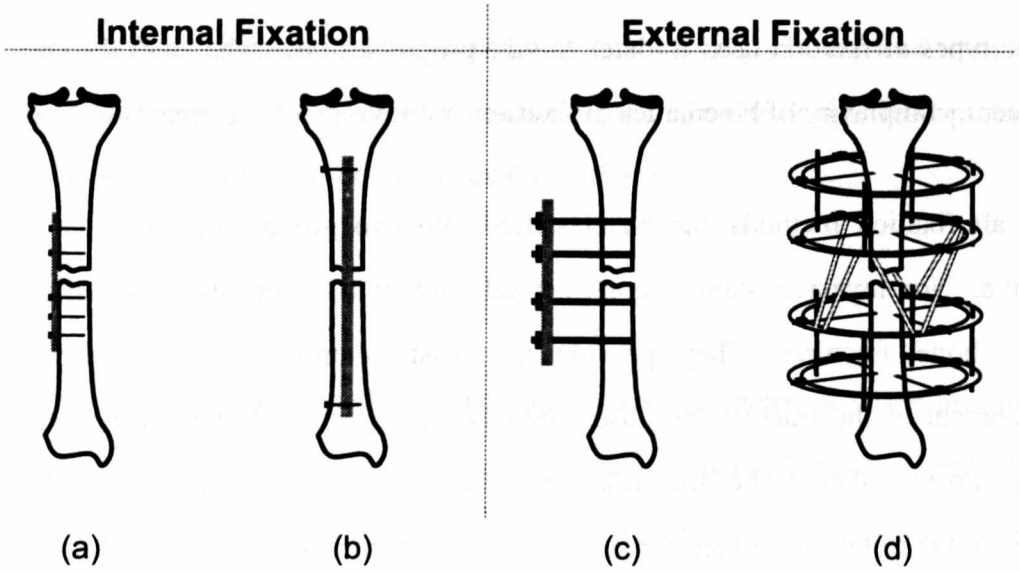


**Figure 7. Examples of invasive fracture fixation methods. a) plate and screws, b) intramedullary nail fixed with screws inside the bone, c) unilateral bar connected to bone via half-pins, d) TSF ring fixator with two accessory rings and connection to bone via 8 fine wires**

Examples of internal fixators would be intramedullary nails and plates. Those fixators are implanted into the limb anatomy for the healing period and act as a splint that shares the load with the bone. The advantages of internal fixators are excellent control over the position of the bone segments, early stability/rigidity and early usage of joints and muscles. Stress shielding, commonly experienced due to high plate stiffness, may lead to delayed union and poor bone formation. The stiff plate may also act as a 'stress raiser', causing a new fracture at the end of the plate. Primary cortical healing is often the mechanism by which fracture heals when plates are used. Hidaka and Gustilo [36] have shown that removal of plates introduces risks of re-fracture of the healed bone. Intramedullary nails (IMN) have an unassailable place in the management of fractures of the femoral shaft. This however is only true for the femur due to the anatomy of the blood supply to the shaft. For other bones, the IMN with or without reaming can interfere with the blood supply, which may negatively influence healing. Furthermore, it is not possible to perform bone transport, shortening, lengthening and postoperative deformity correction, unless a special IMN is used at a specialist treatment centre. The common healing

mechanisms when the IMN is used, are external bridging and later medullary callus formation.

The other group of the invasive fixators is external. These invade minimally human anatomy during treatment periods. The majority of the external fixator's structure (exoskeleton) is located outside the human anatomy. The exoskeleton is connected to the bone segments via fine wires and half/full pins. Axial external fixators (uniaxial / biaxial / monolateral), of which the geometry is normally parallel to the axis of the bone, are connected using pins. Advantages of the axial fixator are simple structure and simple kinematics. However, such fixation has low overall bending stiffness, which is significant since the main axis of the fixator is offset from the load axis of the bone. In addition, it is very complicated (even if possible at all) to perform deformity correction in more than one plane using such fixators. The axial fixators are simple in structure and suitable mainly for stabilising fractured bone segments where low loads are exhibited during treatment. It was observed by Khalily *et al* [7] that the stiffness of axial fixators decreases with increasing load. Since this type of fixator allows micromotion, the typical bone healing is by formation of external bridging callus.

In the present research, all attention is paid to ring fixators, as they are highly versatile, allowing post-operative adjustments. They, contrary to the axial fixators, become stiffer with increasing load [37]. The vertical axis of the ring fixator is aligned with the bone load axis, minimising unwanted bending effects observed in axial fixators. Subject to frame design, it is possible to change the mechanical properties of the frame during the treatment period. Since the exoskeleton of the fixator is located a few inches away from the anatomy, access to the skin and soft tissues is maintained, allowing access of fresh air and post-operative treatment of any damage or infection. Frames can be applied with minimal blood loss or soft tissue damage, due to small diameters of half-pins and fine wires. This in turn provides pain relief and early mobility.

The main disadvantages of the ring fixators are size, form, weight, pin tract infections, lack of means of assessing the fracture stability with the fixator *in situ* and high cost. Few types of ring fixators are available commercially to date. An Ilizarov fixator [10, 28] is one of the more popular ring fixators. It was pioneered by the Prof. Ilizarov in 1950s in the former USSR and has been used over the last 10 years in Europe and the USA. The Taylor Spatial Frame [38] is a recent introduction. Details of it are discussed below.

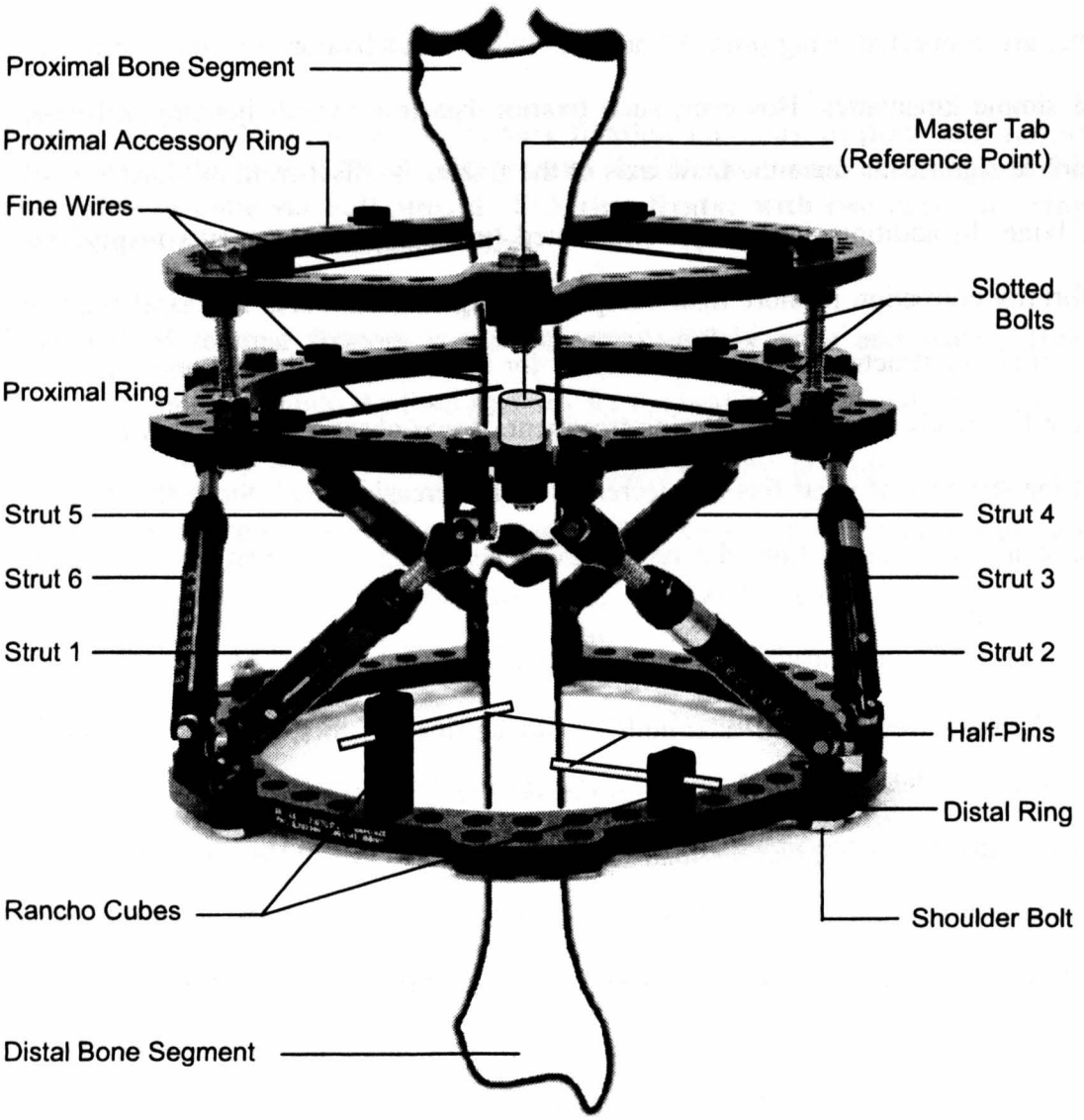


**Figure 8. Taylor Spatial Frame based fixator definitions. Front view.**

## 2.6 Taylor Spatial Frame

A Taylor Spatial Frame (TSF) [38] is the ring fixator introduced to the market by Smith and Nephew, Tennessee, USA, Figure 8. Its main structure is based on the Stewart-Gough platform [39, 40] and consist of two rings and six variable-length struts. The TSF's main application has been multiplanar deformity correction, although it is being used increasingly for fracture management. A range of ring sizes defined by the internal diameter is available: 80, 105, 130, 155, 180, 205, 230, 255 & 300 mm. In addition, the rings come in five different shapes, Figure 9. The struts come in four length groups: extra short (75-96 mm), short (90-125 mm), medium (116-178 mm) and long (169-283 mm). They are connected to the rings at the manufacturer's predefined locations using shoulder bolts. Shoulder bolts allow strut rotation around their major axis, since shoulder height is greater than the ring thickness.

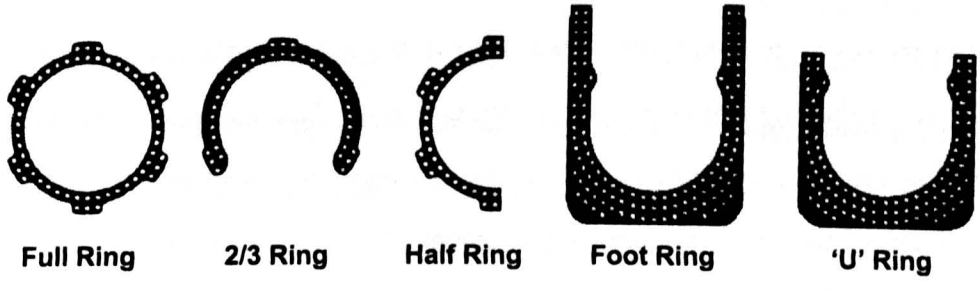


**Figure 9. Types of rings used to construct TSF. Top views.**

The choice of frame components is made by the surgeon and is based on the anatomy constraints and requirements of the injured limb. The connection between the TSF and the anatomy is established via bone-transfixing components: fine wires and/or half-pins. If a combination of half-pins and fine wires is used to transfix the broken bone segments to the TSF, it is common to refer to such a fixator as a hybrid. Fine wires are typically pretensioned in order to increase their stiffness response to axial loads (perpendicular to the wire major axis). They are clamped on the rings using slotted or cannulated bolts. Two wire types, based on section diameters, are available: 1.6 mm & 1.8 mm. Wires can be made either from stainless steel or

titanium alloy. Half-pins are fixed onto the rings using stacks of rancho cubes. Three types of half-pins are available: 4 mm, 5 mm & 6 mm in section diameter. To allow for greater segment stability and transfixing component anchorage space, accessory rings can be mounted on either side of the TSF.

The TSF's unique parallel kinematics enables all six degrees of geometric freedom (three spatial and three rotational) to be altered via variation of the lengths of the struts simultaneously. This gives the surgeon complete freedom to correctly orient and align broken bone segments, which should in principle lead to improved healing. Moreover, as compared to other mechanisms, Stewart-Gough platforms are known to have generally high stiffness and strength to mass ratios, which should increase patient mobility and comfort.

The frame is mounted and defined with reference to a master tab (reference point). The reference point is always located on the proximal (top) ring. Looking from the top, or in the distal direction, the closest strut to the left from the reference point is strut 1 and to the right of it is strut 2. Struts 3-6 are labelled anticlockwise from strut 2. The struts are arranged in such a way that they form sides of trapezoids. The parallel parts of the trapezoids are ring segments between the struts. Typically, one ring segment is significantly shorter than the other one, and therefore the trapezoid is similar to a triangle. This arrangement of struts allows for greater stability of the frame.

The clinical application method of the TSF based fixators is very similar to that of the well-established Ilizarov fixator [10, 28]. Both Ilizarov and TSF fixators use rings located around the injured limb to provide anchorage space for bone-transfixing components and to distribute the load from wires/pins to the longitudinal elements of the frame. Ilizarov rings are made from stainless steel or more recently carbon fibre. Steel rings are radio-opaque while carbon fibre ones are radio translucent allowing clear visualization of the x-rayed fracture. The TSF rings are

made from aluminium alloy and are only partially radio translucent. The same bone-transfixing components are used for both fixators. Typically, two wires or two half-pins are used per ring. Accessory rings can be mounted on either side of the fixators for greater stability and increased anchorage space. The standard straight Ilizarov configuration involves rings interconnected with four longitudinal elements (threaded rods). A hinge can be added to enable deformity correction with the Ilizarov fixator. However, deformity correction and fracture reduction using the Ilizarov fixator is complex and time consuming. Furthermore, it is hard (if possible at all) to correct deformity in more than one plane simultaneously. By contrast, the TSF's kinematics allow simple fracture reduction planning and execution in the full six degrees of freedom.

To sum up, there is a wide range of orthopaedic fixation devices available in the market today. The choice depends on location, type, severity and complexity of the fracture. Severe fractures have been treated successfully using the Ilizarov ring fixator over a number of years, but the TSF has yet further advantages and complications. The next chapter will address forward and inverse kinematics of the TSF that are non-intuitive and require a computer based solution.

# CHAPTER 3 : TSF KINEMATICS

The key to successful application of the TSF is its kinematics. The kinematics allow a surgeon to operate the TSF in six degrees of freedom while reducing a fracture or performing a deformity correction of the bone. There are two types of kinematics: forward and inverse. The forward kinematics relates the strut lengths to the position and orientation of one ring relative to the other, and so also the position and orientation of the bone segments. The general solution of the forward kinematics is complex and computationally intensive. The inverse kinematics relates TSF rings' positions and orientations in space to the strut lengths. The closed-form solution of the inverse kinematics is based on rudimentary vector algebra. The manufacturer of the TSF, Smith and Nephew (S&N), provides the surgeon with an internet tool for manipulating the fracture and the deformity. The closed-form solution to the inverse kinematics is directly implemented in the tool. The forward kinematics is solved via third party software, PRO Engineer [41]. S&N does not have a direct solution of the forward kinematics. Since the internet service is now widely available, it might appear to be sensible to use the online tool. However, at peak times, the service proves to be slow and incurs long waiting times and hence increased cost. This is especially the case for surgeons operating outside the USA, where servers, hosting the kinematics solution, are located. A failure of the internet service would render the TSF impossible to use, as the kinematics are not intuitive. Since S&N does not have their own solution to the forward kinematics, the distribution of the third party personal computer (PC) based software to individual surgeons is both costly and complicated. This chapter presents a solution to the forward kinematics that could eliminate the need for PRO Engineer and enable the distribution of the stand-alone PC applications to the individual surgeons, thus improving the reliability and speed of the kinematics solution.

## 3.1 Review of Previously Published Solutions

The TSF is a specialised form of the Stewart-Gough Platform (SGP) [39, 40]. It is known that the forward kinematics solution of the SGP has up to 40 roots in the complex space for a given set of strut lengths [42]. One of the more recent solution methods was presented by T. Y. Lee and J. K. Shim [43]. They used an algebraic elimination method to derive the $40^{th}$ degree univariate polynomial equation in order to solve the forward kinematics of the SGP. Other closed-form approaches are based on simplification of the SGP geometry. For example, P. Ji and H. Wu [44] obtained a closed-form solution for the SGP by introducing a quaternion to represent the transformation matrix and by restricting the geometry of the platform and the base to similar hexagons. Their method converged to eight possible solutions in the real domain.

In most control and TSF applications, it is not necessary to obtain all possible solutions of the position and orientation of one ring relative to the other, given six strut actuator lengths. Hence, numerical search methods for solving the forward kinematics are an attractive option. Numerical search methods perform best when a sufficiently close estimate of a solution is available and when only one answer is desired. A range of such methods applicable to the most general arrangement of the SGP was presented by J.P. Merlet in 1993 [45]. A Newton-Raphson method is one of the more popular numerical searches. It is based on the steepest gradient descent, and requires a derivative value of a function at every iteration. For multidimensional functions, the partial derivatives of the function are assembled into Jacobian matrix. Further details on the Newton-Raphson method are provided in Section 3.6.1. P. R. McAree *et al* [46] have developed a forward kinematics algorithm for a simplified 3-6 SGP, based on the Newton-Raphson numerical search method. The advantage of their algorithm was that the Jacobian matrix size was 3 by 3, which reduced significantly the number of floating point operations (FLOPS) required. A

comprehensive overview of the work done in the past on the kinematics can be found in Bhaskar Dasgupta's review [47].

Numerical search methods are frequently less computationally intensive compared to polynomial based solutions and therefore are more practical in real-time control applications [45]. However most of the numerical methods, which use gradient to obtain the direction towards solution, fail close to and at force-singular SGP configurations [46], where the SGP loses its stiffness. In 1978, Hunt [48] documented the first force-singular configuration, where the moving plate (ring) can rotate about the line intersected by all six links. In 1986, Fichter [49] found another force-singular configuration, which occurs when the moving plate, parallel to the base (reference ring), is rotated about the major SGP axis by ±90°. In 1988, Merlet [50, 51] used Grassmann Geometry to find force-singular configurations and he verified Hunt's and Fichter's results.

## 3.2 Kinematics and TSF Application Methods

Forward and inverse kinematics are used extensively when planning and applying the TSF. There are three methods (correction modes) of the TSF application to fracture management. They are named as: Chronic, Residual and Total Residual.

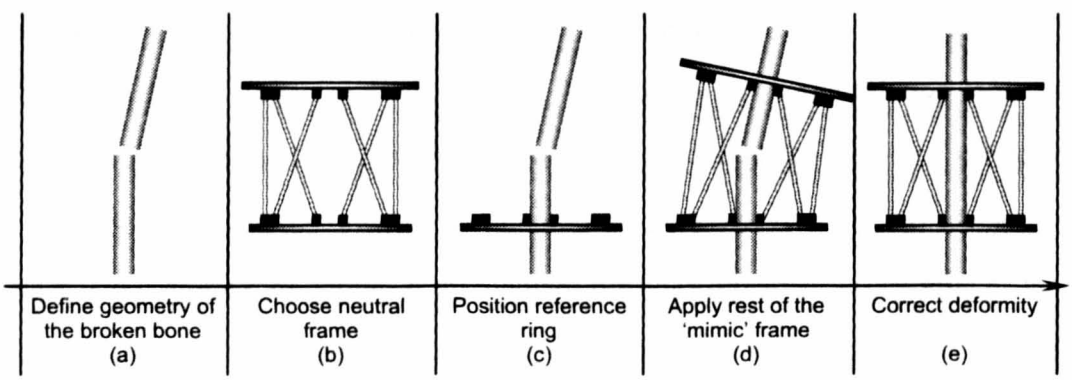


**Figure 10. Chronic TSF application mode**

In the Chronic mode, the frame is initially configured to mimic the fractured bone geometry and is then straightened, reducing both the fracture and the deformity.

Figure 10 presents the chronic method application sequence. Three groups of design parameters are used: fracture geometry, frame configuration (ring types, neutral frame height), and bone-frame position and orientation correlation. The neutral frame height is the parameter that describes the distance between the centres of the TSF rings when the frame is in the neutral configuration, *i.e.* when the rings are parallel and aligned with each other, forming a perfect cylinder. During application, the surgeon first acquires the geometry of the fracture and deformity of the bone using radiological means. Then the choice of frame components as well as neutral height is made. The frame-bone geometry is defined via the relative locations of the reference ring of the TSF and the reference fragment of the fractured bone. It is common practice to use the same type of reference for both the ring and the segment. Inverse kinematics is then used to transform the neutral frame geometry to mimic the fracture geometry, and only then, the frame is applied to the fractured bone. Finally, the frame is straightened to reduce the fracture and the deformity by bringing the TSF to the neutral configuration. Throughout the TSF Chronic application, only inverse kinematics is used, since the ring positions and orientations are known at all times. This is an elegant solution; however it requires precise ring positioning and orientating in order to achieve satisfactory bone segment alignment and positioning, and therefore is not always practical.

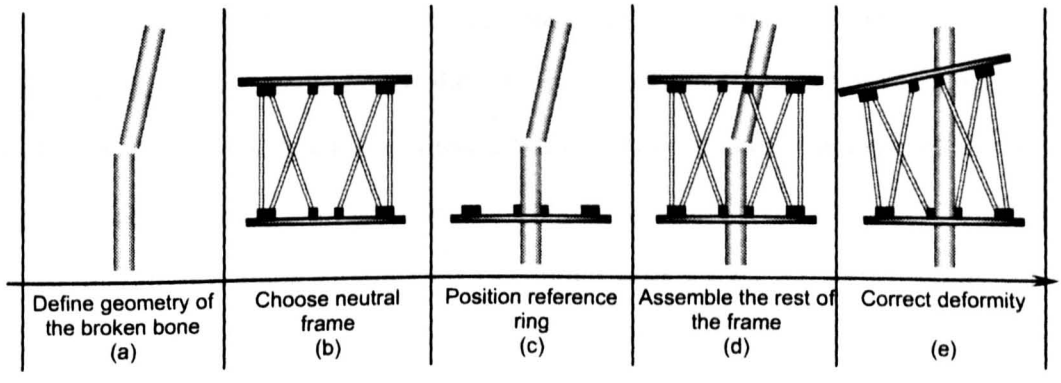


**Figure 11. Residual TSF application mode**

The Residual application method is similar to the Chronic one, except that the neutrally configured frame is first applied. The frame is then deformed in order to

reduce the fracture and the deformity. Figure 11 illustrates the application sequence. Again, three types of parameters are used: fracture geometry, frame configuration, and bone-frame position and orientation correlation. During application, the surgeon first acquires the geometry of the fracture. Then, the frame components and neutral frame height are chosen. This is followed by choice of frame location, which is defined by location of the reference ring relative to the reference segment of the fractured bone. The neutral frame is then applied. The frame is then deformed in order to reduce the fracture and correct the deformity. Throughout the process, only inverse kinematics is used, since the ring's position and orientation are always known. This is another elegant solution. However, it is restricted to small angle/displacement reduction and deformity correction of the broken bone that fits in the neutral frame configuration.

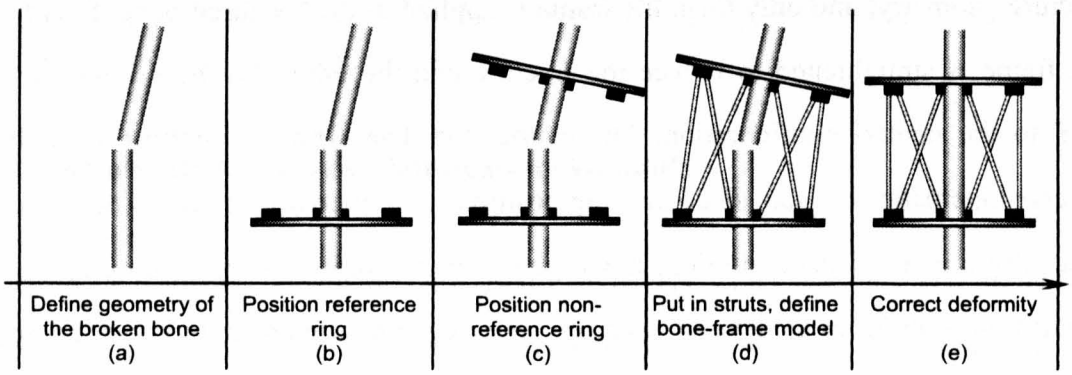


**Figure 12. Total Residual TSF application mode**

The third application is the Total Residual method. It is different from the first two since the surgeon has complete freedom of placement of the rings and therefore initial frame geometry. The frame configuration and fracture geometry parameters are used again. However, all six strut lengths of the initially applied frame are used instead of the neutral TSF height. Forward kinematics is used to process those six strut lengths in order to acquire applied frame geometry. Figure 12 illustrates a typical Total Residual application sequence. As with previously described methods, first the fractured bone geometry is obtained. This is followed by choice of the frame components. The two rings are then applied to the broken bone at clinically

appropriate locations and orientations. The choice of a reference ring and fragment is then made. The rings are then interconnected with six struts and their lengths are read. Forward kinematics is used to locate the non-reference ring position and orientation relative to the non-reference segment of the fractured bone. Finally, inverse kinematics is used to reduce the fracture by varying the geometry of the frame. The Total Residual method is the easiest and most convenient to use clinically. It is also more accurate than the Residual and Chronic methods.

## 3.3 Benefits of Solving TSF Kinematics

The currently provided kinematics solution for the TSF has two drawbacks: it is internet dependent and the placement of the TSF struts is restricted. It was observed in the Bristol Royal Infirmary that the online service is congested at the peak times of the day, resulting in long response delays.

The TSF struts have to be attached to the designated holes on the rings in order for the online tool to be able to solve the kinematics. Some cases require wire and half-pin placements that obstruct the designated strut connections. It is therefore important to be able to relocate the strut connection point while still being able to solve the kinematics and operate the fixator. This chapter looks at the conventional way of solving the kinematics using a numerical search approach and then describes a modification to the conventional method in order to achieve a higher computational efficiency and enable changes to the positions of the strut connection points.

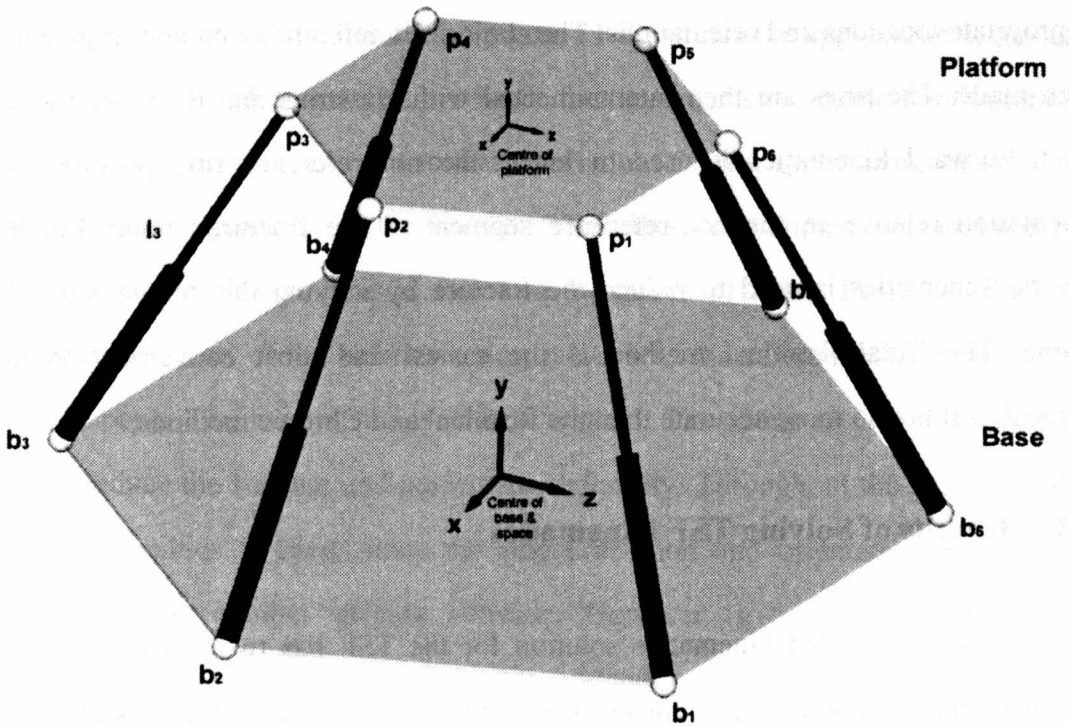


**Figure 13. General Stewart Gough platform geometric model definitions.**

## 3.4 Model Definitions

The solution presented here is derived for the most general configuration of the Stewart-Gough platform. The location of the distal ring of the TSF is regarded as fixed and forms a static base. The proximal ring is free to move and is referred as the platform. The choice of the platform and base can be reversed if required. The connection points between both the base and the platform can be placed arbitrarily, removing the current restriction of the TSF software. The generic model and its definitions, as used for this analysis, are presented in Figure 13. Cartesian homogeneous space is used, with a left hand coordinate system. The origin of the space is located at the centre of the base. The base $\mathbf{b}_{[6x4]}$ and the platform $\mathbf{p}_{[6x4]}$ matrices are defined by six vectors ($\mathbf{b}_{[ix4]} = [x_{bi}\ y_{bi}\ z_{bi}\ 1]$ and $\mathbf{p}_{[ix4]} = [x_{pi}\ y_{pi}\ z_{pi}\ 1]$, where $i = 1..6$) representing connection points relative to the base and platform centres respectively. The platform and the base are connected to each other via six independent variable length links/actuators. Each link is defined by a link vector $[x\ y\ z\ 1]$, which are combined to a links' matrix $\mathbf{L}_{[6x4]}$. Links are 3D pin jointed at the connection points and therefore are free to rotate about all three local axes. The

transformation vector $t = [\alpha\ \beta\ \gamma\ x\ y\ z]$ describes the set of rotations and translations required to position and orient the platform local centre relative to the space centre and is the solution of the forward kinematics. The first three elements represent rotations about $x$, $y$, $z$ axes respectively and the last three elements represent translations in $x$, $y$, $z$ directions. When the platform is oriented and translated according to the vector $t$, the order of the transformations follows the order of the vector elements. Since the base centre is aligned with the space centre, Equation 1 always holds true. Positions of connection points on the platform relative to the space centre can be found using Equation 2.

$$\mathbf{B}_{[6x4]} = \mathbf{b}_{[6x4]} \cdot \mathbf{T}(t_0)_{[4x4]} = \mathbf{b}_{[6x4]}, \quad \text{where} \quad t_0 = [0 \quad 0 \quad 0 \quad 0 \quad 0 \quad 0] \tag{1}$$

$$\mathbf{P}(t)_{[6x4]} = \mathbf{p}_{[6x4]} \cdot \mathbf{T}(t)_{[4x4]} \tag{2}$$

Where $\mathbf{T}_{[4x4]}$ is transformation matrix defined in Equation 3.

$$\mathbf{T}(t)_{[4x4]} = \mathbf{RotX}(t_{[1]})_{[4x4]} \cdot \mathbf{RotY}(t_{[2]})_{[4x4]} \cdot \mathbf{RotZ}(t_{[3]})_{[4x4]} \cdot \mathbf{Trans}(t_{[4]}, t_{[5]}, t_{[6]})_{[4x4]} \tag{3}$$

Where

$$\mathbf{RotX}(\alpha) = \begin{bmatrix} 1 & 0 & 0 & 0 \\ 0 & \cos(\alpha) & \sin(\alpha) & 0 \\ 0 & -\sin(\alpha) & \cos(\alpha) & 0 \\ 0 & 0 & 0 & 1 \end{bmatrix} \tag{4}$$

$$\mathbf{RotY}(\beta) = \begin{bmatrix} \cos(\beta) & 0 & -\sin(\beta) & 0 \\ 0 & 1 & 0 & 0 \\ \sin(\beta) & 0 & \cos(\beta) & 0 \\ 0 & 0 & 0 & 1 \end{bmatrix} \quad \textbf{(5)}$$

$$\mathbf{RotZ}(\gamma) = \begin{bmatrix} \cos(\gamma) & \sin(\gamma) & 0 & 0 \\ -\sin(\gamma) & \cos(\gamma) & 0 & 0 \\ 0 & 0 & 1 & 0 \\ 0 & 0 & 0 & 1 \end{bmatrix} \quad \textbf{(6)}$$

$$\mathbf{Trans}(x, y, z) = \begin{bmatrix} 1 & 0 & 0 & 0 \\ 0 & 1 & 0 & 0 \\ 0 & 0 & 1 & 0 \\ x & y & z & 1 \end{bmatrix} \quad \textbf{(7)}$$

## 3.5 Inverse Kinematics Solution

The aim of solving the inverse kinematics is to determine the lengths of the connecting links/struts of the TSF, knowing the location and orientation of the base and the platform. Once coordinates of the base and the platform connection points are transformed from local to global coordinate systems (relative to the space centre) using Equations 1 & 2, the link vector matrix $\mathbf{L}_{[6x4]}$ can be found using Equation 8.

$$\mathbf{L}(t)_{[6x4]} = \mathbf{P}(t)_{[6x4]} - \mathbf{B}_{[6x4]} \quad \textbf{(8)}$$

The link lengths can then be computed using Pythagoras' theorem as indicated in Equation 9.

$$l(t)_{[i]} = \left|\mathbf{L}(t)_{[i,:]}\right| = \sqrt{\mathbf{L}(t)_{[i,1]}^{\ 2} + \mathbf{L}(t)_{[i,2]}^{\ 2} + \mathbf{L}(t)_{[i,3]}^{\ 2}}, \quad i = 1..6 \tag{9}$$

Note: The fourth element of the link vector is disregarded as it is always zero, due to the homogenous space. This modification improves the computational efficiency of the Equation 9.

## 3.6 Forward Kinematics Solution

The aim of solving the forward kinematics is to find the platform's location and orientation relative to the base, given six connecting link lengths $l^*$. The ideal solution would be to invert directly the inverse kinematics solution. Unfortunately, straightforward inversion is not possible. Therefore, a Newton-Raphson multidimensional numerical search is employed to solve the forward kinematics of the most general SGP.

### 3.6.1 Background Information - Newton-Raphson Method

The Newton-Raphson numerical search method is based on the first two Taylor expansion series elements, presented in Equation 10. Its advantage is that it can find a root $x$ for any continuously differentiable function at a high convergence rate, given a close initial estimate.

$$f(x+h) \approx f(x) + f'(x) \cdot h, \quad \text{where} \quad h \quad \text{is} \quad \text{small} \tag{10}$$

Rearranging Equation 10, Equation 11 is obtained, which relates the change of a function variable to change of a function value.

$$\Delta f = f(x+h) - f(x) = f'(x) \cdot h \tag{11}$$

According to the Newton-Raphson search method, the function has to be minimised to zero, hence $f(x+h) = 0$, and hence the required change to achieve that is

$$h = -\frac{f(x)}{f'(x)} \tag{12}$$

By adding the value of $h$ to $x$, the root estimate is improved. The general Newton-Raphson equation for a 2D continuous differentiable function is presented in Equation 13.

$$x_{n+1} = x_n - \frac{f(x_n)}{f'(x_n)} \tag{13}$$

Using Equation 13 the iterative algorithm of the numerical search can be constructed, where subscript $n$ represents an iteration number. As an example Function 14, is considered for finding of a root.

$$f(x) = 10 \cdot x^2 - 4 \cdot x - 1000 = 0 \tag{14}$$

The function and algorithm graphical representations are presented in Figure 14a, with a starting point (initial guess of the root) $x$ = -51.

The same approach is valid for the n-dimensional problem.

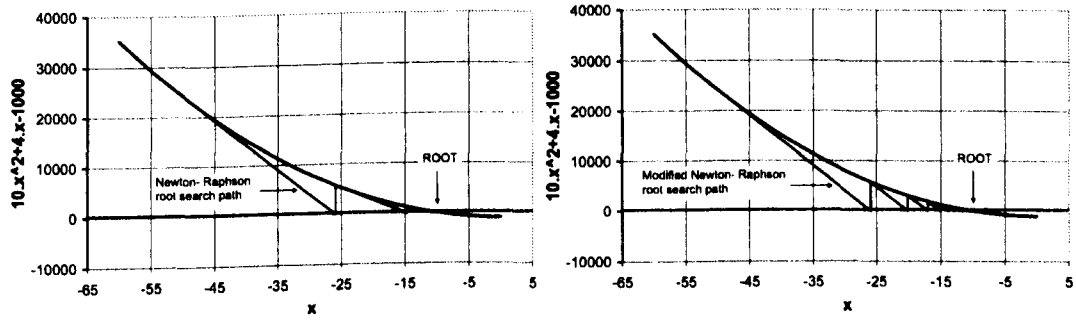


(a) (b)

**Figure 14. (a) – graphical representation of the steps performed by the Newton-Raphson search algorithm; (b) – Graphical representation of the steps performed by the modified Newton-Raphson search algorithm.**

### 3.6.2 Solving TSF Forward Kinematics Using Newton-Raphson Method

In the case of the TSF forward kinematics, the function to be minimised is the error vector $E(t)$ computed as a difference between the link lengths at the estimated position and orientation of the platform $t$ and the desired (given) link lengths $l^*$. Its symbolical representation is Equation 15.

$$E(t) = l(t) - l^* \Rightarrow 0 \tag{15}$$

Using the first two elements of the Taylor expansion series, Equation 15 is linearised.

$$E(t_{n+1}) = E(t_n) + \frac{\mathrm{d}E(t_n)}{\mathrm{d}t} \cdot \Delta t \tag{16}$$

A subscript $n$ next to the transformation vector $t$ represents the iteration number.

Rearranging Equation 16, Equation 17 is obtained:

$$\Delta E = E(t_{n+1}) - E(t_n) = \frac{\mathrm{d}E(t_n)}{\mathrm{d}t} \cdot \Delta t \qquad (17)$$

The error value has to be minimised to zero (Newton-Raphson method), therefore $\Delta E = -E(t_n)$. Hence,

$$E(t_n) = -\frac{\mathrm{d}E(t_n)}{\mathrm{d}t} \cdot \Delta t_n \qquad (18)$$

Multiplying both sides by the inverse of the error vector derivative with respect to transformation vector elements ($\alpha\ \beta\ \gamma\ x\ y\ z$), an improvement of the transformation vector is obtained.

$$\Delta t_n = -\left(\frac{\mathrm{d}E(t_n)}{\mathrm{d}t}\right)^{-1} \cdot E(t_n) \qquad (19)$$

The improvement $\Delta t$ to the estimated transformation vector $t$ is then used to refine the forward kinematics solution. Equation 20 is the core of the iterative numerical search.

$$t_{n+1} = t_n + \Delta t_n \qquad (20)$$

$\mathrm{d}E(t_n)/\mathrm{d}t$ is the Jacobian matrix $\mathbf{J}_{[6x6]}$ of the function $E(t)$, and is defined by Equation 21.

$$\frac{d\,\boldsymbol{E}(t)}{d\,t} = \mathbf{J}_{[6x6]} = \begin{bmatrix} \frac{\partial \boldsymbol{E}(t)}{\partial \alpha}_{[1]} & \frac{\partial \boldsymbol{E}(t)}{\partial \beta}_{[1]} & \frac{\partial \boldsymbol{E}(t)}{\partial \gamma}_{[1]} & \frac{\partial \boldsymbol{E}(t)}{\partial x}_{[1]} & \frac{\partial \boldsymbol{E}(t)}{\partial y}_{[1]} & \frac{\partial \boldsymbol{E}(t)}{\partial z}_{[1]} \\ \frac{\partial \boldsymbol{E}(t)}{\partial \alpha}_{[2]} & \frac{\partial \boldsymbol{E}(t)}{\partial \beta}_{[2]} & \frac{\partial \boldsymbol{E}(t)}{\partial \gamma}_{[2]} & \frac{\partial \boldsymbol{E}(t)}{\partial x}_{[2]} & \frac{\partial \boldsymbol{E}(t)}{\partial y}_{[2]} & \frac{\partial \boldsymbol{E}(t)}{\partial z}_{[2]} \\ \frac{\partial \boldsymbol{E}(t)}{\partial \alpha}_{[3]} & \frac{\partial \boldsymbol{E}(t)}{\partial \beta}_{[3]} & \frac{\partial \boldsymbol{E}(t)}{\partial \gamma}_{[3]} & \frac{\partial \boldsymbol{E}(t)}{\partial x}_{[3]} & \frac{\partial \boldsymbol{E}(t)}{\partial y}_{[3]} & \frac{\partial \boldsymbol{E}(t)}{\partial z}_{[3]} \\ \frac{\partial \boldsymbol{E}(t)}{\partial \alpha}_{[4]} & \frac{\partial \boldsymbol{E}(t)}{\partial \beta}_{[4]} & \frac{\partial \boldsymbol{E}(t)}{\partial \gamma}_{[4]} & \frac{\partial \boldsymbol{E}(t)}{\partial x}_{[4]} & \frac{\partial \boldsymbol{E}(t)}{\partial y}_{[4]} & \frac{\partial \boldsymbol{E}(t)}{\partial z}_{[4]} \\ \frac{\partial \boldsymbol{E}(t)}{\partial \alpha}_{[5]} & \frac{\partial \boldsymbol{E}(t)}{\partial \beta}_{[5]} & \frac{\partial \boldsymbol{E}(t)}{\partial \gamma}_{[5]} & \frac{\partial \boldsymbol{E}(t)}{\partial x}_{[5]} & \frac{\partial \boldsymbol{E}(t)}{\partial y}_{[5]} & \frac{\partial \boldsymbol{E}(t)}{\partial z}_{[5]} \\ \frac{\partial \boldsymbol{E}(t)}{\partial \alpha}_{[6]} & \frac{\partial \boldsymbol{E}(t)}{\partial \beta}_{[6]} & \frac{\partial \boldsymbol{E}(t)}{\partial \gamma}_{[6]} & \frac{\partial \boldsymbol{E}(t)}{\partial x}_{[6]} & \frac{\partial \boldsymbol{E}(t)}{\partial y}_{[6]} & \frac{\partial \boldsymbol{E}(t)}{\partial z}_{[6]} \end{bmatrix}$$

**(21)**

The first element of the Jacobian matrix is

$$\frac{\partial \boldsymbol{E}(t)}{\partial \alpha}_{[1]} = \frac{\partial \left| \mathbf{L}(t)_{[1,:]} \right|}{\partial \alpha} \qquad \textbf{(22)}$$

Substituting Equation 9 into 22 and performing initial differentiation, Equation 24 is obtained.

$$\frac{\partial \boldsymbol{E}(t)}{\partial \alpha}_{[1]} = \frac{\partial \left( \mathbf{L}(t)^2_{[1,1]} + \mathbf{L}(t)^2_{[1,2]} + \mathbf{L}(t)^2_{1,3} \right)^{0.5}}{\partial \alpha} \qquad \textbf{(23)}$$

$$\frac{\partial E(t)}{\partial \alpha}_{[1]} = \frac{0.5}{\left(\mathbf{L}(t)_{[1,1]}^2 + \mathbf{L}(t)_{[1,2]}^2 + \mathbf{L}(t)_{1,3}^2\right)^{0.5}} \cdot \left( 2 \cdot \mathbf{L}(t)_{[1,1]} \cdot \frac{\partial \mathbf{L}(t)_{[1,1]}}{\partial \alpha} + 2 \cdot \mathbf{L}(t)_{[1,2]} \cdot \frac{\partial \mathbf{L}(t)_{[1,2]}}{\partial \alpha} + 2 \cdot \mathbf{L}(t)_{[1,3]} \cdot \frac{\partial \mathbf{L}(t)_{[1,3]}}{\partial \alpha} \right)$$

**(24)**

Rearranging and simplifying renders Equation 25:

$$\frac{\partial E(t)}{\partial \alpha}_{[1]} = \frac{1}{\left|\mathbf{L}(t)_{[1,:]}\right|} \cdot \left( \mathbf{L}(t)_{[1,1]} \cdot \frac{\partial \mathbf{L}(t)_{[1,1]}}{\partial \alpha} + \mathbf{L}(t)_{[1,2]} \cdot \frac{\partial \mathbf{L}(t)_{[1,2]}}{\partial \alpha} + \mathbf{L}(t)_{[1,3]} \cdot \frac{\partial \mathbf{L}(t)_{[1,3]}}{\partial \alpha} \right)$$

**(25)**

Substituting Equation 1, 2 & 8 into Equation 25, the Equation 26 is obtained for the first Jacobian matrix element.

$$\frac{\partial E(t)}{\partial \alpha}_{[1]} = \frac{1}{\left|\mathbf{L}(t)_{[1,:]}\right|} \cdot \left( \mathbf{L}(t)_{[1,1]} \cdot \left( \mathbf{p}_{[1,:]} \cdot \frac{\partial \mathbf{T}(t)}{\partial \alpha} \right)_{[1]} + \mathbf{L}(t)_{[1,2]} \cdot \left( \mathbf{p}_{[1,:]} \cdot \frac{\partial \mathbf{T}(t)}{\partial \alpha} \right)_{[2]} + \mathbf{L}(t)_{[1,1]} \cdot \left( \mathbf{p}_{[1,:]} \cdot \frac{\partial \mathbf{T}(t)}{\partial \alpha} \right)_{[3]} \right)$$

**(26)**

Equation 26 can be further simplified symbolically to Equation 27.

$$\frac{\partial E(t)}{\partial \alpha}_{[1]} = \frac{1}{\left|\mathbf{L}(t)_{[1,:]}\right|} \cdot \mathbf{L}(t)_{[1,:]} \cdot \left( \mathbf{p}_{[1,:]} \cdot \frac{\partial \mathbf{T}(t)}{\partial \alpha} \right) \tag{27}$$

Equations for all other Jacobian matrix elements can be derived similarly, and therefore the general equation for the Jacobian element in row $r$ and column $c$ is:

$$\mathbf{J}_{[r,c]} = \frac{1}{\left|\mathbf{L}(t)_{[r,:]}\right|} \cdot \mathbf{L}(t)_{[r,:]} \cdot \left( \mathbf{p}_{[r,:]} \cdot \frac{\partial \mathbf{T}(t)}{\partial t_{[c]}} \right) \tag{28}$$

Equation 28 can be further optimised for the elements of the Jacobian matrix in columns 4 to 6 inclusively. The optimisation is based on the simplicity of the translation matrix (Equation 7) and therefore transformation matrix (Equation 3) partial derivatives with respect to translations along $x$, $y$ and $z$ axes. The partial derivate with respect to any of the principal translation vectors results in unity in the direction of the chosen translation and zero in other directions. For example, the partial derivative of the transformation matrix **T** with respect to $x$ is represented in Equation 29.

$$\frac{\partial \mathbf{T}(t)}{\partial x} = \begin{bmatrix} 0 & 0 & 0 & 0 \\ 0 & 0 & 0 & 0 \\ 0 & 0 & 0 & 0 \\ 1 & 0 & 0 & 0 \end{bmatrix} \tag{29}$$

Therefore, Equation 28 can be reduced to Equation 30 for Jacobian matrix elements in columns 4-6 inclusively. This optimisation increases computational efficiency.

$$\mathbf{J}_{[r,c]} = \frac{1}{\left|\mathbf{L}(t)_{[r,:]}\right|} \cdot \left( \mathbf{L}(t)_{[r,c-3]} \right) \quad \text{for} \quad c = 4,5\&6 \tag{30}$$

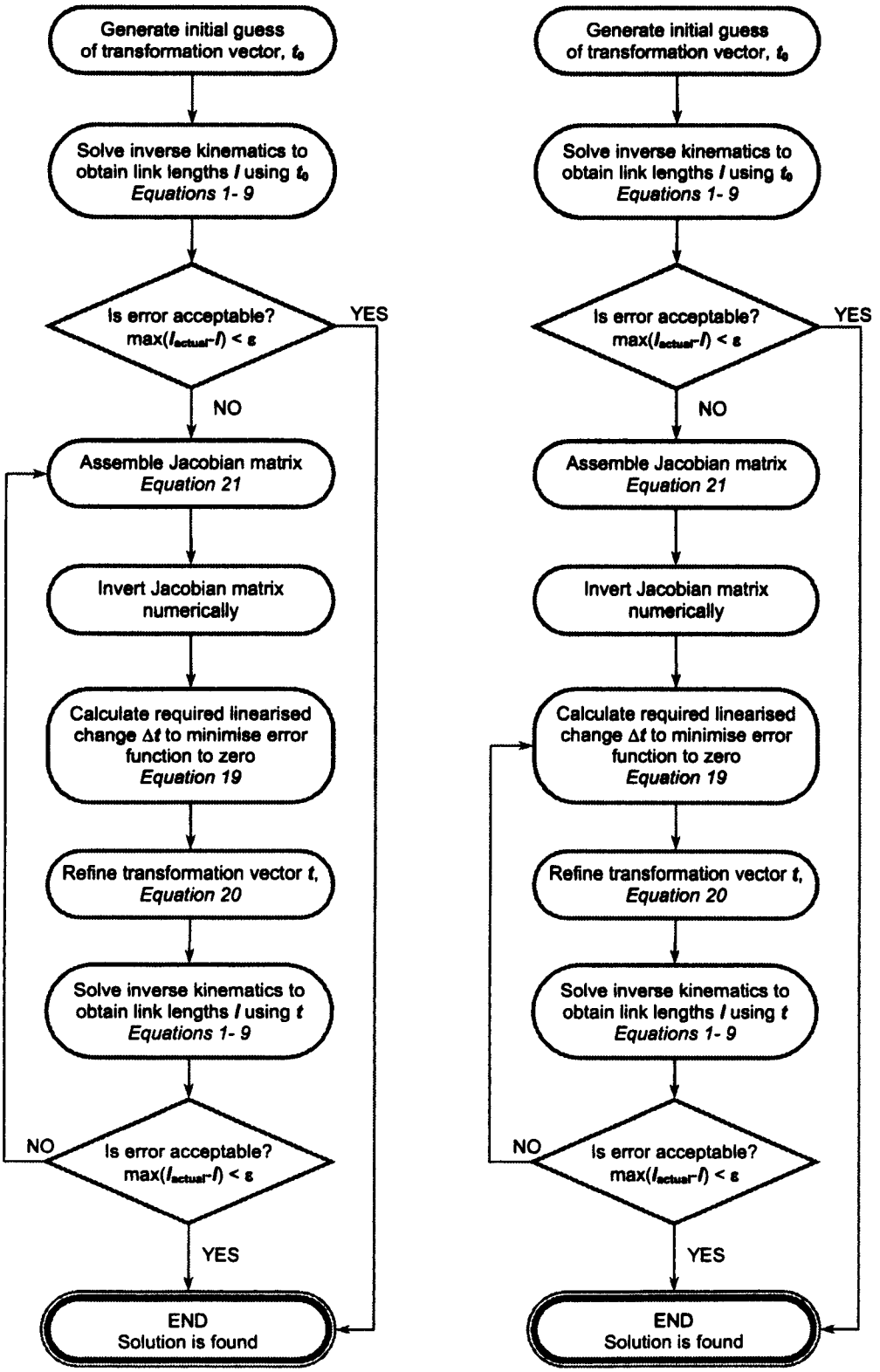


**Figure 15. Flowcharts of two TSF forward kinematics algorithms. (a) – based on Newton-Raphson method; (b) – based on modified Newton-Raphson method.**

### 3.6.3 Implementation of the Newton-Raphson Algorithm in a Computer Program

The logical sequence of the algorithm for solving forward kinematics of the TSF using the Newton-Raphson search method is presented in Figure 15a. Once an initial guess of the platform transformation vector $t_0$ is formed, the inverse kinematics is solved. The error is then calculated by taking the maximum absolute difference between desired (given) link lengths and current link lengths at the estimated position and orientation of the platform $t_0$. If the error is unacceptable, then the first Newton-Raphson iteration is carried out. The direction towards the root (solution) is obtained by assembling and inverting the Jacobian matrix of the TSF error function at the current platform position and orientation $t_0$. The required change to improve the $t_0$ estimate is then calculated by solving a set of linear equations according to the multidimensional Newton-Raphson search algorithm. The improvement is then applied to the $t_0$ resulting in $t_1$. Again, the maximum absolute error between the desired link lengths and the link lengths at the new estimate of $t$ is compared against the numerical accuracy requirement. For cases where the error is unacceptable, an additional Newton-Raphson iteration is carried out. This sequence is repeated until the error converges below the required tolerance, and the algorithm stops.

The algorithm was implemented in Matlab. Table 2 presents the numerical overhead assessment of the algorithm steps based on the count of the floating point operations (FLOPS). FLOPS were counted using Matlab's built-in functions. The assembly and inversion of the Jacobian matrix of the TSF are the most computationally intensive steps. To tackle this, an alternative algorithm, presented in the next section, is considered.

| Operation | FLOPS |
|---|---|
| Calculate the error between given link lengths and the link lenghts obtained using inverse kinematics at $t$ – Equation 15 | 285 |
| Calculate Jacobian matrix at the $t$ – Equation 21 | 990 |
| Invert Jacobian matrix numerically | 667 |
| Calculate the required linearised change to the $t$ in order to minimise the error function – Equation 19 | 72 |
| Refine transformation vector $t$ – Equation 20 | 6 |

**Table 2. FLOPS assessment of the forward kinematics solution steps.**

### 3.6.4 Implementation of the Modified Newton-Raphson Algorithm in a Computer Program

The assumption of the modification is that the Newton-Raphson algorithm presented in the previous section is capable of obtaining the correct direction for the minimisation of the error function in the first iteration, as suggested by Merlet [45]. In the 2D function case, the gradient is worked out only once at the starting point (initial guess/estimate of the root) and then reused for every other iteration, Figure 14b. As can be seen, the number of iterations required to obtain the root is higher than when using the standard Newton-Raphson search method. In a 2D case, such a modification does not add any computational efficiency. However, for high dimensional spaces this might not be the case, since the most computationally demanding steps, assembly and inversion of the Jacobian matrix, are performed only once. The flow chart of the modified algorithm for solving forward kinematics of the TSF is presented in Figure 15b.

## 3.7 Forward Kinematics Solution's Benchmarks

Both numerical search algorithms for solving forward kinematics were implemented in Matlab and were benchmarked against each other. A total of 50000 frame configurations were generated within the usable workspace of the TSF. A 155 mm TSF ring was used for both distal and proximal rings during simulation. The axial distance between ring centres (frame height) was varied in the range of 100 mm – 150 mm. The translational distance (in the ring plane) between ring centres was varied in the range of +/-75 mm. The maximum rotation was restricted to angles of +/-70° in coronal, +/-70° in sagittal and +/-80° in axial planes. The resulting set of configurations has covered conservatively the usable TSF geometry range presented by Feldman *et al* [52]. For each configuration the forward kinematics were solved for a range of initial estimates of the transformation vector. An initial estimate of the forward kinematics solution was calculated by offsetting the true solution with a percentage error of the range. The iteration count, FLOPS count and error convergence were recorded. The gathered data were analysed and the following performance comparisons were carried out:

a) An iterations count comparison for both algorithms based on the error of the initial estimate of the transformation vector: Figure 16.

b) FLOPS count comparison for both algorithms based on the error of the initial estimate of the transformation vector: Figure 17.

c) Failure rate of the modified Newton Raphson algorithm for cases where the standard Newton Raphson algorithm succeeds and vice versa, depending on the error of the initial estimate of the transformation vector: there were no failures recorded for either algorithm within the tested workspace.

d) Convergence comparison of the two algorithms:

- Sum of squared errors versus error of the initial estimate of the transformation vector: Figure 18a.

- Sum of squared errors convergence rate versus error of the initial estimate of the transformation vector: Figure 18b.

The fractional error was calculated by taking the difference between the initial estimate of solution and the true solution and dividing by the workspace range.

The FLOPS count was performed using Matlab's built-in functions.

## 3.8 Discussion of Benchmark Results

Both algorithms were successfully tested within the TSF designated operational space.

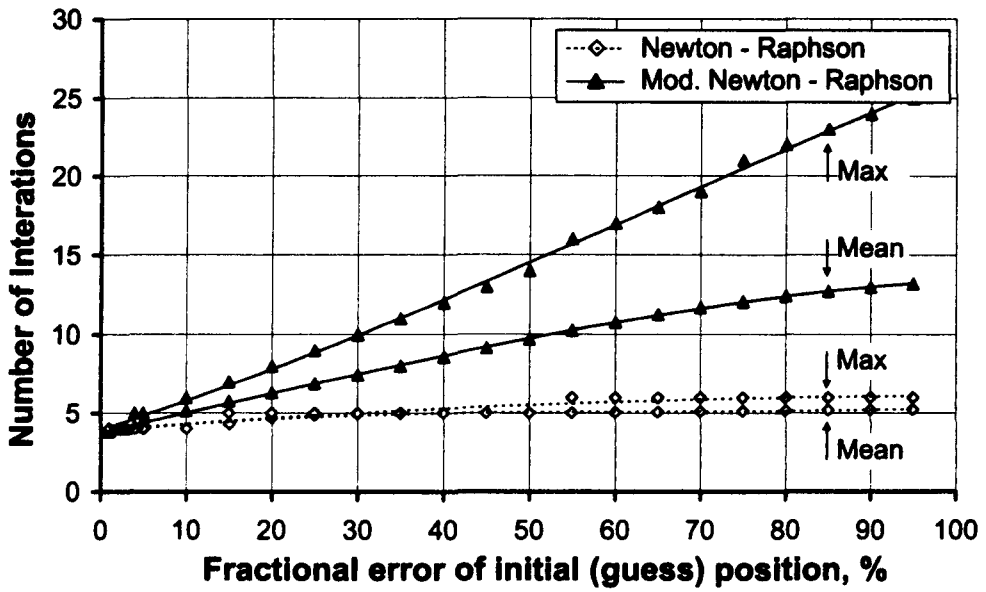


**Figure 16. Graph of the error (%) of an initial estimate of the transformation vector for the platform's position and orientation versus mean and max numbers of iterations taken for algorithms to arrive at the solution for 50000 random cases. Link accuracy tolerance was set to 1 μm (micron).**

Figure 16 suggests that the more accurate initial guesses of the platform positions and orientations required fewer iterations for both algorithms to arrive at a solution. On average, four iterations were required for both algorithms to find a solution given very accurate initial estimates (1% error). Overall, the Newton-Raphson algorithm required fewer iterations to converge to a solution when compared to the modified

Newton-Raphson algorithm. The number of iterations required for the modified Newton-Raphson algorithm significantly increased as the initial estimate of the position and orientation of the platform became less accurate. Finally, the Newton-Raphson algorithm maximum iteration count follows closely the mean count. This is not the case for the modified Newton-Raphson algorithm.

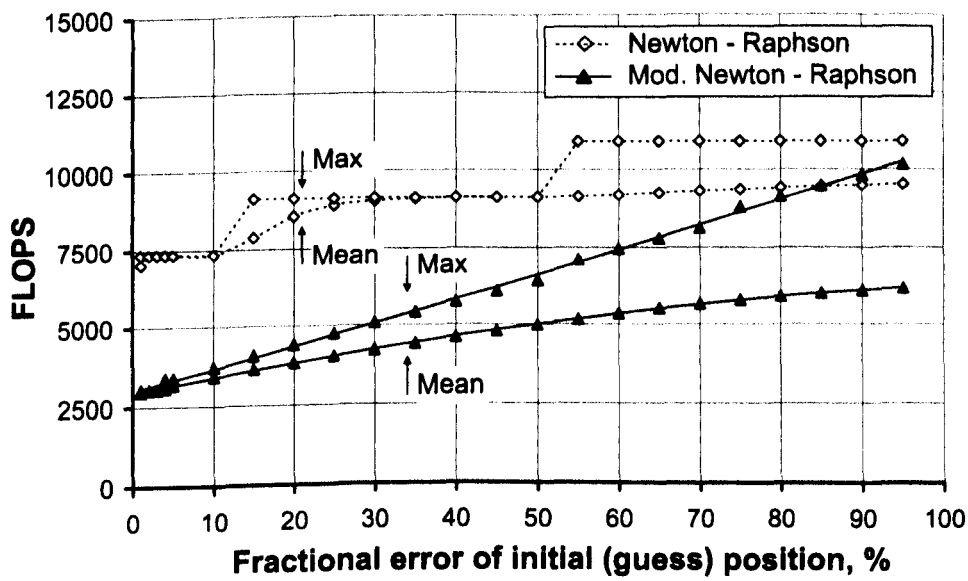


**Figure 17. Graph of the error (%) of an initial estimate of the transformation vector for the platform position and orientation versus mean and max numbers of floating point operations taken for both algorithms to arrive at the solution for 50000 random cases. Link accuracy tolerance was set to 1 μm (micron).**

As can be seen from Figure 18, a second or higher order error convergence rate was achieved easily using the Newton-Raphson algorithm. In our case, the 1 μm link length positioning accuracy was achieved within 4 iterations, given a very crude starting estimate of the transformation vector. The error convergence rate was reasonably constant and independent of the accuracy of the initial estimate. In the case of the modified Newton-Raphson algorithm, the error convergence rate was at least an order less than that of the Newton-Raphson algorithm. The tendency towards unity can be observed as the number of iterations increased.

In terms of floating point operations (FLOPS), the modified Newton-Raphson algorithm proved to be more computationally efficient. Figure 17 presents the mean

and maximum floating point operation counts based on the error of the initial estimate of the platform position and orientation. Again, the more accurate the initial estimate was, the fewer FLOPS were required for both algorithms to arrive to a solution. The modified Newton-Raphson algorithm was computationally more efficient by an average factor of two. In the case of the maximum FLOPS, it should be noted that as the error of the initial estimate increased, the difference in FLOPS number between the two tested algorithms decreased. An additional computational improvement for the modified Newton-Raphson algorithm could be achieved by monitoring the sum of errors squared convergence. If the sum of errors squared increases relative to the previous value of the sum any two times during the numerical search, an additional Jacobian matrix and its inverse would be calculated at the last known configuration.

The modified Newton-Raphson algorithm was implemented in the C# programming language. The average solution time was measured using a PC with Intel Centrino 900 Mhz processor and Windows XP Pro operating system. The results range from 1 to 5 milliseconds, which is more than adequate for the use of the surgeon. The author believes that the computational efficiency of the algorithms can be significantly increased by more efficient coding and inversion of the Jacobian matrix. The implemented algorithm was verified side by side with the online tool provided by S&N. A 100 % agreement of kinematics results was achieved between the two sources. The software with the graphical user interface was written by the author for use of the kinematics solution in a clinical environment and screen shots of it are presented in APPENDIX A.

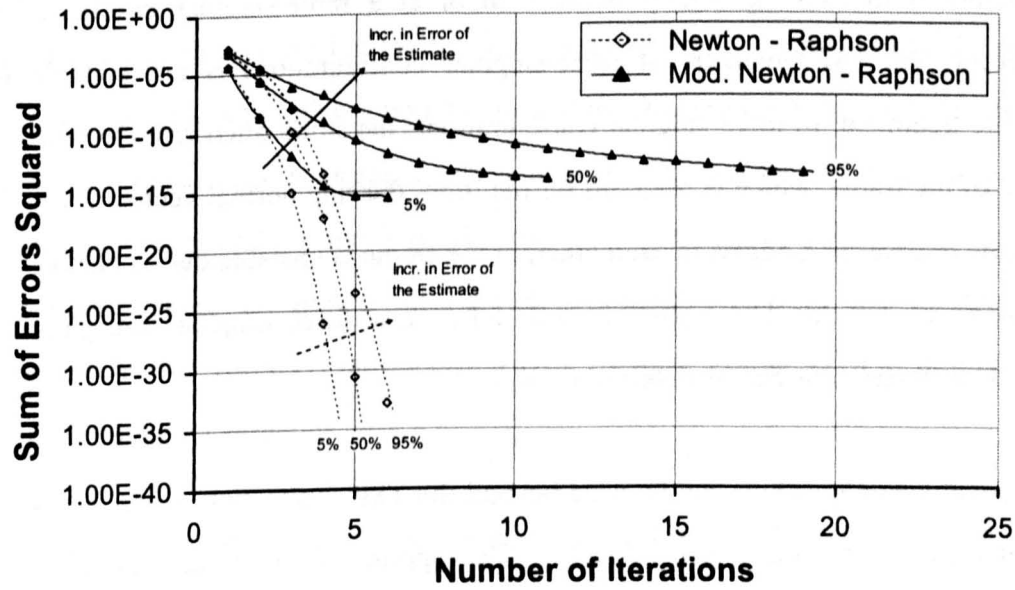


(a)

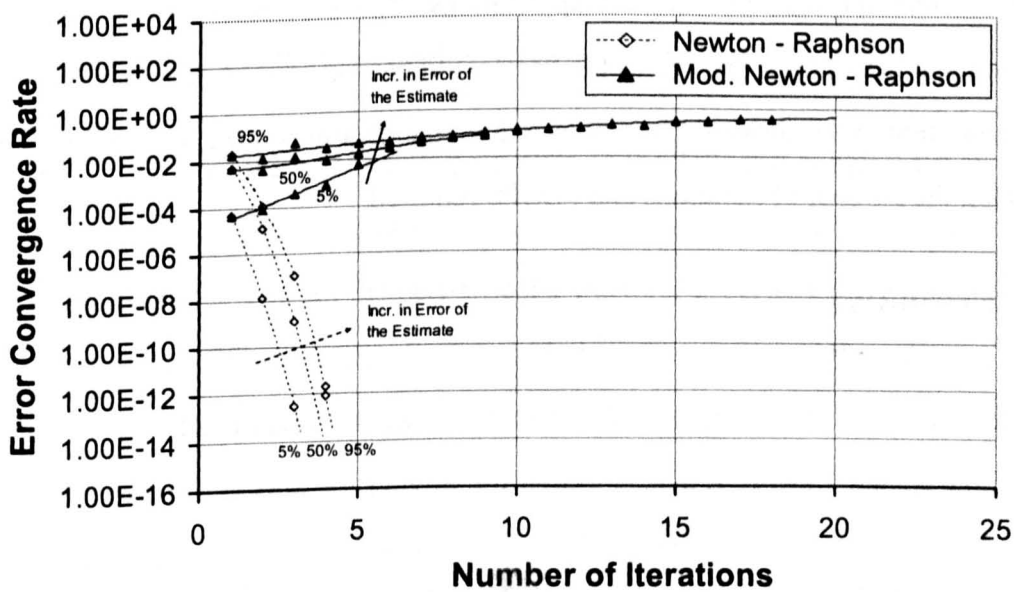


(b)

**Figure 18. Graphs of (a) – iteration count versus mean sum of errors squared of the link lengths for both algorithms for three types of estimates of the transformations vector: 5, 50, 95 % fractional error; (b) – iteration count versus inverse rate of mean sum of errors squared convergence of the link lengths for both algorithms for three types of initial estimates of the transformation vector: 5, 50, 95 % fractional error.**

Both the Newton-Raphson and the modified Newton-Raphson algorithms are prone to failure if the TSF geometry is close to or at a force-singular configuration. However, the TSF geometry at force-singular configurations is not suitable for fracture treatment. In force-singular configurations, the struts often cross the internal space of the frame, which is reserved for the limb, the ring normal vectors are at the extreme or diverging angles to each other, or the frame is unstable due to backlash in components. The Jacobian matrix is rank deficient at force-singular configurations and, if necessary, this can be detected easily.

The developed algorithms can be used beyond the TSF application, since they solve kinematics of the most general SGP. The application is wide ranging from positioning to sensing, as long as the SGP workspace is constrained by its geometry to avoid force-singular configurations. The rapid execution of the algorithms makes them suitable for real-time control applications. The previously known platform position and orientation relative to the base could be reused as an accurate estimate of the solution to the forward kinematics in high bandwidth control applications, thus reducing the number of iterations and FLOPS required.

## 3.9 Conclusions

In this chapter, two numerical algorithms were constructed based on a multidimensional Newton-Raphson search for solving forward kinematics. The first algorithm directly followed ideas of the standard Newton-Raphson numerical search. The second algorithm had a modification such that the direction gradient (inverse Jacobian matrix) was worked out only once. The modification has doubled computational efficiency. Due to the nature of the algorithms, both methods invariably fail close to or at a force-singular configuration of the TSF. However, since the workspace of the TSF does not include singular configurations, both algorithms are stable and useable.

# CHAPTER 4 : MECHANICAL PROPERTIES OF THE TSF

The mechanical environment at the fracture site is generally accepted to be the most significant factor in determining both the rate of the fracture healing and the mode by which union occurs, and is largely controlled by the fixation method. It is, therefore, essential to understand the mechanical properties of orthopaedic fixators and their components. There is limited information available regarding the mechanical properties of the recently introduced Taylor Spatial Frame (TSF), despite its increasing usage by surgeons.

Peri-articular fractures are termed as complex to stabilise due to the lack of space for transfixing components close to joints of bones. In order to stabilise such fractures, additional anchorage space is required on the rings to cater for increased number of transfixing bone to ring components. Often, the TSF is not able to cater for those extra components, since the strut fixation points occupy the space required.

This chapter assesses the mechanical properties of the TSF and compares them to a well documented Ilizarov fixator frame. Furthermore, investigation into the specialised use of the TSF for the peri-articular fractures is carried out, by modifying the fundamental TSF geometry. It is hoped that the results of this chapter will provide both a better understanding of the TSF mechanics and a better clinical outcome for the patients.

## 4.1 Review of the Previously Published Ring Frame Properties

The first ring fixator, the Ilizarov Fixator, was designed and pioneered by Professor Ilizarov in the 1950s and has become the most commonly used circular fine wire external fixator in trauma and orthopaedic surgery. The combination of fine wires to transfix the bones and the ring produce a modest self-stiffening effect under increasing load, and low shear motion at the fracture site [6, 7] which would otherwise inhibit bone healing [9, 10, 28, 30, 53]. The basic Ilizarov frame (ILF,

Figure 19) consists of at least two rings and three threaded rods. With additional components, the basic frame can be converted to a kinematically more advanced mechanism – the Ilizarov 'hinge' (ILH, Figure 19). This allows both fixation and geometrical correction of locations and orientations of the broken bone segments. In the hinged frame, the threaded rods have pin joints, so allowing post-operative variation of the relative angle and alignment of the two rings. However, only small angular deformities may be addressed by the use of hinges and these are difficult and time consuming to apply. Furthermore, the Ilizarov frame, in hinged configuration, cannot easily correct complex deformities that include multiplanar translation or rotation. The hinges must be applied accurately or a new deformity will be introduced and this may be impossible anatomically even for a simple angular misalignment.

There are several published studies on the mechanics of the Ilizarov fixator [6-8, 54-60]. These have examined the effect of applying loads to bone substitutes attached to the Ilizarov frame with fine wires or half-pins. The configuration of fixators in each study has been variable, with different numbers, dimensions and positioning of components, as well as different loading conditions.

More recently, the Taylor Spatial Frame (TSF, Figure 19) has been introduced by Smith and Nephew (S&N), Tennessee, USA [38]. To the author's knowledge, the mechanical properties of the TSF have not been published.

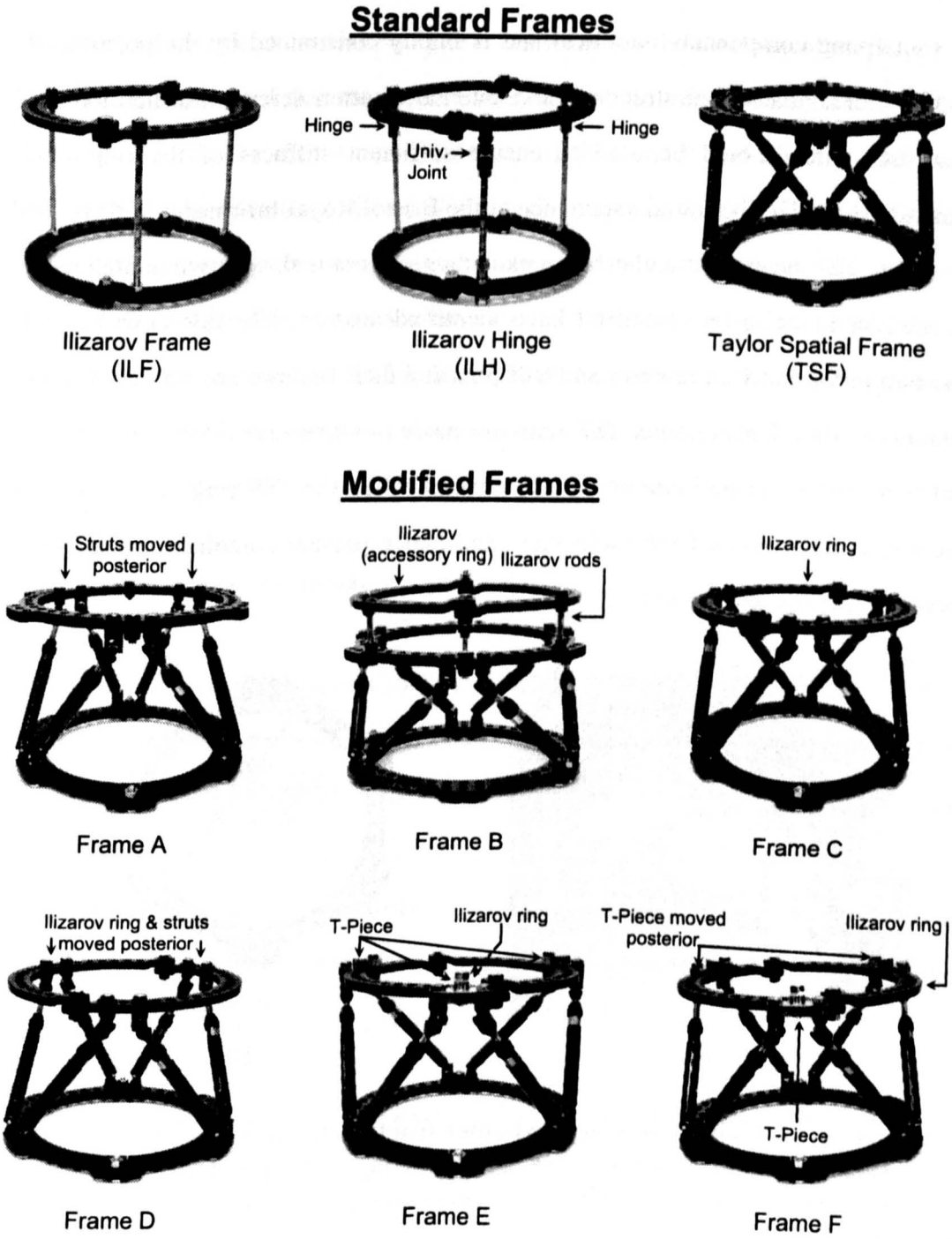


**Figure 19. Test specimens of circular ring fixator frames.**

Peri-articular fractures present a difficult management problem, Figure 20. The use of the TSF for peri-articular fracture management is limited because the six variable length struts must be connected to the manufacturer's predefined locations on the ring. Thus, it is implicit in the TSF construct that the strut position is of primary importance. In contrast, in the treatment of the peri-articular fractures, the position of

the transfixing components is critical and is highly constrained by the position of fracture lines, anatomical structures and internal fixation screws. Furthermore, at least four wires should be used to ensure sufficient stiffness of the ring-bone construct [61, 62]. The initial experience at the Bristol Royal Infirmary (BRI) of the use of the TSF for peri-articular fractures is thus sub-optimal, with wires impinging against struts. DeCoster *et al* [63] have identified anatomically safe corridors for insertion of the transfixing wires and half-pins and their findings are similar to those obtained in BRI. Furthermore, TSF rings are made of aluminium alloy, thus causing scatter of x-rays. In peri-articular fracture cases, when the TSF ring is close to the fracture, it may obstruct the radio view and hence present complications in post-operative fracture assessment.

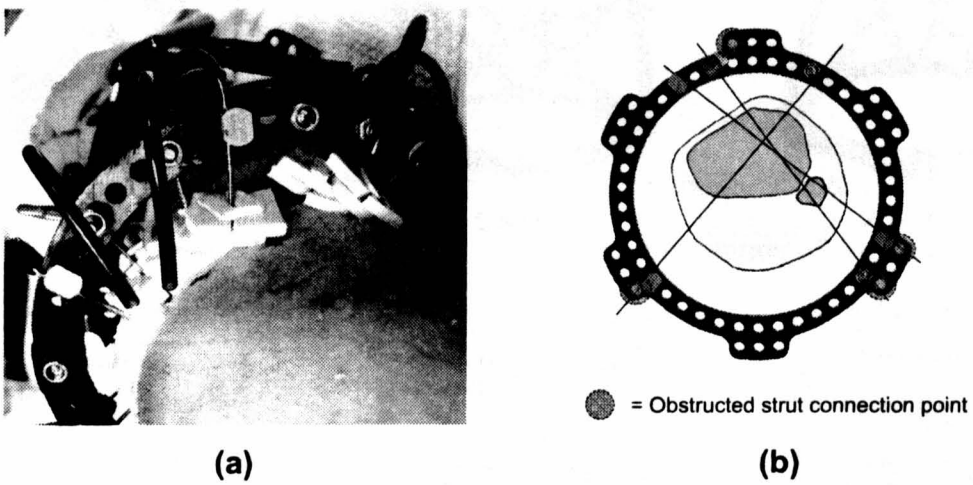


**Figure 20. a) an example of a peri-articular fracture transfixed with 6 fine wires to an Ilizarov ring, top (axial) view. b) strut connection point impingement on the TSF ring by fine wire anchorage requirements for peri-articular fractures, top view.**

## 4.2 Benefits of Testing TSF Stiffness

The TSF is used increasingly as a replacement for the conventional ILF fixator. Fracture management and deformity correction is significantly easier with the TSF, since by altering the lengths of the struts, the fracture can be manipulated in six degrees of freedom. The computer software, provided by S&N, enables easy planning and manipulation of the frame and therefore of the fracture too. While ILF

fixators are well documented, very little is known about the mechanical properties of the TSF. It is believed that mechanical stress and strain between fractured surfaces are controlled by the mechanical properties of the fixator and directly affect the healing methods, Chapter 2. Controlled interfragmentary motion (IFM) is the key parameter to a successful union. It is therefore vital to understand the fixation mechanics and to be able to plan and cater for loads that the patient's limb undergoes during treatment, without precluding beneficial IFM. Failure of the fixator construct must be avoided. Furthermore, it is important to address the fixation issues associated with the difficult-to-stabilise peri-articular fractures.

## 4.3 Materials and Methods

Ring fixators are made of many components and therefore many variables influence the overall construct stiffness. In the past, most investigators have tested complete Ilizarov fixators including artificial bones, pins and wires. The high number of components and consequent geometrical freedom has led to a significant variability in the reported mechanical properties [6-8, 55, 58, 60, 64]. The reported axial and torsional stiffness values for apparently similar configurations vary from 40 to 100 N/mm and 0.7 to 2.5 N·m/deg respectively.

In order to understand the complex fixator behaviour, it makes sense to analyse core components separately and then together. It was decided to test the TSF mechanical properties alone, excluding transfixing bone-frame components, thus eliminating those additional variables. The properties of fine wires and half-pins are analysed separately in Chapter 5. The effects of combining frames and transfixing components are discussed in Chapter 6.

Both the ILF and TSF fixators are readily available today and rival each other. They both work on similar principles, controlling interfragmentary motion (IFM) via fine wires and half-pins. The Ilizarov fixator has proven itself successful in fracture management over a number of years. Therefore, the author felt it important to

compare the TSF to the ILF in order to be able to assess any potential impact of transition from the ILF to the TSF and vice versa.

The peri-articular fractures require modification to the TSF to accommodate increased density of components on the ring. A few types of modifications were proposed and are discussed in more details in Section 4.3.1.3.

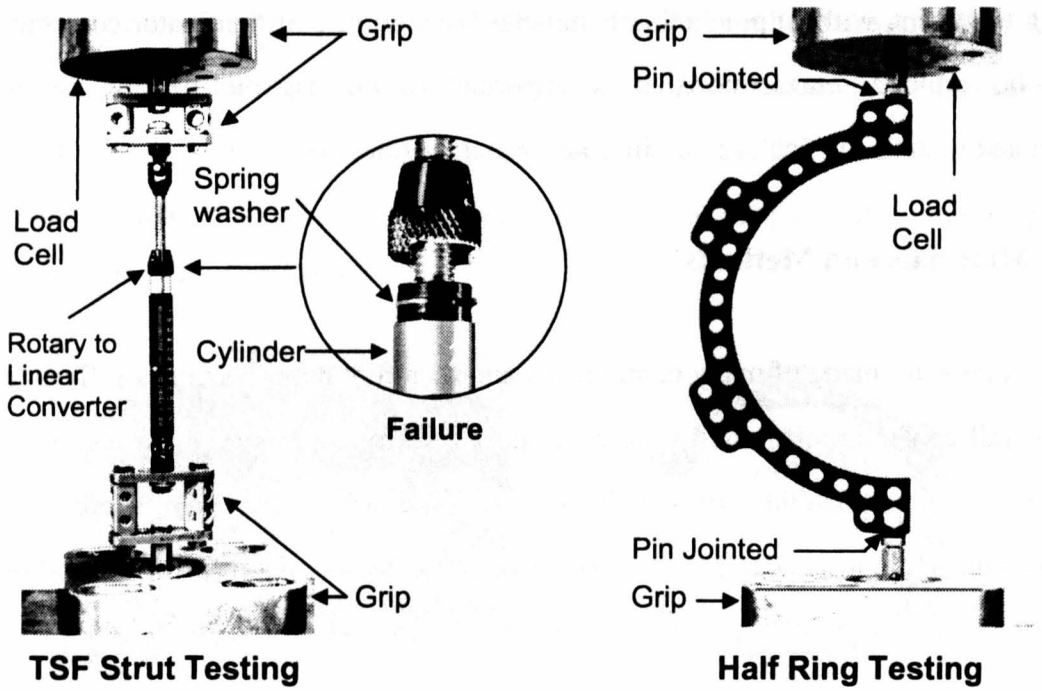


**Figure 21. The half ring and TSF strut mechanical testing setups. The zoomed-in part of the TSF strut failure reveals the spring washer.**

### 4.3.1 Test Specimens

#### 4.3.1.1 Frame Components

Fourteen clinically-used halves of the 155 mm TSF ring (part no.: 7107-0124) and fourteen clinically-used halves of the 160 mm Ilizarov carbon fibre ring (part no.: 10-1356) were tested in a tensile testing machine, Figure 21. Half-rings were loaded axially at their ends, and displacements were recorded. The stiffness results are presented in Table 3. During half-ring tests, the tensile testing machine was set in the

force control mode with a ramp of 1 kN applied at 83 N/s increments. The half-rings were pinned at two extreme end holes and axial load along those holes was applied.

| Component | Stiffness, N/mm | STD |
|---|---|---|
| TSF Half Ring (155 mm) | 177 | 6 |
| Ilizarov Half Ring (160 mm) | 210 | 23 |

**Table 3. Half Ring test results**

The ring interconnecting components are struts in the TSF and threaded rods in the Ilizarov fixator, Figure 22. A medium TSF strut (part no.: 1707-0220) was chosen as a representative component. Thirteen, clinically used, such struts were tested in the tensile testing machine. The specimen length was set to 145 mm, using the scale provided on the strut. Three different types of Ilizarov rods were tested: conventional plain Ilizarov 6 mm threaded rod (ILF Rod, part no.: 10-2305), the hinged rod constructed from two threaded rods and two hinges connected via bolt with a nylon nut, and the 'motor' rod constructed from two threaded rods and a universal joint (ILH Rod [UJ], part no.: 10-2550). Two types of hinged rod were tested, since two types of hinges are available, namely low profile (ILH Rod [L], part no.: 10-1702) and high profile (ILH Rod [H], part no.: 10-1700). All Ilizarov rods were constructed from the new parts supplied by Smith and Nephew, Tennessee, USA (S&N). The length of the rods was set equal to that of the tested TSF strut. All ring connecting components were tested in the force control mode, where force was varied using two cycles of saw waveform of 1.5 kN amplitude. The frequency of the saw wave was set to 0.4 Hz. The force was applied along the major axis of components. Results were averaged for the two cycles and are presented in Figure 23.

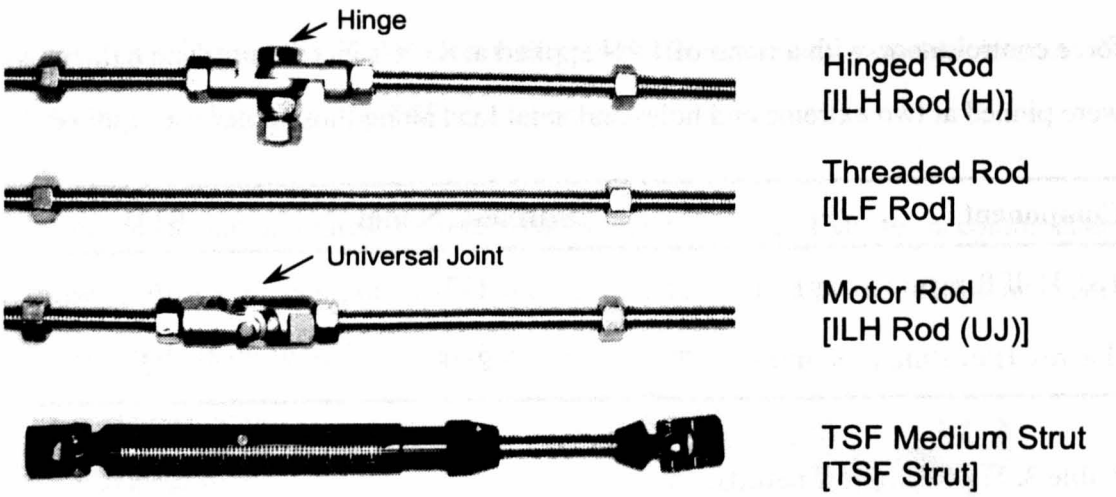


**Figure 22. Conventional ring interconnecting components of circular fixators.**

4.3.1.2 Standard Frames

The size of the TSF specimens was chosen to be representative of the commonly-used frames in Bristol Royal Infirmary (BRI). A standard TSF kit consisting of two 155 mm TSF aluminium rings (part no.: 7107-0124) and six standard medium-length struts (part no.: 7107-0220) was used (Figure 19, TSF). Six such frames were constructed from clinically-used components.

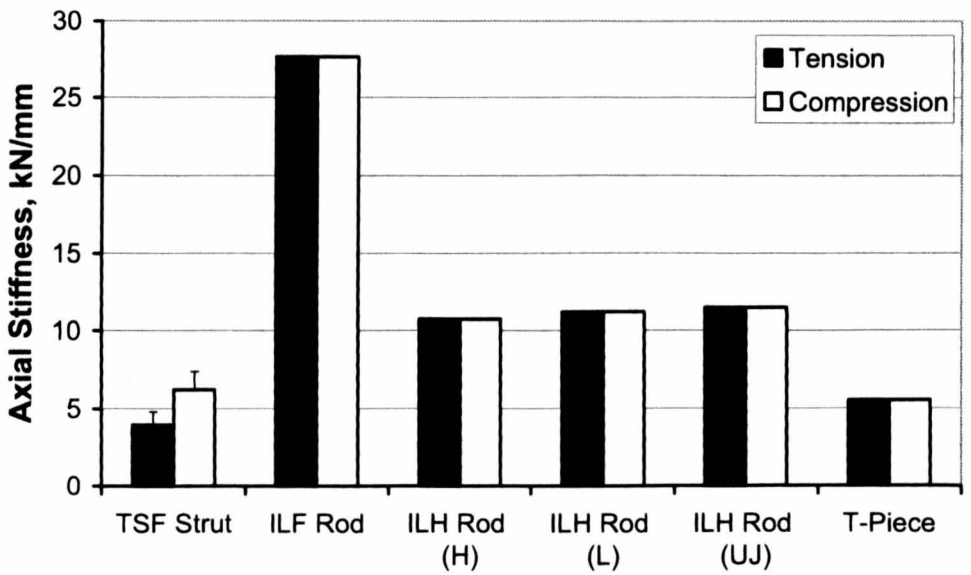


**Figure 23. Axial stiffness of the ring interconnecting components of circular fixators. Thirteen TSF medium struts were tested. The standard deviation of the TSF struts is represented by error bars.**

The Ilizarov frame specimens were constructed in two forms, namely conventional and hinged as illustrated in Figure 19 (ILF & ILH). In the 'hinge' frame, the threaded rods have pin joints near to one end, so allowing post-operative variation of the relative angle and position of the two rings. Both frame types were constructed from new components supplied by S&N. The geometry of the frames was chosen to be comparable to that of the TSF tested. Two 160 mm carbon fibre rings (part no.: 10-1356), three stainless steel 6 mm standard threaded rods, four low profile hinges (part no.: 10-1702) and one universal joint (part no.: 10-2550) were used. For the basic frame configuration it was decided to use three vertical threaded rods, in order to enable direct comparison with the hinged version.

All conventional frames were assembled in the neutral configuration, where two rings were aligned and parallel. The neutral frame height (distance between two ring centres) was set to 130 mm for all the specimens.

#### 4.3.1.3 Peri-articular Frames

Peri-articular fractures, Figure 5b, require high stability and precise 6D alignment in order to ensure a successful healing outcome and avoid jeopardising the limb functionality. It was identified in the BRI that, despite the advantage of the six degrees of freedom, it is very hard to use the TSF for fixation of such fractures. The TSF strut connections obstruct the required ring-bone component anchorage space. Based on a retrospective study performed by Chris Butcher (clinical Ilizarov research fellow at BRI), it was found that in 5 cases out of 10 it would be impossible to use the TSF due to transfixing component anchorage restrictions. In addition, the partially radio opaque aluminium TSF ring close to the fracture complicates radiological investigation. Based on these observations, modifications to the conventional TSF are necessary in order to be able to exploit advantages of the fixator. Six modified configurations (Figure 19) were investigated to confront the problem by the author and Chris Butcher.

1. Frame A – conventional components of TSF frame were used (155 mm ring with standard medium-length struts). Two strut groups (3&4 and 5&6) were connected two ring holes posterior from their designed locations on the proximal ring. The distal ring connections remained at the manufacturer's predefined positions. This frame configuration enables the anchorage of the transfixing component in the previously restricted areas.

2. Frame B – the conventional TSF frame with conventional strut locations was used. An additional 160 mm Ilizarov carbon fibre ring was mounted directly above the ring closest to the peri-articular fracture via three straight threaded rods. In such a way, both the radio opacity and strut connection obstruction problems were addressed.

3. Frame C – conventional TSF frame components were used except for the ring closest to the peri-articular fracture. The TSF ring was replaced with an Ilizarov 160 mm carbon fibre ring of similar size. Locations of struts' connections were spaced similarly as in the TSF ring case. The Ilizarov CF ring is thinner than TSF ring and therefore washers were used at the strut attachment points to limit the backlash. Frame C solves the problem of radio opacity, but does not address the problem of obstruction.

4. Frame D – similarly to Frame C configuration, one of the TSF rings was replaced with a carbon fibre Ilizarov ring. In addition, struts' connections for groups (3&4) and (5&6) were moved posterior by two ring holes on the Ilizarov ring, similarly to Frame A. Again as in Frame C washers were used at the attachment points to limit the clearance and therefore backlash. This configuration addressed both obstruction of anchorage points and radio opacity issues.

5. Frame E – conventional TSF components were used. The proximal TSF ring was replaced with an Ilizarov 160 carbon fibre ring. The TSF struts were attached to the carbon fibre ring via 'in house' developed 'T' shaped pieces (T-Piece), Figure 24a.

T-Pieces were used to reduce the number of holes required to connect the struts to the rings by a factor of two. Furthermore, they provided conversion to the TSF ring thickness, so that no washers were required. The T-Piece was designed to withstand the likely loads and its properties were assessed by mechanical testing, Figure 24b. Figure 23 presents its stiffness measured by fixing it to the support (ring), applying a force (perpendicular to the ring plane) at the strut connection points and measuring displacement. An Engineering drawing of the T-Piece is provided in Appendix B. Frame E addressed both the radio opacity and strut obstruction issues.

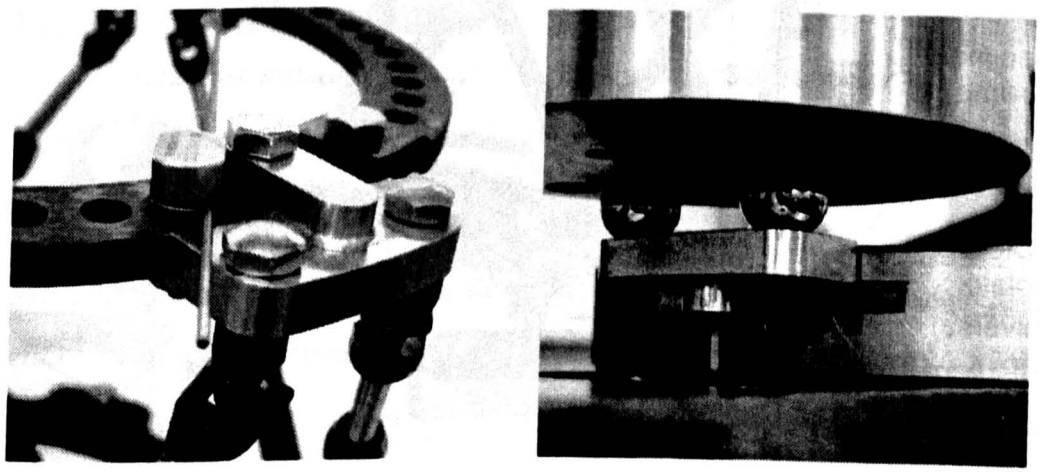

(a) (b)

**Figure 24. T-Piece. a) T-Piece mounted on the 160 mm carbon fibre ring, with fine wire next to it. b) T-Piece being tested in the tensile testing machine. It is held upside-down in the custom made grip, with force applied axially via two ball bearings.**

6. Frame F – same components are used as for Frame E. In addition, the T-Pieces with strut groups (3&4) and (5&6) on the carbon fibre ring were moved by two holes posterior similarly as for Frame A.

Frames were assembled in the neutral configuration, *i.e.* the two rings were aligned and parallel. The neutral frame height (distance between two ring centres) was set to 130 mm for all the frames. Since S&N's provided TSF calculator was not able to solve forward/inverse kinematics of the irregular frames, the solution presented in

Chapter 3 was used to determine required strut lengths. All frames were assembled from clinically-used components.

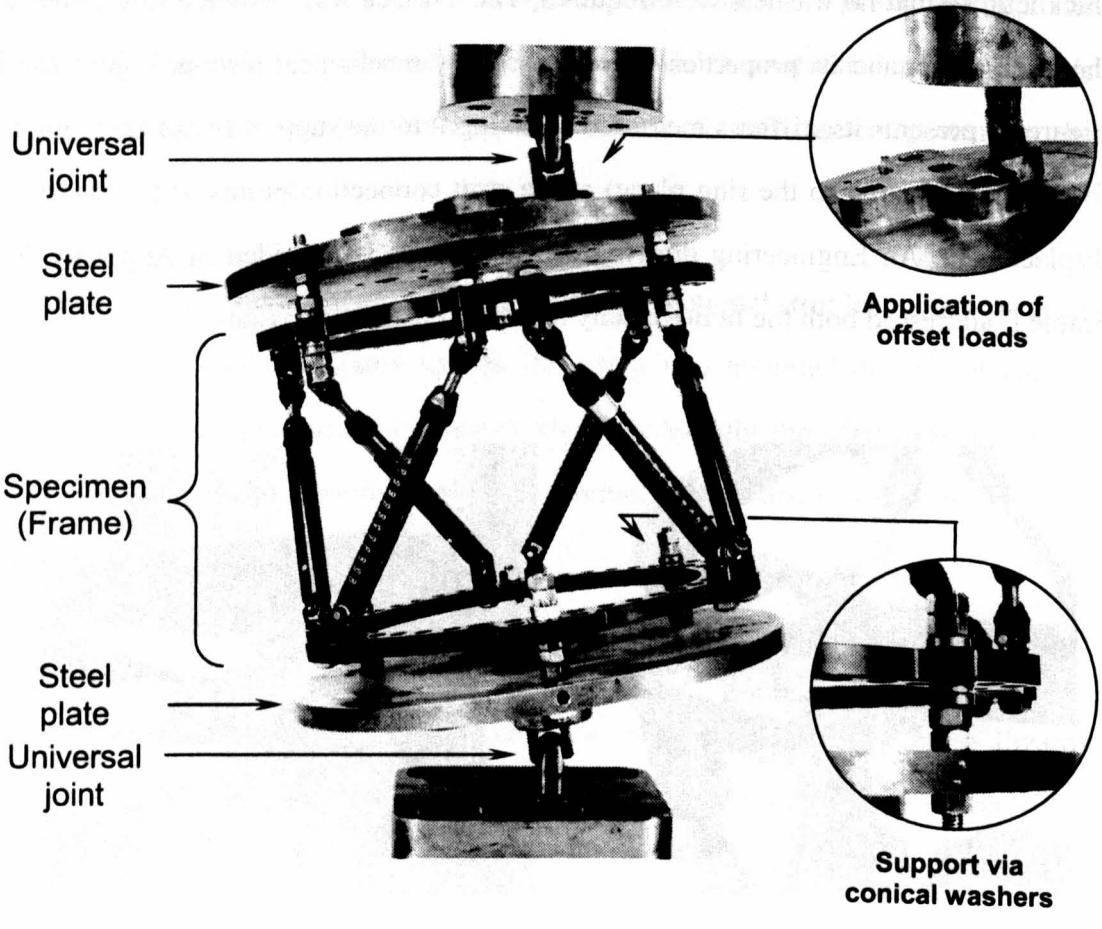


**Figure 25. Front view of the Taylor Spatial Frame held in the 'flexible' configuration in the test rig. A laterally offset load is applied by displacing the upper universal joint 40 mm from the centre of the steel plate.**

### 4.3.2 Methods of Frame Testing

A Roell Amsller HCT 25 tensile testing machine was used to apply loads to the specimens and to record displacements. Figure 25 shows an example of the experimental set-up. A bespoke jig was made for frame testing. The load cell at the top of the machine was attached via a heavy-duty universal joint to a steel plate, which was itself attached to the top ring of the frame at three equally-spaced points via conical washers and nuts as shown in the zoomed-in part of Figure 25. A similar arrangement was used at the lower ring. The purpose of conical washers was to

permit localised ring bending, and thus for tension/compression testing the nuts were merely hand-tightened. For torsional testing, the nuts were tightened sufficiently to prevent slippage of the ring on the fixation bolts, which are smaller in diameter than the ring holes.

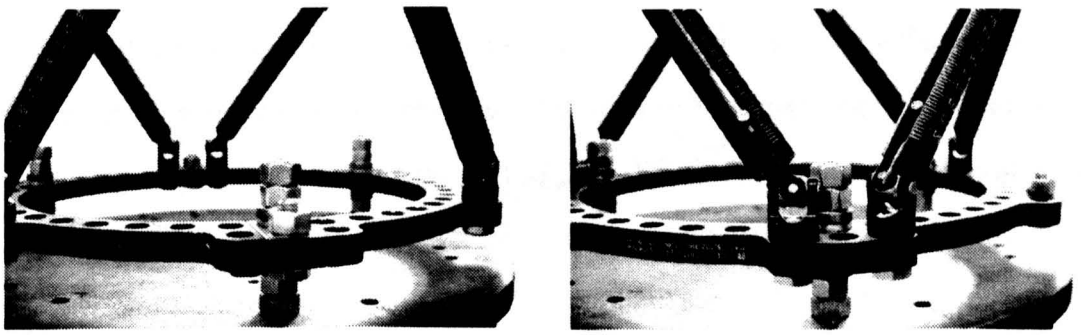


**Figure 26. Support points for 'stiff' and 'flexible' set-ups.**

In order to determine how much the flexibility of the rings might contribute to the overall flexibility of the frame, two loading geometries were used, Figure 26. Firstly, a 'flexible' set-up was devised in which the rings were attached to the circular plates midway between the strut groups/threaded rods. Secondly, a 'stiff' set-up was used, in which the attachments were adjacent. In clinical situations, the wires and half-pins may be attached at a wide range of locations around the perimeter of the rings.

The offset loading modes were applied by displacing the upper universal joint location by 40 mm from the central axis, similarly to Roberts *et al* [65]. Details of offset loading are illustrated in the zoomed-in part of Figure 25. This 40 mm distance was chosen to represent the upper limit of offsets experienced clinically.

The frames were tested in four tension/compression modes, similar to those described in previously published studies [64, 66]: loads were applied purely axially, and also offset medially, anteriorly and posteriorly. Effects of lateral offset load were not tested, since both the TSF and Ilizarov were symmetrical about the AP axis. The frames were also tested in torsion.

Each of the frame tension/compression and offset test mode was cycled sinusoidally 5 times at 0.1 Hz from -0.75 kN to 0.75 kN, followed by 5 cycles from -1.5 kN to 1.5 kN. During these tests, the frames were allowed to rotate freely about their major axis by setting the machine to maintain zero torque. For the torsional tests, the frames were subjected to 5 sinusoidal cycles from -15 N·m to 15 N·m at 0.1 Hz. The axial load actuator was set to maintain zero load, enabling the frame to freely shorten or elongate. The load ranges were chosen to represent the upper limits likely to be experienced by the frames [21-24, 66, 67]. Both axial and torsional load ranges were smaller than the dynamic load range experienced by the long leg bone during normal daily activities, Chapter 2, since injured limbs are not loaded in the same way as intact ones. Furthermore, once the fracture gap is bridged, the load is shared between the fixator and the bone itself. The calibrated accuracy of the tensile/torsion machine was ±1 %.

## 4.4 Results

Figure 27 shows a typical load vs. displacement plot, in this case for the TSF. After making appropriate allowance for the deflection of the plates, universal joints and machine, the frame stiffnesses were estimated from the mean gradient of these plots.

Initially six nominally identical standard TSFs were tested in the axial mode in both the 'stiff' and the 'flexible' set-ups. This was done in order to verify the repeatability of the test results and variability of test specimens. None of the frames yielded nor failed. Their individual stiffnesses were measured, and found to have a standard deviation of 3.8 % (flexible set-up) and 5.8 % (stiff set-up) of the mean stiffness value.

Given these relatively small values of standard deviation and the fact that modified frames were constructed from the previously tested TSF components, the subsequent off-axis tension / compression and torsion tests were performed on just one each of the TSF, and modified frames, supported in both 'flexible' and 'stiff' set-ups. Only a

single specimen of the Ilizarov and Ilizarov 'hinged' frame was tested, since those frames are well documented and they were constructed from brand new components. The results of tests are presented in Figure 28 - Figure 33.

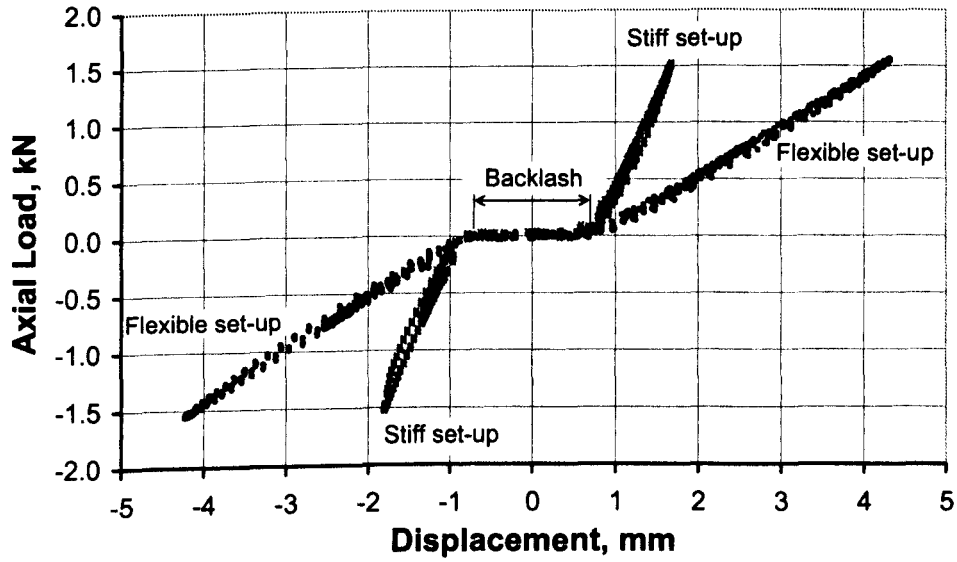


**Figure 27. Typical load displacement curves recorded by the data acquisition system of the Roell Amsller HCT 25 tensile testing machine. The TSF frame was supported in both the 'flexible' and the 'stiff' set-ups and loaded axially for five cycles of +/-0.75 kN and then a further five cycles of +/-1.5 kN.**

## 4.5 Discussion of Results

For all frame types, large differences in axial stiffness were observed between the 'stiff' and the 'flexible' set-ups. In the 'flexible' set-up, a large bending moment is imposed on the rings, leading to significant ring bending and therefore a decrease in stiffness. This, of course, is not so much the case for the 'stiff' set-ups, in which loads are transmitted through points on the rings in close proximity to the strut groups. It is evident from these findings that the manner in which loads are transmitted to the frame has a significant influence on the resultant stiffness. The results also suggest that the rings have significantly lower stiffness than the struts. In clinical situations, the load is transmitted through wires and half pins and hence the attachment locations of the connecting components are important. In most cases, the wires and half-pins are placed somewhere between the strut groups. The variability

in attachment locations may also explain the variation of stiffness results obtained by different researchers for fixators of apparently similar configuration.

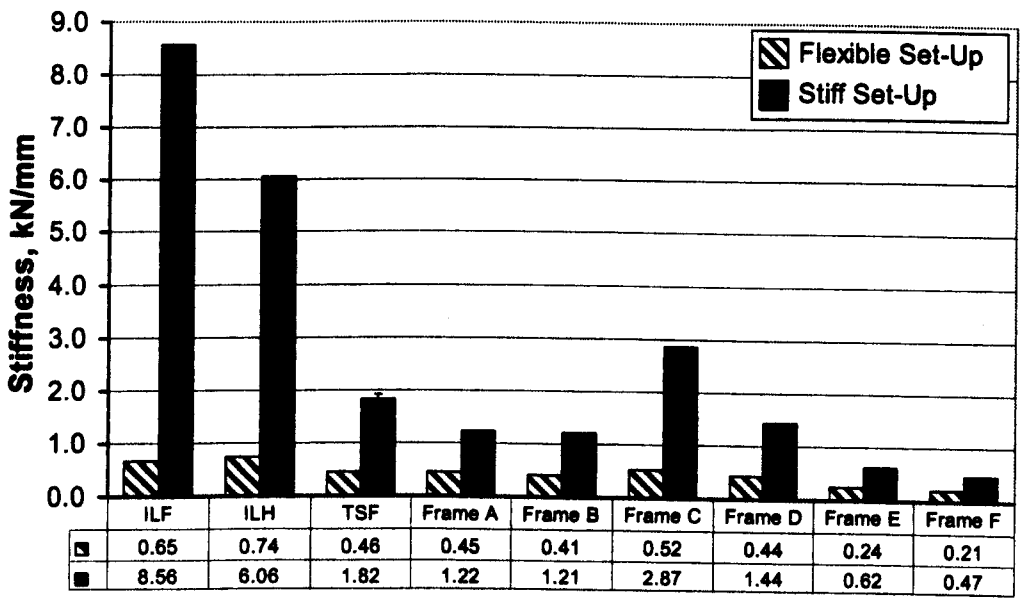


| | ILF | ILH | TSF | Frame A | Frame B | Frame C | Frame D | Frame E | Frame F |
|---|---|---|---|---|---|---|---|---|---|
| ▨ | 0.65 | 0.74 | 0.46 | 0.45 | 0.41 | 0.52 | 0.44 | 0.24 | 0.21 |
| ■ | 8.56 | 6.06 | 1.82 | 1.22 | 1.21 | 2.87 | 1.44 | 0.62 | 0.47 |

**Figure 28. Stiffness of the tested frame specimens loaded axially.**

Under purely axial loads and with the 'stiff' set-up, (Figure 28) the TSF is substantially less stiff than both Ilizarov configurations. This may be explained by the geometry of the frames and stiffness of their components. The stiffness of the threaded rods is significantly higher than that of the TSF strut, Figure 23. Despite using six struts in the TSF, the overall stiffness of the three threaded rods is far higher. Furthermore, the threaded rods of the Ilizarov frame are parallel to the load axis resulting in the maximum axial frame stiffness, whilst the TSF struts are angled resulting in higher deflections when loaded and therefore lower axial frame stiffness. In the 'flexible' set-up, local ring bending is the dominant form of deflection, such that all the frames then had similar stiffness. The Ilizarov frames were stiffer. This can be explained by looking at the ring properties. The Ilizarov ring is made of carbon fibre composite material and is about 20 % stiffer than that of the TSF, Table 3. Furthermore, the pitch circle diameter (PCD) of the ring interconnecting components of the Ilizarov 160 mm ring is 173 mm, while the PCD of the TSF 155 mm ring is 194 mm, Table 4 & Figure 29. PCDs of the bone-to-ring transfixing

connecting components anchorage are similar for both types of ring. This results in a longer bending arm of the ring and therefore bending moment for the TSF, and hence lower frame stiffness.

| Ring Type | Ring Thick.[1], mm | PCD Struts[2], mm | PCD Transf.[3], mm |
|---|---|---|---|
| TSF Ring (155 mm) | 7.5 | 194 | 170 |
| Ilizarov Ring (160 mm) | 6 | 173 | 173 |
| Ilizarov Ring (160 mm) & T-Piece | 6 | 214.8 | 173 |

**Table 4. Geometrical properties of the rings. [1] – Ring thickness. [2] – pitch circle diameter of the connection points for TSF struts. [3] – pitch circle diameter of the connection points for ring-bone transfixing components (*e.g.* fine wires and half-pins)**

The mechanical tests of the TSF struts have revealed that struts have different stiffness in tension and compression, Figure 23. This can be explained by an analysis of the load path in the TSF strut. A single TSF medium strut was loaded in tension to destruction, Figure 21. The strut has failed at the interface of the brass spring washer. This washer is responsible for keeping the strut components together, while allowing the rotation of the rotary-to-linear displacement converter. It also takes the load in tension, while in compression the load is taken directly by the strut cylinder. The author believes this is the reason why the TSF strut has different stiffness properties for tension and compression modes, since the load paths are not the same. Finally, one might expect similar variation in stiffness for the TSF frame as for the TSF strut. This however is not exactly the case, since due to the complex geometry of the frame, this effect is somewhat minimised, Figure 27. When the TSF is loaded in tension, the angle between struts decreases due to elastic strut elongation. Therefore, the strut deformation has lesser effect on the axial displacement, and hence results in the increased axial stiffness of the frame. When the frame is loaded in compression, exactly the opposite happens: the angle between struts increases and deformation has higher influence on the overall axial displacement and hence stiffness. The recorded

average variation between tension and compression axial stiffness of the TSF was less than 3 %, and therefore all results were averaged for pragmatic reasons.

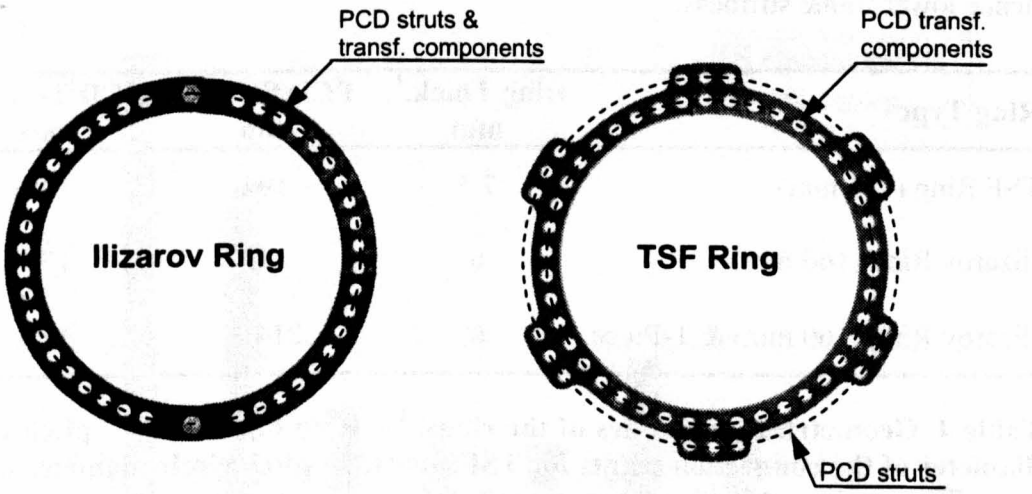


**Figure 29. Ilizarov and TSF ring pitch circle diameter (PCD) definitions.**

When the frames were subjected to loads which were offset by 40 mm anteriorly, posteriorly and medially, the stiffness range of the Ilizarov frame configurations decreased by 80 – 90 %, whilst the TSF frame stiffness range increased slightly (Figure 30-Figure 32). Again, this can be explained by the geometry of the frames. Under these load conditions, the Ilizarov frames' threaded rods (which are rigidly 'built in' to the rings) are no longer aligned with the load axes, and deflect under the resulting bending loads. Loads of 1,500 N led to buckling and significant local plastic deformation of the rods and hence failure of the frame. By comparison, the TSF struts are attached to the rings via universal joints, and so are not required to support any significant bending. Rather, the TSF relies for its stiffness on the axial stiffness of the struts, and no plastic deformation of these was observed.

Torsionally, the TSF was found to be significantly stiffer than the Ilizarov frames, as can be seen from Figure 33. Again, the threaded rods in the Ilizarov frames were subjected to substantial bending loads, whilst the TSF struts remained purely in tension or compression.

In all tests, the hinged Ilizarov frame was found to be marginally less stiff than the conventional Ilizarov frame. This is unsurprising, given the freedom introduced by the pin-joints in the threaded rods and decreased stiffness of ring interconnecting components, Figure 23.

The comparison of the TSF with the Ilizarov frames has demonstrated that the TSF exhibits approximately uniform stiffness across a range of load directions, whilst the Ilizarov frame does not. It is desirable to have certainty of stiffness of the frame across a range of load paths since bones are frequently mounted off central axis of the frame for clinical reasons. It can therefore be concluded that in practice the TSF frame has similar or higher stiffness than the Ilizarov frame. This is especially so when used to correct angular deformities, in which cases the loads may be markedly off-centre.

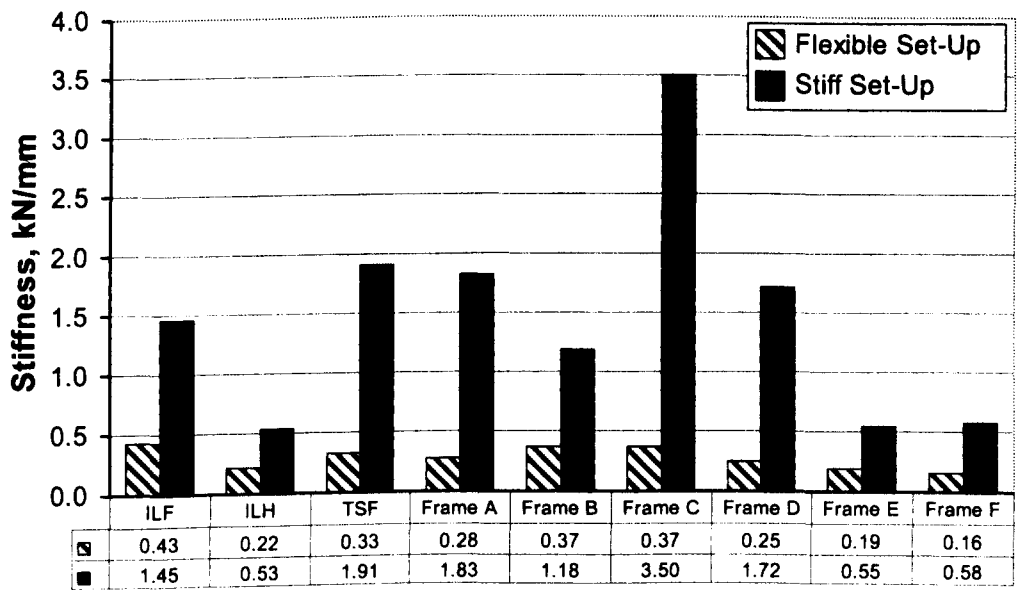


| | ILF | ILH | TSF | Frame A | Frame B | Frame C | Frame D | Frame E | Frame F |
|---|---|---|---|---|---|---|---|---|---|
| ▨ | 0.43 | 0.22 | 0.33 | 0.28 | 0.37 | 0.37 | 0.25 | 0.19 | 0.16 |
| ■ | 1.45 | 0.53 | 1.91 | 1.83 | 1.18 | 3.50 | 1.72 | 0.55 | 0.58 |

**Figure 30. Stiffness of frame specimens subjected to anteriorly offset load.**

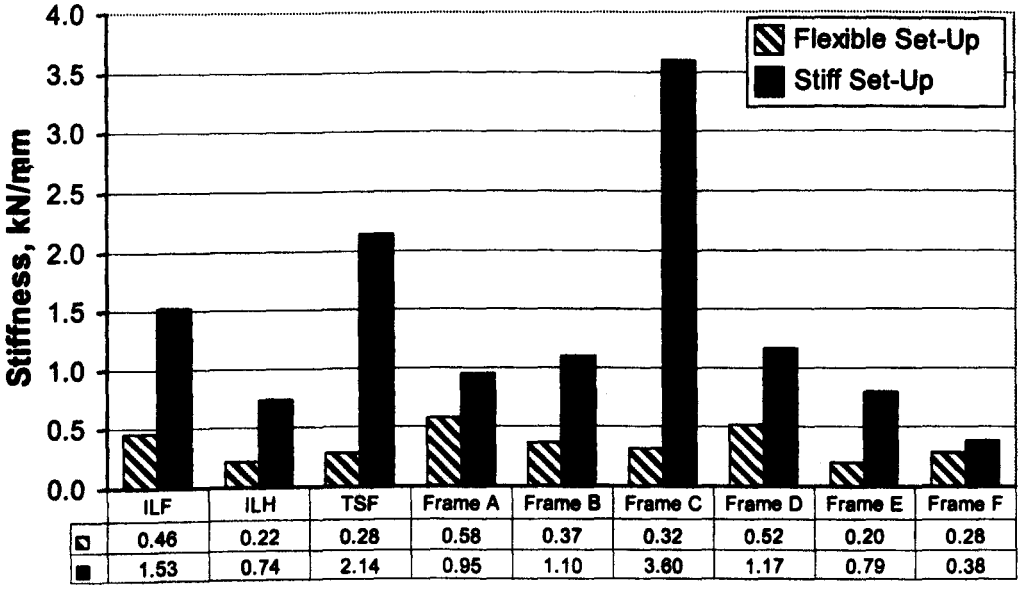


| | ILF | ILH | TSF | Frame A | Frame B | Frame C | Frame D | Frame E | Frame F |
|---|---|---|---|---|---|---|---|---|---|
| ▨ | 0.46 | 0.22 | 0.28 | 0.58 | 0.37 | 0.32 | 0.52 | 0.20 | 0.28 |
| ■ | 1.53 | 0.74 | 2.14 | 0.95 | 1.10 | 3.60 | 1.17 | 0.79 | 0.38 |

**Figure 31. Stiffness of frame specimens subjected to posteriorly offset load.**

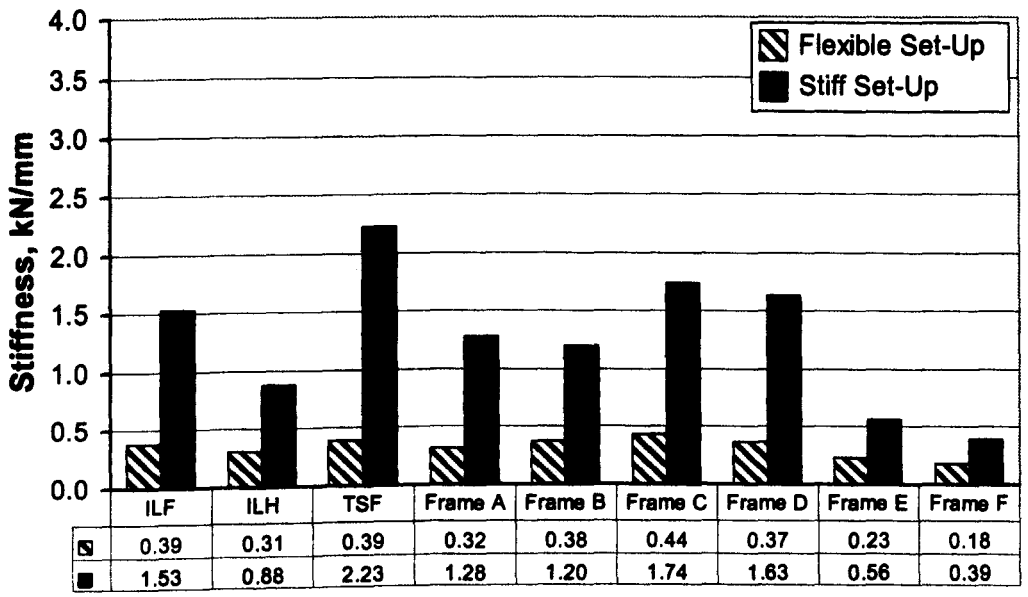


| | ILF | ILH | TSF | Frame A | Frame B | Frame C | Frame D | Frame E | Frame F |
|---|---|---|---|---|---|---|---|---|---|
| ▨ | 0.39 | 0.31 | 0.39 | 0.32 | 0.38 | 0.44 | 0.37 | 0.23 | 0.18 |
| ■ | 1.53 | 0.88 | 2.23 | 1.28 | 1.20 | 1.74 | 1.63 | 0.56 | 0.39 |

**Figure 32. Stiffness of the frame specimens subjected to laterally offset load.**

None of the modified frames has failed during mechanical testing. Frames A, B and D have only slightly altered the standard TSF mechanical properties. Results suggest that moving TSF strut groups (3&4) and (5&6) posteriorly reduces the frame stiffness for posteriorly offset loads; however, such load direction is unlikely in clinical situations. Rings are centred normally round the limb rather than the bone,

which in turn results the bone shift anterior due to the soft tissues presence *e.g.* muscles. The use of the T-Piece (Frame E & F) has produced lower stiffness constructs than that of the TSF. The T-Piece has increased the PCD of strut connection points (Table 4), hence larger bending moments were produced on the rings, and the stiffness has decreased. Interestingly, the use of the Ilizarov ring instead of the TSF ring (Frame C) has increased the stiffness of the frame. This can be explained by its smaller PCD diameter and higher ring stiffness. The torsional stiffness of all modified frames was similar to that of the TSF and far superior to that of Ilizarov frames.

The significance of the 'weak' or 'flexible' frame stiffness to the overall fixator stiffness is discussed in Chapter 6.

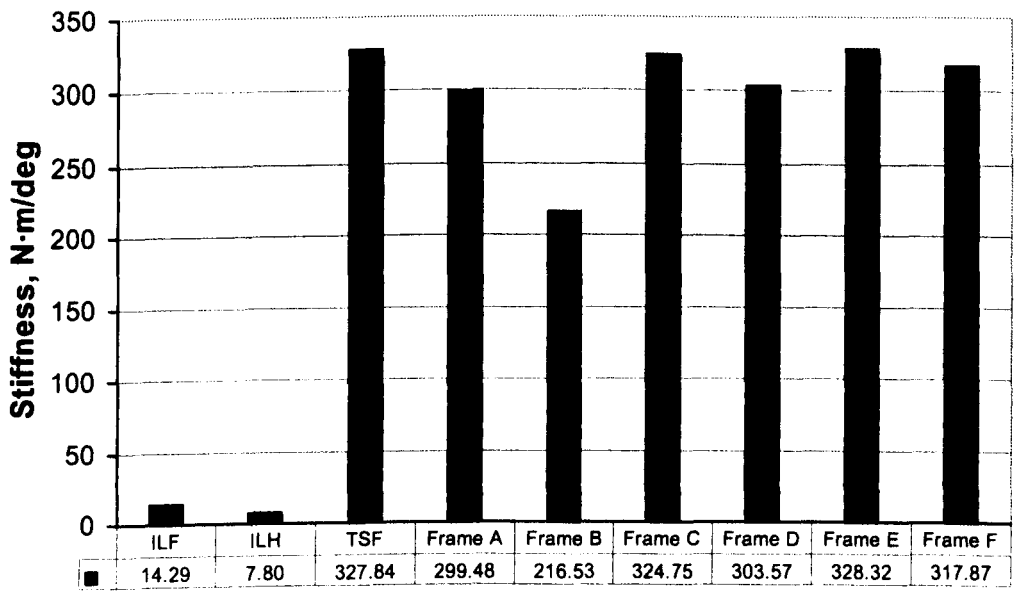


**Figure 33. Torsional stiffness of frame specimens.**

Finally, the experimental results suggest that increasing ring diameter will lower the stiffness of the TSF construct in the 'flexible' set-up, since the PCD will increase and hence bending arm and moment. The second variable affecting the stiffness of the frame is the ring separation. It is possible to speculate, that as the separation decreases, the angle between struts increases, making the overall frame less stiff. A

further investigation is required to understand how ring size and separation correlate with frame stiffness. However, it is beyond the scope of this PhD.

## 4.6 Conclusions

In this study, the Taylor Spatial Frame was directly compared to the basic Ilizarov fixator frame and a modified hinged form. It was found that the TSF has nearly uniform stiffness properties for a range of loads and is of similar or greater stiffness to the Ilizarov frames for off-axis loads. In addition, the TSF is significantly stiffer in torsion. The application of the loads and therefore placement of bone-ring connecting components plays an important role in determining the frame stiffness. Finally, it is possible to alter the TSF in order to cater for extra anchorage space required for bone-ring transfixing components of peri-articular fractures. Two feasible alternatives have been shown to produce good results: first, using a carbon fibre ring mounted above the standard TSF and second, using a carbon fibre ring instead of one of the rings of the TSF with strut groups 3&4 and 5&6 moved posteriorly. Both modified constructs have demonstrated stiffness properties similar to those of the standard TSF.

# CHAPTER 5 : FINE WIRES AND HALF-PINS

Fine (typically 1.8 mm diameter) wires and half-pins (4, 5 & 6 mm diameter) are key components of the TSF fixator. Their primary function is to secure the connection between the bone and the TSF. Their secondary function is the control of interfragmentary motion (IFM). Since the wires and half-pins are small in diameter, they cause minimal invasive damage to the anatomy. However, as at least eight of them are used in a typical fixator set-up there remains a risk of infection. Fine wires are the weakest and most flexible components of the TSF fixator. It is therefore important to understand the effect of the fine wires on the fixator stiffness. In this chapter, simple ways to model both fine wires and half-pins are presented. The modelling is then used to analyse mechanical properties of the ring – wire and ring – half-pin constructs for the TSF. The author published part of this chapter in an original article [68] with special reference to an Ilizarov fixator.

## 5.1 Previous Work on Fine Wires and Half-Pins

The fine wire is a commonly used component of the ring fixators. It is used in both Ilizarov and TSF fixation devices. The unique property of the fine wire is that its stiffness increases with increasing load and hence large displacements are prevented, while small motion is allowed. Aronson and Harp [54] have demonstrated that wires exhibit self-stiffening non-linear behaviour when loaded perpendicularly to their major axis. This loading direction is generally termed 'axial' as it is along the major axis of the bones and frame. Self-stiffening non-linear behaviour is believed to be a factor in successful operation of the Ilizarov fixator and therefore of the TSF. Small-amplitude interfragmentary motion (IFM) between broken bone segments is introduced under small axial loads, such as partial load-bearing by the patient. Under higher loads, the tension in the wire increases significantly, so also inhibiting high amplitudes of motion. Controlled interfragmentary motion is believed to promote callus formation and therefore to accelerate bone healing [9-14, 16-18, 28]. Two

wire diameters, manufactured by Smith & Nephew (Memphis, Tennessee, USA), are used commonly with both the Ilizarov and TSF fixators: 1.6 mm and 1.8 mm. The wires are made of high strength stainless steel or titanium alloy and secured to the frame rings using slotted or cannulated bolts. To secure the fine wire, two anchor points are required on the ring. In order to gain additional axial fixator stiffness, the wires are pre-tensioned. Four values of initial tension can be applied using a tensioning device, supplied with the fixator kit. Calibrated tension marks are at 50 kgf (491 N), 90 kgf (883 N), 110 kgf (1079 N) and 130 kgf (1275 N). Watson *et al* [69] have identified that the accuracy of this device is within 4 %. When the wire clamping bolt (cannulated or slotted) head is tightened, the wire beneath it becomes slightly extruded along its length as it deforms plastically. This deformation typically causes the wires to lose 22 % of their pre-tension during clamping [69]. Many researchers have analysed wires in order to determine the optimal values of pre-tension and control effectively the mechanical properties of the Ilizarov fixator. Both numerical modelling and mechanical testing have been performed [8, 37, 54, 60, 70-72].

The key measure of the wire performance is its stiffness when subjected to loads perpendicular to its long axis, and defined by the ratio of load applied to its resultant displacement. In addition to fundamental material properties (modulus of elasticity, yield stress, Poisson's ratio, etc), five independent variables that influence such stiffness have been identified: wire length (which corresponds to the ring internal diameter), wire diameter, initial wire pre-tension, bolting torque and ring stiffness. Bronson *et al* [8] have demonstrated through statistical analysis that the most significant variables are length of the fine wire, and then pre-tension. Variations in wire diameter and ring stiffness have been shown to have relatively little influence on the overall fixator performance. A number of studies [37, 54, 70] have noted that when loads in excess of 50 N were applied to a single wire, the wire lost around 30 % of its initial pre-tension. Initially it was believed that the main reason for this was slippage occurring at the ring/bolt interface. Wire bolting torque ranges were

studied to combat this problem. A 20 N·m bolting torque has been identified as optimal [54]. In later studies, it was identified that in addition to slippage the wires were yielding and there was a limit to which wires should prudently be pre-tensioned [37, 71].

The disadvantages of use of wires include pain, infection, frame complexity and soft tissue impalement and have been reported by [55, 56, 60].

Hybrid ring fixators use a combination of fine wires and half-pins [60]. Half-pins come in a range of diameters (4, 5 & 6 mm) and are made of high strength stainless steel or titanium alloy. It is common to use half-pins for cases when limited anchoring space is available, *e.g.* bone fractures close to joints. The half-pin is fixed via rancho cubes and therefore requires only a single anchorage point, which in turn occupies a single hole of the ring. The main advantage of the use of half-pins is that they offer generally stiff fixation, require minimum anchorage space, cause minimal damage of the surrounding soft tissues and can be used in anatomically safe areas [6, 73]. The disadvantages are non-axial micro-motion and increased risk for skin infection [74]. When half-pins are loaded, the displacements are introduced axially, laterally and angularly [7, 75]. Both lateral and angular displacements result normally in undesirable shear motion [17, 76]. Finally, half-pins cause more damage to the anatomy than fine wires, since larger diameter tunnels are required to accommodate them.

To the author's knowledge, no wire or half-pin stiffness studies combined with TSF rings have been previously reported.

## 5.2 Benefits of Fine Wire and Half-Pin Modelling

It is important to plan fixator stiffness in order to achieve satisfactory fracture healing. The stiffness of the fixator influences the stiffness of the fracture, and hence the level of the interfragmentary micro-motion (IFM). Small controlled IFM

accelerates healing, while large amplitudes and strains at fracture can cause severe damage. This implies that benefits will result from an understanding of the mechanical properties of the fixator and its components. Since fine wires exhibit non-linear behaviour it is crucial to estimate their performance in order to implement the fixation and perform treatment successfully. Not only knowing the behaviour of a single wire, but also that of a group of wires is important. If half-pins are used, it is important to estimate their contribution to the fixation too.

## 5.3 Modelling Wire as a Chain

Several researchers have used comprehensive finite element analyses to model fine wires. These have shown that, for axial loads (*i.e.* as above, parallel to the major bone axis and perpendicular to the major axis of the wire) over 50 N there is substantial wire yielding and consequential plastic deformation at or very near to the bolt/ring interface due to bending [37, 70, 71]. Hillard *et al* [17] considered a 1.8 mm diameter wire displaced by 5 mm and spanning a 180 mm ring. They demonstrated that if the wire was assumed to deform purely elastically, the stress at such locations would exceed 250 % of the measured yield stress of the fine wire material. Furthermore, the intrinsic bending stiffness of such a wire is typically 2 - 3 N/mm [68], as compared to typically 30-40 N/mm when pre-tensioned. Therefore, the wire can be modelled approximately as being pinned rather than built in at the bolt/ring interface, with displaced shape as sketched in Figure 34. This enables the wire to be modelled as a simple fully-flexible elastic chain instead of a solid bar, with uniform tension throughout the wire length. Additionally, it can be assumed that the fine wire is free to slide through the bone, that there is similarly localised yielding at the wire/bone interface and zero slippage at the bolts. A model, which correlates wire tension, applied axial load (perpendicular to the wire) and displacement in the load direction can then be derived using the following assumptions:

1. The bending stiffness of the fine wire can be ignored. Under loading the wire yields locally at the attachment points, so reducing excessive stress with permanent deformation.

2. There is uniform tension along the wire.

3. The bending stiffness of the wire at the interface of the bone is negligible.

4. The wire has uniform material properties.

5. The wire is free to slide through the bone.

6. The ring is sufficiently stiff that it does not deflect significantly when the wires are loaded.

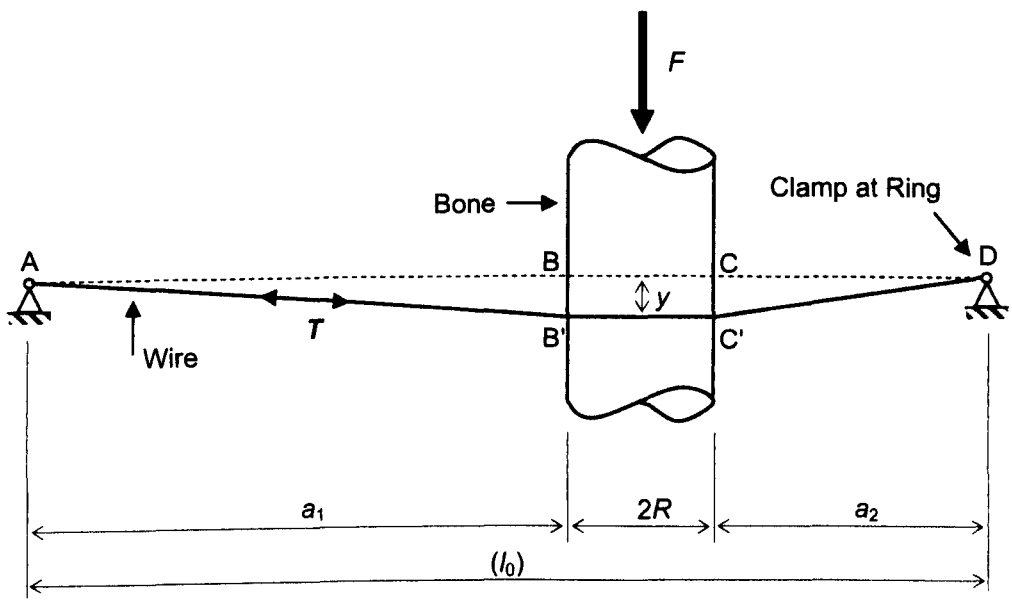


**Figure 34. Diagram of the axially loaded fine wire model. Front view.**

The original length of the wire (Figure 34) before load $F$ is applied can be calculated using Equation 31.

$$l_0 = a_1 + 2 \cdot R + a_2 \tag{31}$$

From triangle ΔABB', according to the Pythagoras' theorem:

$$\mathrm{AB'} = \sqrt{a_1^2 + y^2} \tag{32}$$

Similarly from triangle ΔDCC',

$$\mathrm{C'D} = \sqrt{a_2^2 + y^2} \tag{33}$$

The wire length $l$ after load $F$ is applied and the bone is displaced by distance $y$ is

$$l = \mathrm{AB'} + 2 \cdot R + \mathrm{C'D} \tag{34}$$

Therefore the difference between the original and loaded wire lengths is:

$$\begin{gathered} \Delta l = l - l_0 \\ \Delta l = \sqrt{a_1^2 + y^2} + \sqrt{a_2^2 + y^2} - (a_1 + a_2) \end{gathered} \tag{35}$$

Strain in the wire caused by $\Delta l$ is

$$\varepsilon = \frac{\Delta l}{l_0} \tag{36}$$

Therefore, the additional tension in the wire caused by bone displacement is:

$$|T_+| = A \cdot E \cdot \varepsilon \tag{37}$$

Adding the pre-tension of the wire to this tension gives the total tension in the wire:

$$|T| = |T_0| + |T_+| \tag{38}$$

The force $F$ can be resolved from the tension vector and the geometry of the wire:

$$\begin{aligned} F &= |T| \cdot (\sin(\angle \mathrm{BAB'}) + \sin(\angle \mathrm{CDC'})) \\ F &= |T| \cdot \left( \frac{y}{\mathrm{AB'}} + \frac{y}{\mathrm{C'D}} \right) \end{aligned} \tag{39}$$

Substituting the results of the previous equations into equation 39, a final equation correlating force, wire pre-tension and displacement is found.

$$F = y \cdot \left( |T_0| + A \cdot E \cdot \frac{\sqrt{a_1^2 + y^2} + \sqrt{a_2^2 + y^2} - (a_1 + a_2)}{a_1 + 2R + a_2} \right) \cdot \left( \frac{1}{\sqrt{a_1^2 + y^2}} + \frac{1}{\sqrt{a_2^2 + y^2}} \right) \tag{40}$$

Finally, rearranging Equation 40, the axial fine wire stiffness can be found readily.

$$k = \frac{F}{y} = \left( |T_0| + A \cdot E \cdot \frac{\sqrt{a_1^2 + y^2} + \sqrt{a_2^2 + y^2} - (a_1 + a_2)}{a_1 + 2R + a_2} \right) \cdot \left( \frac{1}{\sqrt{a_1^2 + y^2}} + \frac{1}{\sqrt{a_2^2 + y^2}} \right) \tag{41}$$

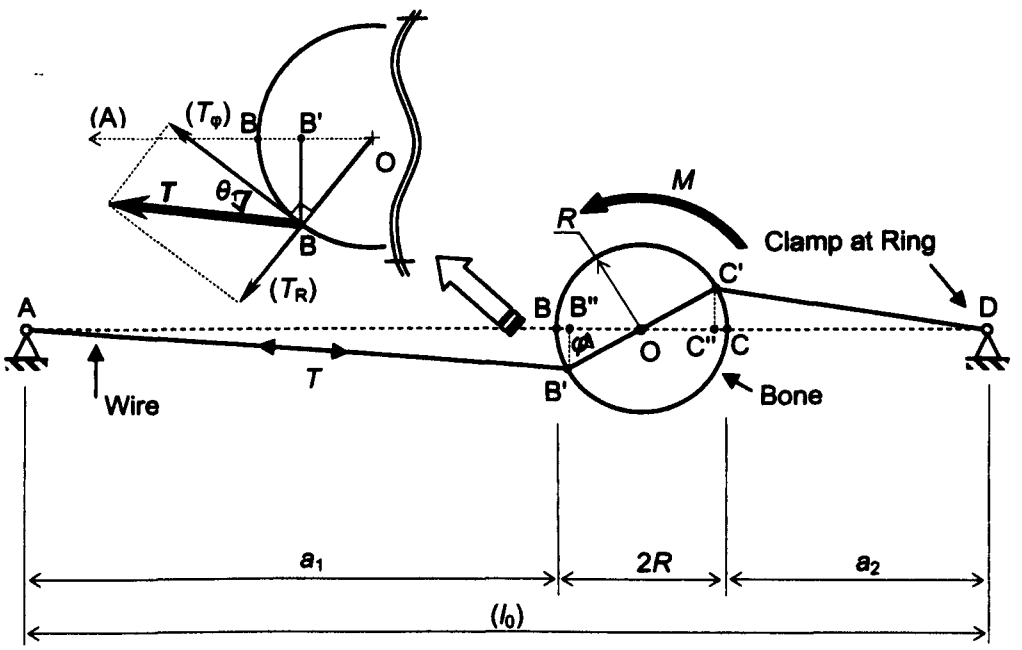


**Figure 35. Diagram of the torsionally loaded fine wire model. Axial (top) view.**

Using the same assumptions and a similar approach, the deflection of the wire when subjected to load via torsion around the long axis of the bone may be calculated. Figure 35 presents the configuration of the model. From triangle ΔAB"B', according to the Pythagoras theorem:

$$AB' = \sqrt{(AB'')^2 + (B'B'')^2} \tag{42}$$

Where

$$B'B'' = R \cdot \sin(\varphi) \tag{43}$$

$$AB'' = AB + BB'' = a_1 + BB'' \tag{44}$$

$$BB'' = BO - B''O = R - R \cdot \cos(\varphi) = R \cdot (1 - \cos(\varphi)) \quad \textbf{(45)}$$

Substituting Equations 43, 44 and 45 into 42, the loaded wire length on the left hand side of the model can be found:

$$AB' = \sqrt{a_1^2 + 2 \cdot R \cdot (a_1 + R) \cdot (1 - \cos(\varphi))} \quad \textbf{(46)}$$

A similar equation for the loaded length of the wire on the right hand side of the model can be derived:

$$C'D = \sqrt{a_2^2 + 2 \cdot R \cdot (a_2 + R) \cdot (1 - \cos(\varphi))} \quad \textbf{(47)}$$

Therefore the overall loaded wire length when the bone is turned about its central axis by angle $\varphi$ is:

$$l' = AB' + C'D + 2 \cdot R \quad \textbf{(48)}$$

The change in wire length therefore is:

$$\Delta l = l' - l \quad \textbf{(49)}$$

$$\Delta l = AB' + C'D - (a_1 + a_2) \quad \textbf{(50)}$$

The corresponding strain in the wire is:

$$\varepsilon = \frac{\Delta l}{l} \tag{51}$$

And the tension due to this strain is:

$$|T_+| = A \cdot E \cdot \varepsilon \tag{52}$$

Adding the pre-tension of the wire and this tension results in the total tension in the wire:

$$|T| = |T_0| + |T_+| \tag{53}$$

$$|T| = |T_0| + A \cdot E \cdot \frac{\sqrt{a_1^2 + 2 \cdot R \cdot (a_1 + R) \cdot (1 - \cos(\varphi))} + \sqrt{a_2^2 + 2 \cdot R \cdot (a_2 + R) \cdot (1 - \cos(\varphi))} - (a_1 + a_2)}{a_1 + a_2 + 2 \cdot R} \tag{54}$$

The tension in the wire can then be used to calculate the torque required to rotate the bone by angle $\varphi$. Only the component of the tension that is tangential to the surface of the bone at the point of the wire penetration will contribute to the torque. First, the angle between the tangential component of tension and wire tension vector must be found. Figure 35 contains a zoomed-in diagram of the model with tension vector at the left bone interface. The angles of the end deflections of the wire can be found using equations 55 & 56.

$$\angle \mathrm{BAB'} = \tan^{-1}\frac{\mathrm{B'B''}}{\mathrm{AB''}} = \tan^{-1}\frac{R\cdot\sin(\varphi)}{a_1 + R\cdot(1-\cos(\varphi))} \tag{55}$$

$$\angle \mathrm{CDC'} = \tan^{-1}\frac{\mathrm{C'C''}}{\mathrm{C''D}} = \tan^{-1}\frac{R\cdot\sin(\varphi)}{a_2 + R\cdot(1-\cos(\varphi))} \tag{56}$$

The angle $\theta_1$ between the tension vector $\boldsymbol{T}$ and the tangential component $T_\varphi$ of the tension vector can be found using information of the triangle $\Delta$B'AO. Similarly, the angle $\theta_2$ can be found using information of the triangle $\Delta$C'DO on the right hand side of the model.

$$\theta_1 = (\pi - \varphi - \angle \mathrm{BAB'}) - \frac{\pi}{2} \tag{57}$$

$$\theta_2 = (\pi - \varphi - \angle \mathrm{CDC'}) - \frac{\pi}{2} \tag{58}$$

Finally, an equation relating the moment applied to the bone, wire tension and displacement can be constructed:

$$M = |\boldsymbol{T}|\cdot R\cdot(\cos(\theta_1)+\cos(\theta_2)) \tag{59}$$

By substitution of Equations 54-58 into Equation 59, the relationships between applied moment $M$, angular displacement $\varphi$ and wire tension $\boldsymbol{T}$ can be calculated. The torsional stiffness of the fine wire can be found readily by dividing the applied moment $M$ by the resultant angular displacement $\varphi$.

## 5.4 Modelling Half-Pin as a Cantilever

To the author's knowledge, there are no published numerical or theoretical data on the pure half-pin model to date. The reason for this is believed to be the simplicity of half-pin mechanics. While intrinsic bending is not the key factor for the stiffness of the ring-wire construct, it is the only property that ensures rigid connection between the fixator's frame and the fractured bone. The half-pin can be modelled as a solid cantilever with a round section. It can be assumed that it is rigidly fixed at the ring interface via a rancho cube, Figure 36. If the load is applied through the centre of the bone, the axial displacement can be estimated using Equation 60 ([77] page 189, 1a).

$$y = \frac{F \cdot l_0^3}{3 \cdot E \cdot I} \tag{60}$$

Therefore the axial stiffness, defined as force required to displace the bone axially, is

$$k = \frac{F}{y} = \frac{3 \cdot E \cdot I}{l_0^3} \tag{61}$$

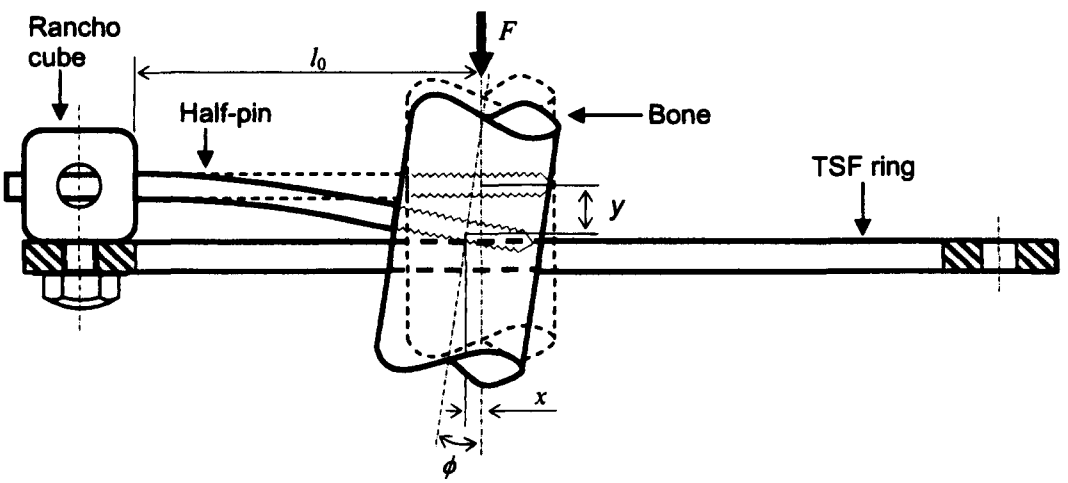


**Figure 36. Diagram of the half-pin model that is loaded axially. Front view.**

Where $I$ is the second moment of area of the cross-section of the half-pin

$$I = \frac{\pi \cdot d^4}{64} \tag{62}$$

The resulting axial stiffness of the half-pin therefore is

$$k = \frac{3 \cdot \pi \cdot E \cdot d^4}{64 \cdot l_0^3} \tag{63}$$

Torsional stiffness can be modelled similarly, Figure 37. The angular displacement of the bone, due to the applied moment around the bone central axis, is represented in Equation 64, ([77] page 194, 3a).

$$\varphi = \frac{M \cdot l_0}{E \cdot I} \tag{64}$$

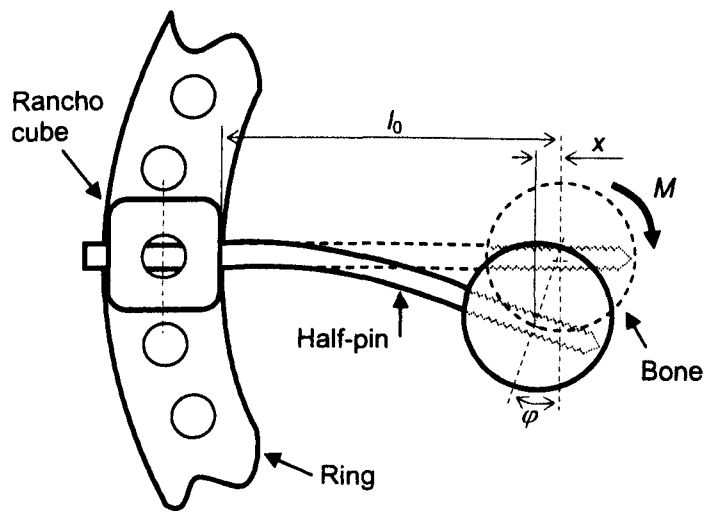


**Figure 37. Diagram of the half-pin model loaded in torsion. Axial (top) view.**

Therefore the 'angular' torsional' stiffness of the pin is

$$k = \frac{M}{\varphi} = \frac{E \cdot I}{l_0} \tag{65}$$

Substituting equation 62 to 65, the final expression for the 'angular' stiffness is obtained.

$$k = \frac{\pi \cdot E \cdot d^4}{64 \cdot l_0} \tag{66}$$

The half-pin gains permanent deformation when the stress in any part of the pin material exceeds the yield value, $\sigma_y$. Permanent deformation is not desired in orthopaedic fixation since the bone alignment is permanently affected. Therefore, the load capacity of the half-pin is defined by the maximum load that the half-pin can withstand before yielding. Both axial and angular loads applied to the bone result in a half-pin bending. The highest stress is at the outer fibre of the half-pin material. Equation 67 relates the bending moment to the maximum stress in the outer fibre of material.

$$\frac{M}{I} = \frac{2 \cdot \sigma}{d} \tag{67}$$

Hence, the maximum bending capacity of the half-pin is:

$$M = \frac{2 \cdot \sigma_y \cdot I}{d} \tag{68}$$

Substituting the second moment of area $I$, Equation 62, into Equation 68, the bending moment capacity of the half-pin is obtained.

$$M = \frac{\pi \cdot \sigma_y \cdot d^3}{32} \tag{69}$$

The maximum torque capacity for the half-pin, loaded through the bone in torsion, corresponds directly to the bending moment capacity. In the axial load case, the bending moment is caused by the axial load on the pin via the bone, and therefore is:

$$M = F \cdot l_0 \tag{70}$$

Finally, the axial load capacity $F_{max}$ of the half-pin can be derived by rearranging Equation 70 and substituting Equation 69. It should be noted, that Equation 71 does not take into account the shear stress contribution, since it is relatively negligible.

$$F_{max} = \frac{\pi \cdot \sigma_y \cdot d^3}{32 \cdot l_0} \tag{71}$$

## 5.5 Results of Fine Wire and Half-Pin Models

The derived wire model was validated by comparison of the results with the results obtained by other researchers [37, 70, 71]. The same scenario configurations were modelled and compared to previously published results. To the author's knowledge, there is limited information available for the TSF and therefore the comparison was carried out for Ilizarov frames only. The derived model is valid for both Ilizarov and TSF ring/wire constructs, since the same wires are used for both of these. Results of the validation are presented in Figure 38.

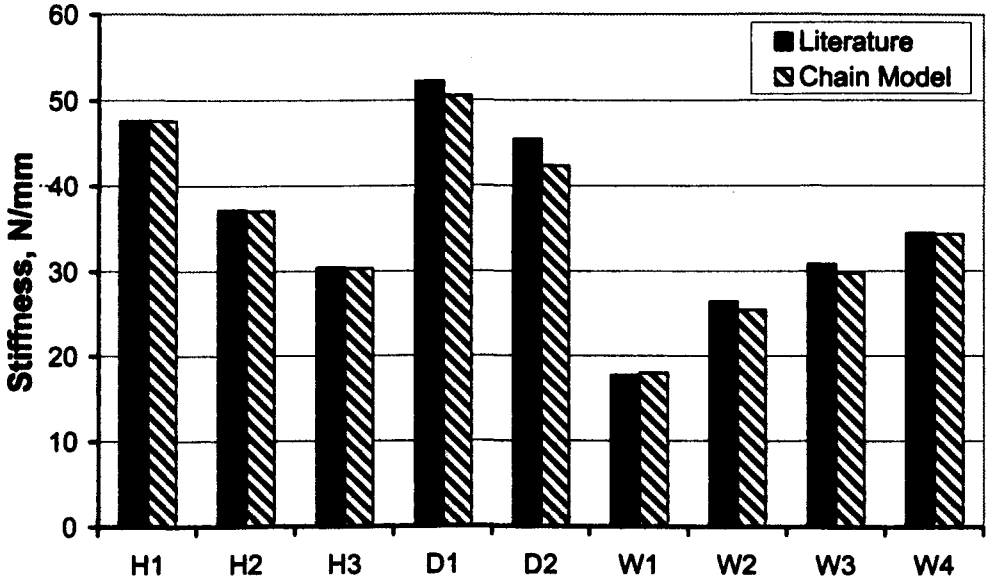


| | Wire dia *d* mm | Free length, mm | Load per wire N | Pre-tension N, kgf | Method | Quoted stiffness[1] N/mm | Modelled stiffness[2] N/mm | Source |
|---|---|---|---|---|---|---|---|---|
| H1 | 1.8 | 140 | 200 | 981 N | FE | 47.61 | *47.62* | [37], Figure 9 |
| H2 | 1.8 | 180 | 200 | 981 N | FE | 37.17 | *37.06* | [37], Figure 9 |
| H3 | 1.8 | 220 | 200 | 981 N | FE | 30.44 | *30.33* | [37], Figure 9 |
| D1 | 1.8 | 165 | 200 | 110 kgf | EXP | 52.21 | *50.50* | [70], Figure 4C[3] |
| D2 | 1.8 | 165 | 125 | 110 kgf | EXP | 45.45 | *42.35* | [70], Figure 4C[4] |
| W1 | 1.8 | 185 | 50 | 50 kgf | EXP | 17.73 | *17.98* | [71], Figure 5 |
| W2 | 1.8 | 185 | 50 | 90 kgf | EXP | 26.45 | *25.45* | [71], Figure 5 |
| W3 | 1.8 | 185 | 50 | 110 kgf | EXP | 30.86 | *29.79* | [71], Figure 5 |
| W4 | 1.8 | 185 | 50 | 130 kgf | EXP | 34.48 | *34.37* | [71], Figure 5 |

[1]The values of the stiffness were measured from the figures and are thus not absolutely accurate.
[2]Stiffness obtained using the chain model in same setup as other authors
[3]Stiffness value taken from stable part of the curve, after first few cycles
[4]Stiffness value taken during the first cycle before slip occurred at 250N load

**Figure 38. Comparison of wire stiffness obtained by other researchers with those modelled under same loading scenarios using the chain model.**

The wire properties were modelled for a range of TSF ring diameters. The spanning length of the wires was set to the internal diameter of the TSF ring. Ten TSF ring types were modelled (80, 105, 130, 155, 180, 205, 230, 255, 275 & 300 mm) together with 1.8 mm diameter fine wires. Two wire pre-tensions were simulated: 90 kgf and 110 kgf. For all models, the wire's material properties were taken from [37]. The wires were loaded through a modelled bone. The modelled bone diameter was set to 30 mm and it was positioned at the centre of the ring-wire construct. The load was applied incrementally, until the modelled wire yielded. The results of single wire models are presented in Figure 39 - Figure 44.

The obtained single wire stiffness results were then analysed for stiffness when few of them are used. It was assumed that wires share the load equally. Wire-ring constructs were loaded to 800 N axially in order to simulate an 80 kg person fully load-bearing, and up to 32 N·m torsional loads based on the findings of Duda *et al* [23] (4 % body-weight-metres) through the modelled bone. The results of multiple wire stiffnesses are presented in Figure 45 & Figure 46.

The half-pin stiffness was estimated for a range of the lengths, based on ring diameters. For each ring size, the half-pin length was set to half the internal diameter of the ring. Three types of half-pin diameters were modelled: 4 mm, 5 mm & 6 mm. 316L stainless steel was used as a base model material [78, 79]. The stiffness was modelled for both axial and torsional loading. Both axial and torsional loads were applied at the far end (from the clamp) of the half-pin. Results are presented in Figure 47.

Finally, the half-pin load capacity (*i.e.* load at which yield occurs) was assessed. The axial load capacity is dependant on the half-pin length and therefore, a range of lengths was considered. The half-pin lengths were set to half the internal diameter of ten types of TSF rings. The results are presented in Figure 48.

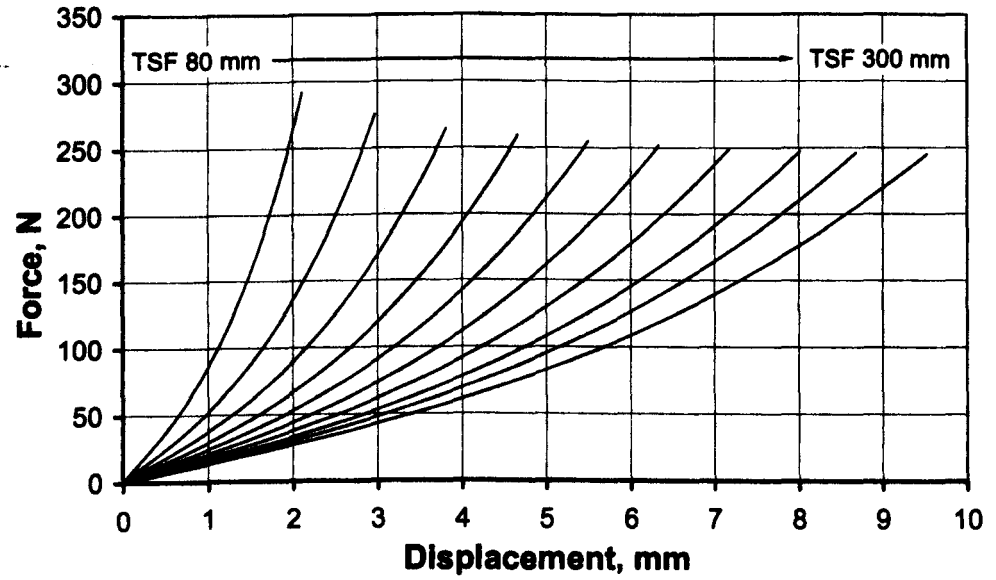


(a)

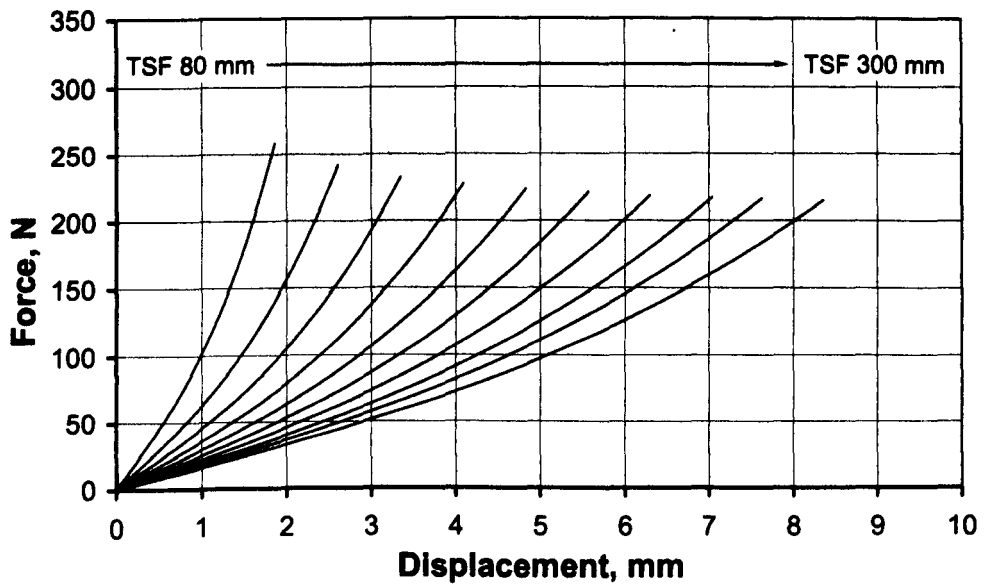


(b)

**Figure 39. Axial load-displacement curves for 1.8 mm wires for a range of TSF rings (80, 105, 130, 155, 180, 205, 230, 255, 275 & 300). a) – wires pre-tensioned to 90 kgf, b) – wires pre-tensioned to 110 kgf. Load-displacement curves terminate when wires yield across full length.**

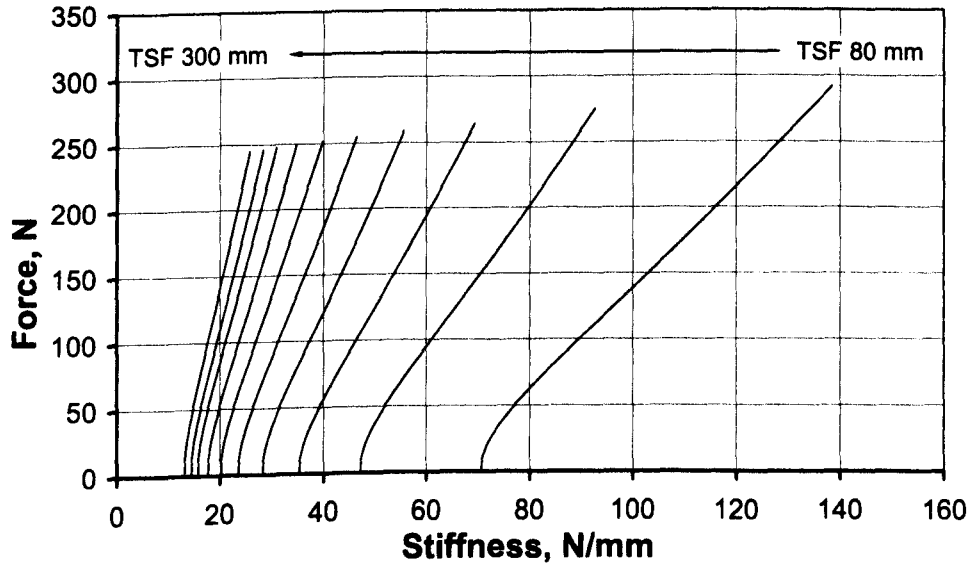


(a)

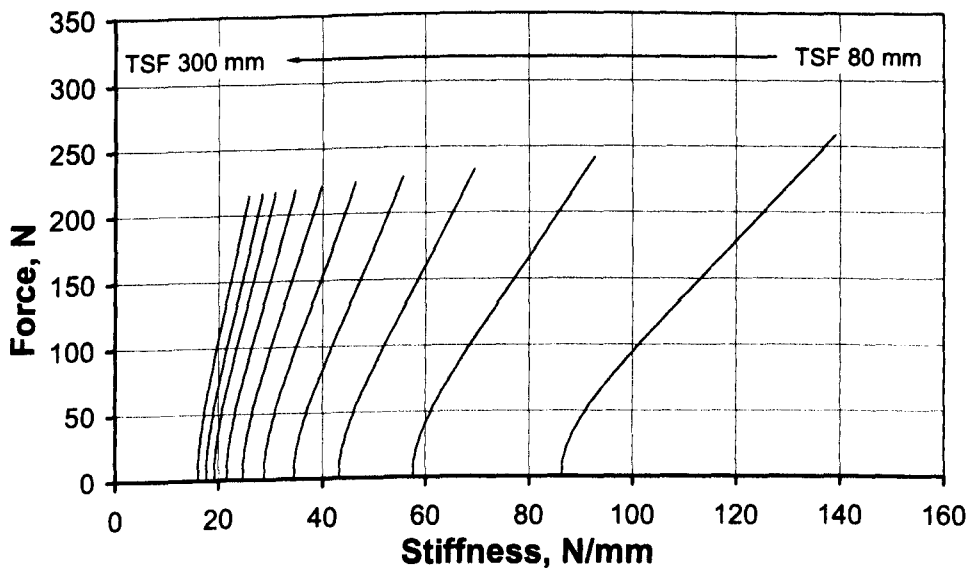


(b)

**Figure 40. Axial load-stiffness curves for 1.8 mm wires for a range of TSF rings (80, 105, 130, 155, 180, 205, 230, 255, 275 & 300). a) – wires pre-tensioned to 90 kgf, b) – wires pre-tensioned to 110 kgf. Load-stiffness curves terminate when wires yield across full length.**

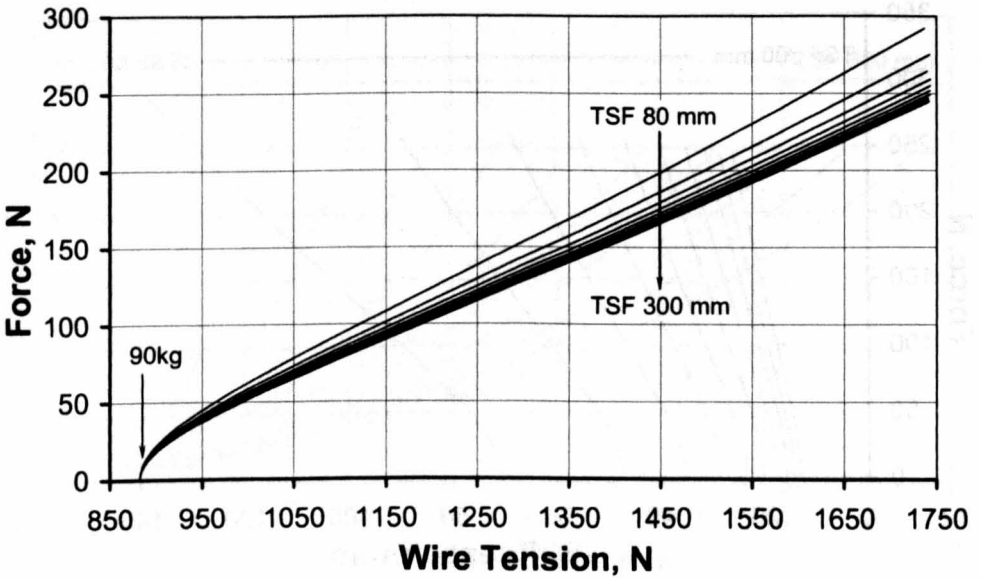


(a)

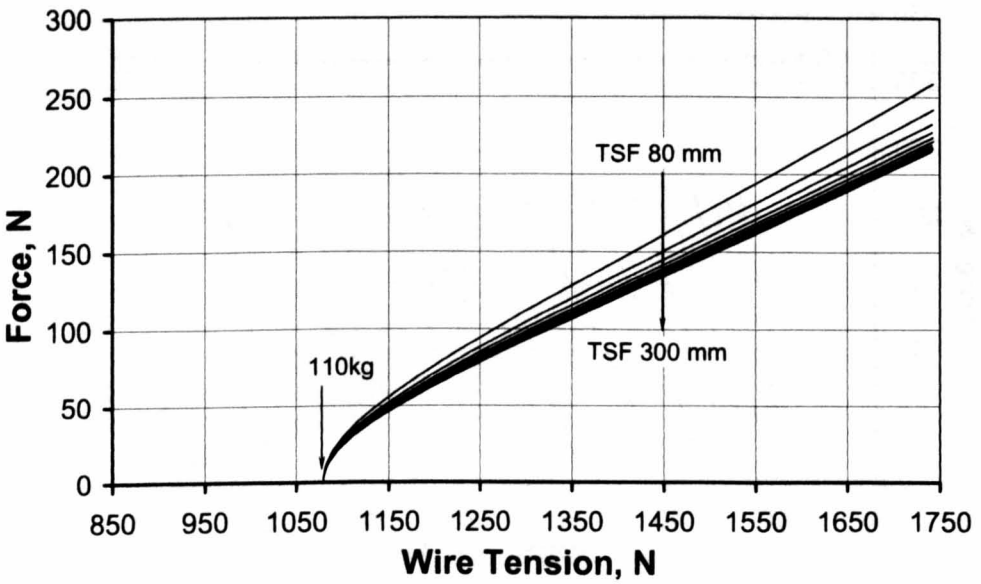


(b)

**Figure 41. Axial load – 1.8 mm wire tension curves for a range of TSF rings (80, 105, 130, 155, 180, 205, 230, 255, 275 & 300). a) – wires pre-tensioned to 90 kgf, b) – wires pre-tensioned to 110 kgf. Load-tension curves terminate when wires yield across full length.**

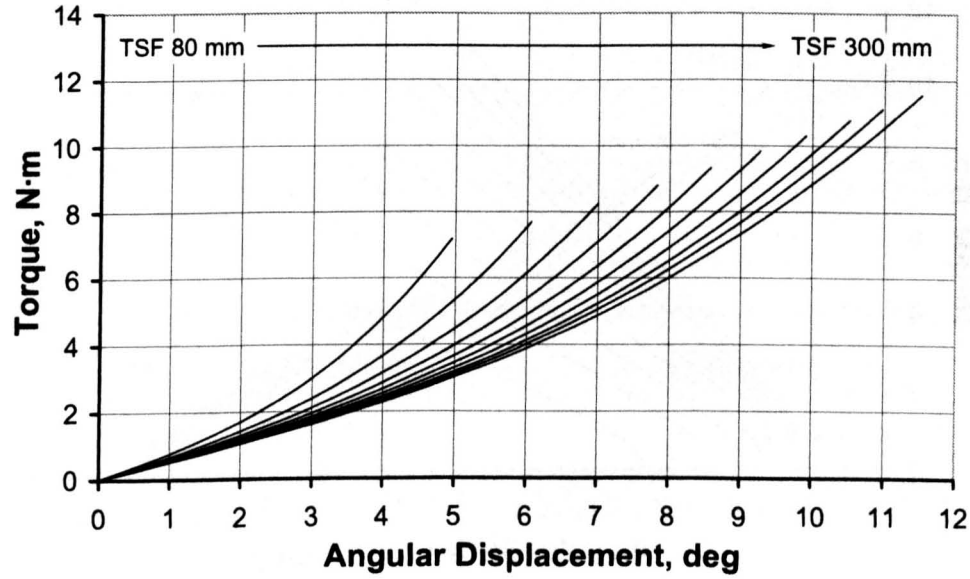


(a)

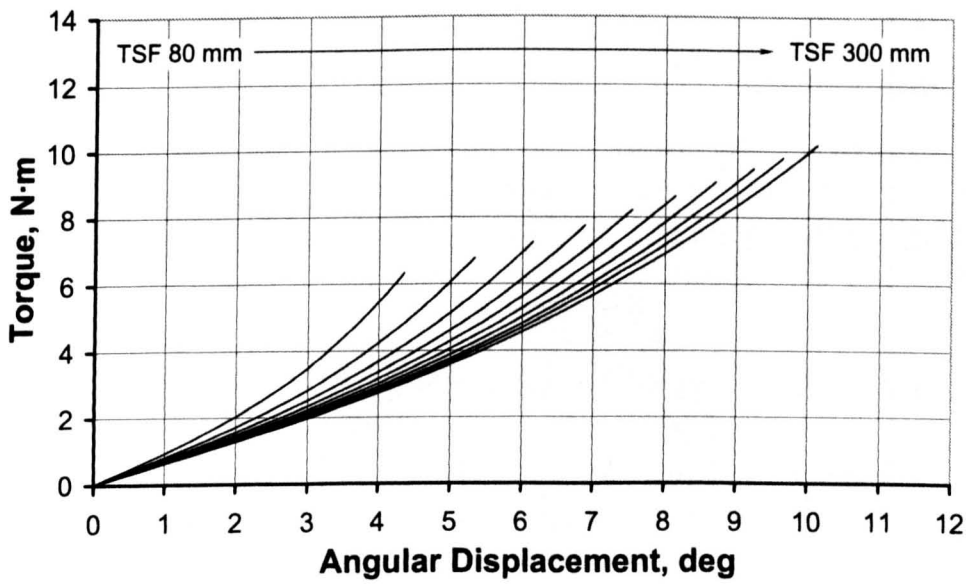


(b)

**Figure 42. Bone torque – angular displacement curves for 1.8 mm wires for a range of TSF rings (80, 105, 130, 155, 180, 205, 230, 255, 275 & 300). a) – wires pre-tensioned to 90 kgf, b) – wires pre-tensioned to 110 kgf. Torque-displacement curves terminate when wires yield across full length.**

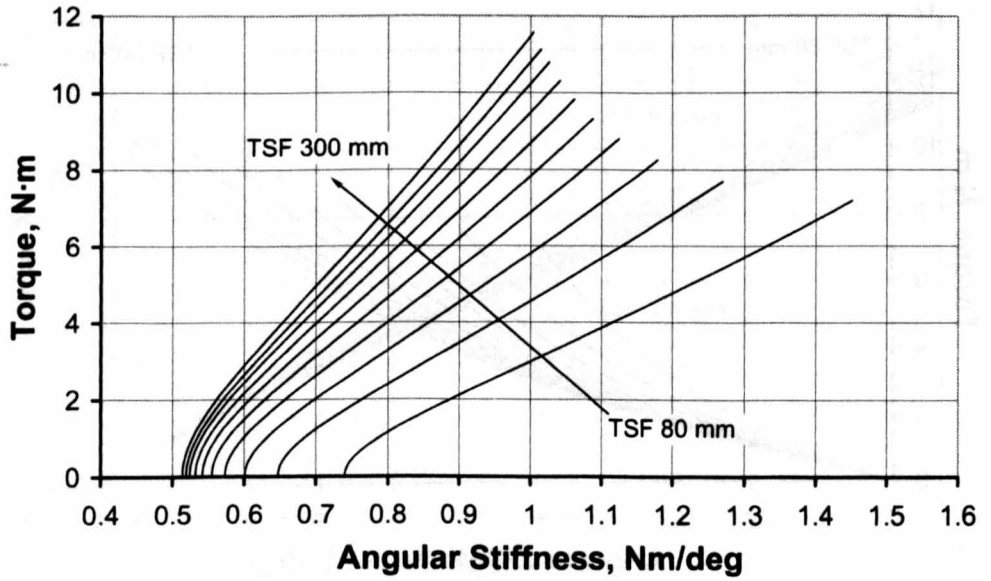


(a)

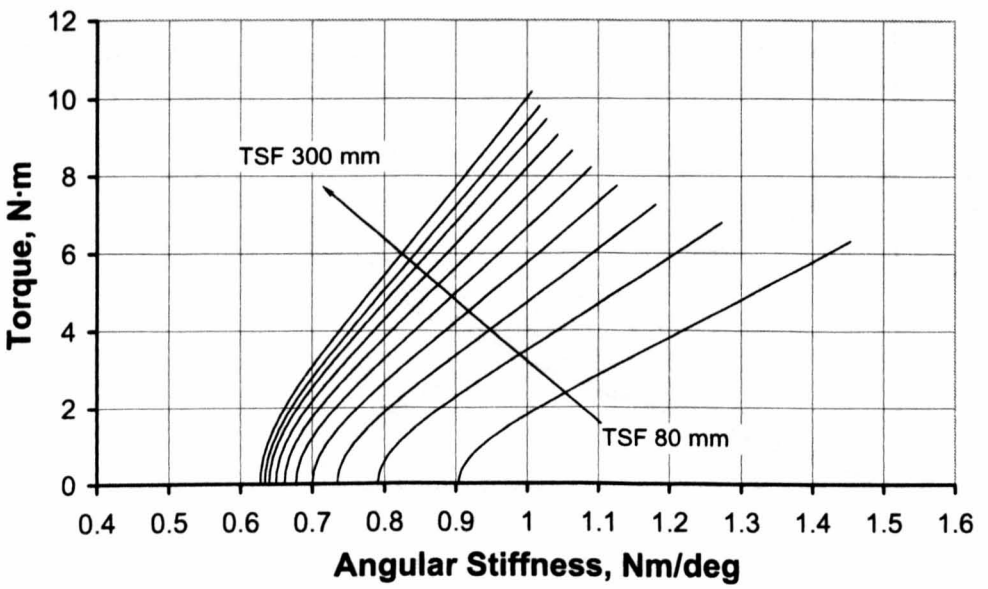


(b)

**Figure 43. Bone torque – angular stiffness curves for 1.8 mm wires for a range of TSF rings (80, 105, 130, 155, 180, 205, 230, 255, 275 & 300). a) – wires pre-tensioned to 90 kgf, b) – wires pre-tensioned to 110 kgf. Torque-stiffness curves terminate when wires yield across full length.**

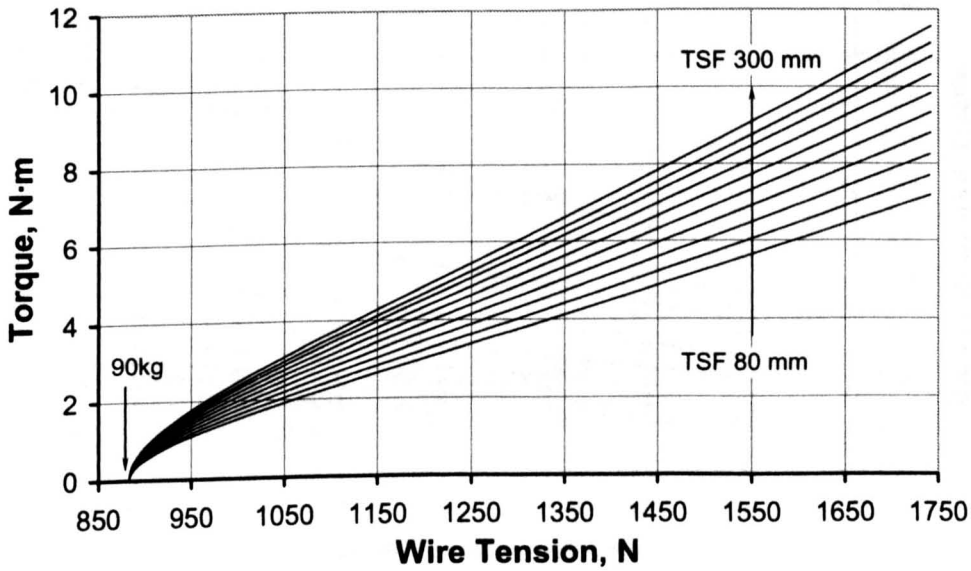


(a)

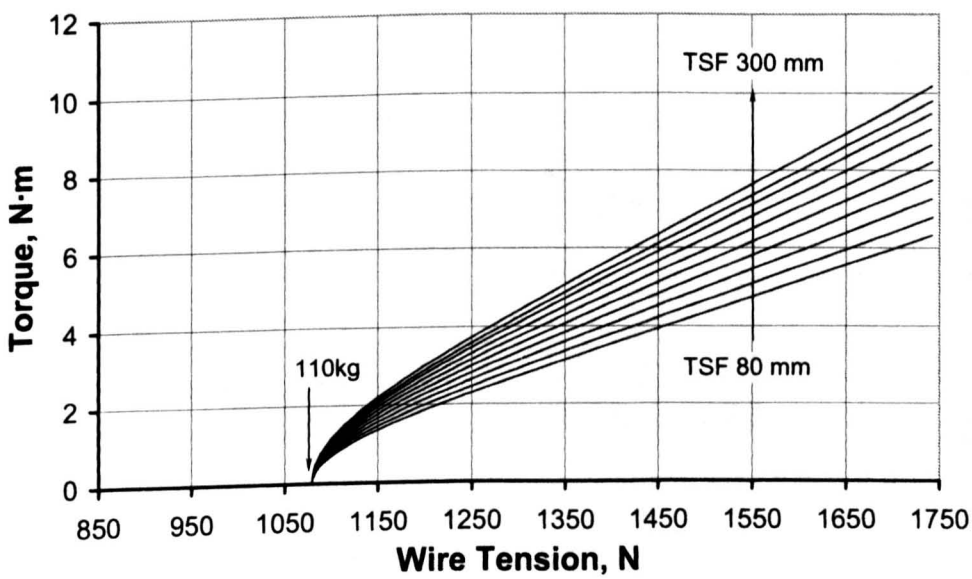


(a)

**Figure 44. Bone torque – 1.8 mm wire tension curves for a range of TSF rings (80, 105, 130, 155, 180, 205, 230, 255, 275 & 300). a) – wires pre-tensioned to 90 kgf, b) – wires pre-tensioned to 110 kgf. Torque-tension curves terminate when wires yield across full length.**

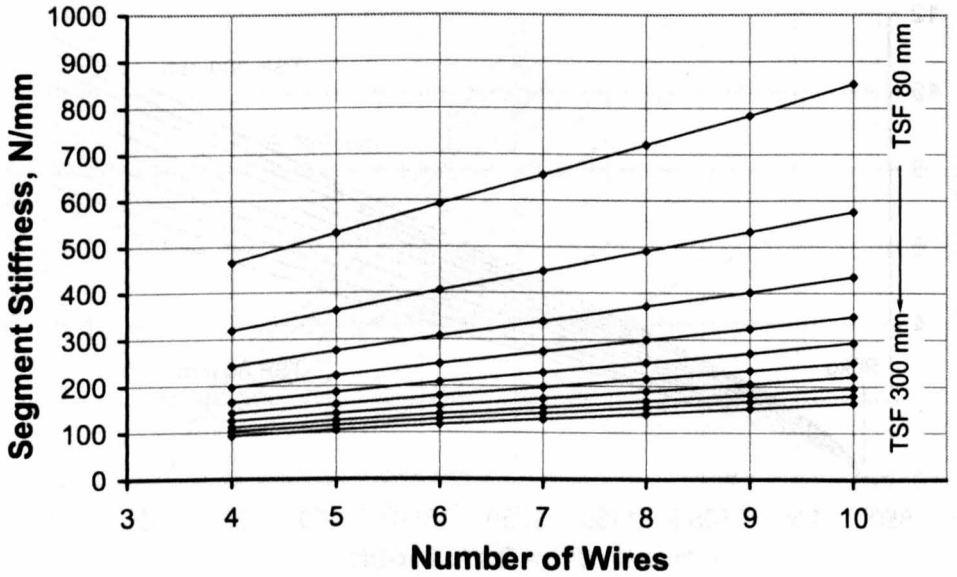


(a)

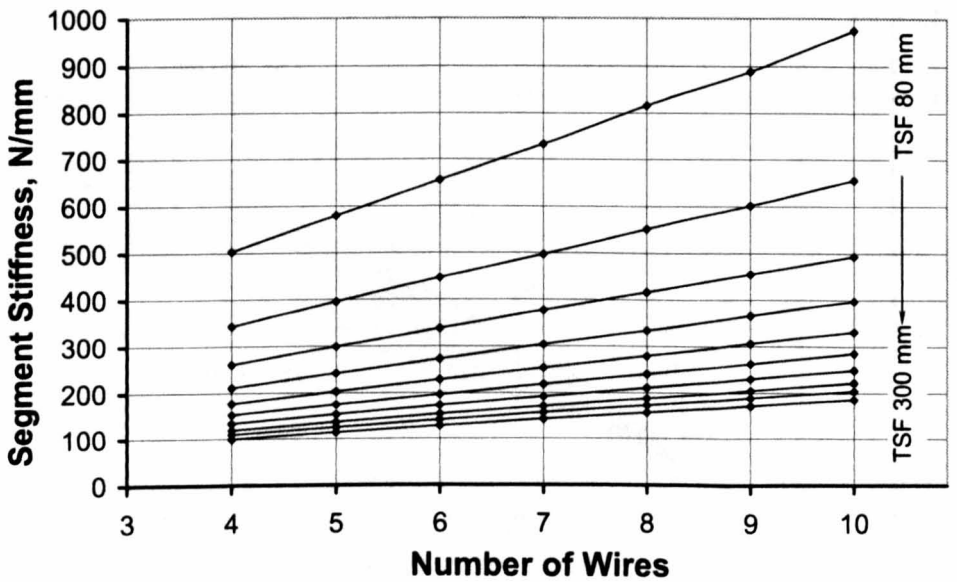


(b)

**Figure 45. Axial frame segment stiffness versus number of wires used for a range of TSF rings (80, 105, 130, 155, 180, 205, 230, 255, 275 & 300) and 1.8 mm wires. a) – wires pre-tensioned to 90 kgf, b) – wires pre-tensioned to 110 kgf. 800 N axial load was applied to the segment.**

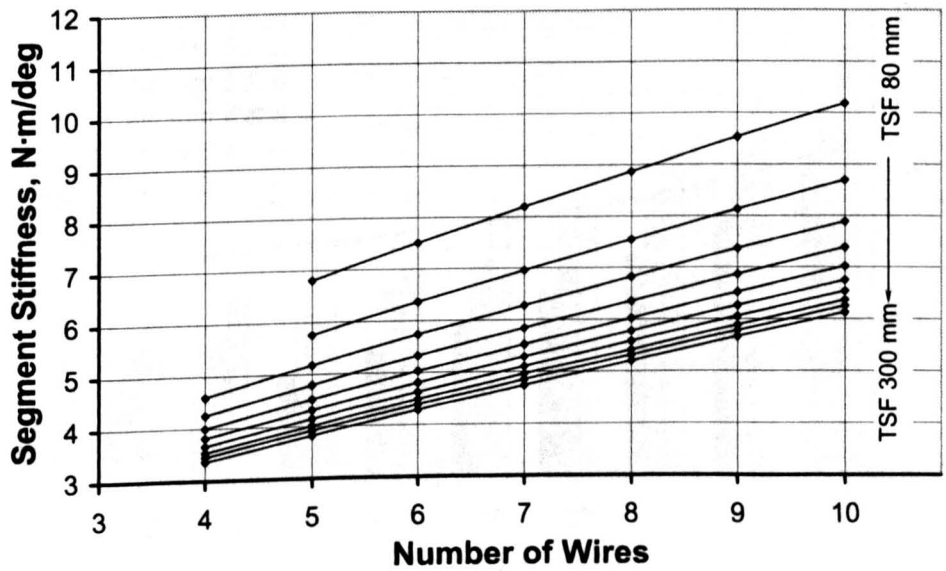


(a)

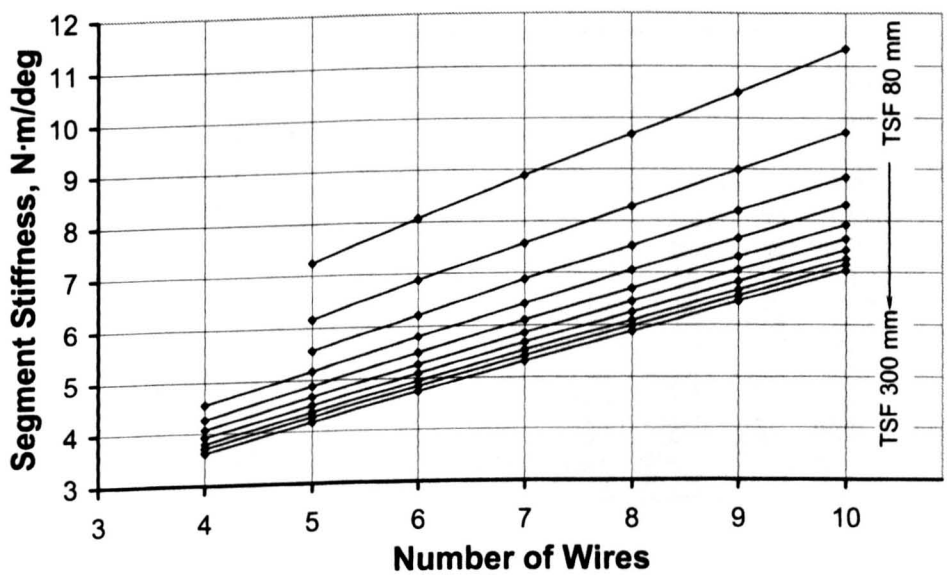


(b)

**Figure 46. Torsional frame segment stiffness versus number of wires used for a range of TSF rings (80, 105, 130, 155, 180, 205, 230, 255, 275 & 300) and 1.8 mm wires. a) – wires pre-tensioned to 90 kgf, b) – wires pre-tensioned to 110 kgf. 32 N·m torsional load was applied to the segment.**

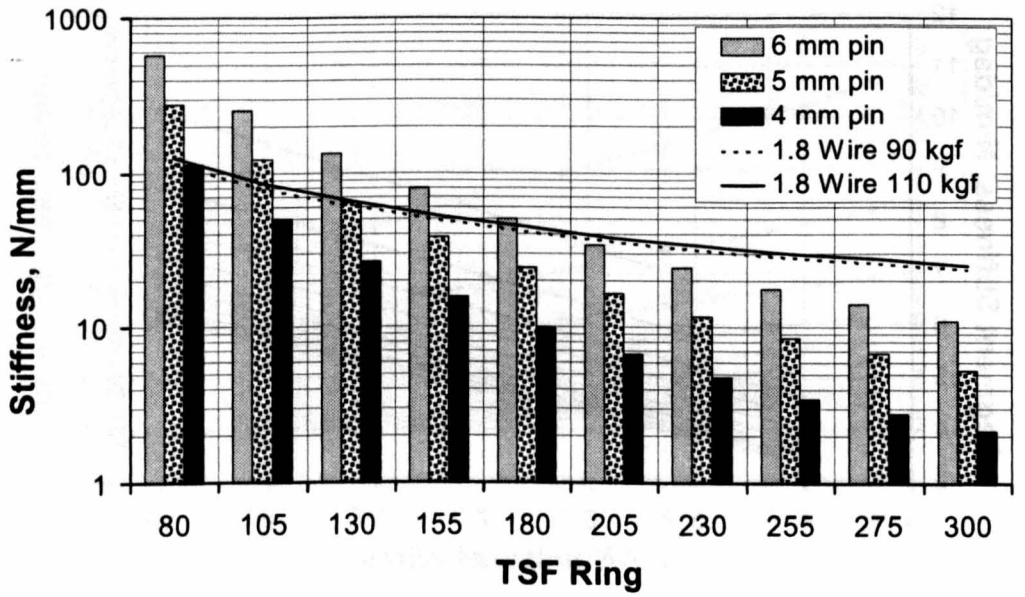


(a)

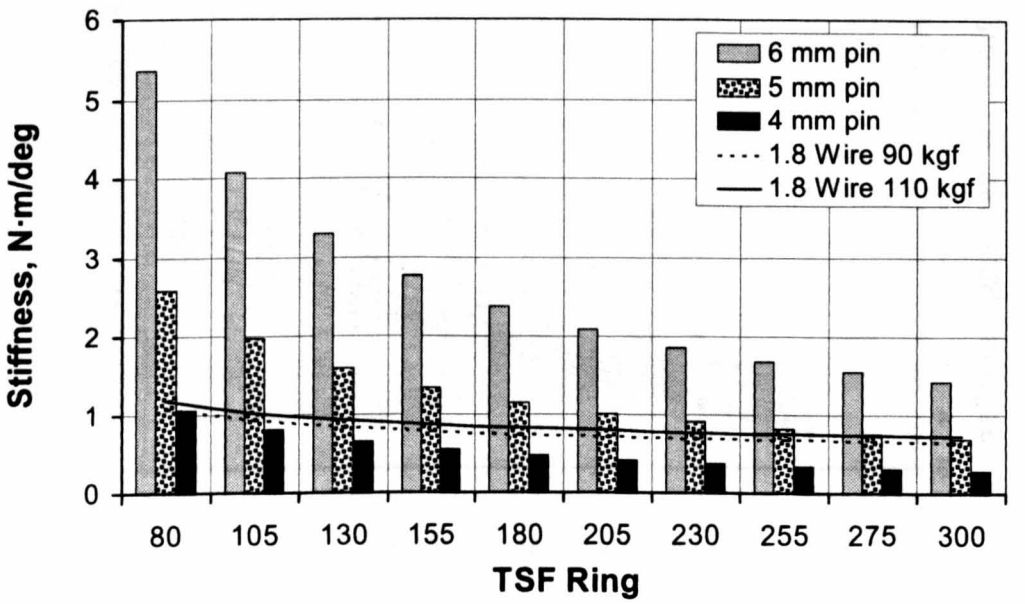


(b)

**Figure 47. Elastic stiffness of stainless steel half-pins for a range of lengths based on the internal radius of the TSF rings. Wire stiffness was calculated for 1.8 mm diameter wire loaded to 200 N axially and 3.75 N·m torsionally via 30 mm diameter bone. a) axial stiffness, b) angular(torsional) stiffness.**

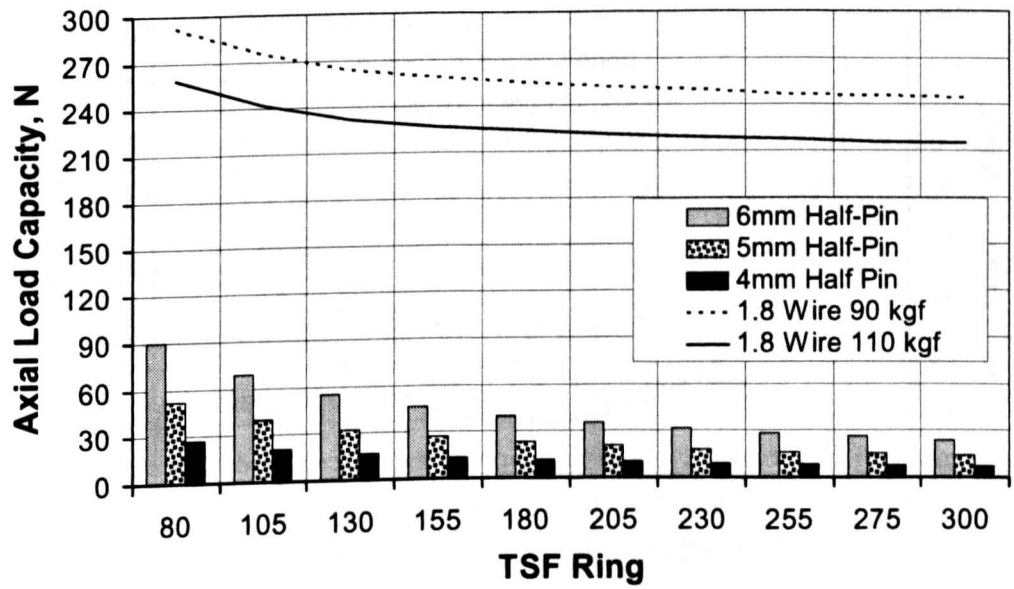


(a)

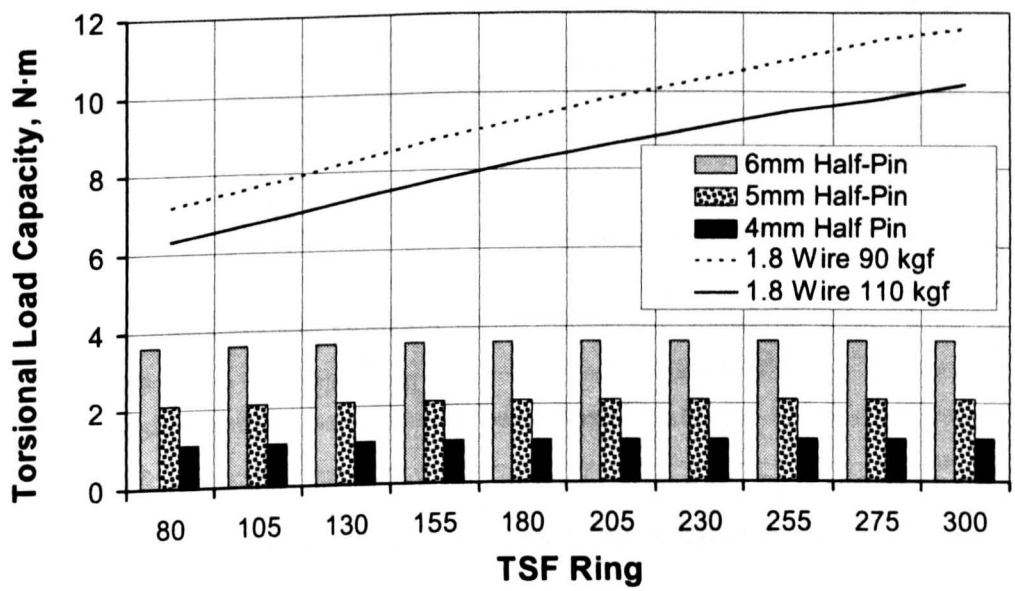


(b)

**Figure 48. Axial (a) and torsional (b) load capacities of half-pins and fine wires.**

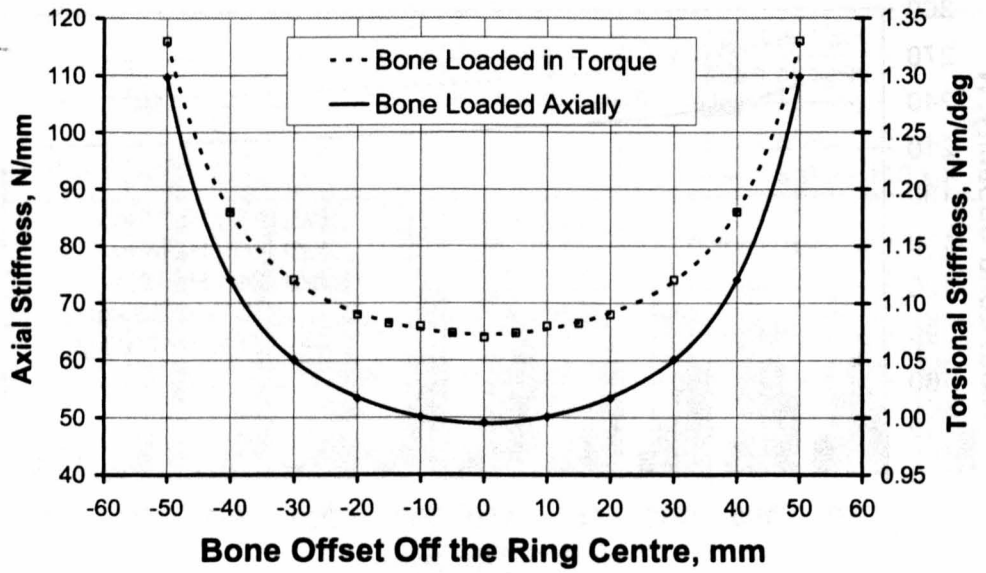


(a)

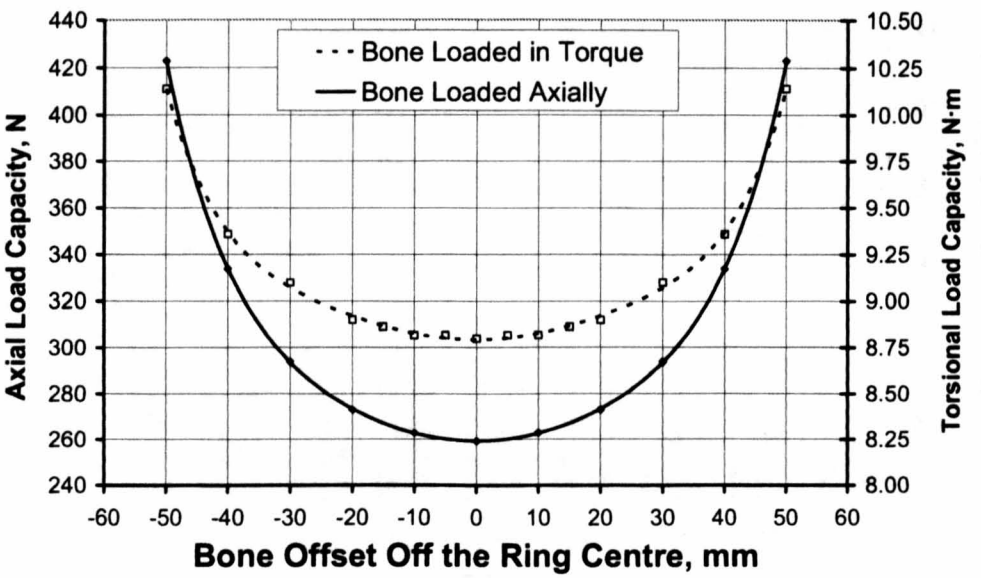


(b)

**Figure 49. Effects of bone offset from the centre of the ring/wire on the system stiffness (a) and load capacity (b). A 1.8 mm diameter wire was modelled on the 155 TSF ring, pre-tensioned to 90 kgf, and loaded through 30 mm diameter bone. Wire was loaded to 200 N axially and 3.75 N·m torsionally.**

## 5.6 Discussion of Results

### 5.6.1 Validation of the Chain Model

The results of the wire chain model were compared to the experimental and FE model results of other authors [37, 70, 71], Figure 38. A very close agreement was achieved, indicating that the wire's intrinsic bending stiffness is of low significance for highly tensioned wires. It is however not possible to compare directly the chain model results with some other researchers' findings [54, 70], as in these latter cases slippage of the wire between bolt and ring interface was reported. The slippage of the wire reduced the pre-tension and hence the axial stiffness of the wire-ring system.

| Material | Density<br>$\rho$, kg/m$^3$ | Elastic Modulus<br>E, GPa | Yield Strength 0.2% Proof<br>$\sigma_y$, MPa | Tensile Strength<br>$\sigma_t$, MPa |
|---|---|---|---|---|
| Stainless Steel 316L | 8000 | 193 | 170 | 485 |
| Titanium Alloy Ti6Al4V | 4420 | 114 | 828 | 897 |

**Table 5. Stainless steel and titanium alloy material properties.**

Few previous researchers have attempted to investigate the behaviour of the fine wire when loaded through torsion around the long axis of the bone. Bronson *et al* [8] have measured torsional resistance of such a system and recorded value was 0.84 N·m/deg (using a 160 mm Ilizarov ring and a 1.8 mm diameter wire tensioned to 883 N). Orbay *et al* [72] found the stiffness of such a system to be 0.6 N·m/deg. A direct comparison with chain model results is not possible unfortunately, because neither authors identified the applied torque range for their results. However, as can be seen from Figure 43, the present author's results are of similar magnitude to those obtained by other investigators. Both axial and torsional wire stiffness are not linear, Figure 39 & Figure 42, and exhibit self-stiffening effect as previously reported by

Aronson and Harp [54]. Finally, if instead the titanium alloy was used as a base material, the stiffness results are expected to decrease, since the modulus of elasticity is 40 % smaller for titanium compared to stainless steel, Table 5.

In clinical situations, the TSF ring is centred round the limb rather than the fractured bone. This results normally in the bone being offset. The chain model suggests that in such cases the stiffness of the ring-wire construct will increase, as shown in Figure 49a.

### 5.6.2 Load Capacity of the Fine Wire

In both axial and torsion load modes (defined as previously with respect to the frame), there is a maximum load that a wire can withstand without yielding, Figure 41 & Figure 44. 1.8 mm diameter wires typically yield at a tensile load of 1730 N, [37]. In most cases, based on the chain model, an individual wire can withstand axial (with respect to the frame) loads of 200 N and torsional loads of 6 N·m. As the ring diameter increases, the tolerance for the maximum axial load decreases. It is opposite for the torsion mode, where short spanning wire requires less bone rotation to cause high strains. Figure 40 & Figure 43 present the fine wire axial and torsional stiffness correlation with the ring diameter and wire pre-tension. As the ring diameter and hence the wire span decreases, the ring-wire construct stiffness increases. In addition, as the wire pre-tension increases, the ring-wire construct stiffness increases.

In the present fine wire analysis, only two values of initial pre-tension were considered: 90 kgf and 110 kgf. The increase of the initial pre-tension stiffens up the ring-wire construct, but at the same time undermines the load capacity. Based on the findings of Hillard *et al* [37] and Watson *et al* [69], it may be concluded that operational wire pre-tension should not exceed 1000 N. Localised yielding and loss of pre-tension during clamping always reduce the tension of the wire, and has to be taken into account. When the wire tension stress exceeds the material's yield strength, the wire gains a permanent increase in length. Initially, this results in a

decrease of the pre-tension, followed by excessive wire length and loss of control of the bone segment's location. The number of wires used to secure a segment of the broken bone should be carefully planned, taking into account a patient's body weight and ensuring that load per wire does not exceed 200 N axially and 6 N·m torsionally. In leg-lengthening cases, additional loading factors should be considered, as axial loads over 1000 N have been reported [67].

Similarly to stiffness properties, the load capacity of the fine wire increases as the bone is positioned off the centre of the ring, Figure 49b.

### 5.6.3 Multiple Fine Wires

If more wires are used to secure the bone segments onto the ring, the stiffness of the ring-wires system is expected to increase. Based on Figure 45 & Figure 46 it can be concluded that it is true for both axially and torsionally loaded ring-wires systems. The correlation between number of wires and stiffness of the ring-wires construct is reasonably linear despite the non-linear behaviour of the wire. This agrees with the findings of Orbay *et al* [72]. Similar to a single wire, the increase of the initial wire pre-tension increases the stiffness of the ring wire construct, albeit only marginally. The smaller the ring diameter, and hence the free spanning wire length, the stiffer the ring-wires construct is. It should be noted that for torsional loads in excess of 24 N·m, a minimum of five wires per segment should be used for ring sizes 80, 105 and 130 in order to avoid excessive fine wire yielding.

### 5.6.4 Pins

Results of a basic cantilever pin model have been presented in Figure 47 and Figure 48. Two geometric parameters directly influence the half-pin stiffness: diameter and length. As diameter increases, the half-pin stiffness increases at the fourth order rate. As the length of the half-pin increases, the axial stiffness decreases at the third order rate axially and the first order rate torsionally. The modelled material of the half-pin

was 316L stainless steel. If instead the titanium alloy were to be used, the stiffness results might be expected to decrease, since the modulus of elasticity is 40 % smaller for titanium compared to stainless steel, Table 5. It should be noted that the current model has assumed the rigid connection of the pin to the ring interface and therefore the infinite support (ring) stiffness. In reality, this is not entirely true. The ring is capable of flexion as shown in Chapter 4. This in turn makes the half-pins less stiff. However if more than one half-pin or a mix of fine wires and half-pins is used to secure the segment of the bone, some guiding at the pin/bone interface will be evidenced. The pin is effectively 'built in' at the bone in such cases. This results in stiffening of the half-pin by a factor of four axially ([77] p189 1a &1b) and eight torsionally ([77] p494-5 3a & 3b). Neither bending at the ring nor guiding at the bone is absolute and therefore the author believes that a simple cantilever model of the half-pin provides adequate approximation. Furthermore, if the half-pin were pinned at the ring and guided at the bone/pin interface ([77] p190 1f & p196 3f), the same numerical results would be achieved.

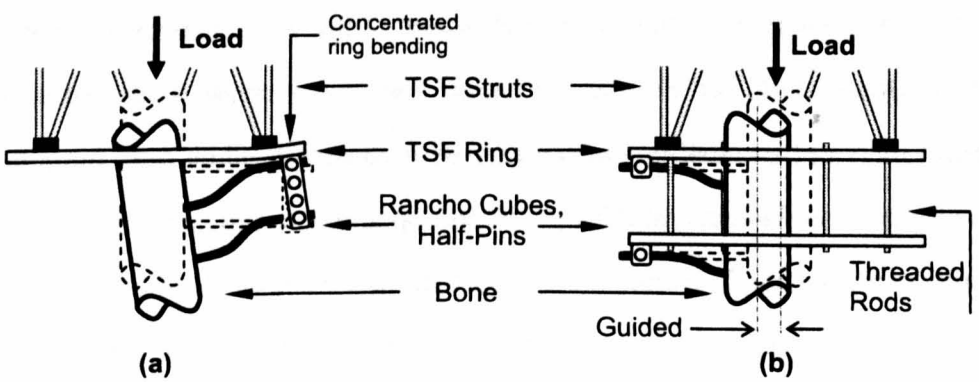


**Figure 50. Half-pin fixation to the TSF. a) two half-pins are supported from size four rancho cube (not recommended). b) two half pins are supported from size one rancho cubes attached onto separate rings.**

Hybrid fixators use a combination of half-pins and fine wires. In some cases, hybrid fixation uses some of the unilateral fixator components [7, 64, 75]. This is not the case in the TSF application, since the TSF is primarily responsible for deformity correction and fracture reduction. Some non-linear behaviour of hybrid fixators has been observed in the past [7, 75]. This can be attributed to the hybrid fixator

components other than half-pins. A few pins supported by a single monolateral bar or a stack of rancho cubes (Figure 50a), introduce high levels of concentrated bending moments at the ring attachment point, which in turn introduce non-linear behaviour of the fixator. The moment arm increases as the bone rotates around the attachment point of the pins on the ring due to ring bending. Such an arrangement results in fixator stiffness decrease with increasing load, introduction of severe shear and angulations [7, 54, 56, 58, 80]. The author believes that half-pins should be kept evenly spaced on the ring, and if necessary additional support (accessory) rings should be introduced avoiding significant ring bending and hence fixator weakening, Figure 50b.

The theoretical stiffness of a 6 mm diameter stainless steel half-pin of 90 mm length is higher than that of the fine wire for rings up to 205 mm, Figure 40 & Figure 47. Smaller diameter and titanium pins are weaker due to their material and geometrical properties. Calhoun *et al* [60] has tested rings with half-pins. Their experimental findings indicated that axial stiffness of the two 4 mm half-pins was 55 N/mm (27.5 N/mm per pin) and three 70 N/mm (23.3 N/mm per pin). Waanders *et al* [59] have reported that single pin contribution to the overall fixator stiffness was in the range 4 - 30 N/mm (half-pin lengths 40 - 120mm). Such low results indicate significant ring bending when compared to the present model's results. The load capacity of the stainless steel half-pins is presented in Figure 48. The axial load capacity of a single half-pin (46 N – 6 mm pin, 77.5 mm long) is on average 200 N lower, while torsional load capacity is 2-3 times lower than that of a single wire. This suggests that when applying half-pins, more of them will be required for high load applications, *e.g.* bone lengthening. However, the exact material properties of the half-pin are unknown to the author, and load capacity values can vary, with varying yield stress.

If more than one half-pin is used, the stiffness of half-pins adds up linearly and is expected to show a linear relationship, similar to that of fine wires. However, in

practical situations this might not be the case. If pins are close together on a single ring, the bending load is concentrated only on a part of the ring, similar to that for uniaxial fixators.

In clinical situations, the rings are centred round the limb rather than the bone. This results in the offset of the bone anterior due to the presence of soft tissues, especially muscles in long bone cases. The length of the pin will also be affected, normally shortened and therefore stiffened.

## 5.7 Conclusions

This study has shown that wires can be considered to act essentially as extensible chains and that simple models can be used to relate axial load to axial displacement as well as torsional load to angular displacement for ring-wire systems. The axial and torsional ring-wire construct stiffness increase linearly with the number of wires used. Decreasing ring diameter and increasing wire pre-tension results in the increase of the ring-wire construct stiffness. However, the increase of wire pre-tension decreases the load capacity of the construct.

The half-pins can be successfully used instead of wires at anatomically restricted areas. Results of a simple cantilever model suggest that half-pins have similar stiffness to that of fine wires. Increasing half-pin diameter and decreasing length increases half-pin stiffness.

The concentrated ring bending can significantly reduce the ring - half-pins construct stiffness, and therefore spacing the bending load evenly round the fixator might be necessary. The load capacity of the half-pins is relatively small compared to fine wires and hence precautions are recommended for high load applications. Finally, both fine wires and half-pins made of stainless steel offer higher stiffness compared to those of titanium.

# CHAPTER 6 : MODELLING OF THE FIXATOR'S STIFFNESS

Transfixing components (fine wires and half-pins) together with a frame constitute the orthopaedic fixator. So far, the properties of the transfixing components and the TSF have been studied separately. The aim of this chapter is to present a simple model to combine properties of the components in order to estimate the overall fixator's stiffness.

## 6.1 Review of the Previous Work on Fixator Stiffness Estimation

A number of researchers have investigated stiffness properties of the Ilizarov fixator in the past [6-8, 55, 58, 62, 64, 74, 75, 80, 81]. The high number of components and complexity of configurations has let to a high variability of their results for apparently similar configurations.

Two stiffness assessment methods have been used. The 'overall' method involved loading the fixator specimen to the clinically experienced maximum load and recording the maximum displacement between segments of the bone. The load was then divided by the displacement in order to estimate the stiffness of the specimen. Since fine wires and therefore fixator exhibit non-linear stiffness behaviour, a second method of stiffness assessment was suggested by Podolsky and Chao [58] and followed by other researchers [8, 74]. The 'regional' method involved monitoring the displacement as the load was applied. Typically, the applied load was divided into four equal ranges. Linear regression was used to estimate stiffness properties for each of the ranges.

To the author's knowledge, no stiffness properties have been reported for the TSF-based fixators.

## 6.2 Benefits of Fixator Stiffness Modelling

It is important to establish the correct mechanical environment at the fracture site in order to achieve a strong and functional union. It is therefore crucial to know the stiffness properties of the fixator, so that IFM can be influenced by the surgeon. Previous attempts to assess the overall fixator stiffness properties relied on mechanical testing. This has led to high variability of the results due to the variety of configurations used, namely number and locations of wires and half-pins. It is therefore sensible to analyse properties of the frames and the transfixing components on their own, and then use a model to combine them. It is hoped that the results of this chapter will provide a simple means of planning and assessing stiffness of the TSF-based fixator.

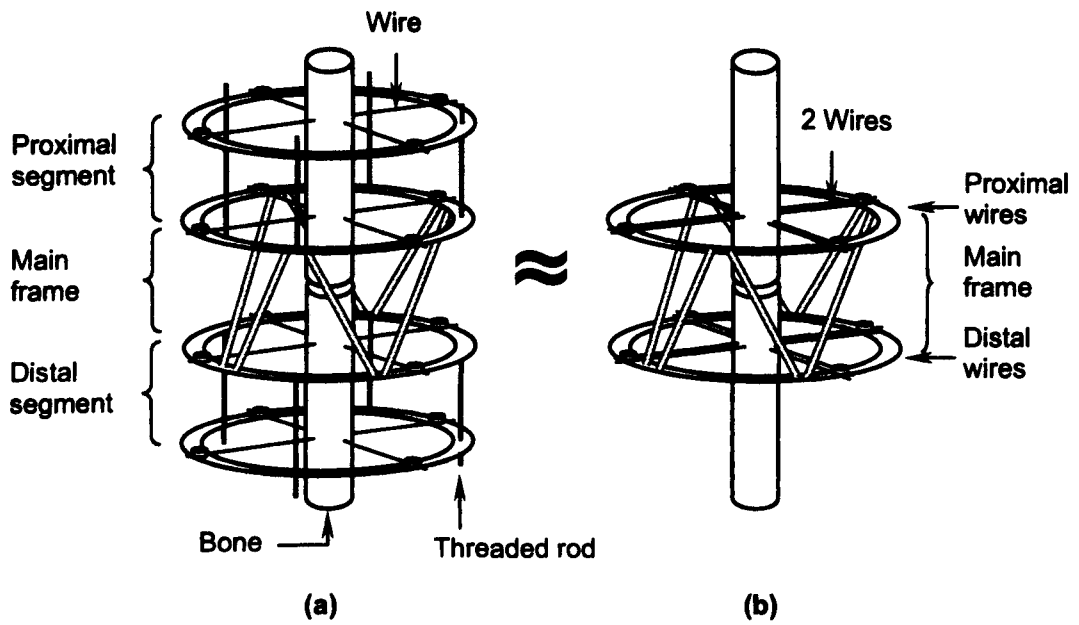


**Figure 51. Components and arrangement of the standard TSF based fixator. Both distal and proximal ends of the fractured bone are secured onto the rings using 4 wires per segment. The system on the left (a) is approximately equivalent to the system on the right (b) for axial and torsional loads assuming the stiffness of the proximal and distal frame segments is significantly higher than that of the fine wire.**

## 6.3 Modelling the Fixator

The stiffness of the fixator is influenced by the choice of the frame and bone transfixing components. If the fixator is split into three separate parts: proximal wires, frame and distal wires, as shown in Figure 51, its overall axial and torsional stiffness could be calculated using equation 72. Subscripts 'pw', 'dw' and 'f' indicate proximal wire, distal wire and frame respectively.

$$\frac{1}{k_{\text{Overall}}} = \frac{1}{N_{\text{pw}} k_{\text{pw}}} + \frac{1}{k_{\text{f}}} + \frac{1}{N_{\text{dw}} k_{\text{dw}}} \qquad \textbf{(72)}$$

Equation 72 is a valid approximation as long as the frame's proximal and distal segments are significantly stiffer than the transfixing components. If fine wires are used, the approximation is reasonable, since typical wire axial (transverse) stiffness was derived in the range of 25-115 N/mm in Chapter 5, depending on wire pretension and ring diameter. The TSF axial stiffness, when constructed of two 155 mm aluminium alloy rings and interconnected with six medium struts was measured as 400 - 1800 N/mm, Chapter 4.

Similar range differences were observed for the torsional values. The fine wire's stiffness ranged from 0.5 – 1.5 N·m/deg and the TSF stiffness was measured as 328 N·m/deg.

Half-pins exhibit similar stiffness to that of the fine wires, Chapter5.

If fine wires are used to transfix bone to frame, Equation 72 assumes identical properties for all of them, including wire diameter, length and pretension. The load is therefore shared equally among all wires supporting the segment of the broken bone. The number of wires ($N_{\text{pw}}$, $N_{\text{dw}}$) used to transfix each bone segment is typically from 4 to 6. In order to verify the validity of the Equation 72, models were constructed

similar to those assessed by other authors [6, 8, 58, 64, 74] and results were compared. Since no published data were available for the TSF fixator stiffness, the Ilizarov fixators were modelled for validation purposes. Other authors used four threaded rods instead of three to construct Ilizarov fixators, and therefore the Ilizarov frame stiffness values, obtained in Chapter 4 were scaled by a factor of 4/3. A summary of the modelled frame configurations is presented in Table 6. Values in brackets indicate assumed properties for the fixator configurations, which were omitted in some of the publications. Two steps were used in selecting modelled wire stiffness values $k_{pw}$ and $k_{dw}$. First, wire loading was identified by dividing the load applied to the bone segment by the number of wires used to transfix that segment. Then the stiffness value of a single wire was read from the load-stiffness graphs (Chapter 5) for the load obtained in the first step. A similar approach was used to identify single wire stiffness for the other segment.

| Label | FL | LU | BR | PO | WI | WI1 | WI2 | WI3 |
|---|---|---|---|---|---|---|---|---|
| Reference | [6] | [64] | [8] | [58] | [74] | [74] | [74] | [74] |
| Type of Stiffness | Overall | Overall | Region | Region | Region | Region | Region | Region |
| Ring Size, mm | 150 | 180 | 150 | 150 | 160 | 160 | 160 | 160 |
| Ring Material | (Steel) | (Steel) | (CF) | Steel | CF | CF | CF | CF |
| Bone Ø, mm | (30) | (30) | 38 | 25.4 | 31 | 31 | 31 | 31 |
| Wire Ø, mm | 1.8 | 1.8 | 1.8 | 1.8 | 1.8 | 1.8 | 1.8 | 1.8 |
| Wire Pretension, kgf | 90 | 150 | 90 | 90 | 80 | 80 | 80 | 80 |
| Half-Pin Ø, mm | - | - | - | - | - | (5) | (5) | (5) |
| Axial Load, N | (200) | 300 | 215-415 | 700-900 | 300-350 | 300-350 | 300-350 | 300-350 |
| Torsion, N·m | (10.0) | 10.0 | (10.0) | 0.2-0.3 | 4.0-9.0 | 4.0-9.0 | 4.0-9.0 | 4.0-9.0 |
| Ilizarov Rods | 4 | 4 | 4 | 4 | 4 | 4 | 4 | 4 |
| *Proximal Segment* | | | | | | | | |
| No of Wires | 4 | 3 | 4 | 4 | 3 | 1 | 2 | - |
| No of Pins | - | - | - | - | - | 1 | 1 | 3 |
| *Distal Segment* | | | | | | | | |
| No of Wires | 4 | (4) | 4 | 4 | 4 | 2 | 4 | - |
| No of Pins | - | - | - | - | - | 2 | - | 4 |

**Table 6. Summary of Ilizarov configurations tested by other authors.**

In addition to standard fine wire Ilizarov fixators, hybrid fixators (WI1, WI2 & WI3) were considered. The modelling of the stiffness of the mixture of half-pins and fine wires was more complicated. While fine wires and half-pins have similar stiffness properties, they are not identical and so do not share the segment load equally. An iterative approach was used to find the stiffness of the wire for a particular load, so that displacements resulting in pins concurred with those resulting in wires.

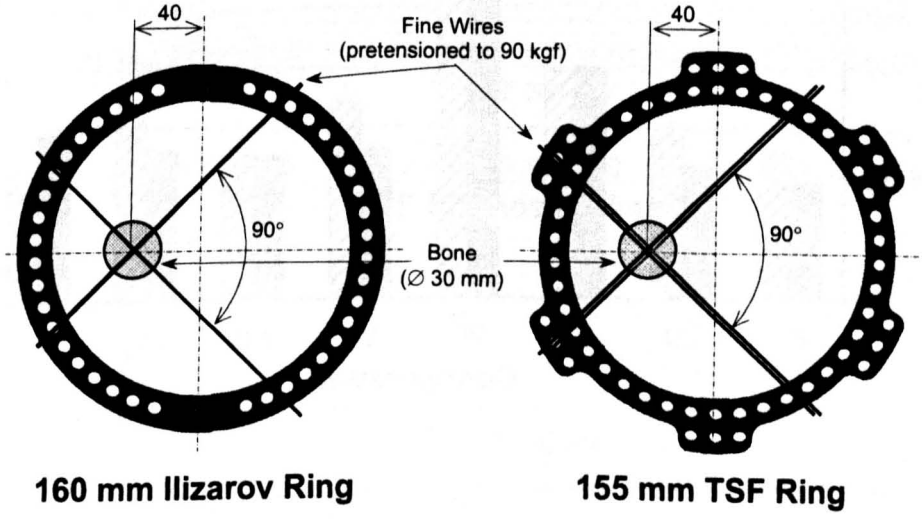


**Figure 52. Fine wire arrangement for modelling of offset loads on the proximal ring.**

When modelling offset loading, described in Chapter 4, the arrangement of the fine wires and modelled bone has been altered. The bone and wires were shifted by 40 mm off-centre for the proximal part of the fixator, Figure 52. The distal bone segment remained centrally transfixed.

Figure 53 presents the comparative results of the Ilizarov fixator stiffness measured by other authors and ones obtained using Equation 72.

## 6.4 Discussion

The obtained values for fine wire Ilizarov fixators reasonably agree (Figure 53) and verify the validity of the assumptions made for Equation 72. The general trend was that modelled stiffness values were greater than the experimentally obtained ones.

The variability can be explained by the effect of wire loosening during clamping [69], inexactness of the Ilizarov frame stiffness and variation of the component properties.

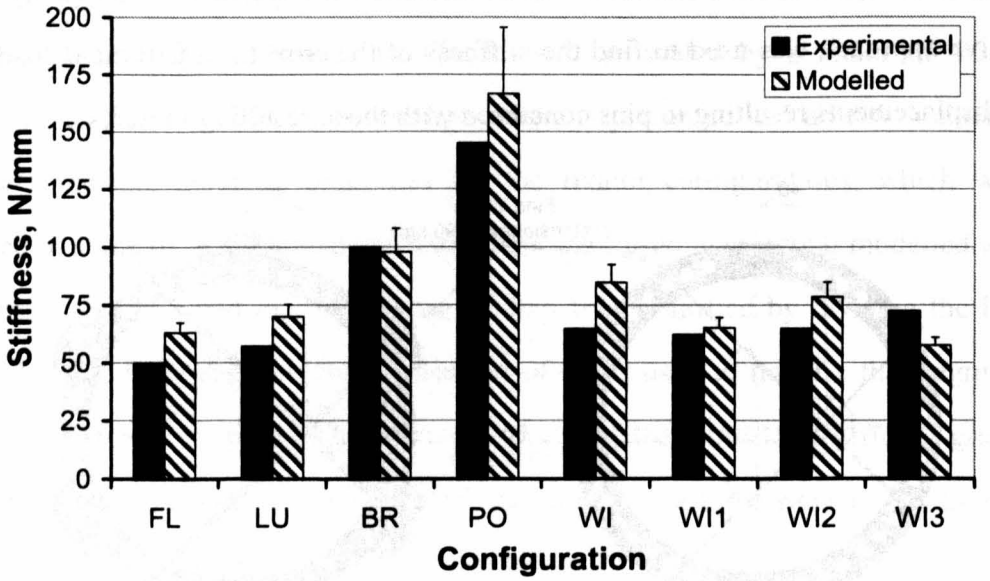


**(a)**

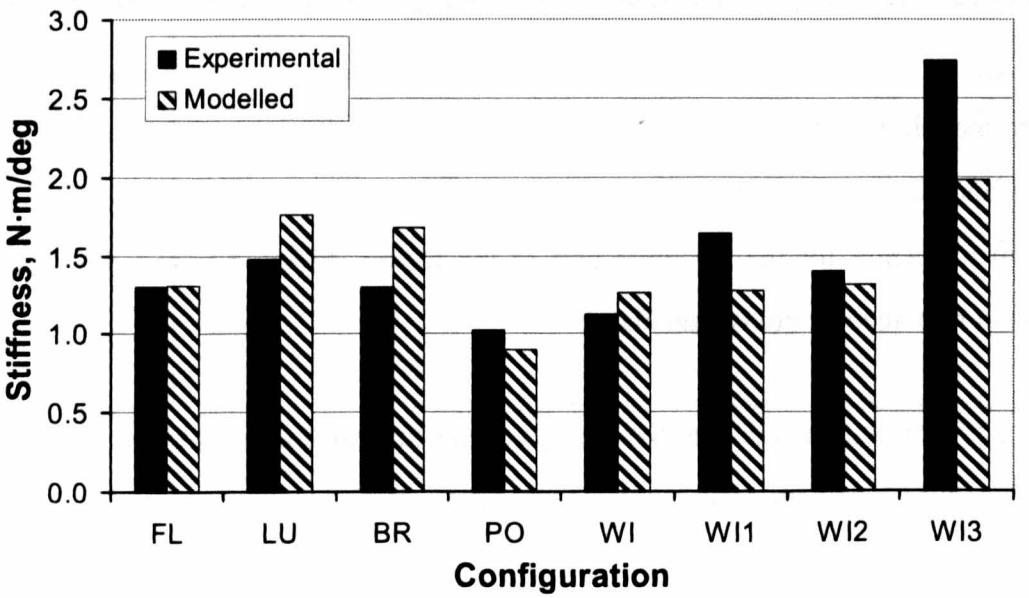


**(b)**

**Figure 53. Axial (a) and torsional (b) stiffness of the conventional (FL, LU, BR, PO, WI) and hybrid (WI1, WI2, WI3) Ilizarov fixators. The range bars indicate anticipated variation between stiff and flexible set-ups of the frames.**

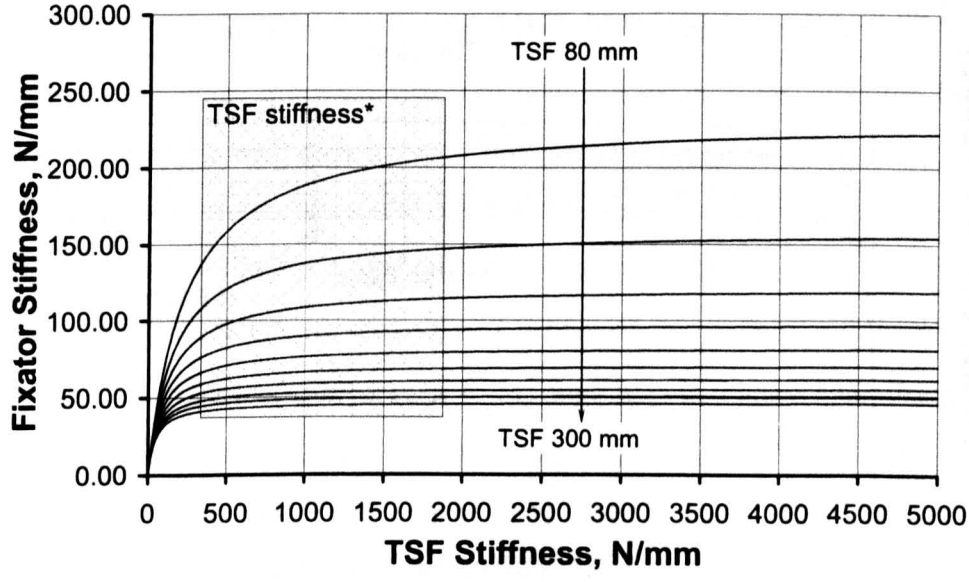


(a)

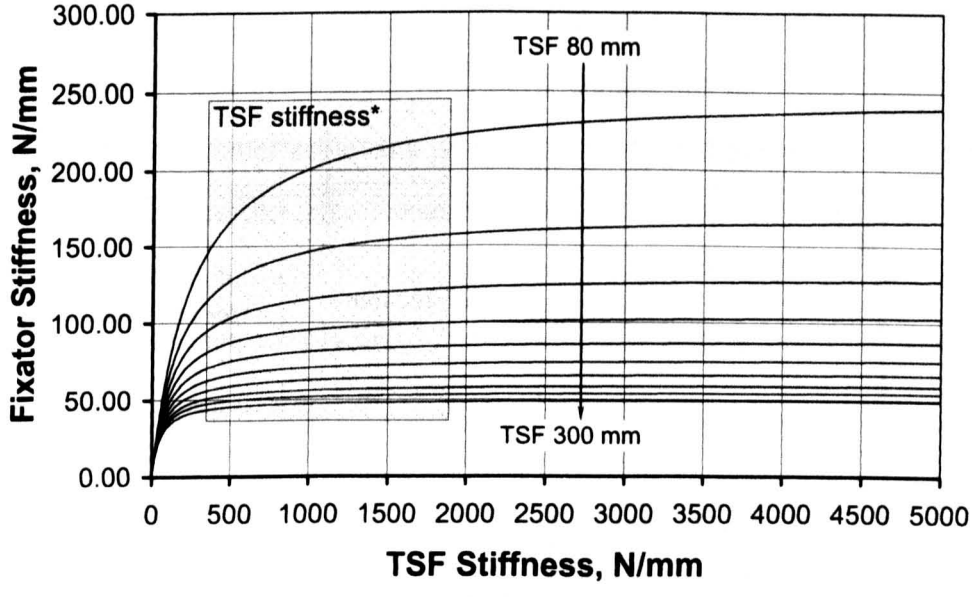


(b)

**Figure 54. Frame stiffness versus overall fixator stiffness for a range of frames (80, 105, 130, 155, 180, 205, 230, 255, 275 & 300) loaded axially. Wires were modelled as 1.8 mm in diameter with initial pre-tension of a) 90 kgf and b) 110 kgf. They were centrally loaded to 800 N via a 30 mm diameter bone. Eight wires were used, four per segment. * - the stiffness range of the neutral TSF constructed of two 155 rings and separated by 130 mm.**

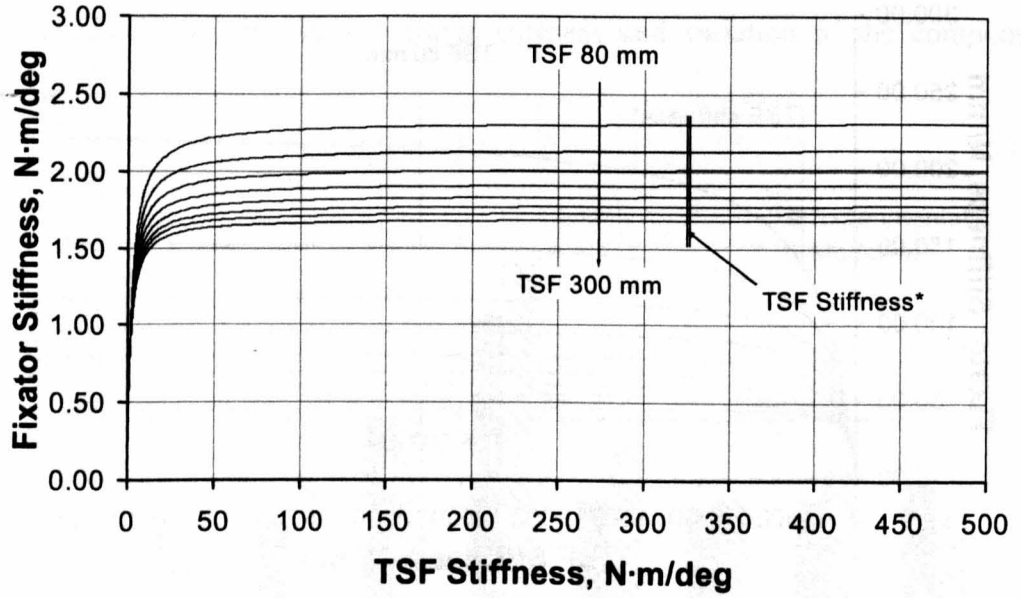


(a)

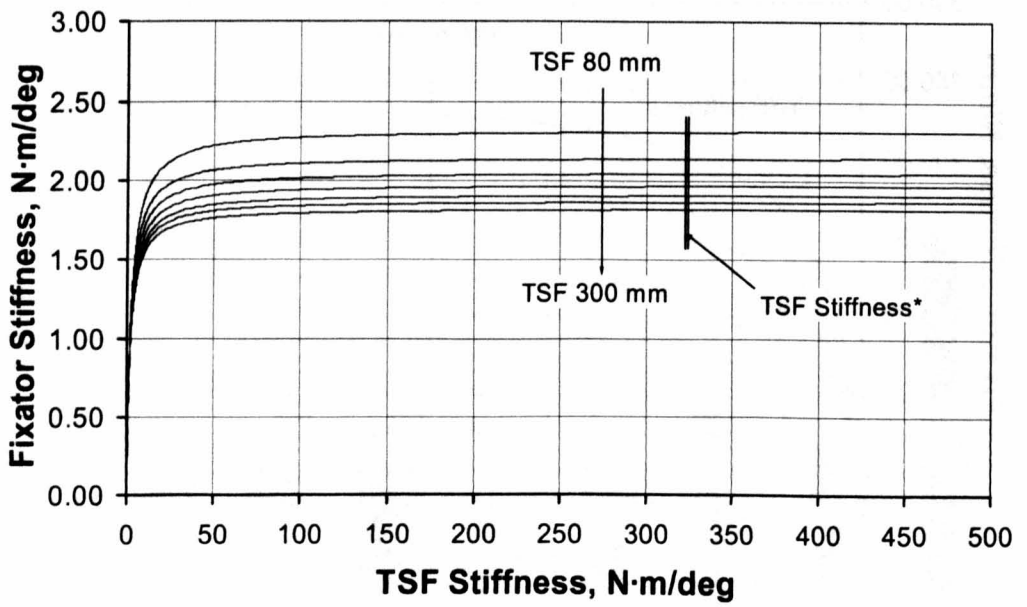


(b)

**Figure 55. Frame stiffness versus overall fixator stiffness for a range of frames (80, 105, 130, 155, 180, 205, 230, 255, 275 & 300) loaded in torsion. Wires were modelled as 1.8 mm in diameter with initial pre-tension of a) 90 kgf and b) 110 kgf. They were centrally loaded to 32 N·m via a 30 mm diameter bone. * - the stiffness of the neutral TSF constructed of two 155 rings and separated by 130 mm.**

The modelled stiffness of hybrid fixators gave satisfactory results. The torsional stiffness has been underestimated for the fixator WI3, which used half-pins only to transfix bone segments. Since the type and diameter of half-pins, used for fixation, have not been documented, the reason for this difference remains unclear.

The difference in the Ilizarov frame stiffness resulting from the 'stiff' and 'flexible' wire anchorage placement (described in Chapter 4), has minor influence on the overall fixator stiffness as can be seen from range bars in Figure 53a. This can be attributed to the fact that wires are significantly less stiff than the frame itself.

Figure 54 & Figure 55 relate frame stiffness to the overall fixator stiffness, for both axial and torsional loads. The fixators were constructed of various size TSF rings, and stiffness values were estimated using Equation 72. An 80 kg person, fully load bearing on the fixator was modelled. Four wires were used per bone segment to establish bone to frame connection. The results suggest that the wires rather than the frame limit the maximum achievable fixator stiffness, as they are the most flexible components. Secondly, the ring diameter (size) has a direct effect on the achievable stiffness. Thirdly, higher wire pretension produces a stiffer fixator. Increasing frame stiffness over 1 kN/mm axially and 100 N·m/deg only adds a minor increase to the overall stiffness of the fixator.

The TSF fixator's torsional and axial stiffnesses properties are presented in Figure 56. Results suggest that the stiffness of the circular fixator is mainly governed by the use of the transfixing components. It can be concluded that both the TSF and the Ilizarov fixators have similar stiffness and should in principle result in the similar IFM. The variation of stiffness between configurations with 'stiff' and 'flexible' transfixing component anchorage is minimised by the stiffness behaviour of fine wires and is 10 % - 30 %. This could be the reason for the variation of the stiffness values presented by other authors for apparently similar Ilizarov fixator configurations.

It is common to centre the TSF rings round the injured limb rather than the bone. This results in the bone being offset anteriorly and medially relative to the ring centre due to soft tissue presence *e.g.* muscles. If loads were applied off-central axis of the fixator, the results are expected to change. As has been shown in Chapter 5, the higher stiffness can be expected for the TSF fixators, due to ring-wire construct stiffness increase. This effect can be seen in Figure 56 and the observation agrees with the results of Fleming *et al* [6].

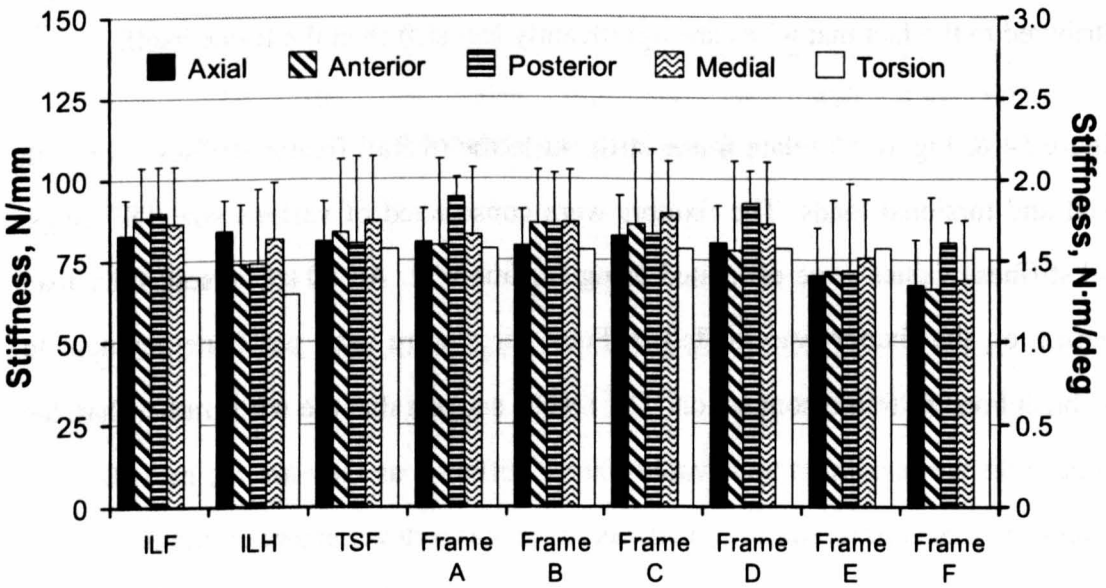


**Figure 56. Stiffness of the fixators with eight 1.8 mm wires (four per segment) pretensioned to 90 kgf. Frames were loaded through 30 mm O.D. modelled bone to 800 N axially and 15 N·m torsionally. The offset load cases (anterior, posterior & medial) applied axial load to the proximal ring of the frame via an offset (40 mm of central fixator axis) bone in the appropriate direction. The range bars indicate the difference between transfixing component anchorage at 'stiff' and 'flexible' frame set-up points.**

If fine wires are used to transfix frame to bone, the modified TSF for peri-articular fractures exhibit very similar properties to those of the original TSF, Figure 56. The details of frame modifications were presented in Chapter 4. It can be concluded that minor changes to the TSF frame stiffness are introduced, by moving strut groups 3&4 and 5&6 posterior by two holes (Frame A,D) or use of an additional accessory ring (Frame B). Frame B & D address radio opacity issues and allow clear fracture

visualisation. The use of the 'T-Pieces' (Frames E & F) result in less stiff constructs compared to the standard TSF based fixator.

The results suggest that the typical TSF fixator stiffness is of 80 N/mm. Therefore, in order for 0.5 mm of beneficial interfragmentary motion to occur (Chapter 2), the axial load of 40 N is required. The patients are encouraged to load bear after surgery and therefore significantly higher axial loads are anticipated. It is possible to speculate that higher loads cause larger strains and pain for the patient, therefore preventing further loading, or the load is shared between the fixator and the fractured bone. Further implications of low axial stiffness of the TSF fixator are discussed in Chapter 9.

## 6.5 Conclusions

A simple model for combining properties of the fixator's components has been presented and verified. The TSF based fixator stiffness is governed largely by the transfixing component properties. The variation in the reported stiffness of the Ilizarov fixator with apparently similar configurations can be attributed to the variation of the transfixing component anchorage locations, and this has been shown to affect the fixator stiffness by 10 % - 30 %. The further the bone is from the central axis of the fixator, the stiffer the overall construct is. Finally, the proposed modifications for the peri-articular fracture fixation alter the TSF-based fixator properties minimally. Moving strut groups 3&4 and 5&6 posterior by two holes or use of an additional accessory ring produces the best results.

# CHAPTER 7 : ACCURACY OF THE TSF AND CORRECTION METHOD

Mechanisms allow motion. A clearance distance between adjacent parts of mechanisms (*e.g.* joints, gears), allows movement, simple assembly and reduced friction. Unless moving parts are preloaded, slack (backlash) is evidenced as the load on the mechanism is reversed or the mechanism is unloaded. During the transition of this load (force, moment), an unconstrained motion occurs resulting in a displacement and/or a rotation. Slack is not absent from the Taylor Spatial Frame (TSF). The TSF strut is a mechanism that contains joints and a rotary/linear displacement converter. When strut components are not preloaded, slack exists resulting in uncertainty of the true length of the TSF strut. Furthermore, this slack influences the accuracy of the frame geometry. Other variable geometry fixators, such as an Ilizarov hinged frame, are also susceptible to slack. To the author's knowledge, the slack influence on the ring fixator's geometrical accuracy and on the success of treatment is an unexplored and undocumented area. This chapter analyses the effects of slack in the struts on the TSF positional and orientation accuracies and consequently the accuracy to which the broken bone segments can be positioned and aligned.

## 7.1 TSF Load States

The TSF load state depends on the treatment method employed. The TSF can be in three load states: unloaded, tension and compression, Figure 57. If limb lengthening is performed, the frame is in compression as the soft tissues resist the distraction. When a patient is load bearing on the frame, the compression load is further increased and thus the frame remains always in compression throughout the treatment.

It is common to apply some compression between fractured bone ends to help the unification for the majority of trauma fractures. Since bones resist compression, the

frame is in tension. However when patient is load bearing on the fractured bone, the frame can transit into compression.

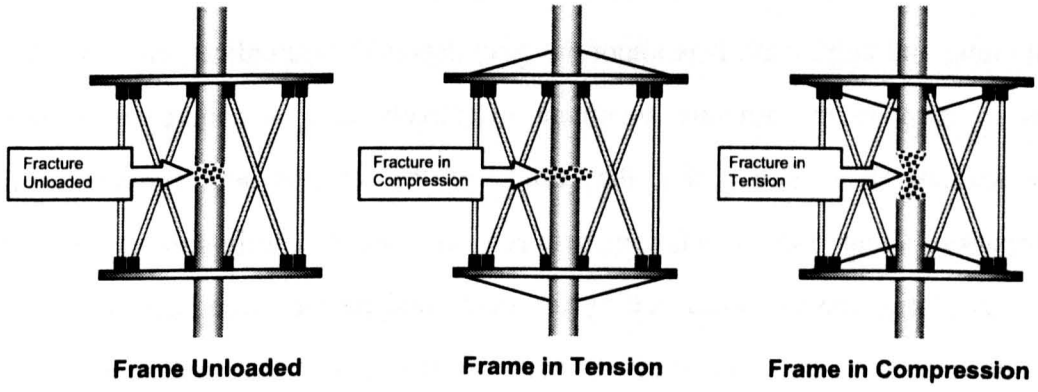


**Figure 57. TSF load states. Displaced wires indicate frame state and forces applied to bone segments.**

The third state of loading is evidenced for complex fractures where compression of the bone ends cannot be applied, *e.g.* oblique, spiral and comminuted fractures. In such cases, the fracture is reduced and maintained at small or no compression. When load bearing, the frame undergoes both tension and compression. This is normally the case at the early stage of healing.

When the frame undergoes tension to compression and vice versa, some unconstrained motion is present at the fracture site between bone segments. It has been observed anecdotally that patients experience high levels of pain as a result of such motion. The origin of the pain is believed to be high strains exerted on the newly-laid bone tissue. It is therefore important to understand the influence of slack on the uncertainty of the TSF geometry and if required to control it.

Slack can also pose a problem when performing deformity correction. The surgeon can set the lengths of struts of the TSF in 1 mm increments only. Furthermore, the actual strut lengths can be of different magnitude than those anticipated due to a backlash in the strut components. This can result in alignment and positioning errors during fracture reduction or deformity correction. Part of this chapter is dedicated to analysis of the implications of slack on the Total Residual correction method.

## 7.2 Benefits of TSF Accuracy Analysis

The slack in the TSF frame introduces uncertainty in the accuracy of the bone positioning and alignment. It is important to understand the implications of slack in order to manage the fracture treatment effectively and to counteract possible complications. It is hoped that the results of this chapter will provide useful information about the correlation between the frame configurations and the geometrical uncertainty introduced by the slack, and enable surgeons to decide on the significance of the slack itself. In addition, it is hoped that understanding the influence of the slack on the positional and orientational accuracy of the rings would also help to optimise the TSF design, reduce the need for residual corrections and improve patients' outcomes.

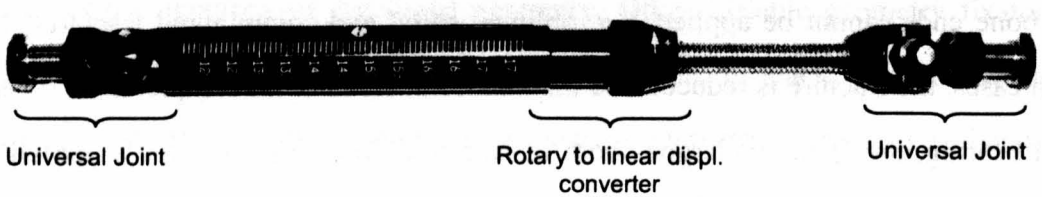


**Figure 58. A standard medium TSF strut.**

## 7.3 Origin of the Slack

The TSF is constructed of struts and rings. If rings are constructed from two half-rings, the joints between them are established via a set of bolts and nuts, which are tightened to ensure rigidity. Rings do not exhibit slack on their own, as they are static structural components. On the other hand, the TSF strut is a mechanism, consisting of two universal joints and one rotary-to-linear displacement converter, Figure 58. All these components introduce slack to the TSF strut and consequently to the TSF. The displacement converter is preloaded, however the preload is minimal. Small loads on the TSF can cause slackness of this mechanism, too. Example sources of the small load would be gravity and inertia of the limb when it is lifted off the floor.

Twelve clinically-used medium struts were tested in the tensile testing machine. The struts were loaded axially (in the direction of the major axis of the strut) in both tension and compression for five cycles. The slack was measured in the range from ±30 N in order to include the slack of the rotary to linear displacement converted. The typical load – displacement curve is presented in Figure 59. The average slack found in twelve specimens was 1.5 mm with standard deviation of 0.15. It is anticipated that the same slack is applicable to other standard strut types (extra short, short and long) since all of them employ the same design and geometry of the mechanisms.

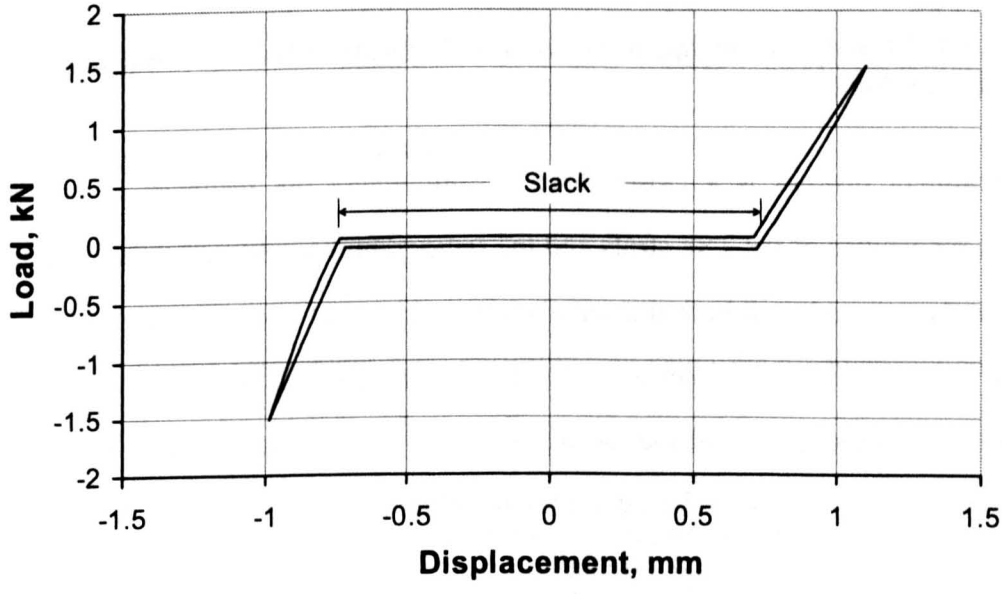


**Figure 59. Load – displacement curve of the standard medium TSF strut.**

## 7.4 Slack and Deformity Correction Method

It is common practice to perform a complex fracture reduction in more than one degree of freedom with the TSF. The rings are attached to the fractured bone segments via fine wires and/or half-pins. Six interconnecting struts are then placed between the rings, and the fracture and deformity are reduced. This application of the TSF is called the Total Residual correction method. The complete process of the treatment using the Total Residual method is illustrated in Figure 60.

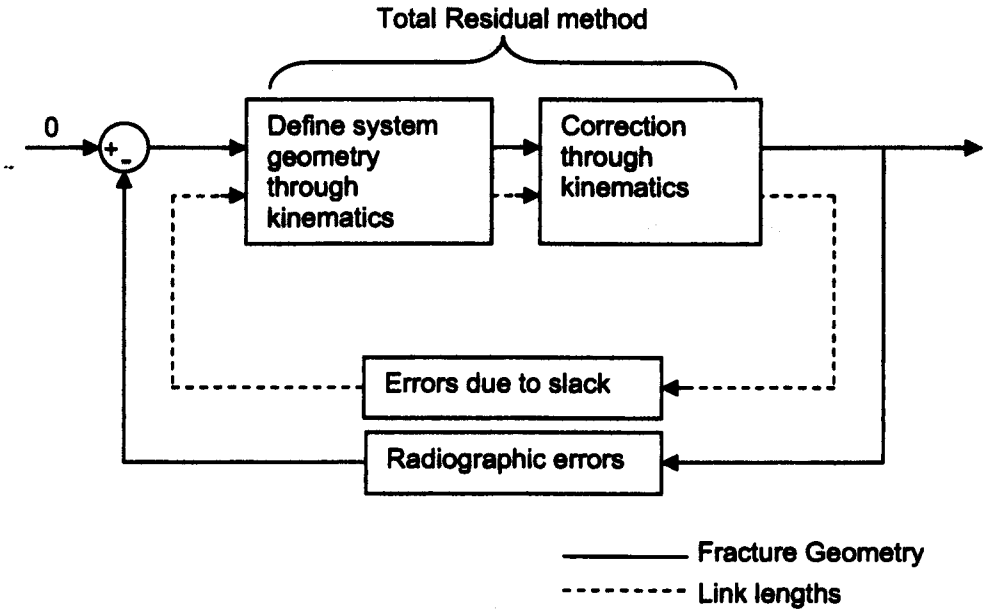


**Figure 60. Closed loop of the iterative Total Residual fracture and deformity reduction method.**

The treatment process is a closed loop system where the feedback is provided through the lengths of the TSF struts and the radiographic assessment of the fracture. The loop is repeated until both the satisfactory mechanical bone axis restoration and the fracture reduction are achieved. Two sources of errors are present in the system. The first one is the quality of the radiographs and the accuracy of their assessment. The second is the errors in the geometrical definition of the system: broken bone segment relative locations and orientations with respect to the frame. The second source of the error is directly related to the slack in the TSF strut, since the Total Residual application method is using forward kinematics to relate the position of the fractured bone segments to the frame. The Total Residual correction method requires choosing the reference segment and defining the relative position of the other segment. The user is then asked to define the position of the reference ring relative to the reference segment of the bone. Six strut lengths are then used to define the position of the other ring relative to the non-reference bone segment via forward kinematics solution. If the link lengths are not accurate, the relative position and orientation of the whole system are affected and the deformity correction and fracture reduction are not fully achieved. Since the process is a closed loop system,

eventually a satisfactory result can be attained. However additional iterations raise cost and affect the time and success of healing. Furthermore, high amounts of radiation can cause severe damage to the exposed patient's anatomy and therefore are not desirable.

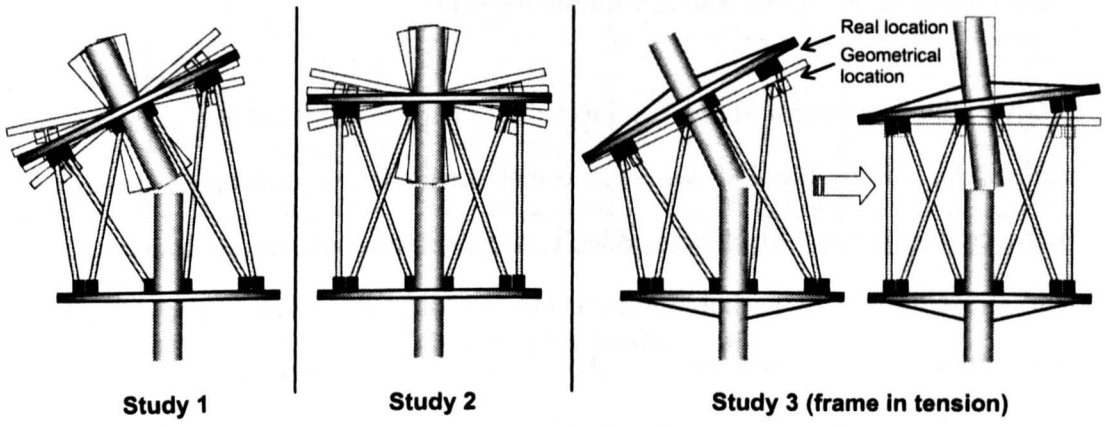


**Figure 61. Slack assessment studies**

## 7.5 Assessing the TSF Slack

Three types of slack assessment were performed by using the kinematics algorithm developed by the author and described in Chapter 3:

Study 1: the assessment of the overall positional and orientational accuracies of the TSF rings and the midshaft fracture. The usable TSF workspace was covered with uniformly distributed frame configurations and the effect of slack was added to the TSF strut lengths, Figure 61. The resulting change of the position and orientation of both the rings and the midshaft fracture were measured. The gathered results are applicable to the TSF geometrical accuracy in the operational workspace.

Study 2: the assessment of the positional and orientational accuracies of the TSF rings and the midshaft fracture in the neutral TSF configurations. The TSF rings were set parallel and aligned with each other, forming a perfect cylinder (neutral configuration). Slack was added to the TSF strut lengths and the resulting

positional and orientational changes were recorded, Figure 61. The assessment was an increased density subset of the Study 1. The results of Study 2 are especially applicable to the limb shortening/lengthening cases and other general cases when the TSF is straightened during the fracture reduction or deformity correction (Chapter 3, Section 2, Chronic method).

Study 3: the assessment of the Total Residual method positional and orientational accuracies. The usable TSF workspace was covered with uniformly distributed frame configurations. Slack was added to the TSF strut lengths, according to two load states of the frame: compression and tension. Both fracture and deformity were then reduced according to the Total Residual correction method, by straightening the bent frame, Figure 61. The Total Residual method took into account neither slack nor TSF load state, and therefore geometrical inaccuracies were induced. The resulting positional and orientational errors at the midshaft fracture were recorded. The results of this study directly relate to the accuracy of the Total Residual correction method for the pre-stressed frames, which remain in tension or compression throughout the treatment.

The algorithms used for each study are presented in Figure 62. For all three studies, three slack ranges of the TSF strut were modelled: ±0.25 mm, ±0.50 mm and ±0.75 mm, whereas ±0.75 mm represents the currently observed slack range in the medium struts. The same slack range is used for extra short, short and long struts as the same mechanisms are used in all of them. Four types of standard struts (extra short, short, medium and long) and eight types of rings (105, 130, 155, 180, 205, 230, 255 & 300 mm) were used to construct the TSF models. All models were constrained to having all six struts of the same type and rings of the same diameter. Table 7 summarises the configurations used. The crossed combinations were excluded due to low frame stability.

| Type / Type | Angles between struts for frames in the neutral configuration, deg | | | | | | | | | | | |
|---|---|---|---|---|---|---|---|---|---|---|---|---|
| | Extra Short Strut | | | Short Strut | | | Medium Strut | | | Long Strut | | |
| | MIN | NTRL | MAX | MIN | NTRL | MAX | MIN | NTRL | MAX | MIN | NTRL | MAX |
| **Ring** | | | | | | | | | | | | |
| 105 | 53 | 61 | 70 | 40 | 49 | 57 | 28 | 35 | 44 | 18 | 22 | 30 |
| 130 | 68 | 78 | 92 | 51 | 62 | 73 | 35 | 44 | 55 | 22 | 28 | 37 |
| 155 | 84 | 98 | 118 | 62 | 76 | 91 | 42 | 53 | 67 | 26 | 33 | 45 |
| 180 | ~~103~~ | ~~124~~ | ~~175~~ | 74 | 91 | 113 | 50 | 62 | 80 | 31 | 39 | 53 |
| 205 | ~~126~~ | | | ~~86~~ | ~~109~~ | ~~144~~ | 57 | 72 | 95 | 35 | 45 | 61 |
| 230 | ~~174~~ | | | ~~100~~ | ~~132~~ | | 65 | 83 | 111 | 40 | 50 | 69 |
| 255 | | | | ~~117~~ | | | ~~74~~ | ~~95~~ | ~~133~~ | 44 | 57 | 78 |
| 300 | | | | | | | ~~92~~ | ~~123~~ | | 54 | 69 | 98 |

**Table 7. Angles between struts for the neutral frame configurations. The crossed combinations were excluded from studies 1 & 3.**

For studies 1 & 3, two thousand uniformly distributed strut length sets were generated for each ring-strut combination, in order to cover the usable TSF geometrical range. The maximum rotation was restricted to angles of ±25° in coronal, ±60° in sagittal and ±25° in axial planes. The translational ring offsets were restricted to the maximum motion of ±25 mm coronally, ±20 mm sagittally and ±30 mm of shortening/lengthening. The range was chosen to represent the usable range of frame configurations based on [52].

For study 2, the frames were modelled based on the neutral height of the TSF. Neutral height is the distance between ring centres of the neutral TSF. For each ring set, the minimum and maximum neutral heights were computed based on the shortest and the longest standard strut values available from the manufacturer. The frame configurations were then constructed in the neutral frame height range in 1 mm increments. This was performed for all eight types of rings.

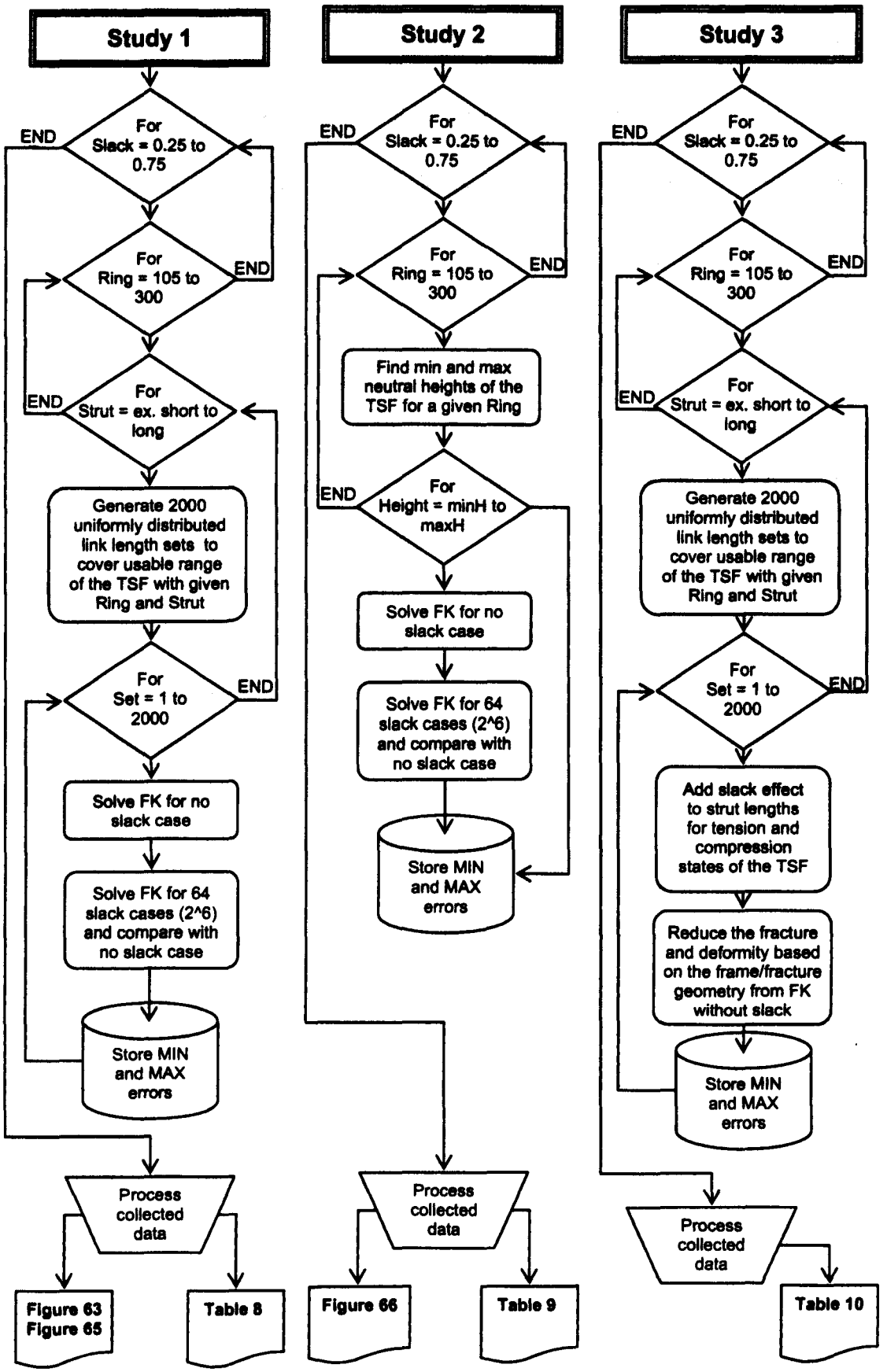


**Figure 62. Flowcharts of the three algorithms used to assess the strut slack influence on the TSF geometrical accuracy.**

For the first two studies, for each strut length set, the original position and orientation (no slack) of the frame was computed and compared against the 64 cases ($2^6$) of the maximum/minimum original strut length variations due to slack. For the third study, for each link set only tension and compression cases were analysed, whereas either all six struts are longer or shorter by the amount of the slack throughout the treatment period. It was decided to decouple the general slack of the frame, covered in Studies 1 & 2, from Study 3. The currently employed Total Residual method was used to calculate the transformations required to reduce the fracture and the deformity. The frame position and orientation relative to the bone were then recomputed to include the slack effects in both tension and compression states, and the correction was applied using the previously determined (no slack) set of transformations. The errors were calculated by comparing the results of the slack cases to the ideal (no slack) geometrical case.

The maximum errors in position/orientation and the resulting micromotion (the length of the displacement vector between fracture surfaces) of the ring and the midshaft fracture were recorded for all three studies. The ring micromotion was computed based on the positional errors of the ring. The midshaft micromotion was computed based on the change of the proximal bone end position due to change of the ring position and orientation caused by slack in the TSF strut. In all cases, the lengths of the proximal and distal bone segments were set to the half of the original (no slack) axial distance between the rings, in order to represent realistic scenarios. The modelled bones were fixed perpendicular to ring planes at the centres of the rings. The master tab of the fixator was always aligned with the major foot axis and the reference was set to the distal ring/segment.

## 7.6 Slack Influence on TSF Accuracy

### 7.6.1 Slack in the Unloaded TSF, Study 1

In total 126,000 frame configurations (21 ring/strut configurations x 2000 strut length sets x 3 slack ranges) were tested and results were recorded for study 1, Table 8. The TSF angular orientation uncertainty ranged from 0.7° – 7.7° for ±0.75 mm of slack in the struts. The relative ring positional uncertainty has ranged from 1.5 – 11.8 mm. The resulting unconstrained interfragmentary motion (UIFM) at the midshaft fracture has ranged from 2.6 – 16.5 mm. Such high levels of unconstrained micro-motion would cause severe strains on the newly-laid bone tissue at the fracture site, and thus result in high levels of pain. The freshly-laid granulated tissue can tolerate up to 100 % of strain [19]. This suggests that the fracture gap should be in the range of 1.3 – 8.3 mm in order for the UIFM not to impinge on the early stage of healing. As the healing progresses and the granulated tissue is converted to cartilage, the tolerable strain level decreases down to 10 %. The high levels of the UIFM can now cause severe damage to the cartilage and hence precautions are recommended to counteract the slackness of the struts in the unloaded frames.

Figure 63, shows mean values of the UIFM for combinations of ring diameters and strut types. The amount of the UIFM due to the slack is influenced by three factors: the amount of slack in the strut, the ring diameter and the ring separation. Ring separation is controlled by the lengths of the struts. Generally, decreasing the distance (strut lengths) between the rings, decreases the amount of the UIFM. Decreasing ring diameter increases the amount of the UIFM. Therefore, the minimum UIFM can be achieved using larger diameter rings with a reasonably small distance between them. The least UIFM was observed for the 180mm rings interconnected with short struts.

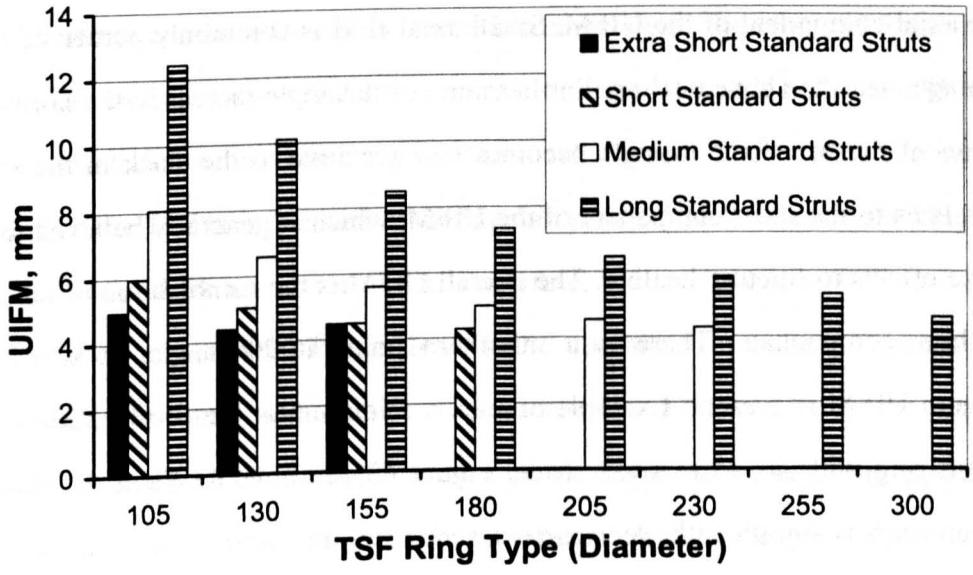


**Figure 63. Mean unconstrained interfragmentary motion (UIFM) at the midshaft fracture for ring-strut combinations with the ±0.75 mm strut slack, study 1.**

| Strut slack / TSF Slack | ±0.25 mm | | | | ±0.5 mm | | | | ±0.75 mm | | | |
|---|---|---|---|---|---|---|---|---|---|---|---|---|
| | MIN | MAX | MEAN | STD | MIN | MAX | MEAN | STD | MIN | MAX | MEAN | STD |
| ***Angular*** | | | | | | | | | | | | |
| AP Rot, deg | 0.3 | 2.0 | **0.6** | 0.2 | 0.6 | 3.8 | **1.1** | 0.3 | 0.8 | 6.5 | **1.7** | 0.5 |
| ML Rot, deg | 0.3 | 2.1 | **0.5** | 0.1 | 0.5 | 3.4 | **1.0** | 0.3 | 0.8 | 5.3 | **1.5** | 0.4 |
| AX Rot, deg | 0.2 | 2.6 | **0.7** | 0.6 | 0.5 | 5.2 | **1.4** | 1.2 | 0.7 | 7.7 | **2.1** | 1.8 |
| ***Ring*** | | | | | | | | | | | | |
| X Ring, mm | 0.8 | 3.9 | **1.8** | 0.7 | 1.6 | 7.9 | **3.6** | 1.4 | 2.4 | 11.8 | **5.4** | 2.1 |
| Y Ring, mm | 0.5 | 2.5 | **0.6** | 0.1 | 1.0 | 4.1 | **1.3** | 0.3 | 1.5 | 7.6 | **1.9** | 0.4 |
| Z Ring, mm | 0.7 | 3.7 | **1.6** | 0.7 | 1.5 | 7.4 | **3.2** | 1.4 | 2.2 | 11.0 | **4.8** | 2.1 |
| UIFM Ring, mm | 0.9 | 3.9 | **1.8** | 0.7 | 1.9 | 7.9 | **3.6** | 1.4 | 2.8 | 11.9 | **5.4** | 2.2 |
| ***Midshaft fracture*** | | | | | | | | | | | | |
| X Bone, mm | 0.6 | 5.0 | **1.9** | 0.7 | 1.2 | 10.1 | **3.8** | 1.3 | 1.8 | 15.2 | **5.7** | 2.0 |
| Y Bone, mm | 0.5 | 2.7 | **0.7** | 0.2 | 1.0 | 4.4 | **1.3** | 0.3 | 1.5 | 8.1 | **2.0** | 0.4 |
| Z Bone, mm | 0.7 | 4.9 | **1.9** | 0.7 | 1.4 | 9.7 | **3.8** | 1.5 | 2.1 | 15.0 | **5.7** | 2.2 |
| UIFM Bone, mm | 0.9 | 5.4 | **2.0** | 0.7 | 1.7 | 10.7 | **4.1** | 1.4 | 2.6 | 16.5 | **6.1** | 2.1 |

**Table 8. The strut slack influence to the TSF geometrical accuracy in the operating envelope using four standard types of struts and 105 – 300 TSF rings. The values represent total movement, *i.e.* value of 0.2 is equivalent to ±0.1.**

The results can be explained by the analysis of the triangles formed from two struts and a rig segment in between them, Figure 64. As the angle between the struts increases, the rate of change of the height of the triangle increases, too. This relates

to the axial component of the UIFM. Small axial IFM is commonly perceived to be advantageous to the bone healing. Furthermore, as the angle increases, the horizontal position of the tip of the triangle becomes less sensitive to the slack in the struts. This relates to the shear component of the UIFM, which is generally believed to add adverse effects to fracture healing. The overall UIFM is the combination of the axial and shear components. There is a minimum point at 90° angle, at which the minimum UIFM is present. Example of such a minimum is the combination of the 130 mm ring with six extra short struts, Figure 63 & Table 7. When the distance between rings is significantly decreased and the resulting angle between the struts is far beyond 90° the UIFM can reach intolerable magnitude.

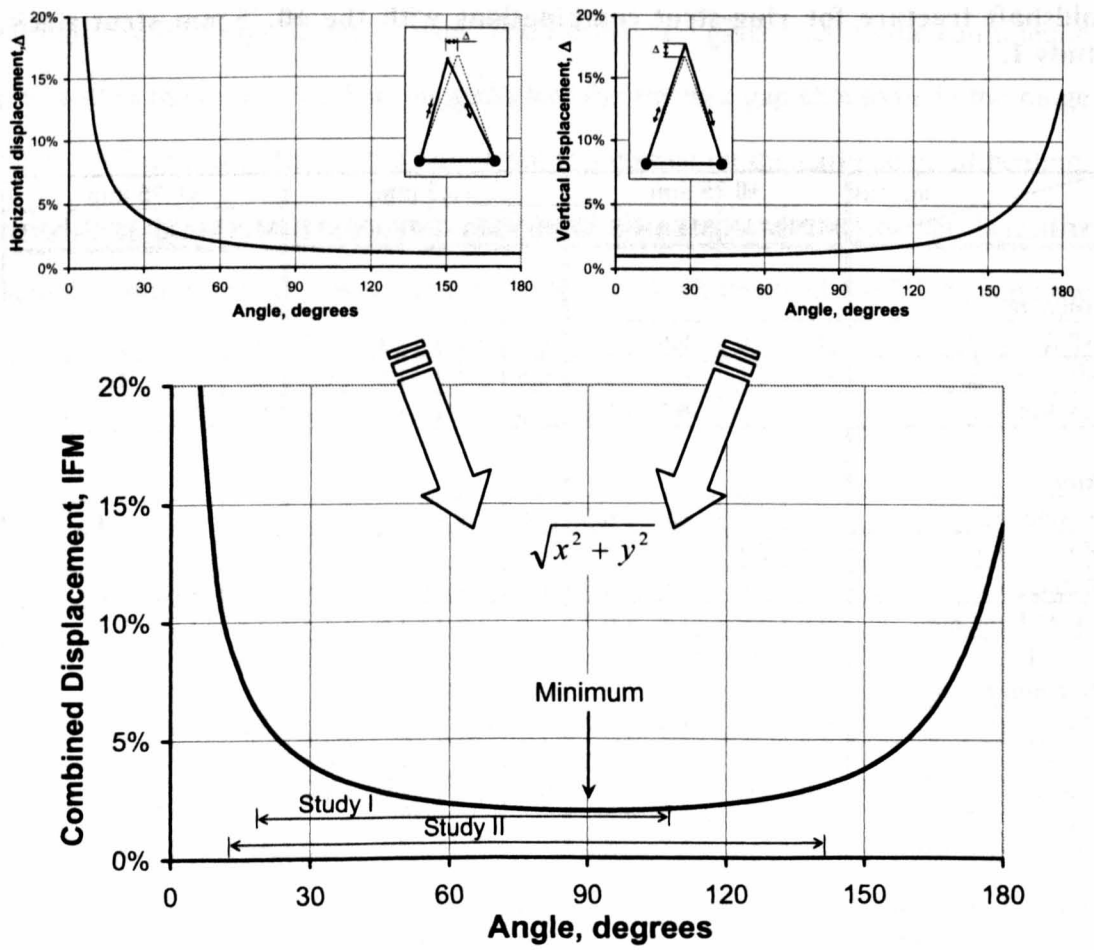


**Figure 64. Analysis of the strut slack effect on the TSF geometrical accuracy based on the triangles analogy. The slack modelled is 1 % of the link length. The IFM is expressed as a percentage of the original link length.**

The TSF struts can be adjusted in 1 mm increments and therefore ±0.5 mm slack range of the study 1 indicates the theoretical accuracy to which both the TSF rings and the midshaft fracture can be positioned and aligned. The overall geometrical accuracy of the TSF is influenced by both parameters of the TSF strut: the length of the increment and the amount of slack. Therefore, the results of the TSF strut slack ranges of ±0.5 mm and ±0.75 mm have to be combined in order to quantify the overall TSF positional and orientational accuracies. This results in the angular accuracy range of ±0.6° – ±6.45° with a mean value of ±1.47°, ring positional accuracy range of ±1.25 mm – ±9.85 mm with a mean value of ±3.36 mm, and positional accuracy of the midshaft fracture of ±1.25 mm – ±12.65 mm with a mean value of ±3.71 mm. Reducing the amount of slack in the frame can significantly improve TSF's positional and orientational accuracies.

It is a common practice to place the rings at least 30 mm away from either side of the fracture. This is done to minimise a risk of further fracture splitting and loss of the fixation stability. The holes are drilled in the injured bone, and pins and/or wires are placed to establish bone-ring connection. The pins and wires transmit the load from the bone to the ring and vice versa. If insufficient bone tissue separates the pin/wire from the fracture, there is a likelihood of a further fracture cracking. In addition, locating the rings and therefore wires and pins away from the fracture can potentially assist healing, by minimising further damage to the already damaged fracture anatomy. Therefore, there is a limit to a minimum ring separation. The other restriction is on the maximum ring diameter that can be used. Although the use of larger ring diameters tends to reduce the amount of the UIFM in the TSF, the frame stiffness is also reduced. As the ring diameter increases, the wire span increases too, resulting in a decrease of wire axial stiffness (in the direction of the load applied to the wire). Furthermore, the large diameter rings imply inconvenience to patients as it becomes hard to move with such frames. It is therefore important to take into consideration a number of factors when planning the TSF configuration.

Finally, the amount of slack in the struts and the UIFM were reasonably linearly related, Figure 65.

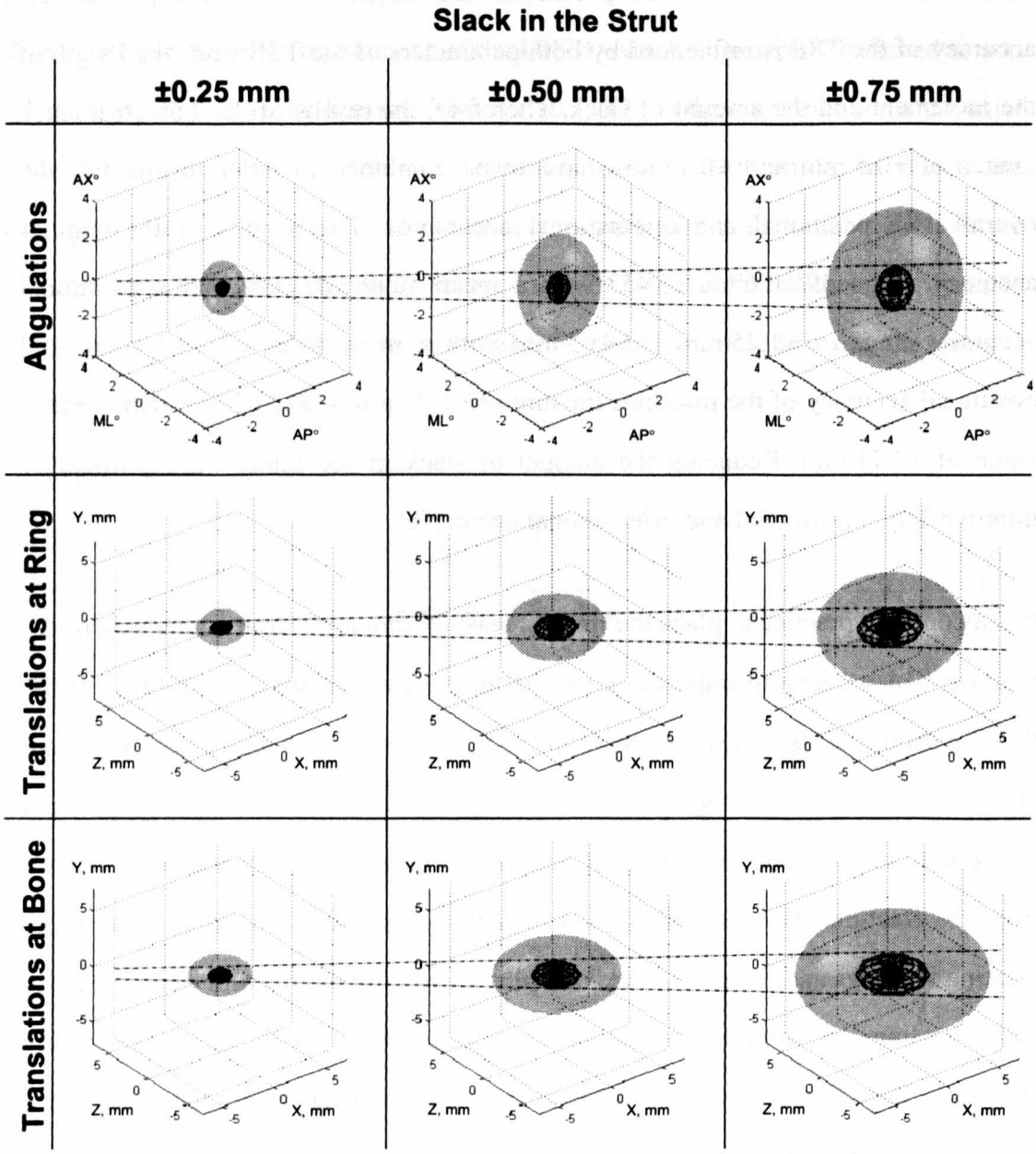


**Figure 65, Graphical representation of the TSF positional and orientational uncertainties for three TSF strut slack ranges, study 1. The inner ellipsoidal represents the minimum slack range, the middle ellipsoid – the mean range and the outer ellipsoid – the maximum range.**

### 7.6.2 Unconstrained IFM in Neutral Frames, Study 2

The second study of the influence of slack on the frame and fracture positional and orientational accuracies has concentrated on the frame configurations that are most commonly used. It is common to apply TSF rings to the deformed fracture and then to straighten the frame, thus reducing both the fracture and the deformity. In trauma cases, it is common to reduce the fracture during surgery.

In total, some 6000 frame configurations were tested. The complete set of results is presented in Table 9. The angular uncertainty range due to slack of ±0.75 mm was recorded as 0.7° – 6.9° and the ring positional uncertainty range as 1.5 – 11.7 mm. As expected, the uncertainty range was slightly narrower compared to that measured in the first study (Section 7.6.1), since the second study was the subset of the first one.

| Strut slack / TSF Slack | ±0.25 mm | | | | ±0.5 mm | | | | ±0.75 mm | | | |
|---|---|---|---|---|---|---|---|---|---|---|---|---|
| | MIN | MAX | **MEAN** | STD | MIN | MAX | **MEAN** | STD | MIN | MAX | **MEAN** | STD |
| ***Angular*** | | | | | | | | | | | | |
| AP Rot, deg | 0.3 | 1.4 | **0.5** | 0.1 | 0.6 | 2.7 | **1.0** | 0.3 | 0.9 | 4.1 | **1.5** | 0.4 |
| ML Rot, deg | 0.3 | 1.2 | **0.4** | 0.1 | 0.5 | 2.4 | **0.9** | 0.2 | 0.8 | 3.7 | **1.3** | 0.3 |
| AX Rot, deg | 0.2 | 2.3 | **0.7** | 0.5 | 0.5 | 4.6 | **1.4** | 0.9 | 0.7 | 6.9 | **2.1** | 1.4 |
| ***Ring*** | | | | | | | | | | | | |
| X Ring, mm | 0.9 | 3.9 | **1.7** | 0.6 | 1.8 | 7.8 | **3.3** | 1.3 | 2.7 | 11.7 | **5.0** | 1.9 |
| Y Ring, mm | 0.5 | 1.6 | **0.6** | 0.1 | 1.0 | 3.2 | **1.2** | 0.3 | 1.5 | 4.8 | **1.9** | 0.4 |
| Z Ring, mm | 0.8 | 3.7 | **1.5** | 0.6 | 1.7 | 7.3 | **3.0** | 1.2 | 2.5 | 11.0 | **4.5** | 1.8 |
| UIFM Ring, mm | 0.9 | 3.9 | **1.7** | 0.6 | 1.9 | 7.8 | **3.3** | 1.3 | 2.8 | 11.7 | **5.0** | 1.9 |
| ***Midshaft fracture*** | | | | | | | | | | | | |
| X Bone, mm | 0.6 | 3.2 | **1.3** | 0.5 | 1.2 | 6.3 | **2.6** | 1.1 | 1.8 | 9.5 | **3.9** | 1.6 |
| Y Bone, mm | 0.5 | 1.6 | **0.6** | 0.1 | 1.0 | 3.2 | **1.2** | 0.3 | 1.5 | 4.8 | **1.9** | 0.4 |
| Z Bone, mm | 0.7 | 3.7 | **1.5** | 0.6 | 1.4 | 7.3 | **3.0** | 1.2 | 2.1 | 11.0 | **4.5** | 1.9 |
| UIFM Bone, mm | 0.9 | 3.7 | **1.5** | 0.6 | 1.7 | 7.3 | **3.0** | 1.2 | 2.6 | 11.0 | **4.6** | 1.8 |

**Table 9. The strut slack influence to the TSF geometrical accuracy in the operating envelope of neutral frame using four standard types of struts and 105 – 300 TSF rings. The values represent total movement, *i.e.* value of 0.2 is equivalent to ±0.1.**

Similarly to study 1, it was observed that generally a decrease in the ring axial separation and an increase in the ring diameter resulted in the reduction of the UIFM,

Figure 66. However, there was a point at which the trend was sharply reversed. This can be explained by looking at the triangles analysis, described in Section 7.6.1. There is a point at which the UIFM is at its minimum. The angles between the struts at those points were measured and all of them equated to 90°. As the angles became more obtuse, the overall slack started to increase dramatically. The maximum slack for such cases was in the direction of the central frame axis. This could also affect the TSF axial stiffness. As the angle between struts becomes highly obtuse, the TSF axial stiffness decreases dramatically, because small strains in struts can cause large axial displacements between the rings.

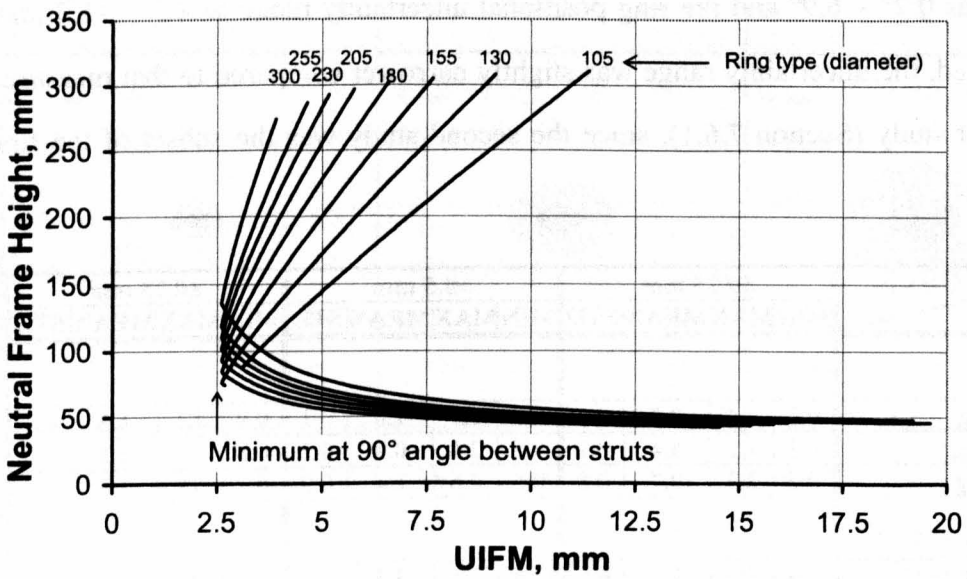


**Figure 66. Maximum unconstrained interfragmentary motion (UIFM) at the midshaft fracture caused by the ±0.75 mm strut slack in the neutral TSF, study 2.**

The summary of the ring-strut combinations and the resulting angle range between the struts for neutral frames is provided in Table 7. As can be seen, most possible frame configurations have acute angles between the struts, and only few will pass the 90° angle threshold.

Finally, the UIFM at the ring (applicable to peri-articular fractures) was greater than that at the midshaft fracture, Table 9. The off-centre displacement resulted in the

rotation of the ring towards the centre of the other ring, and thus reduction of the displacement at the fracture site. The change in the axial separation between bone segments was minimal due to the small angle of rotation and vertical bone orientation. However, this was not the case for the 'bent' frames (Study 1), where the axial displacement component was significant. The relatively higher UIFM was observed at midshaft fractures in study 1.

### 7.6.3 Slack and Total Residual Correction Method, Study 3

The third study was principally different to the first two. It examined the influence of the uncertainty introduced by the slack to the accuracy of the Total Residual correction method. Table 10 presents the results. The total error range was recorded as 0.4° – 0.8° rotationally and 0.8 –1.4 mm positionally for the slack of ±0.75 mm. The trends are similar to ones in Sections 7.6.1 and 7.6.2. In most cases, the best results were achieved using large rings with small separations between them.

| Slack in strut | ±0.25 mm | ±0.5 mm | ±0.75 mm |
|---|---|---|---|
| ***Rotations*** | | | |
| AP rotation, deg | 0.4 | 0.5 | 0.7 |
| ML rotation, deg | 0.5 | 0.6 | 0.8 |
| AX rotation, deg | 0.3 | 0.3 | 0.4 |
| ***Transitions at bone*** | | | |
| AP (X), mm | 0.6 | 0.9 | 1.1 |
| AX (Y), mm | 1.1 | 0.9 | 0.8 |
| ML (Z), mm | 0.7 | 1.2 | 1.4 |

**Table 10. Maximum effects (95 % range) of slack in the struts to the accuracy of currently employed Total Residual correction method. Frames were assumed to remain in tension or compression throughout the treatment period. The values represent total movement, *i.e.* value of 0.2 is equivalent to ±0.1.**

The error ranges were small when compared to the errors obtained during analogue measurements of the radiograms. However, as the X-Ray technology becomes digitised, the radiological errors are likely to reduce sharply, making errors caused by slack important.

### 7.6.4 Improving TSF Accuracy

There are a number of ways to reduce the slack in the TSF. One way is to minimise the clearance between the components in order to reduce the backlash. The choice depends on the manufacturer and can be an expensive option.

The other way is to over-constrain the system by an introduction of the seventh strut. This can eliminate the UIFM; however, this method does not eliminate the uncertainty in the true strut length.

The third way is to use a washer at one end of the strut, Figure 67b. The Stewart-Gough Platform (hexapod) links are connected via one joint with three axes of rotation and one joint with two axes of rotation. The TSF strut has two joints that both have three rotational axes. Two axes are provided by the universal joint and the third one is provided by a clearance between the shoulder bolt and the ring, Figure 67a. The washer can be placed between the shoulder bolt and the ring at one end of the strut. This converts the three axes joint to a two axes joint and eliminates ±0.2 mm of slack. Such an arrangement results in more than 30 % reduction of the UIFM, Table 8. On the downside, the ability of the strut to rotate about its major axis will be impinged, and hence the strut axial orientation will have to be carefully planned during the TSF application time. It is important to enable both the patient and the surgeon to read the feedback information of the strut about its length.

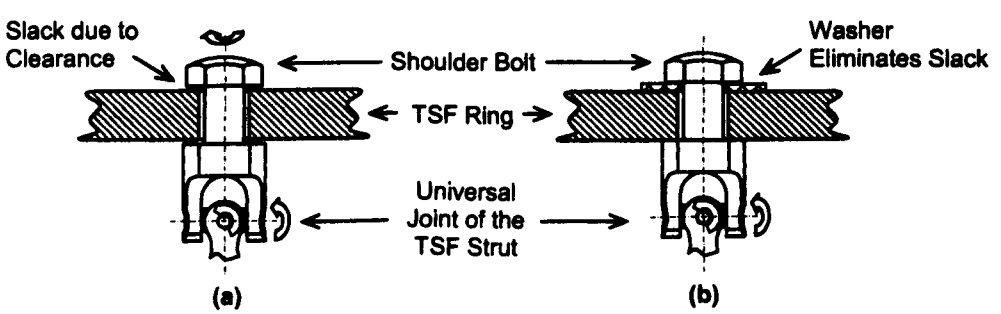


**Figure 67. Reducing slack by addition of a washer.**

As far as the Total Residual correction method is concerned, errors there can be eliminated mathematically. The slack could be incorporated by taking into account the TSF load state and refining the lengths of the struts accordingly. This way the accurate bone-frame geometrical model could be constructed, thus eliminating the currently possible source of errors. This implies modifications to the Total Residual algorithm used on the TSF website.

## 7.7 Conclusions

Understanding of the effects of slack in struts is important for frames that are unloaded or transit from loaded to unloaded states during healing. It has been shown that slack can cause critical strains on the newly-laid bone tissue. The least amount of unconstrained interfragmentary motion due to slack was observed in frames with struts at 90° angle to each other. This implies small ring separation and large ring diameters. Slack can be minimised by reducing tolerances between moving components, over-constraining the TSF, and introduction of a washer between the strut and the ring. Finally, the uncertainty in strut lengths due to slack affects the accuracy of the currently employed Total Residual correction-planning algorithm. This can be resolved mathematically by taking into account the frame load state and the amount of slack in the strut.

# CHAPTER 8 : TSF AUTOMATION

Mechanical fracture stimulation has shown evidence of promoting callus formation and hence bone fracture healing [8-18]. Current methods involve generation of mechanical stimulus by patient load bearing on the fractured limb during the treatment period. The weight of the patient causes deflections within the fixator that in turn cause an interfragmentary motion (IFM). Two types of IFM are normally distinguished: axial and shear. Small axial motion is associated with the positive effects on healing [9-14, 16-18, 28]. Shear motion is believed to cause adverse effects [10, 28-30], although a recent study [82] has suggested that shear motion applied to oblique factures can also enhance callus formation. During the treatment period, control of the IFM relies on the fixator's mechanical properties and the load direction applied by the patient. It is therefore difficult to plan and execute the exact prescribed motion at the fracture site. An attractive alternative is to stimulate the motion via the fixator, by introducing active components to the Taylor Spatial Frame (TSF). In such a way, a more controllable stimulus could be applied.

This chapter looks at the feasibility of an active TSF, as well as at some practical considerations of implementing it. Furthermore, a prototype has been developed, built and tested by the author.

## 8.1 Benefits of Automated Fixator

Current external orthopaedics fixators are passive devices whose configuration and hence stiffness are determined by the surgeon. The loads applied by a patient are not constant, having varying directions and magnitudes. During the treatment period, the patient's broken bone / frame system is often subjected to undesirable impacts, due to the patient's limited control of the injured limb. The TSF's variable length strut can be adjusted in one millimetre increments implying mean angular and positional accuracy of the TSF $\pm 0.39°$ and $\pm 1.35$ mm respectively, (Chapter 7). During deformity correction, the patient changes strut lengths once a day in 1 mm or greater

increments. If instead more gradual adjustments were used, the patient would have less pain and bone formation would be more reliable [83-89]. Ilizarov [28] has shown that continuous bone distraction causes bone formation that resembles the true tissue regeneration.

An active fixator could potentially improve patient's comfort and quality of fracture healing in the following ways:

a. Accurately reduce fractures and align broken bone segments.

b. Perform the deformity correction and fracture reduction in a controlled smooth motion as opposed to daily incremental one (once a day, minimum step 1 mm).

c. Generate controlled mechanical stimulus at the fracture site while the patient is at rest.

d. Be used for surgeon training, demonstration, and patient education purposes in clinics and surgeon workshops.

e. Prevent injuries from unforeseen impacts, by adjusting frame geometry (real-time) in order to reduce strains at the fracture site.

The TSF is based on a Stewart-Gough platform [39, 40] and therefore is a suitable subject for such automation. Its unique properties of six degrees of freedom and high stiffness to mass ratio provide the crucial criteria required for the active external fixator. Six variable struts could be replaced with mechanically driven ones, which in turn connected to the control system would create an active TSF.

## 8.2 Design Specifications

It was decided to design the demonstrator of the active TSF that would be able to display the mechanical stimulus applied to the fracture as well as be an aid to the

surgeon's training. For this purpose, the following design criteria have been considered:

1. The system should be light and mobile, so that it can be transported easily.

2. The system should resemble the standard TSF. The key principles of the TSF should be maintained.

3. If the system is interfaced to a personal computer (PC), the overhead to the PC should be minimal, so that laptops have sufficient processing power.

4. The demonstrator of the active TSF should be able to provide 50 N of axial thrust. 50 N should provide sufficient thrust for conceptual demonstration, but not the real, *in vivo*, use. Considerations for the *in vivo* application are provided in Section 8.4 of this chapter.

5. The demonstrator of the active TSF should be able to respond quickly to a change of geometry. The maximum axial speed of the actuator of 5 mm/s should therefore be adequate. This should provide suitable transformation times for demonstrations.

6. The active TSF should be able to align and position broken bone segments gradually and accurately. It has been shown in Chapter 7 that accuracy of the TSF varies reasonably linearly with the amount of length uncertainty in the strut. Therefore, given the present accuracy of the 1 mm of the TSF strut, the author felt that 0.1 mm should be sufficient to provide clinically adequate fixator positional and angular accuracies of less than 1 mm and 1°.

## 8.3 System Design

Three key components of the active TSF system have been identified: a personal computer (PC), a control/electronics box (EBox) and an active frame (TSF rings interconnected with six active struts), Figure 68. It was decided to use electro-drive system for the active struts, due to size and load constraints. The purpose of the

EBox was discrete low-level control of active struts, hence removing a processing overhead from the PC. The PC function was input/output interface for the user and forward/inverse kinematics solver.

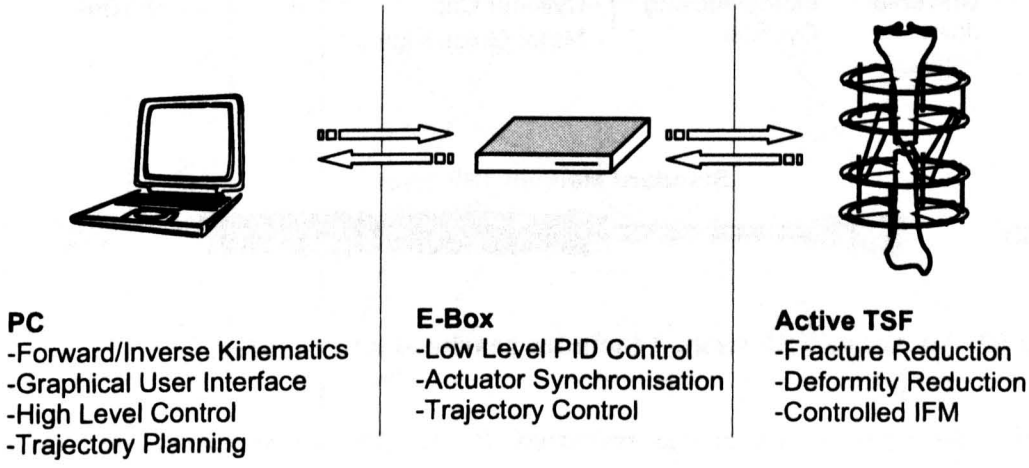


**Figure 68. System arrangement of the active TSF.**

### 8.3.1 An Active TSF Strut

The key design requirements for the active strut were small volume, light weight, resemblance to the existing TSF strut and low driving voltage/current (< 24 V, < 2 A, safety for the patient). Furthermore, the actuator had to produce 10 N thrust at 5 mm/s speed. The market was searched for a readily available actuator that met the design criteria but none was found. It was therefore decided to design and build the actuator 'in house'. The details of the actuator design process, component selection and final product are presented in Appendix C. The final actuator design consisted of a D. C. motor connected to a gearhead and incremental encoder. It was housed in a specially designed cylinder that has removed axial and radial loads from the gearhead and hence the motor shaft, Figure 69. The overall theoretical actuator performance characteristics are presented in Figure 70. Four main parameters (speed, current, output power and efficiency) have been derived against the output thrust. The positional resolution of the encoder was 0.0014 mm, which exceeded the design specification.

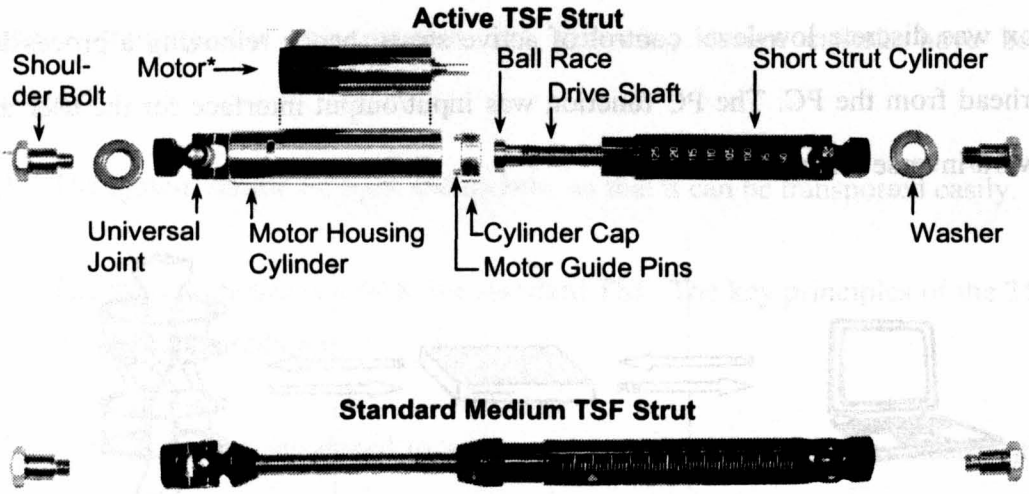


**Figure 69. An Active TSF strut. * includes gearhead and encoder.**

A minimalist actuator design was proposed. It was decided to use existing strut components to minimise both the design and manufacture lead time, and cost. The drive shaft was mated with the cylinder of the short strut, via a custom-fitted brass insert with an internal M6 thread. The universal joints from the standard TSF strut were reused at the ends of the actuator. However, in contrast to the standard TSF arrangement, the washers were sandwiched between shoulder bolts and universal joints. This removed the degree of freedom of the actuator to rotate axially in order to create the boundary condition required for the actuator to function.

Finally, an oil-based lubricant was used between surfaces of the drive shaft and the cylinder of the short strut in order to minimise friction and sound pollution.

### 8.3.2 Electronics

The electronics box (EBox) specification requirements were: small/portable volume, powered from the mains electricity supply, interfaced with a PC, sufficient processing power to execute low level control within a 1 ms turn-around time, and sufficient power output to drive the active struts.

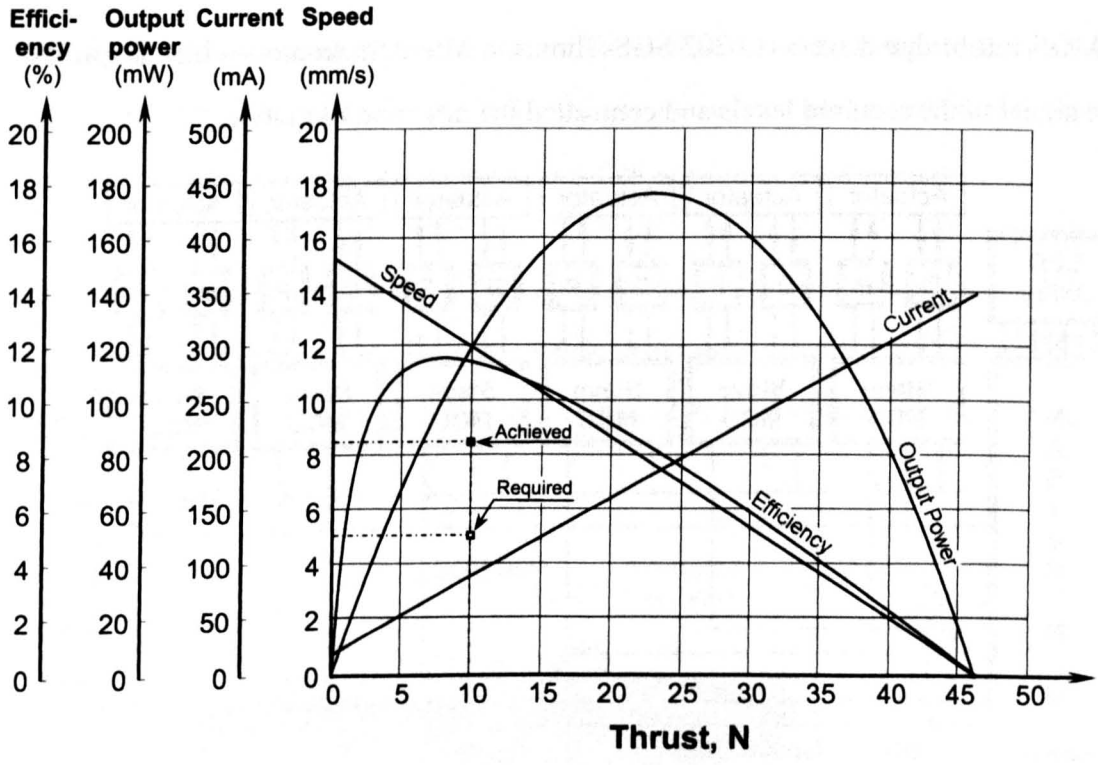


**Figure 70. Theoretical performance data of the TSF active strut.**

The organisation of the components of the EBox circuit is presented in Figure 71. It was decided to use six digital microcontroller units (MCU) as computational components for the low level control of actuators. All six MCUs were set as slave devices and were interfaced to the master MCU via the inter-integrated-circuit ($I^2C^{TM}$) communication bus, developed by Phillips Electronics [90]. Each of the slave MCUs had a dedicated status/debug line, a synchronisation (SYNC) line and a reset (RST) line. This enabled synchronisation, status reporting, debugging, resetting and power saving to be performed. The master MCU was connected to the personal computer (PC) via an RS232 interface. Its primary function was to bridge the PC and the slave MCUs, by translating serial communication to the $I^2C$ communication and vice versa. The secondary function was to display status of the electronics via an LED array. Further details of the circuits and the implementation are presented in Appendix C.

The active struts were driven by the power stage using pulse-width modulation signals (PWM). The PWM signals from the slave MCUs were passed to the six

DMOS full bridge drivers (L6202 SGS-Thomson Microelectronics) which amplified the signal to the required levels and controlled the direction of motion.

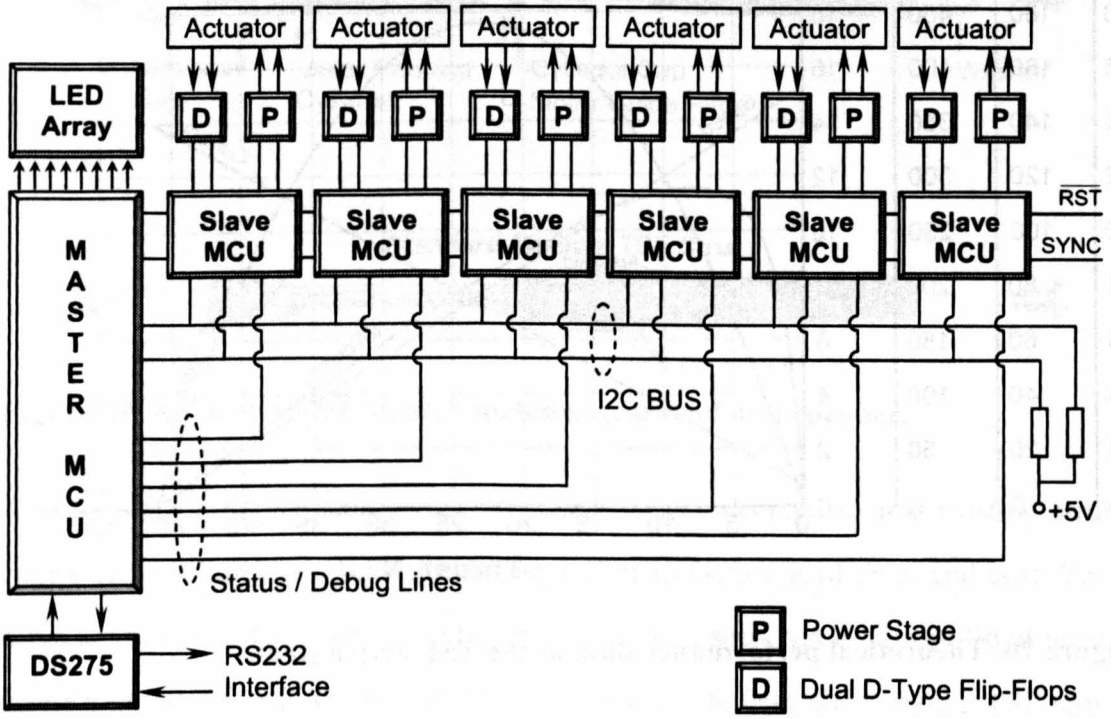


**Figure 71. Block diagram of the EBox.**

The feedback circuit was implemented using Dual D-Type flip-flops, which decoded the pulse trains coming from the motor encoder to two (up and down) streams of pulses. A comparison of the up and down pulses determined the actuator position.

The circuit was implemented on two circuit boards. It was decided to separate the logic components including the MCUs from the power electronics (DMOS-Bridges). The interface was established via two connection headers A & B, Figure 72. This has added the flexibility of modifying the power electronics without redesigning the control circuits.

The hardware limit switches were not implemented for the active TSF application, since software limit switching was sufficient. However, the design of the circuit caters for two dedicated hardware channels per actuator for this purpose.

Both logic and power electronics were powered from a single PSU, Traco Power TXL 100-0534T, Switzerland. The PSU was chosen so that all input voltages were supported round the world, should the active TSF need to be used abroad.

The interface between the circuit (EBox) and actuators was established via six RJ45 connections. A single 8 pin 'D' type female connector provided RS232 interface connection to the PC. The interface pin outs and further details on the PSU are provided in Appendix C.

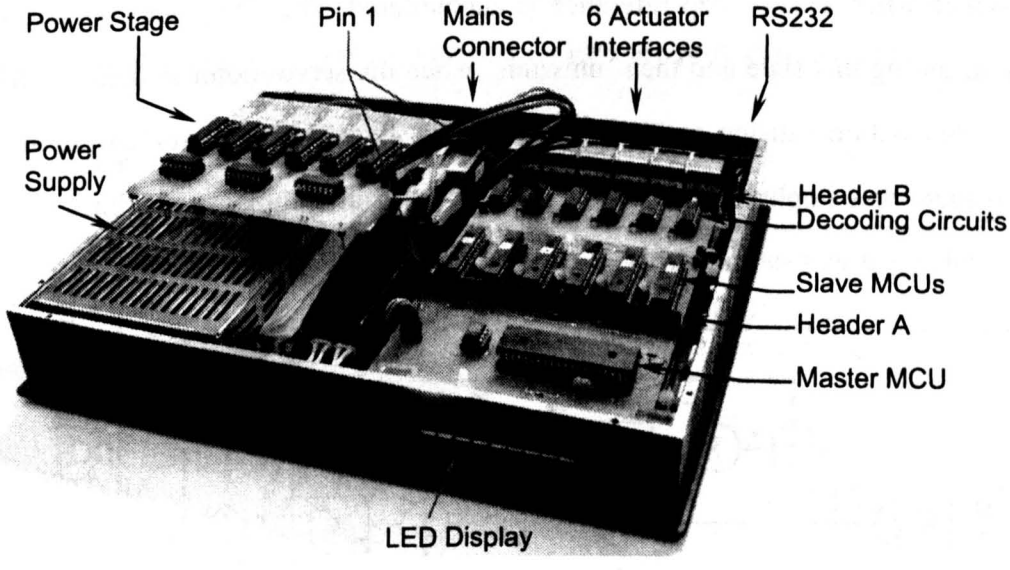


**Figure 72. The EBox. The power stage sits on the headers A and B, however it was moved on top of the power supply for clarity of this figure.**

### 8.3.3 Control

An internal (low level) actuator control diagram is presented in Figure 73. The core control of the actuator position was based on the Proportional plus Integral plus Derivative (PID) control algorithm that is well documented in [91, 92] and was implemented on the slave MCU level. The position reference signal *u(k)* and other control variables were sent from a PC via the RS232 interface to the master MCU, which in turn sent the reference value to the appropriate slave MCU. The positional feedback was received from the motor shaft encoder in the pulse train format, which

was decoded into up and down pulses using two dual D type flip-flops. The slave MCU then compared counts of up and down pulses at every control loop iteration and the actuator current position was adjusted accordingly. The error between current position and the reference signal was then calculated and was passed to the PID routine. The PID routine calculated the control signal, which resulted in the PWM value and motion direction. The core PID algorithm is known to suffer from an integrator wind-up phenomenon. The integrator wind-up is a condition that occurs when a large position error is present in the system that saturates the control signal, for instance when a large step reference is encountered. The integrator continually builds up during this state and then 'unwinds' when the servo-motor system reaches its final destination causing excessive oscillations. To tackle this problem an anti-windup logic was implemented, which disabled integral summation at times when the control signal was saturated.

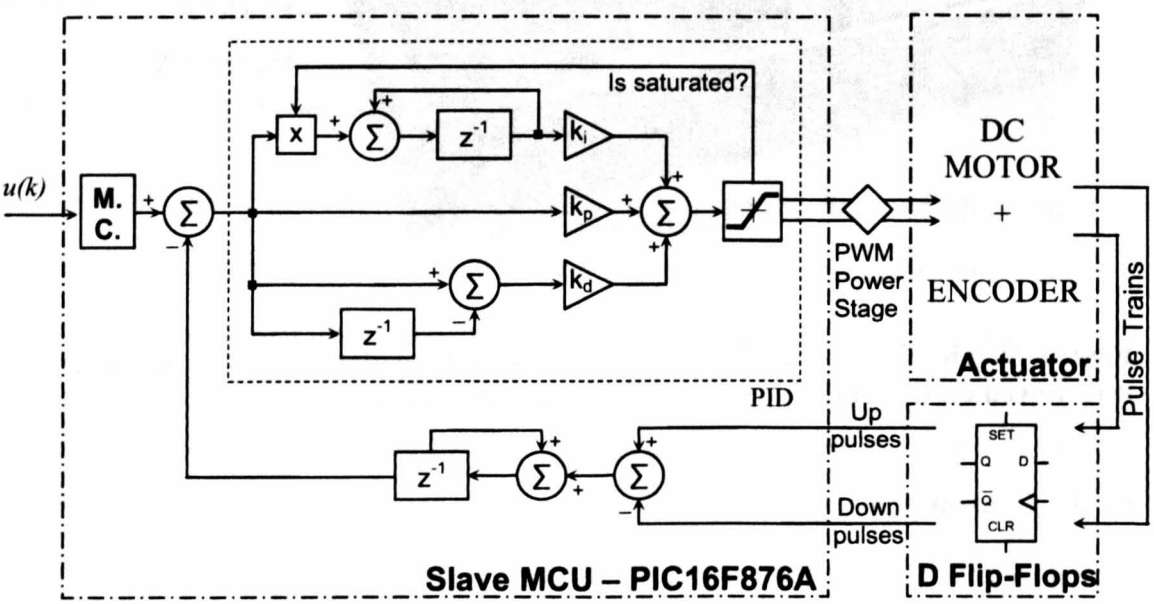


**Figure 73. Internal control loop diagram of a single actuator. M.C. block represents the motion control algorithm.**

The reference signal *u(k)* was passed through a motion control (M. C.) block, Figure 73, before entering the PID loop. Two types of motion control modes were implemented: pure PID and trajectory. In the pure PID mode, the incoming reference value was directly passed to the PID control loop. This produced the fastest response

of the active strut to the control input. The PID control gains were obtained using Ziegler-Nichols tuning method. An example response to a step input is presented in Figure 74.

In the trajectory control mode, the speed and acceleration of the actuator were controlled in addition to the position. This allowed smooth operation, reduced strain on the actuator and overall structure, and controlled movement time. A linear piecewise velocity trajectory was implemented for this purpose. System response to a step input with trajectory control enabled is presented in Figure 74. Further details on the PID and trajectory control implementations are provided in Appendix C.

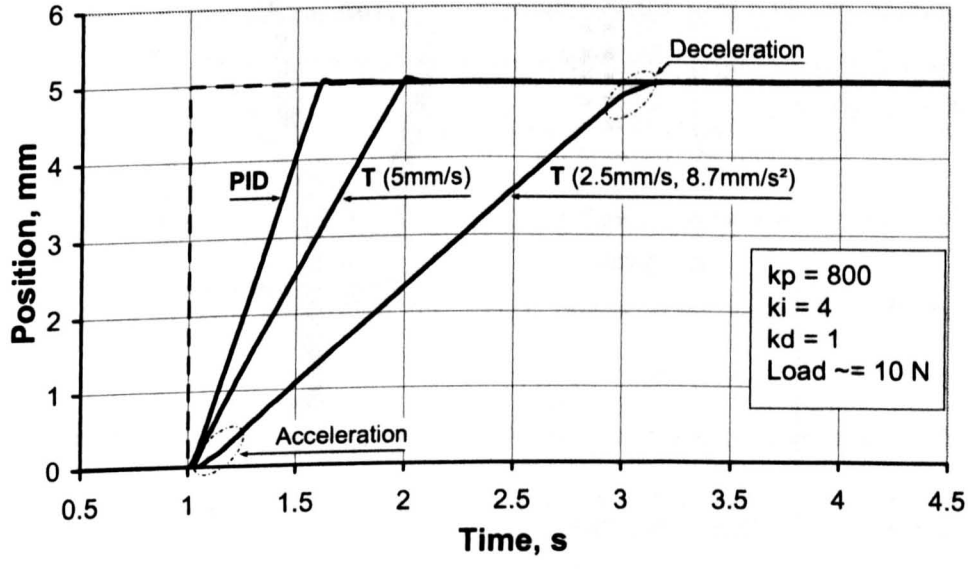


**Figure 74. Response of the active TSF strut to the step input of 5 mm. PID – pure PID control. T (5mm/s) – trajectory control with infinite acceleration and peak speed of 5 mm/s. T(2.5mm/s, 8.7mm/s$^2$) – trajectory control mode with 2.5 mm/s peak speed and 8.7 mm/s$^2$ acceleration.**

### 8.3.4 Software

#### 8.3.4.1 Personal Computer Level

The main user interface for the control of the active TSF was implemented at the PC level. The PC was responsible for providing the user with a visual/numerical

feedback and maintaining communication with the EBox. A win32 communication library was written by the author in a C# programming language. The library was designed to be event driven and therefore caused minimum overhead on the processor of the PC. It supported command cueing and buffering.

The communication library 'talked' to the EBox via the RS232. A set of commands for the EBox is provided in Appendix C. Those can be executed from any terminal software that has access to the RS232 port to which the EBox is connected.

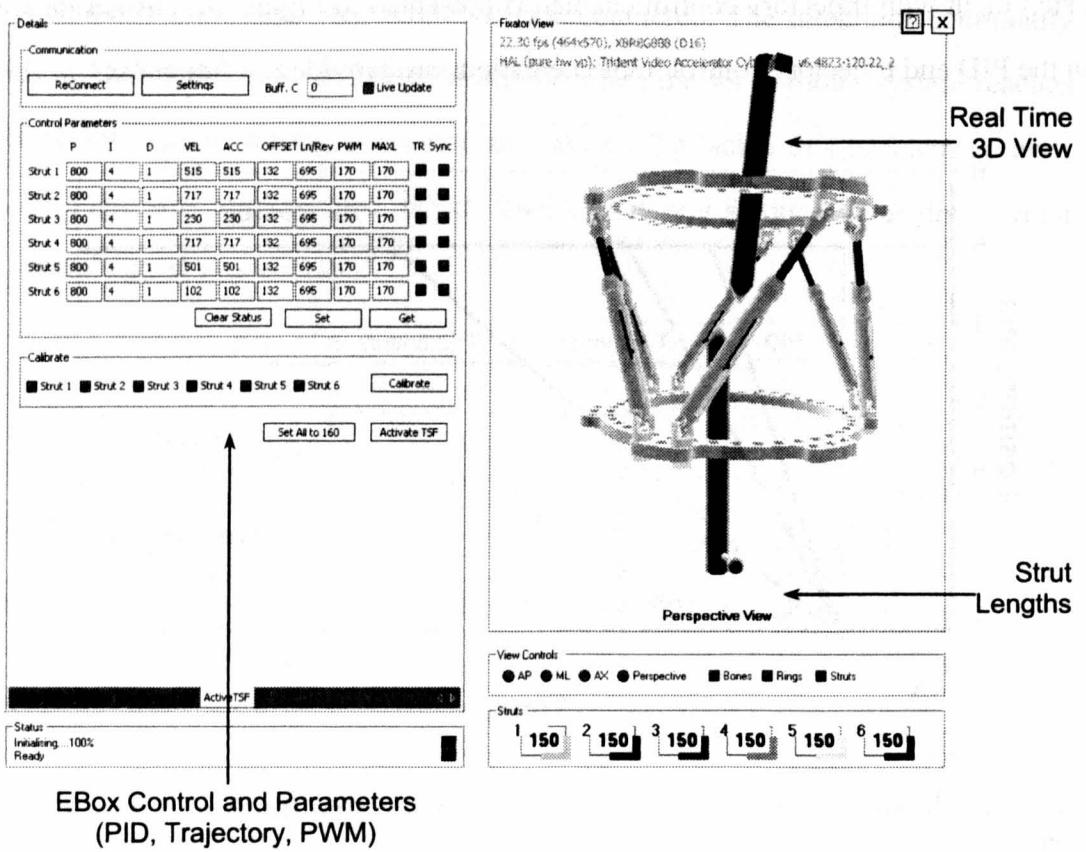


**Figure 75. A screenshot of the EBox control software.**

The communication library was used in conjunction with the user interface (windows application) to provide the user with simple means of control and visual data feedback. Forward and inverse kinematics (Chapter 3) were used to generate a real-time on-screen graphic representation of the active TSF operation. A screenshot of the PC software is provided in Figure 75. In addition, the software was able to

plan the geometry of the standard passive TSF, without the active TSF presence. Additional screenshots of the software are provided in Appendix A.

#### 8.3.4.2 Master MCU

The master MCU was responsible for maintaining the communication link between the PC and slave MCUs. It was converting data between two types of communication buses: serial and $I^2C$.

Two types of command-passing modes from the master to the slave MCUs were implemented: instantaneous and synchronised. In the instantaneous mode, the slave MCU executed a command immediately upon receipt of it. In the synchronised mode, the slave MCU waited for the master MCU to send the start event via a dedicated hardware synchronisation line. This enabled simultaneous execution of commands on all six slave MCUs.

The master MCU also controlled the EBox power state, using a dedicated line connected to the reset line of all slave MCUs. When the slave MCUs were placed in reset mode, the power stage was turned off, thus saving energy. Further details on the implementation of the software of the master MCU can be found in Appendix C.

#### 8.3.4.3 Slave MCU

The slave MCU was responsible for execution of the commands received from the master MCU and actuator control. The PID and motion control were implemented in the slave MCU thus removing processing overhead from the PC. Further details on slave MCU software implementation, including variable definitions can be found in Section 8.3.3 and Appendix C.

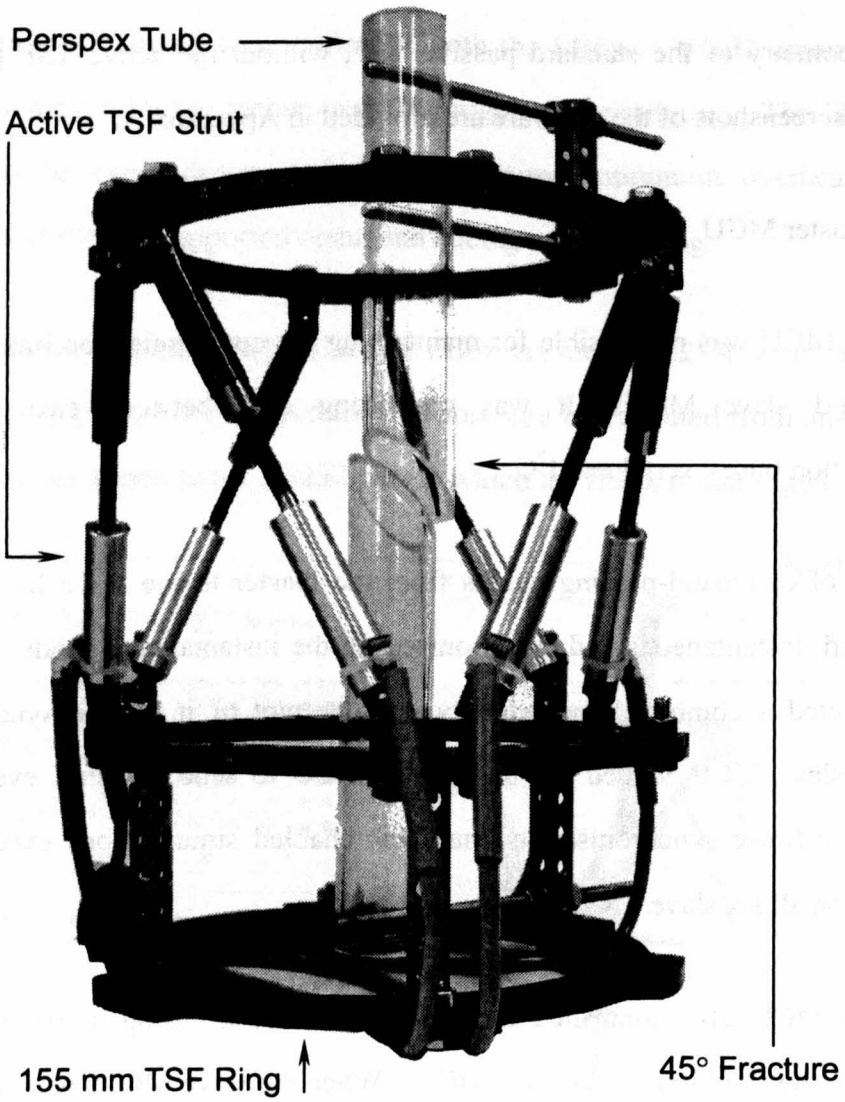


**Figure 76. An active TSF.**

## 8.4 Discussion

An active TSF demonstrator tool resembling the standard TSF has been developed and built by the author, Figure 76. The key components of it were active struts, EBox and PC software. The overall system was tested and gave satisfactory results. Smooth movement and accurate positioning of the bone segments were achieved. The forward and inverse kinematics solutions, presented in Chapter 3, have been verified by reducing the gap (fracture) between two Perspex tubes that were positioned arbitrarily. The gap and frame parameters were used in conjunction with forward and inverse kinematics to plan the reduction. The synchronous TSF strut control together with trajectory control ensured that all struts have started and

finished motion simultaneously, despite the different travel distances. The fracture could be cycled easily with various amounts of the IFM in various vectorised directions, demonstrating controlled mechanical stimulus.

Figure 77 present a typical response of the TSF to a cyclic demand of the IFM of 2 mm amplitude at 0.125 Hz sine wave. The values presented are the changes of the bone position and orientation relative to the original values. The stimulus (IFM) vector was set at 45° angle from the vertical axis of the bone. The vector was also rotated by 60° about the axis of the bone relative to the proximal strut connection group 1&2 counter clockwise. AP, ML and AX translations (defined in Figure 3) represent components of the IFM vector projected onto anatomical axes. The results achieved were satisfactory. The angles of the bones had to be maintained at constant values during the application of the stimulus. Only small angular and positional discrepancies were present.

An additional accuracy test was carried out using a digital Vernier gauge calibrated to 0.01 mm accuracy. Four measurements were taken for axial and rotational displacements. Results are presented in Table 11. A high level of precision was achieved providing higher than 0.1 mm and 0.1° positional and orientational accuracy.

| Requested Change, mm | Achieved Change, mm | Requested Change, deg | Achieved Change, deg |
|---|---|---|---|
| 0.00 | 0.00 | 0.00 | 0.00 |
| 2.50 | 2.46 | 5.00 | 5.01 |
| 5.00 | 5.02 | 10.00 | 9.94 |
| 7.50 | 7.46 | 15.00 | 14.91 |
| 10.00 | 10.03 | 20.00 | 20.09 |

**Table 11. Experimental results of the active TSF accuracy assessment.**

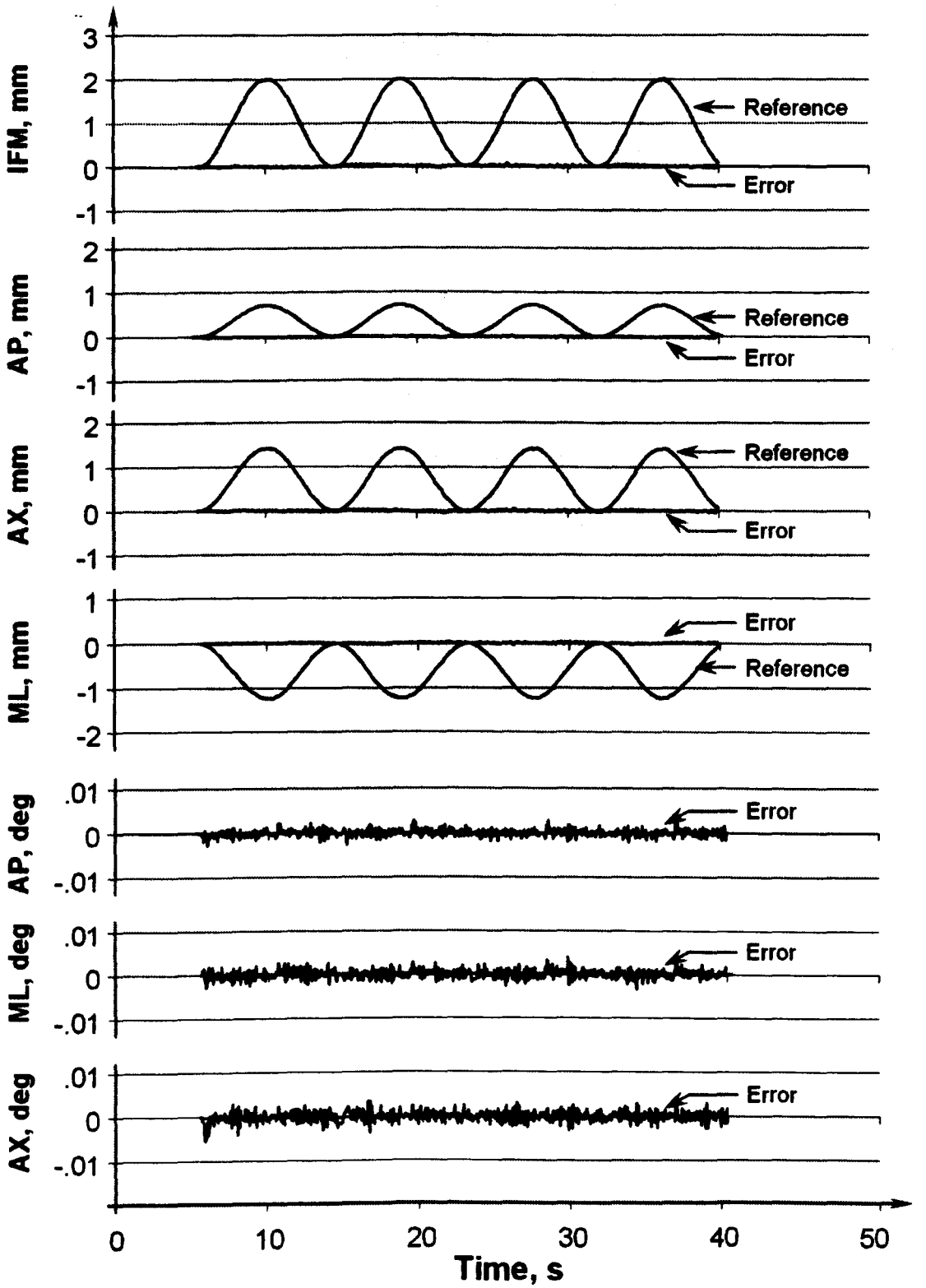


**Figure 77. An active TSF response to a cyclic motion of 2 mm.**

The active strut has been designed and built to meet the design specification. The performance of the strut and its response to a step input in both trajectory and pure PID modes is presented in Figure 74. The top speed of the actuator at the design load of 10 N was 8.2 mm/s. This was somewhat 30 % lower than the theoretical estimate, Figure 70. The difference can be attributed to the unaccounted friction in universal joints and the ball race, as well as to the inexactness of the friction coefficient. The energy efficiency of the actuator is low, since a lot of energy is lost due to friction and hence heat generation. Therefore, a better design, possibly including the ball screw mechanism, would be needed, if the active TSF were used in a mobile, battery powered, application.

A smooth operation of the active TSF strut has been demonstrated, Figure 74. The PID mode provided the fastest response to the demand signal. The control gains were chosen to achieve the fastest response to 0.1 mm positional accuracy. Trajectory control allowed limiting the peak actuator speed. If acceleration and deceleration of the actuator were used at the beginning and the end of the movement, the smoother response was achieved, preventing overshoots and large inertial forces.

The EBox was successfully implemented, Figure 72. It can be interfaced to any PC platform that has RS232 connectivity. Only a basic terminal software (*e.g.* hyper terminal) is required to control the struts of the active TSF. The overall system properties are summarised in Table 12. As can be seen, various actuators can be controlled using the developed electronics, including other applications. The power stage provides sufficient current even for high-power actuators. However, it should be noted that active cooling might be required for DMOS Bridges. The choice of voltage also extends the versatility of the EBox. Although the included power supply is capable of providing a maximum voltage of 24 V, the higher voltage power supply and hence actuators can be used. The actual limit of the integrated full bridges is 48 V.

Should higher positioning precision be required, the higher resolution encoder could be utilised.

| Parameter | Value |
|---|---|
| Input Voltage | 88-264 VAC, 47- 63 Hz |
| Max power consumptions | 220 W |
| Size (width x depth x height) | 285 mm x 230 mm x 50 mm |
| Weight | 3 kg |
| PWM switching frequency | 20 kHz |
| PWM resolution | 8 bits |
| Number of actuators supported | 1-6 |
| Control Type | PID, Trajectory |
| Control turn around time | 0.8 ms |
| Power supply for actuator | 12 V, 24 V (max 48 V[A]) |
| Peak output current | 3A[B] |
| Maximum encoder step | 320 000 lines / s |
| RS232 Communication | 57.6k bps, 8 data bits, no parity, 1 stop bit |
| Operating temperature range | 5-30C (no active cooling) |
| Output voltage for external use | 5 V |
| Limit switch support per actuator[C] | 2 x TTL / Analogue (0-5V) |

**Table 12. EBox technical specifications. [A] not supported by the installed PSU. [B] active cooling might be required for the DMOS full bridge. [C] only implemented in hardware, no software support.**

If the active TSF was used *in vivo* then the design specification would require more powerful active struts. For example, if a 200 N thrust per actuator is considered as a design load, six such actuators can produce more than a 1000 N thrust which would be sufficient for an average weight person. High speed of the actuators for the deformity correction and mechanical stimulation by the active TSF *in vivo* can be dangerous and thus is not required. The author believes that 0.5 mm/s movement speed is more than sufficient for the application. Performing the similar analysis as in Appendix C, including design factor of 2, suggests that the same type of gearhead 14/1 is suitable with gear ratio of 246. This in turn means that a motor capable of 1.87 mN·m at 7380 rpm would be required. The housing design of the active strut would have to be revised for the new design specification. The diameters of the gearhead and the motor would remain the same; only their lengths would increase. If

length were an issue then an alternative would be to use a larger diameter motor and gearhead. The structural strength of the housing has to be taken into account as well. For the *in vivo* application, a stainless steel housing would be recommended, as well as a stronger ball race. In addition to mechanical design considerations, some sterile precautions would have to be set in place between the active frame and the patient. Additional casing of the active strut or the appropriate wrapping of the injured limb could be used. No changes to the EBox would be required for the *in vivo* application.

## 8.5 Conclusions

The active TSF demonstrator tool prototype has been presented in this chapter. It has been shown that it is possible to design the suitable active struts and to motorise the TSF for the *in vivo* application. Forward and inverse kinematics have been verified using the demonstrator tool.

# CHAPTER 9 : DISCUSSION OF RESEARCH

The aim of this chapter is to discuss the results of the previous chapters. In addition, implications for the orthopaedic field are explored.

## 9.1 TSF Kinematics

Kinematics is the key to a successful application of the TSF fixator for fracture and deformity reduction. An iterative numerical solution for both forward and inverse kinematics of the TSF fixator has been presented in Chapter 3. The solution presented exhibits a high convergence rate and can be implemented on a personal computer or a mobile device, *e.g.* PDA (personal digital assistant). The processor overhead was optimised by reusing the inverse of the Jacobian matrix of the TSF from a previous iteration and only updating it when the error convergence rates were unsatisfactory. The developed algorithms allow freedom of the TSF component geometrical positioning and hence are suitable for operating modified frames built for peri-articular fracture fixation. Forward kinematics algorithms fail at or close to singular frame configurations. This is not an issue for the use of the TSF, since singular configurations are not practical for fracture fixation.

The developed algorithm can be used beyond the medical application, wherever a high stiffness Stewart-Gough platform is employed, *e.g.* telescope positioning, multi-degree of freedom actuators etc.

## 9.2 Mechanical Properties of TSF Fixators

The core mechanical properties of the TSF have been identified and investigated, in Chapters 4-7. It has been shown that the stiffness of the fixator is largely influenced by the choice of the bone-transfixing components rather than the frame itself, Chapter 6.

When planning fixator configuration, it is important to consider the load capacity of the fixator. Wires and half-pins limit the maximum load that the fixator can operate within an elastic range. The load capacity values for various length half-pins and wires were presented in Chapter 5. None of the TSF specimens failed plastically during testing. This suggests that frames were capable of tolerating 1.5 kN axial and offset loads as well as 15 N·m torsion load.

Once the minimum number of the transfixing components has been identified, the stiffness of the fixator can be planned. The stiffness of the fixator could be increased by increasing the pretension of the fine wires, increasing the number of wires used and decreasing the ring diameter (wire span). Ring separation is also a factor influencing the TSF stiffness. Decreasing ring separation decreases fixator axial stiffness, due to increasing angles between struts. However, only a marginal decrease in stiffness is expected, since the TSF stiffness would still be significantly higher than that of a fine wire. Another factor influencing fixator stiffness is the wire crossing angle, as has been shown by [6, 8]. The author believes that this factor has two origins: the difference in transverse ring load reaction and ring support points. The ring support points will influence the fixator stiffness, as has been shown in Chapter 4 'stiff' and 'flexible' set-ups. Again, this difference is expected to cause 10 - 30 % difference to the overall axial fixator stiffness, due to the relatively high TSF stiffness when compared to fine wires. Finally, mounting the bone off-central axis of the frame increases stiffness of the fixator.

The current TSF configuration is not well suited for fixation of peri-articular fractures. Suitable modifications to the standard TSF configuration have been suggested in Chapter 4, which introduced minor changes to the mechanical properties of the fixator. Moving strut groups 3&4 and 5&6 by two holes posteriorly or introducing an additional accessory ring have produced the most satisfactory results.

The present research has only considered frames in neutral configurations, where rings were parallel and aligned with each other and the mechanical testing was carried out on clinically used components. In addition, small test sample numbers were used, due to time and budget constraints. Therefore, some variation of results would be expected for frames constructed from brand-new components with larger sample sizes. However, this variation is expected to be minimal since fine wires cause the dominant deflections. If 'bent' frames (rings are not parallel and/or their centres are not aligned) were used, the author anticipates changes in stiffness properties, and a further investigation would be required to quantify them. This would be further complicated by the effect of transfixing components on the IFM. The wire stiffness is low axially, however not so much laterally, especially if olive wires are used. The same applies to half-pins. Therefore, for 'bent' configurations, the wire-induced interfragmentary motion would be affected, promoting sideways shear. Based on evidence of both axial and off-axis load tests on the neutral TSF, the author expects the TSF to produce similar or greater stiffness compared to the Ilizarov hinged frame. The stiffness of the fixators is expected to be governed by the stiffness properties of the transfixing components.

Slack in frames has been shown to be capable of producing significant strains due to the uncontrolled motion in the unloaded frames, so leading to high levels of pain. A minimum slack configuration involves struts angled to each other at 90°. In general, slack can be minimised by increasing ring diameter and reducing ring separation. This in turn would reduce the stiffnesses of both the frame and wires. A careful balance therefore has to be achieved between the slack and stiffness of the fixator. A few slack minimisation techniques that do not affect the fixator stiffness have been proposed in Chapter 7. The use of washers between shoulder bolts and rings at one end of strut fixation eliminates more than 30 % of the slack in the frame. Alternatively, over-constraining the frame by introduction of a seventh strut eliminates slack all together.

Slack introduces uncertainty in the position and orientation of the broken bone segments when the frame is loaded. This could be resolved mathematically, by taking into account the frame load state and the amount of backlash in each strut using the kinematics algorithms presented in Chapter 3.

## 9.3 Significance of Findings to Orthopaedic Surgery

The stiffness of the fixator is an important factor for fracture healing, since it controls the mechanical environment at the fracture site. It has been shown [14, 16, 31] that interfragmentary strain influences the rate and success of healing. Despite many attempts that have been made to identify the ideal level of strain, no comprehensive testing has been performed on humans and therefore it is hard to confirm what levels of strain are most beneficial. The mechanical properties of bony tissue reveal that the strains of up to 100 % are acceptable during the early stages of healing while significantly smaller 2 % strains are acceptable in later stages [19]. The axial stiffness of the typical TSF fixator ranges from 50 – 200 N/mm depending on the configuration employed and load direction. This suggests that there will typically be in the order of 4 mm - 16 mm of motion for an average weight adult when fully load-bearing on the completely fractured bone, provided there is a sufficiently large gap for this to occur. In practice, the gap size may be 1 mm - 3 mm and therefore collision between fractured bone segments may occur, resulting in reduced loading on the fixator. Despite the large possible motion and hence high axial flexibility, there is much evidence of successful fracture healing, and this is supported by healing in plaster cast fixation which does allow this degree of motion [27]. Therefore, the concept of fracture healing being the result of defined strain control by the fixator, throughout the repair process, has to be questioned. It is evident that there must be some other factors influencing micro-motion and bone healing. It is possible to speculate that some of the load is taken by the surrounding tissues and some by the newly-laid bone itself, thus reducing the load on the frame and thus the amount of motion at the fracture site. It could also be speculated that the

circular fixator acts like a guiding system for the fractured bone segments, readily allowing axial displacement whilst preventing bone angulations and shear motions. The load and displacement amplitudes in the axial bone direction are controlled by the patient rather than by the mechanical properties of the fixator. All this suggests that there is a need for more clinical research in order to understand better the true role of external fixators.

## 9.4 Automation of TSF Fixators

The concept of automation of the active ring fixator is an attractive option since it can provide controlled mechanical stimulus to the fracture. An active TSF prototype implementation has been presented in Chapter 8. Both electronics and actuator (active strut) designs together with the control strategies have been developed. The developed fixator can be utilised to demonstrate the concept of the mechanical stimulus and to aid surgeon training, by providing visual means of fracture management.

The demonstrator tool has verified the kinematics solutions developed in Chapter 3.

The *in vivo* design of the active TSF has been considered. Only the active strut design would require modification in order to produce and sustain a larger thrust.

The active strut energy efficiency would need improving for the low weight and small volume battery powered applications. This could be achieved by using a ball screw mechanism for the drive shaft. The mobile active TSF could be utilised for fracture shielding against unfavourable strains, generated by impacts of the injured limb due to the patient's low ability to control it. The scaling down of electronics would be required for such application. This is possible by use of surface mount integrated circuits together with multiple-layer printed circuit boards. The developed infrastructure and components of the electronics circuits are highly suitable for such an implementation.

# CHAPTER 10 : CONCLUSIONS

The principal aim of this thesis is the exploration of the Taylor Spatial Frame (TSF) based ring orthopaedic fixator. The following areas were therefore addressed: kinematics, mechanical properties and automation possibilities. A new solution to the kinematics of the TSF has been derived. Simple but effective models of the mechanical properties have been developed. Strategies for automation of motion of the frame have been developed and implemented. The principal benefits are seen as the delivery of a practical guide for surgeons and therefore better outcomes for patients presented with complex fractures and deformities in the long leg bones. This chapter is structured to provide a concise overview of results and findings as a result of the research, by addressing the key research questions stated in the introductory chapter. In addition, a summary of contributions to the body of knowledge and further research suggestions are provided.

## 10.1 Summary of Research Findings

TSF's kinematics

a. It is possible to solve rapidly forward and inverse kinematics on both ordinary and handheld computer devices.

b. The algorithms for solving both forward and inverse kinematics have been presented in Chapter 3.

c. A computational improvement by a factor of two was achieved over the standard Newton-Raphson algorithm by reusing the Jacobian matrix and its inverse from previous iterations, and re-computing it only when the error convergence was not acceptable.

TSF's mechanical properties

a. The axial, off-axis and torsional stiffnesses of the standard TSF have been quantified in Chapter 4.

b. The TSF is significantly stiffer in torsion than the Ilizarov frame.

c. Axial and off-axis stiffnesses are affected greatly by the load-point locations on the rings, suggesting that placing of the stiff bone-transfixing components close to the ring interconnecting components result in greater overall fixator stiffness.

d. The TSF is less stiff axially than the Ilizarov frame.

e. The TSF is stiffer than the Ilizarov hinge frame, when loaded with off-axis loads.

f. TSF exhibits similar stiffness for axial and off-axis loads.

g. It is possible to modify the TSF to allow more space for the bone-transfixing components for the peri-articular fractures by moving strut groups 3&4 and 5&6 by two ring holes posteriorly, Chapter 4, without altering significantly the neutral frame stiffness properties. Alternatively, the Ilizarov carbon fibre ring can be used as an accessory ring for the transfixing component mounting.

h. A new simple method was derived and verified for modelling ring - fine wire mechanical behaviour.

i. Simple means of stiffness estimation were provided and verified for the half-pins – ring systems.

j. Higher fine wire pretension results in the higher axial stiffness, but lower load capacity.

k. Increase in wire span (ring diameter) decreases wire stiffness properties.

l. Increasing the number of wires to transfix the bone segment to the frame increases axial and torsional stiffness linearly.

m. A simple means of planning fixator stiffness has been presented in Chapter 6.

n. Fine wires largely dictate the stiffness attainable by the ring fixator.

o. The difference in axial stiffness between the TSF and Ilizarov fixators is very small, if fine wires are used to transfix broken bone segments to the frame.

p. The TSF is constructed of two rings and six struts. The length of the TSF strut can be adjusted in 1 mm increments only, which is equivalent to +/- 0.5 mm slack in the strut. The geometrical accuracy for such a system was investigated in Chapter 7 and the results were presented in Table 8.

q. The TSF slack, resulting from the backlash in the frame components, can produce significant strains on the newly-laid bone tissue that could potentially be damaging.

r. The minimum amount of slack was observed for frame configurations in which struts were at a 90° angle to each other.

s. Placing a washer between the shoulder bolt of the strut and the ring at one end of the strut can eliminate up to 30 % of the slack in the TSF.

t. The introduction of additional seventh strut can eliminate slack by over-constraining the TSF.

u. If the frame load state is known, the positional and orientational uncertainties introduced by the slack can be mathematically taken into account through forward and inverse kinematics and hence eliminated.

TSF automation

a. It is possible to develop an active TSF similar to the standard TSF and is capable of sustaining operational loads.

b. It has been demonstrated that it is possible to use the active TSF to apply controlled mechanical stimulus to the fracture.

c. An active demonstrator tool has been developed and built.

## 10.2 Summary of Contributions to Knowledge

The author has:

a. Developed a quick algorithm for solving kinematics of the general Stewart-Gough platform, suitable for use with the TSF.

b. Quantified previously unknown mechanical properties of the TSF.

c. Presented a simple, but accurate, model for fine wire stiffness modelling.

d. Suggested and investigated possible modifications to the TSF for peri-articular fractures.

e. Performed analysis of fine wire influence on mechanical properties of the circular fixation devices.

f. Identified TSF slack as a potential setback to healing and accuracy of fracture reduction.

g. Investigated the slack effects on the operational accuracy of the TSF and proposed slack minimisation techniques for the unloaded frames.

h. Designed and developed the prototype of an active TSF, including electronics, software, control strategy and actuators.

i. Provided considerations for the *in vivo* design of the active TSF.

j. Demonstrated the controlled mechanical stimulus.

k. Published the original journal article about the simple way to model fine wires. Additional articles about TSF kinematics, mechanical properties and automation will be published.

## 10.3 Suggestions for Further Research

TSF kinematics:

a. Develop algorithms based on forward and inverse kinematics for accurate fracture reduction path planning and knee straightening.

b. Identify the Jacobian matrix properties that relate to the stability and stiffness of the TSF.

TSF mechanical properties:

a. Analyse mechanical properties of the fixators consisting of two different diameter rings.

b. Analyse the behaviour of the cascaded TSF (two TSF segments: 3 rings, 12 struts) for managing segmental fractures.

c. Test other than 155 mm ring TSF frames for the mechanical properties.

d. Investigate 'bent' frame (rings are not parallel and/or misaligned) mechanical properties and compare those with the Ilizarov hinged frame.

e. Derive a more accurate half-pin – ring stiffness model. Test half-pin material properties.

TSF automation

a. Implement the active TSF for the *in vivo* use.

b. Manufacture scaled-down electronics for mobile *in vivo* use.

c. Interface load cells to actively shield the fracture from external forces, and hence from undesirable impacts.

d. Develop an autonomous radio frequency controlled strut containing the power source, actuation mechanism and control electronics. The I2C bus in present EBox design could be replaced by the radio link.

Cross-field suggestions:

a. Investigate slack in the Ilizarov hinge.

b. Clinically quantify levels and directions of IFM, which are beneficial to fracture healing.

c. Investigate mechanical interaction between limb tissues and circular frame.

## REFERENCES


1. **Kay NRM.** *Litigants' epicondylitis.* The Journal of Hand Surgery: Journal of the British Society for Surgery of the Hand, 2003. 28(5): p. 460-464.

2. **Ali AM, El-Shafie M, and Willett KM.** *Failure of fixation of tibial plateau fractures.* Journal of Orthopaedic Trauma., 2002. 16(5): p. 323-9.

3. **Delamarter RB, Hohl M, and Hopp E, Jr.** *Ligament injuries associated with tibial plateau fractures.* Clinical Orthopaedics & Related Research., 1990(250): p. 226-33.

4. **Benirschke SK, Agnew SG, Mayo KA, Santoro VM, and Henley MB.** *Immediate internal fixation of open, complex tibial plateau fractures: treatment by a standard protocol.* Journal of Orthopaedic Trauma., 1992. 6(1): p. 78-86.

5. **Marsh JL, Smith ST, and Do TT.** *External fixation and limited internal fixation for complex fractures of the tibial plateau.* Journal of Bone & Joint Surgery - American Volume., 1995. 77(5): p. 661-73.

6. **Fleming B, Paley D, Kristiansen T, and Pope M.** *A biomechanical analysis of the Ilizarov external fixator.* Clinical Orthopaedics & Related Research., 1989(241): p. 95-105.

7. **Khalily C, Voor MJ, and Seligson D.** *Fracture site motion with Ilizarov and "hybrid" external fixation.* Journal of Orthopaedic Trauma., 1998. 12(1): p. 21-6.

8. **Bronson DG, Samchukov ML, Birch JG, Browne RH, and Ashman RB.** *Stability of external circular fixation: A multi-variable biomechanical analysis.* Clinical Biomechanics, 1998. 13(6): p. 441-448.

9. **Goodship AE and Kenwright J.** *The influence of induced micromovement upon the healing of experimental tibial fractures.* Journal of Bone & Joint Surgery - British Volume, 1985. 67(4): p. 650-5.

10. **Ilizarov GA.** *The tension-stress effect on the genesis and growth of tissues. Part I. The influence of stability of fixation and soft-tissue preservation.* Clinical Orthopaedics & Related Research, 1989(238): p. 249-81.

11. **Waanders NA, Richards M, Steen H, Kuhn JL, Goldstein SA, and Goulet JA.** *Evaluation of the mechanical environment during distraction*

*osteogenesis.* Clinical Orthopaedics & Related Research, 1998(349): p. 225-34.

12. **Wolf S, Janousek A, Pfeil J, Veith W, Haas F, Duda G, and Claes L.** *The effects of external mechanical stimulation on the healing of diaphyseal osteotomies fixed by flexible external fixation.* Clinical Biomechanics, 1998. 13(4-5): p. 359-364.

13. **Wolf JW, White AA, Panjabi MM, and Southwick WO.** *Comparison of cyclic loading versus constant compression in the treatment of long-bone fractures in rabbits.* Journal of Bone & Joint Surgery - American Volume, 1981. 63(5): p. 805-810.

14. **Claes LE, Heigele CA, Neidlinger-Wilke C, Kaspar D, Seidl W, Margevicius KJ, and Augat P.** *Effects of mechanical factors on the fracture healing process.* Clinical Orthopaedics & Related Research, 1998(355 Suppl): p. S132-47.

15. **Gardner TN, Evans M, and Simpson H.** *Temporal variation of applied inter fragmentary displacement at a bone fracture in harmony with maturation of the fracture callus.* Medical Engineering & Physics, 1998. 20(6): p. 480-484.

16. **Kenwright J and Goodship AE.** *Controlled mechanical stimulation in the treatment of tibial fractures.* Clinical Orthopaedics & Related Research, 1989(241): p. 36-47.

17. **O'Doherty DM, Butler SP, and Goodship AE.** *Stress protection due to external fixation.* Journal of Biomechanics, 1995. 28(5): p. 575-586.

18. **Sarmiento A, Schaeffer JF, Beckerman L, Latta LL, and Enis JE.** *Fracture healing in rat femora as affected by functional weight-bearing.* Journal of Bone & Joint Surgery - American Volume, 1977. 59(3): p. 369-75.

19. **Perren SM.** *Physical and biological aspects of fracture healing with special reference to internal fixation.* Clinical Orthopaedics & Related Research, 1979(138): p. 175-96.

20. **Manolagas SC.** *Editorial: Cell Number Versus Cell Vigor--What Really Matters to a Regenerating Skeleton?* Endocrinology, 1999. 140(10): p. 4377-4381.

21. **Glitsch U and Baumann W.** *The three-dimensional determination of internal loads in the lower extremity.* Journal of Biomechanics, 1997. 30(11-12): p. 1123-1131.

22. **Heller MO, Bergmann G, Deuretzbacher G, Durselen L, Pohl M, Claes L, Haas NP, and Duda GN.** *Musculo-skeletal loading conditions at the hip during walking and stair climbing.* Journal of Biomechanics, 2001. 34(7): p. 883-893.

23. **Duda GN, Schneider E, and Chao EYS.** *Internal forces and moments in the femur during walking.* Journal of Biomechanics, 1997. 30(9): p. 933-941.

24. **Schneider E, Michel MC, Genge M, Zuber K, Ganz R, and Perren SM.** *Loads acting in an intramedullary nail during fracture healing in the human femur.* Journal of Biomechanics, 2001. 34(7): p. 849-857.

25. **McKibbin B.** *The biology of fracture healing in long bones.* Journal of Bone & Joint Surgery - British Volume, 1978. 60-B(2): p. 150-62.

26. **Kenneth J and Koval MD.** *Orthopaedic Knowledge Update 7: Home Study Syllabus.* 1st ed. 2002, New York: Amer Acad of Orthopaedic Surgeons.

27. **McKellop H, Hoffmann R, Sarmiento A, and Ebramzadeh E.** *Control of motion of tibial fractures with use of a functional brace or an external fixator. A study of cadavera with use of a magnetic motion sensor.* Journal of Bone & Joint Surgery - American Volume, 1993. 75(7): p. 1019-25.

28. **Ilizarov GA.** *The tension-stress effect on the genesis and growth of tissues: Part II. The influence of the rate and frequency of distraction.* Clinical Orthopaedics & Related Research, 1989(239): p. 263-85.

29. **Ilizarov GA.** *Clinical application of the tension-stress effect for limb lengthening.* Clinical Orthopaedics & Related Research, 1990(250): p. 8-26.

30. **Richards M, Goulet JA, Weiss JA, Waanders NA, Schaffler MB, and Goldstein SA.** *Bone regeneration and fracture healing. Experience with distraction osteogenesis model.* Clinical Orthopaedics & Related Research, 1998(355 Suppl): p. S191-204.

31. **Kenwright J and Gardner T.** *Mechanical influences on tibial fracture healing.* Clinical Orthopaedics & Related Research, 1998(355 Suppl): p. S179-90.

32. **Noordeen MHH, Lavy CBD, Shergill NS, Tuite JD, and Jackson AM.** *Cyclical Micromovement and Fracture Healing.* Journal of Bone & Joint Surgery - British Volume., 1995. 77(4): p. 645-648.

33. **Perren SM and Cordey JTcois.** *The concept of interfragmentary strain.* In: Uhthoff, H.K. (Ed.), Current Concepts of Internal Fixation of Fractures, 1980: p. Springer, Berlin, pp. 63–77.

34. **Evans FG.** *Stress and strain in bones.* 1957, Springfield: Thomas.

35. **Yamada H.** *Strength of biological materials.* 1970, Baltimore: Williams & Wilkins.

36. **Hidaka S and Gustilo RB.** *Refracture of bones of the forearm after plate removal.* Journal of Bone & Joint Surgery - American Volume, 1984. 66(8): p. 1241-3.

37. **Hillard PJ, Harrison AJ, and Atkins RM.** *The yielding of tensioned fine wires in the Ilizarov frame.* Proc Instn Mech Engrs, 1998. 212: p. 37-47.

38. **Taylor HS and Taylor JC,** *Orthopaedic fixation device, Patent No: 5,702,389.* 1997, Smith & Nephew Richards, Inc.: USA. p. 1-24.

39. **Stewart D.** *A Platform with six degrees of freedom.* Proceedings of Institution of Mechanical Engineers, Part I, 1965. 180(15): p. 371-386.

40. **Gough VE and Whitehall SG.** *Universal tyre test machine.* Proceedings, Ninth International Technical Congress FISITA(IMECHE), 1962: p. 117.

41. **NetIdeas.** *http://www.netideasinc.com/EngineeringSolutions.jsp.* Viewed at 11/08/2005.

42. **Raghavan M.** *Stewart platform of general geometry has 40 configurations.* ASME Journal of Mechanical Design, 1993. 115: p. 227-280.

43. **Lee TY and Shim JK.** *Forward kinematics of the general 6-6 Stewart platform using algebraic elimination.* Mechanism and Machine Theory, 2001. 36: p. 1073-1085.

44. **Ji P and Wu H.** *A Closed-Form Forward Kinematics Solution for the 6-6 Stewart Platform.* IEEE Transactions on robotics and automation, 2001. 17(4): p. 522-526.

45. **Merlet JP.** *Direct kinematics of parallel manipulators.* IEEE transactions on robotics and automation, 1993. 9(6): p. 842-846.

46. **McAree PR and Daniel RW.** *A Fast, Robust Solution to the Stewart Platform Forward Kinematics.* Journal of robotic systems, 1996. 13.

47. **Dasguptaa B and Mruthyunjaya TS.** *The Stewart platform manipulator: a review.* Mechanism and Machine Theory, 2000. 35: p. 15-40.

48. **Hunt KH.** *Kinematic Geometry of Mechanisms.* Oxford University Press, 1978.

49. **Fichter EF.** *A Stewart Platform-Based Manipulator: General Theory and Practical Construction.* Int. Journal of Robotics Research, 1986. 5(2): p. 157-182.

50. **Merlet JP.** *Parallel Manipulators, Part 2: Theory, Singular Configurations and Grassmann Geometry.* Technical Report No. 791, INRIA, France, 1988.

51. **Merlet JP.** *Singular Configurations of Parallel Manipulators and Grassmann Geometry.* The international journal of robotics research, 1989. 8(5): p. 45-56.

52. **Feldman DS, Shin SS, Madan S, and Koval KJ.** *Correction of Tibial Malunion and Nonunion With Six-Axis Analysis Deformity Correction Using the Taylor Spatial Frame.* J. Orthop. Trauma, 2003. 17(8): p. 549-554.

53. **Yamagishi M and Yoshimura Y.** *The biomechanics of fracture healing.* JBJS, 1955. 37-A(5): p. 1035-1068.

54. **Aronson J and Harp JH.** *Mechanical considerations in using tensioned wires in a transosseous external fixation system.* Clinical Orthopaedics & Related Research, 1992. 280: p. 23-29.

55. **Gasser B, Boman B, Wyder D, and Schneider E.** *Stiffness characteristics of the circular Ilizarov device as opposed to conventional external fixators.* Journal of Biomechanical Engineering., 1990. 112(1): p. 15-21.

56. **Kummer FJ.** *Biomechanics of the Ilizarov external fixator.* Clinical Orthopaedics & Related Research., 1992(280): p. 11-4.

57. **Nele U, Maffulli N, and Pintore E.** *Biomechanics of radiotransparent circular external fixators.* Clinical Orthopaedics & Related Research., 1994(308): p. 68-72.

58. **Podolsky A and Chao EY.** *Mechanical performance of Ilizarov circular external fixators in comparison with other external fixators.* Clinical Orthopaedics & Related Research., 1993(293): p. 61-70.

59. **Waanders NA, Lawton JN, Steen H, Goulet JA, and Goldstein SA.** *Clinical estimation of ilizarov fixator axial stiffness based on wire and half pin contributions.* Bulletin - Hospital for Joint Diseases., 1993. 53(4): p. 10-2.

60. **Calhoun JH, Li F, Bauford WL, Lehman T, Ledbetter BR, and Lowery R.** *Rigidity of half pins for the Ilizarov external fixator.* Bulletin Hospital for Joint Diseases, 1992. 52(1): p. 21-26.

61. **Ali AM, Yang L, Hashmi M, and Saleh M.** *Bicondylar tibial plateau fractures managed with the Sheffield Hybrid Fixator. Biomechanical study and operative technique.* Injury., 2001. 32(Suppl 4): p. SD86-91.

62. **Watson JT, Ripple S, Hoshaw SJ, and Fhyrie D.** *Hybrid external fixation for tibial plateau fractures: clinical and biomechanical correlation.* Orthopedic Clinics of North America., 2002. 33(1): p. 199-209, ix.

63. **DeCoster TA, Crawford MK, and Kraut MA.** *Safe extracapsular placement of proximal tibia transfixation pins.* Journal of Orthopaedic Trauma, 2004. 18(8): p. S43-S47.

64. **Lundy WL, Albert MJ, and Hutton WC.** *Biomechanical comparison of hybrid external fixators.* Journal of Orthopaedic Trauma., 1998. 12(7): p. 496-503.

65. **Roberts CS, Dodds JC, Perry K, Beck D, Seligson D, and Voor MJ.** *Hybrid External Fixation of the Proximal Tibia: Strategies to Improve Frame Stability.* Journal of Orthopaedic Trauma, 2003. 17(6): p. 415-420.

66. **Gardner TN, Evans M, Simpson AH, Kyberd PJ, and Kenwright J.** *A method of examining the magnitude and origin of "soft" and "hard" tissue forces resisting limb lengthening.* Medical Engineering & Physics., 1997. 19(5): p. 405-11.

67. **Simpson AH, Cunningham JL, and Kenwright J.** *The forces which develop in the tissues during leg lengthening. A clinical study.* Journal of Bone & Joint Surgery - British Volume., 1996. 78(6): p. 979-83.

68. **Nikonovas A and Harrison AJL.** *A simple way to model wires used in ring fixators: analysis of the wire stiffness effect on overall fixator stiffness.* Proc Instn Mech Engrs: J. Engineering in Medicine, 2005. 219: p. 31-42.

69. **Watson MA, Mathias KJ, Maffulli N, and Hukins DWL.** *The effect of clamping a tensioned wire: Implications for the Ilizarov external fixation system.* Proceedings of the Institution of Mechanical Engineers, Part H: Journal of Engineering in Medicine, 2003. 217(2): p. 91-98.

70. **Delprete C and Gola MM.** *Mechanical performance of external fixators with wires for the treatment of bone fractures. Part II: Wire tension and slippage.* Journal of Biomechanical Engineering, Transactions of the ASME, 1993. 115(1): p. 37-42.

71. **Watson MA, Matthias KJ, Maffulli N, and Hukins DWL.** *Yielding of the clamped-wire system in the Ilizarov external fixator.* Proceedings of the Institution of Mechanical Engineers, Part H: Journal of Engineering in Medicine, 2003. 217(5): p. 367-374.

72. **Orbay GL, Frankel VH, and Kummer FJ.** *The effect of wire configuration on the stability of the Ilizarov external fixator.* Clinical Orthopaedics & Related Research, 1992. 279: p. 299-302.

73. **Green SA.** *Ilizarov external fixation. Technical and anatomic considerations.* Bulletin of the Hospital for Joint Diseases Orthopaedic Institute, 1988. 48(1): p. 28-35.

74. **Windhagen H, Glockner R, Bail H, Kolbeck S, and Raschke M.** *Stiffness characteristics of composite hybrid external fixators.* Clinical Orthopaedics & Related Research, 2002. 405: p. 267-276.

75. **Pugh KJ, Wolinsky PR, Dawson JM, and Stahlman GC.** *The Biomechanics of Hybrid External Fixation.* Journal of Orthopaedic Trauma, 1999. 13(1): p. 20-26.

76. **Rubin C, Gross T, Qin YX, Fritton S, Guilak F, and McLeod K.** *Differentiation of the Bone-Tissue Remodeling Response to Axial and Torsional Loading in the Turkey Ulna.* Journal of Bone and Joint Surgery, 1996. A78(10): p. 1523-1533.

77. **Young WC and Budynas RG.** *Roark's formulas for stress and strain.* 7th ed. 2002, London: McGraw-Hill.

78. **Azom.** *Typical physical properties for 316 grade stainless steels.* http://www.azom.com/details.asp?ArticleID=2382, Viewed on 24/06/2005.

79. **Davison BL, Cantu RV, and Van Woerkom S.** *The magnetic attraction of lower extremity external fixators in an MRI suite.* Journal of Orthopaedic Trauma, 2004. 18(1): p. 24-27.

80. **Calhoun JH, Li F, Ledbetter BR, and Gill CA.** *Biomechanics of the Ilizarov fixator for fracture fixation.* Clinical Orthopaedics & Related Research., 1992(280): p. 15-22.

81. **Yilmaz E, Belhan O, Karakurt L, Arslan N, and Serin E.** *Mechanical performance of hybrid Ilizarov external fixator in comparison with Ilizarov circular external fixator.* Clinical Biomechanics, 2003. 18(6): p. 518-522.

82. **Park S-H, O'Connor K, McKellop H, and Sarmiento A.** *The Influence of Active Shear or Compressive Motion on Fracture-Healing.* Journal of Bone & Joint Surgery - American Volume, 1998. 80(6): p. 868-878.

83. **Aronson J.** *Experimental and clinical experience with distraction osteogenesis.* Cleft Palate Craniofac Journal, 1994. 31(6): p. 473-481; discussion 481-2.

84. **Atar D, Lehman WB, Grant AD, Strongwater A, Frankel V, and Golyakhovsky V.** *Treatment of complex limb deformities in children with the Ilizarov technique.* Orthopedics, 1991. 14(9): p. 961-7, 1991 Sep.

85. **Dahl MT and Fischer DA.** *Lower extremity lengthening by Wagner's method and by callus distraction.* Orthopedic Clinics of North America, 1991. 22(4): p. 643-649.

86. **Dahl MT, Gulli B, and Berg T.** *Complications of limb lengthening. A learning curve.* Clinical Orthopaedics & Related Research, 1994. 301: p. 10-18.

87. **Fischgrund J, Paley D, and Suter C.** *Variables affecting time to bone healing during limb lengthening.* Clinical Orthopaedics & Related Research, 1994. 301: p. 31-37.

88. **Kenwright J and White SH.** *A historical review of limb lengthening and bone transport.* Injury, 1993. 24(Suppl 2): p. S9-19.

89. **Paley D.** *Current techniques of limb lengthening.* Journal of Pediatric Orthopedics, 1988. 8(1): p. 73-92.

90. **Philips.** *The I2C - Bus Specification.* http://www.semiconductors.philips.com/markets/mms/protocols/i2c/, 2000. Version 2.1.

91. **O'Dwyer A.** *Handbook of PI and PID controller tuning rules.* 2003, London: Imperial College Press.

92. **Ogata K.** *Discrete-time control systems.* 2nd ed. 1995, Upper Saddle River, N.J: Prentice Hall.

93. **Microchip.** *PIC16F87XA Data Sheet.* www.microchip.com, 2003. DS39582B.

94. **Bucella T.** *Servo Control of a DC-Brush Motor.* Microchip Application Notes, 1997. AN532.

95. **Bowling S and Chandler AZ.** *PIC18CXXX/PIC16CXXX DC Servomotor Application.* Microchip Application Notes, 2000. AN696.

96. **Fischer RL.** *Using the PICmicro(r) MSSP Module for Master I2C Communications.* Microchip Application Notes, 2000. AN735.

97. **Bowling S.** *Using the PICmicro® SSP for Slave I2C Communication.* Microchip Application Notes, 2000. AN374.

# APPENDIX A – SCREEN SHOTS OF THE DEVELOPED SOFTWARE

The software for the TSF kinematics, fracture reduction, deformity correction and an active TSF control has been written by the author in C# programming language in the .NET environment. Below are screen-shots of the software interface and brief descriptions of them.

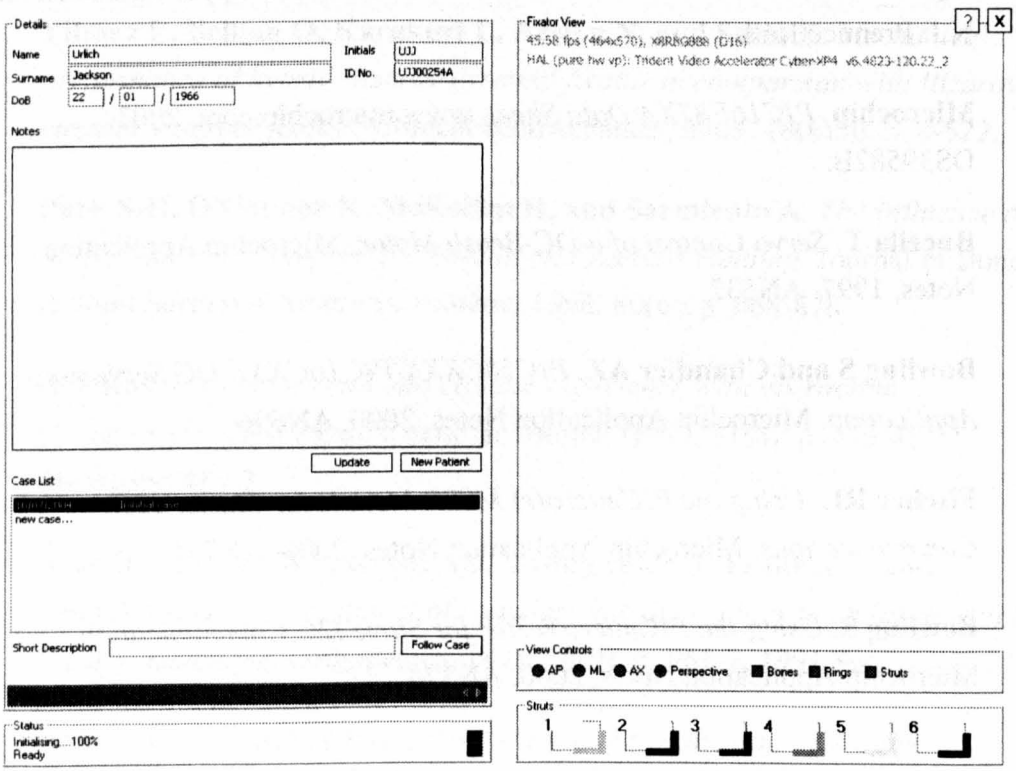


First screen, where the surgeon can input data about the patient. The database control was implemented to store patients' details.

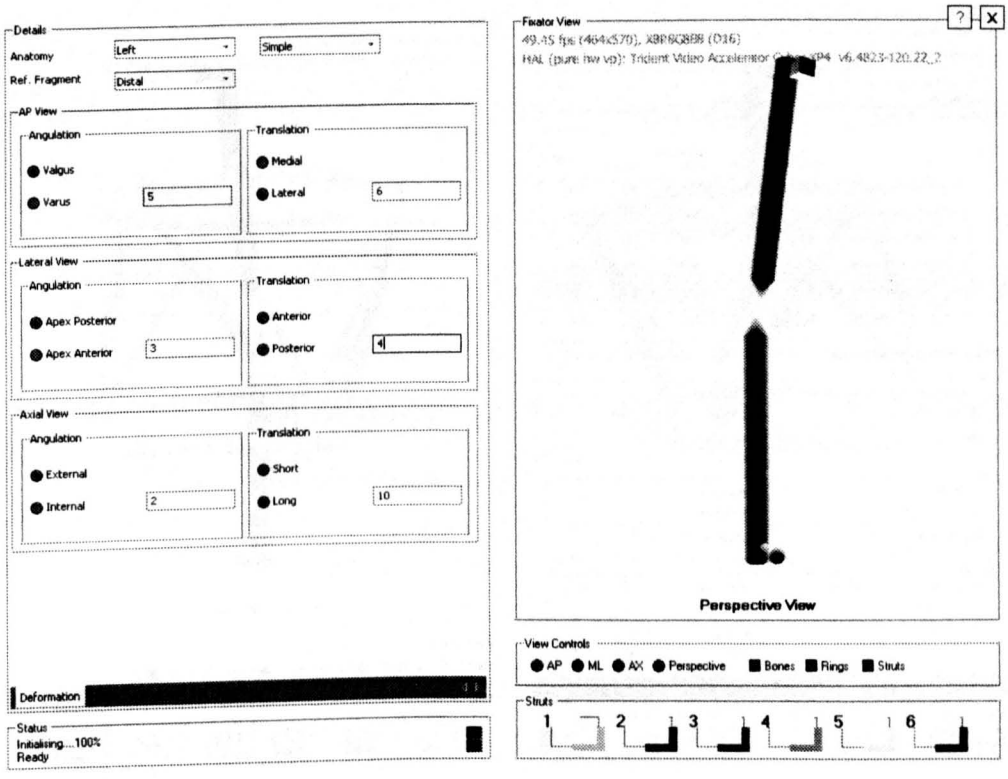


Deformity / fracture definition window. The surgeon can define the fracture/deformity geometry in full six degrees of freedom. The graphical view presents visual feedback for numerical information. It was implemented using Direct3D (part of Microsoft DirectX).

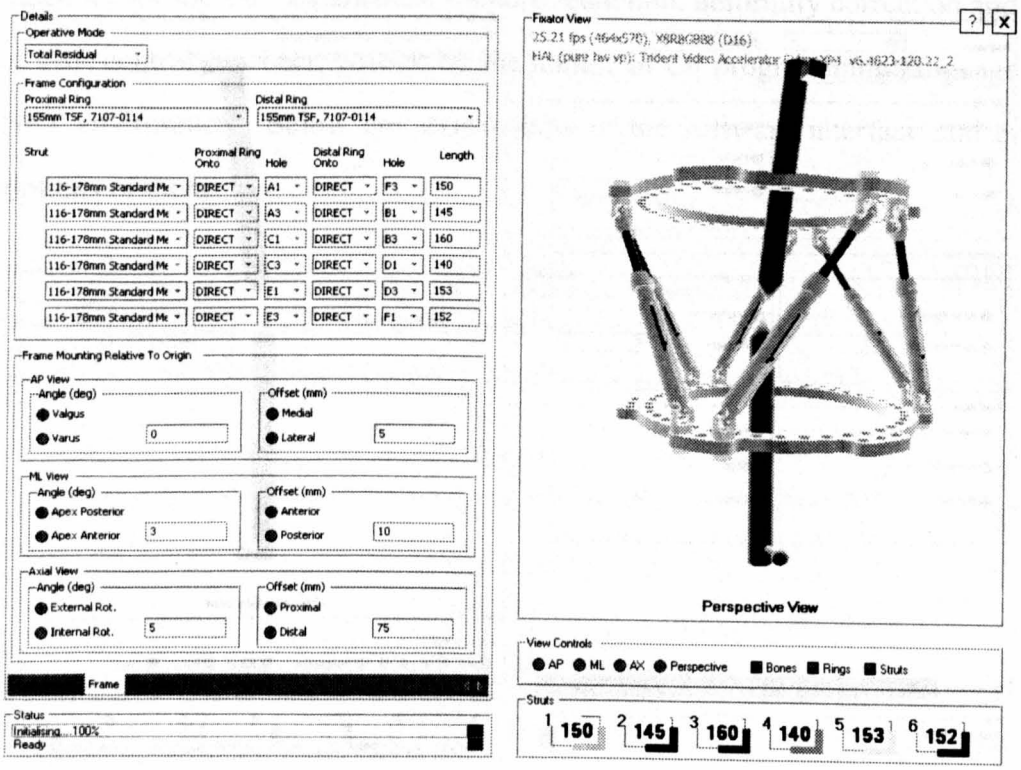


The TSF and its mounting parameters. The frame components and their locations can be defined in this screen. The frame is also mounted relative to the reference segment. The graphical representation presents an active view of the frame and bone.

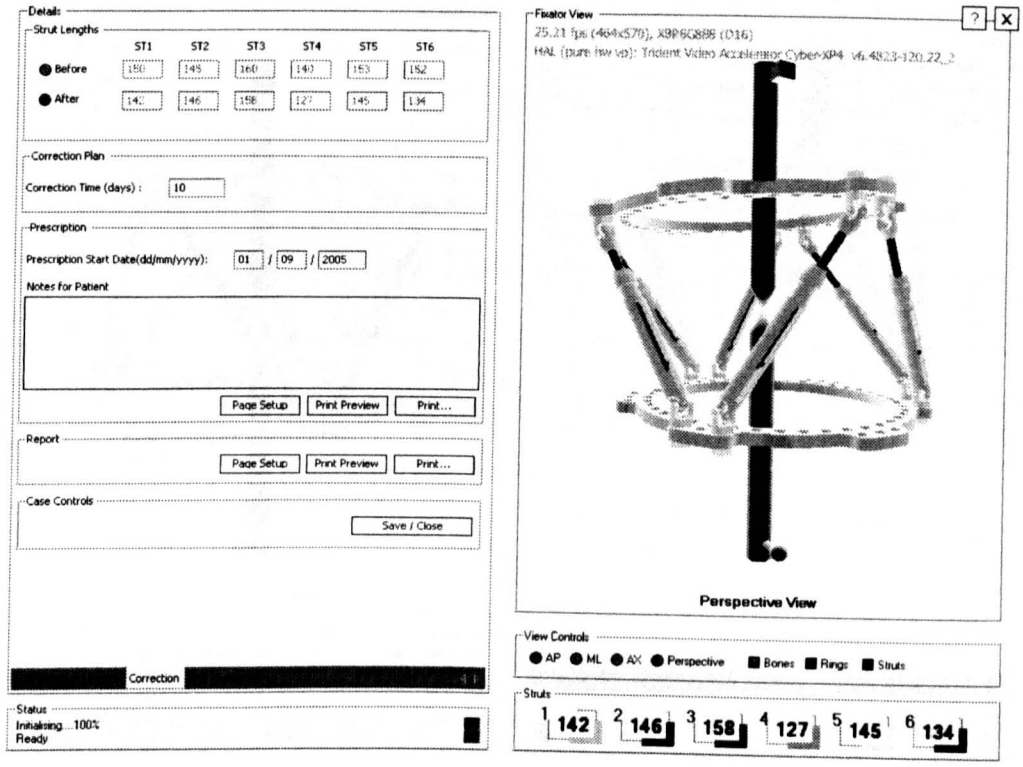


Correction. The forward and inverse kinematics are used 'behind' the screen to calculate and assemble the prescription of strut length modifications for deformity correction or fracture reduction. A print engine was created for report printing for both the patient and surgeon.

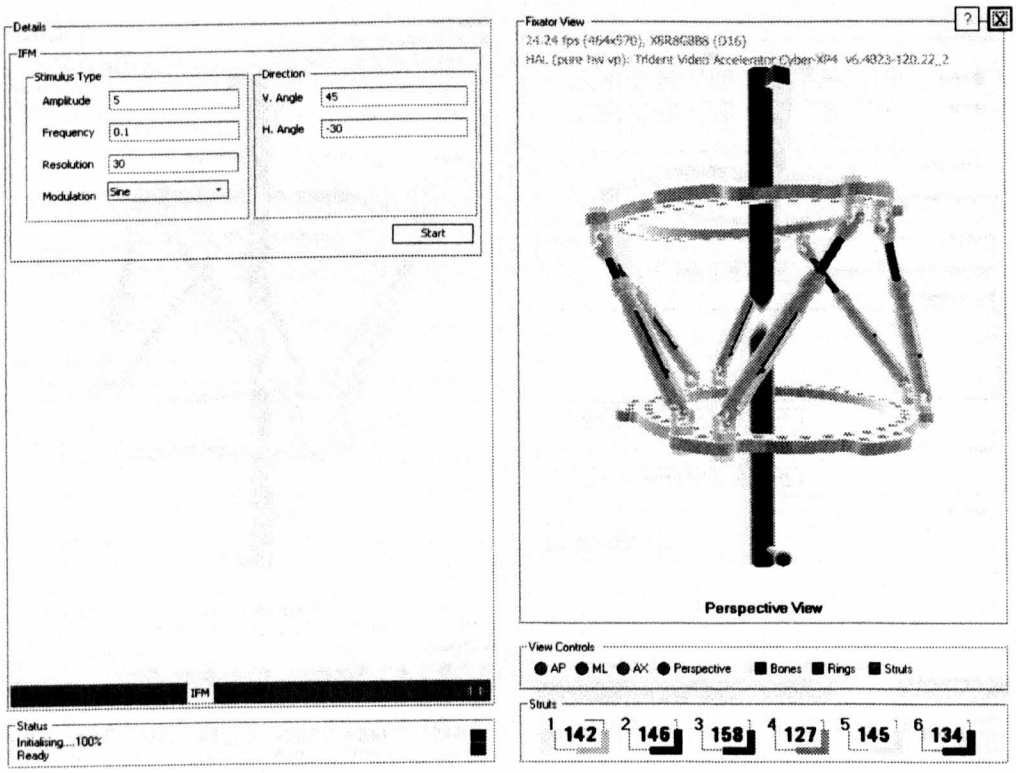


Interfragmentary motion (IFM) control screen is used in conjunction with an active TSF. It defines and controls the magnitude, direction and frequency of the applied mechanical stimulus.

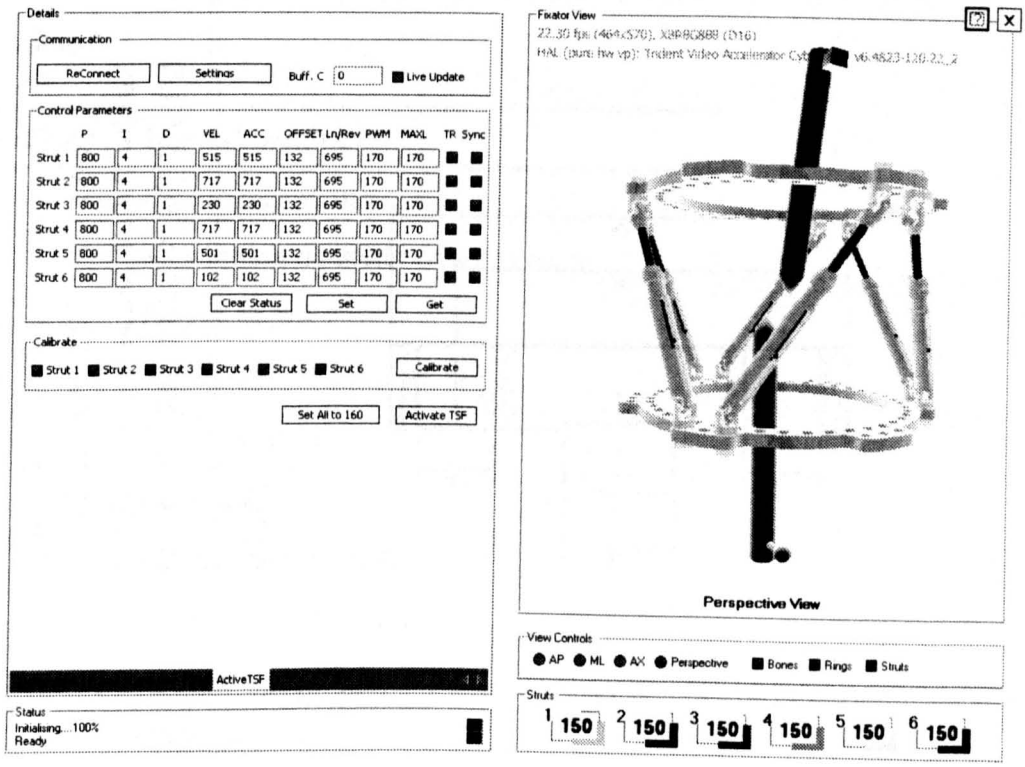


Control parameters of the EBox and the active TSF. A range of parameters can be set using this screen, including the RS232 communication, and controller gains of the EBox.

# APPENDIX B - Engineering Drawing of the T-Piece

| RevNo | Revision note | Date | Signature | Checked |
|---|---|---|---|---|

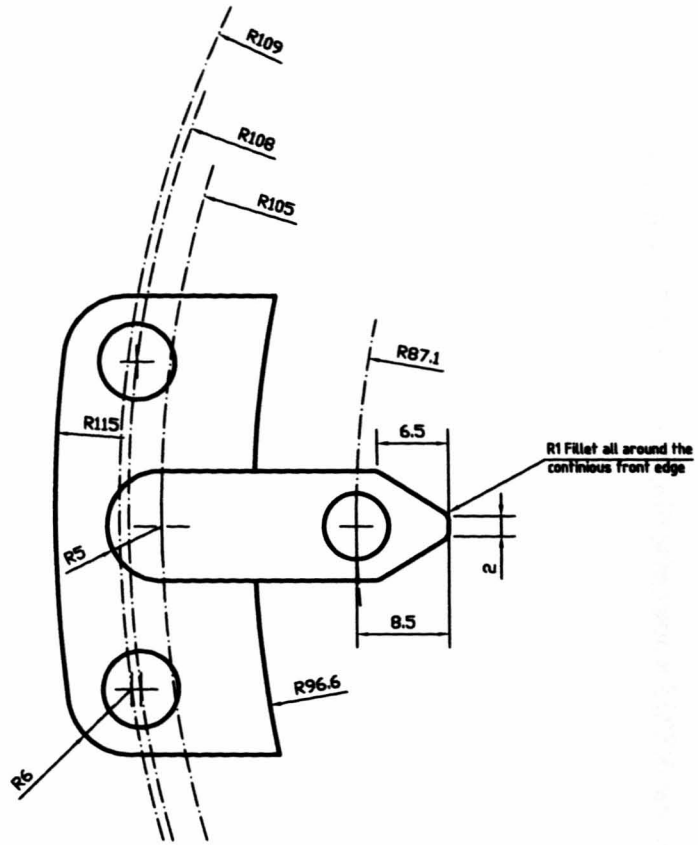


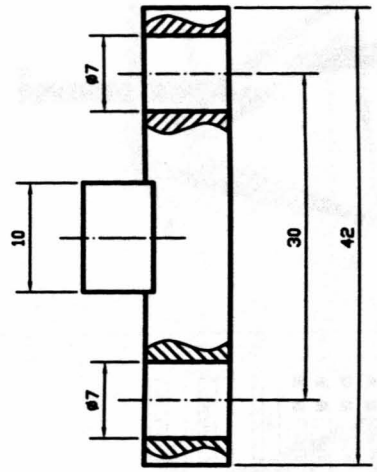


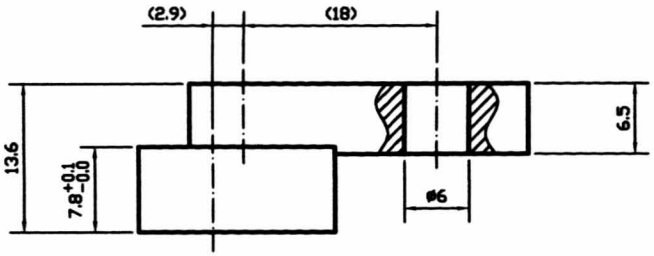


Notes:

==========

Material: Stainless Steel 316 LN
Finish: All external sharp edges
to be removed by R0.5 fillet.
Manufacturing Tolerance: +/- 0.1mm unless
otherwise stated

| LHP | Qnt.:2 | All dimensions in mm unless otherwise stated | | | Article No./Reference | |
|---|---|---|---|---|---|---|
| Designed by A. Nikonovas | | Checked by AJH, CB | Approved by - date AJH, CB - 29/05/2003 | File name | Date 28/05/2003 | Scale 2:1 |
| Arkadijus Nikonovas | | T-PIECE for 160 RING | | | | |
| | | TP001 | | | Edition A | Sheet 1/1 |

# APPENDIX C – DETAILS OF THE ACTIVE TSF DESIGN

**Notation**

| Symbol | Description, units |
|---|---|
| $a$ | Linear acceleration, $m/s^2$ |
| $d_m$ | Mean pitch diameter of a thread, m |
| $D.F.$ | Design factor |
| $\varphi$ | Pitch angle of a thread, rad |
| $F$ | Axial force, N |
| $i$ | Gear ratio |
| $I$ | Electrical current, A |
| $\mu$ | Coefficient of friction |
| $n$ | Angular speed, rpm |
| $\eta$ | Efficiency |
| $P$ | Power, W |
| $R$ | Resistance (Impedance), Ω |
| $T$ | Torque, N·m |
| $U$ | Voltage, V |
| $v$ | Linear velocity, m/s |
| $x$ | Linear displacement, m |

**Summary**

A concept of automation of the active ring fixator is the attractive option since it can provide controlled mechanical stimulus to the fracture healing process. The author has designed and built a demonstrator tool that resembles the TSF based orthopaedic ring fixator and enables demonstration of the controlled mechanical stimulus. This appendix contains technical details of the active TSF design and implementation.

## 1. An Active TSF Strut Design

The design requirements were small volume, light weight, resemblance to the existing TSF strut and low driving voltage/current (< 24 V, < 2 A, safety for the patient). Furthermore, the actuator had to produce 10 N thrust at 5 mm/s speed.

Two types of actuator drive mechanisms have been considered: in-line and 90 degrees. In the 90 degrees drive system the motor shaft is at 90 degrees to the drive shaft. The advantage of such a system is that higher gearing ratios can be achieved, for lower volume gearboxes. However, since the servo-motor is at 90 degrees to the actuator drive shaft axis, there is no resemblance to the standard TSF strut assembly. The motor shaft of the 'in-line' actuator is aligned with the gearbox shaft axis, which in turn is aligned with the drive shaft axis. The in-line actuator design has met the aesthetic design criterion and therefore was given the priority, while the 90 degrees actuator was considered as a fallback option only. Two options for the drive shaft have been considered: a ball screw mechanism and a simple threaded rod and nut mechanism. It was not possible to find a ball screw mechanism that would fit the design volume, and therefore the simple threaded rod and nut mechanism was chosen. Disadvantages of the choice were increased friction in the system, backlash and wear; however, the advantages were low cost, low volume and simple manufacture. It was decided to use a M6 stainless steel shaft with a 1 mm pitch, similar to that used in the standard TSF strut. This implied the peak design speed of the shaft of 300 rpm (5 x 60). Brass material was chosen for the nut. A simple

analysis has been carried out in order to identify a required torque to drive the threaded shaft for lifting the design load. The required driving torque was calculated using equation 1. The friction coefficient $\mu$ for the static lubricated brass-steel interface was assumed to be 0.19, the thread angle $\varphi$ was 3.31°, and the mean diameter $d_m$ of the threaded shaft was 5.5 mm. The design factor (D.F.) of 2 was used to scale up the design load to cater for unaccounted friction sources in the active strut design (ball race, universal joints, etc...).

$$T = \left(\frac{\sin\varphi + \mu \cdot \cos\varphi}{\cos\varphi - \mu \cdot \sin\varphi}\right) \cdot \text{D.F.} \cdot F \cdot \frac{d_m}{2} \quad [\text{mN} \cdot \text{m}]$$
$$T = \left(\frac{\sin 3.31 + 0.19 \cdot \cos 3.31}{\cos 3.31 - 0.19 \cdot \sin 3.31}\right) \cdot 2 \cdot 10 \cdot \frac{5.5}{2} = 13.8 \ \text{mN} \cdot \text{m} \qquad (1)$$

It was important to choose the right combination of the servomotor and the gearbox in order to achieve the required design torque. The motor and the gearbox diameters were restricted to those similar to the TSF strut. Furthermore, either motor or gearbox had to cater for the attachment of a suitable encoder for a position feedback.

Faulhaber GmbH (Germany) has been used as a supplier for motors, gearheads and encoders. The gearhead type was chosen based on the structural (withstanding twice the required torque) and volume criteria (diameter less 14 mm). A series 14/1 planetary gearhead satisfied both design constraints. In order to maximise gearhead–motor system efficiency, the theoretical reduction ratio has been calculated by dividing a recommended gearhead input speed by the required output speed. Then a gearhead reduction ratio $i$ was selected from the catalogue that had an equal or smaller reduction rate than that of the theoretical one. A 14:1 reduction ratio was found suitable for the active strut design. The required gearhead input (motor) speed to achieve the peak design speed was therefore 14x300 = 4200 rpm. The required input torque to drive the gearhead was calculated using Equation 2, where $\eta_g$ is gearhead efficiency.

$$T_M = \frac{T}{i \cdot \eta_g} = \frac{13.8}{14 \cdot 0.8} = 1.23 \quad \text{mN} \cdot \text{m} \tag{2}$$

The third motor parameter, the power of the motor, was calculated using Equation 3.

$$P = T_M \cdot n = 1.23 \cdot 4200 \cdot \frac{\pi}{30 \cdot 1000} = 0.54 \quad \text{W} \tag{3}$$

The d.c. motor (1319 012SR) was then selected which gave at least 1.5 times more output power than the one obtained by calculation and had a nominal voltage of 12 V. The selected motor met the physical dimension design constraints. The required motor operational torque was less than half of the stall torque, which ensured good life performance. In order to aid the selection of power supply and power electronics the stall current was calculated using Equation 4.

$$I = \frac{U}{R} = \frac{12}{34.6} = 0.347 \quad \text{A} \tag{4}$$

The encoder was chosen to match the motor. The IE2-50 encoder had 50 lines resolution and used Hall Effect technology to detect the lines. It was attached to the back of the motor and therefore one revolution of the gearhead shaft produced 700 encoder lines (50 x 14). Since the pitch of the threaded shaft of the actuator was 1 mm, the positioning accuracy was 0.0014 mm, which exceeds the design specification.

The gearhead could only take 5 N of axial load, which is far less than the design load of 10 N. It was therefore necessary to design the system that removed the axial load from the motor, so that motor-gearhead 'saw' torsional load only. A special housing for the motor and gearhead was designed for this purpose (refer to drawings at the end of this appendix). An aluminium alloy cylinder housed the motor, gearhead and the encoder, and sustained the axial loads. A cylinder cap was fitted with the ball race that was also attached to the drive shaft. The motor-gearhead was then attached at the other end with 0.3 mm clearance between the cylinder cap and the front surface of the gearhead. Such an arrangement removed the axial load, by diverting it to the ball race rather than to the gearhead. The clearance distance ensured that the

gearhead remained axially unloaded, despite a small backlash in the ball race. The torsional load was taken by the gearhead and the reactions were provided by the cylinder cap via two sliding pins. The pins acted as guides for the motor allowing sliding axially but constraining axial rotation. The weight of the gearhead–motor–encoder was supported by the drive shaft. The drive and gearhead shafts were interconnected rigidly via a grub screw. Finally, Loctite Retainer 601 adhesive was used to join the cylinder cap to the cylinder.

Existing strut components were used to complete the design of the active strut. The drive shaft was mated with the cylinder of the short strut, via a custom-fitted brass insert with an internal M6 thread. The universal joints from the standard TSF strut were reused at the ends of the actuator. However, in contrast to the standard TSF arrangement, the washers were sandwiched between shoulder bolts and universal joints. This removed the degree of freedom of the actuator to rotate axially in order to create the boundary condition required for the actuator operation. The disadvantage of such a system is that if the distal and proximal rings turn axially relatively to each other the strut length is affected. However, small angles are anticipated, and correction is possible through software.

An oil-based lubricant was used between surfaces of the drive shaft and the cylinder of the short strut to minimise friction and sound pollution. The drawings of the active strut are attached at the end of this appendix.

## 2. Electronics

The electronics box (EBox) specification requirements were small/portable volume, powered from the mains electricity supply, interfaced with a PC, sufficient processing power to execute control within a 1 ms turnaround time, and sufficient power output to drive the active struts.

It was decided to use a PIC16F876a digital microcontroller unit (MCU) [93] as a key computational component in the electronics design. The choice was based on the following advantages:

1. Relatively low cost.
2. DIL packaged, which allows easy assembly onto the board.
3. Re-programmable.
4. Low power consumption.
5. Hardware support for USART, $I^2C$ bus and PWM (Pulse Width Modulation).
6. Maximum clock speed of 20 MHz, 0.2 microsecond instruction execution time.
7. Sufficient memory to implement the control software.
8. Onboard non-volatile memory for storage of settings and data.

An alternative option was to use a Digital Signal Processor; however these required specialist equipment for implementation.

Six PIC16F876A MCUs were used to control actuators. All six were set as slave devices with addresses from 1-6 and were interfaced to the master MCU (PIC16F877A) via the inter integrated circuit ($I^2C^{TM}$) communication bus, developed by Philips Electronics [90]. The $I^2C$ bus was chosen, since it required only two wired lines for all six slaves and the distances between the devices were short. The bus clock frequency was set to 1 MHz. Each of the slave MCUs had a dedicated status/debug line, a synchronisation (SYNC) line and a reset (RST) line. This enabled synchronisation, status reporting, debugging, resetting and power saving to be performed. The master MCU was interfaced to the personal computer (PC) via an RS232 interface at 57.6 kBits/s baud rate, no parity bits and 1 stop bit. Its primary function was to bridge the PC and the slave MCUs, by translating serial communication to the $I^2C$ communication and vice versa. The secondary function

was to display status of the electronics via an LED display. The circuit diagram of the master MCU is presented in Figure 1. The circuit diagram of the slave MCU is presented in Figure 2. The clock signal for all MCUs was provided by 20 Mhz external resonators. Decoupling capacitors were used at the power supply tracks close to the MCUs, in order to improve circuit stability.

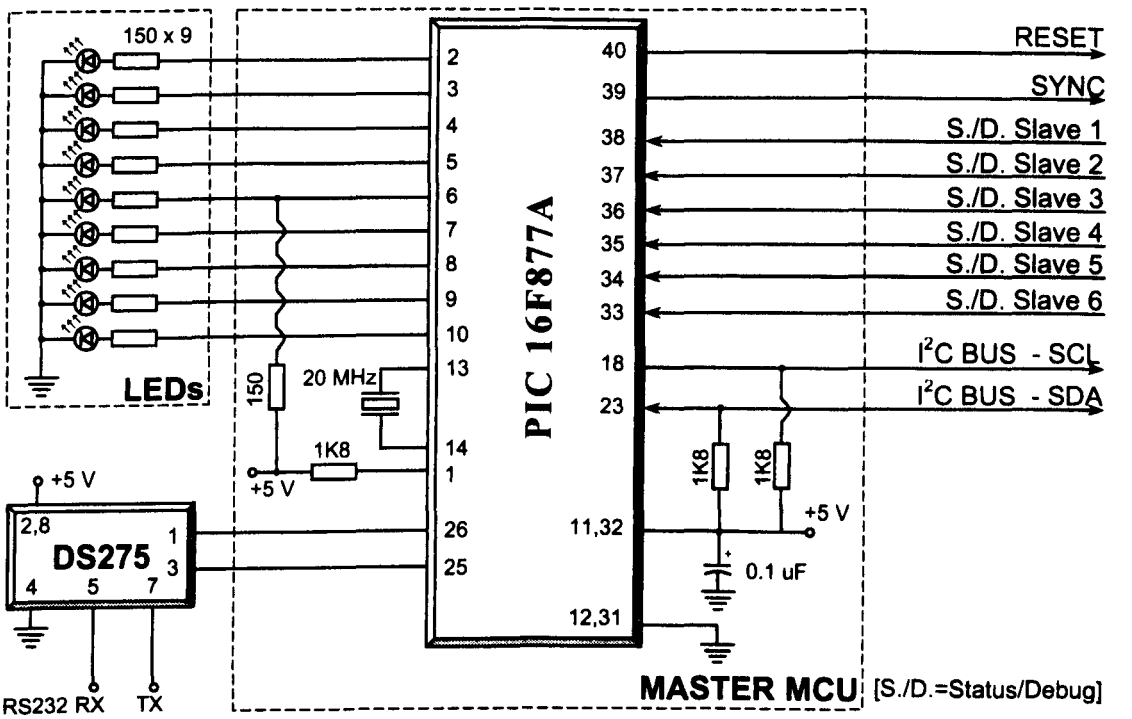


**Figure 1. Master MCU circuit.**

It was decided to drive the active struts using pulse width modulation signals (PWM). The choice was made based on the hardware support of MCUs, minimum component count and hence low cost and volume required for the implementation. The PWM signals from the slave MCUs were passed to the six DMOS full bridge drivers (L6202 SGS-Thomson Microelectronics) that have amplified the PWM signal to the required levels. Furthermore, the bridges controlled the direction of the motor. The details of the power stage circuit are presented in Figure 3. Two outputs from each of the slave MCUs were utilised to control the bridges and hence the motors. One logic output controlled direction, while other one provided the PWM signal. Two logical signals were required for setting the direction of current in the DMOS Bridge. Therefore the direction output from the slave MCU was passed

through logical 'NOT' gate (Figure 3), so that a pair of logical signals was obtained: 01 and 10. The enable line of the DMOS Bridge was connected to the slave PWM signal. Some capacitors were used to stabilise the response of the circuit and to decouple components. The maximum peak current that each DMOS Bridge could source was 5 A, which was superior to the maximum requirements of a single active strut – 0.347 A. This ensured the minimum heat dissipation, which in turn meant that no active cooling was required and hence silent operation. The power stage was fed directly from a power supply unit (PSU) and therefore the output voltage to the motor was controlled by the PSU output. For this application the active struts were designed to work with 12 V and hence 12 V were provided by the PSU.

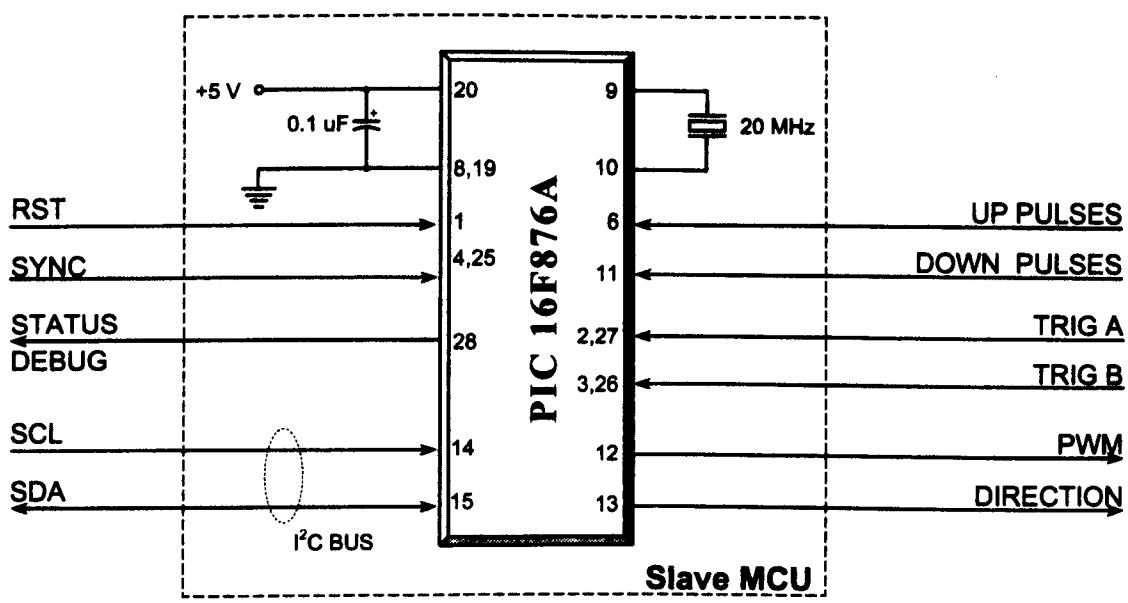


**Figure 2. Slave MCU circuit.**

The feedback circuit (Figure 4) was implemented using Dual D-Type flip flops, which decoded the pulse trains coming from the motor encoder to two (up and down) streams of pulses, Figure 5. The up and down pulse streams were hooked to the hardware counters of the slave MCUs. At every control cycle, the counters were read and the difference was added to a current position of the actuator. The slave MCU has two hardware counters of 8 bits wide. This allows maximum of 256 encoder lines to be registered in any control cycle. If the control frequency was 1.25 kHz then

the total of 320000 lines could be registered per second, which equates to 27428 rpm (320 000 lines / 700 lines per revolution x 60 seconds).

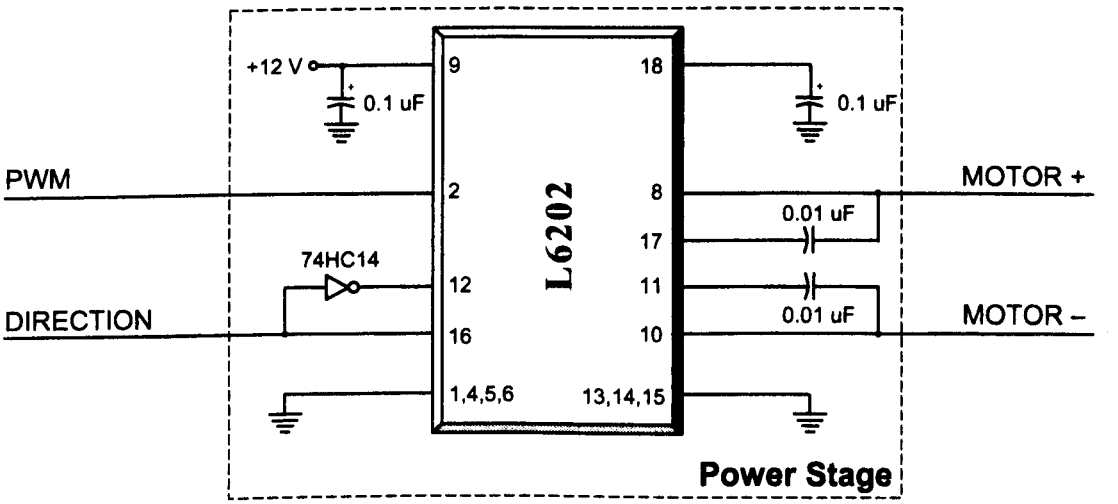


**Figure 3. Power stage circuit.**

Two, double layer, Printed Circuit Boards (PCB) were designed by the author, and were manufactured in the electronics workshop. It was decided to separate the logic components including the MCUs from the power electronics. The interface was established via two connection headers A & B, Table 1. This added flexibility of modifying the power electronics without redesigning the control circuits.

The hardware limit switches were not implemented for the active TSF application, since software limit switching was sufficient. However, the PCB circuit caters for two dedicated hardware channels per actuator for limit switches. The input levels of both channels are TTL/CMOS compatible, analogue signal compatible and can provide hardware interrupts to the software of the slave MCU.

| Head. A | Description | Head. B | Description |
|---|---|---|---|
| 1 | Direction of actuator 1 | 1 | Channel B of Encoder 1 |
| 2 .. | PWM signal for actuator 1 | 2 | Channel A of Encoder 1 |
| 3 | $I^2C$ Bus Clock Line | 3 | + Power Line of Motor 1 |
| 4 | N/A | 4 | – Power Line of Motor 1 |
| 5 | N/A | 5 | + 5 V |
| 6 | $I^2C$ Bus Data Line | 6 | Trigger A of Actuator 1 |
| 7 | Status Line of actuator 1 | 7 | Trigger B of Actuator 1 |
| 8 | Direction of actuator 2 | 8 | Channel B of Encoder 2 |
| 9 | PWM signal for actuator 2 | 9 | Channel A of Encoder 2 |
| 10 | $I^2C$ Bus Clock Line | 10 | + Power Line of Motor 2 |
| 11 | N/A | 11 | – Power Line of Motor 2 |
| 12 | N/A | 12 | + 5V |
| 13 | $I^2C$ Bus Data Line | 13 | Trigger A of Actuator 2 |
| 14 | Status Line of actuator 2 | 14 | Trigger B of Actuator 2 |
| 15 | Direction of actuator 3 | 15 | Channel B of Encoder 3 |
| 16 | PWM signal for actuator 3 | 16 | Channel A of Encoder 3 |
| 17 | $I^2C$ Bus Clock Line | 17 | + Power Line of Motor 3 |
| 18 | N/A | 18 | – Power Line of Motor 3 |
| 19 | N/A | 19 | + 5V |
| 20 | $I^2C$ Bus Data Line | 20 | Trigger A of Actuator 3 |
| 21 | Status Line of actuator 3 | 21 | Trigger B of Actuator 3 |
| 22 | Direction of actuator 4 | 22 | Channel B of Encoder 4 |
| 23 | PWM signal for actuator 4 | 23 | Channel A of Encoder 4 |
| 24 | $I^2C$ Bus Clock Line | 24 | + Power Line of Motor 4 |
| 25 | N/A | 25 | – Power Line of Motor 4 |
| 26 | N/A | 26 | + 5V |
| 27 | $I^2C$ Bus Data Line | 27 | Trigger A of Actuator 4 |
| 28 | Status Line of actuator 4 | 28 | Trigger B of Actuator 4 |
| 29 | Direction of actuator 5 | 29 | Channel B of Encoder 5 |
| 30 | PWM signal for actuator 5 | 30 | Channel A of Encoder 5 |
| 31 | $I^2C$ Bus Clock Line | 31 | + Power Line of Motor 5 |
| 32 | N/A | 32 | – Power Line of Motor 5 |
| 33 | N/A | 33 | + 5V |
| 34 | $I^2C$ Bus Data Line | 34 | Trigger A of Actuator 5 |
| 35 | Status Line of actuator 5 | 35 | Trigger B of Actuator 5 |
| 36 | Direction of actuator 6 | 36 | Channel B of Encoder 6 |
| 37 | PWM signal for actuator 6 | 37 | Channel A of Encoder 6 |
| 38 | $I^2C$ Bus Clock Line | 38 | + Power Line of Motor 6 |
| 39 | N/A | 39 | – Power Line of Motor 6 |
| 40 | N/A | 40 | + 5V |
| 41 | $I^2C$ Bus Data Line | 41 | Trigger A of Actuator 6 |
| 42 | Status Line of actuator 6 | 42 | Trigger B of Actuator 6 |
| 43 | N/A | 43 | N/A |

**Table 1. Pin outs of the headers on the computational board for the power stage board.**

Both logic and power electronics were powered from a single PSU, Traco Power TXL 100-0534T, Switzerland. The PSU was chosen so that all input voltages were supported round the world, should the active TSF need to be used abroad. The PSU had three lines of converted voltage outputs set at 5 V, 12 V and 24 V, with maximum current capacities of 12 A, 3 A and 2 A respectively. All processing electronics and logics circuits were connected to 5 V power supply rail. The 12 V supply rail was connected via a 2 A fuse to the power stage. The 24 V rail was left unused. However, if actuators required overdriving, or different types of actuators were used, this rail could have been utilised.

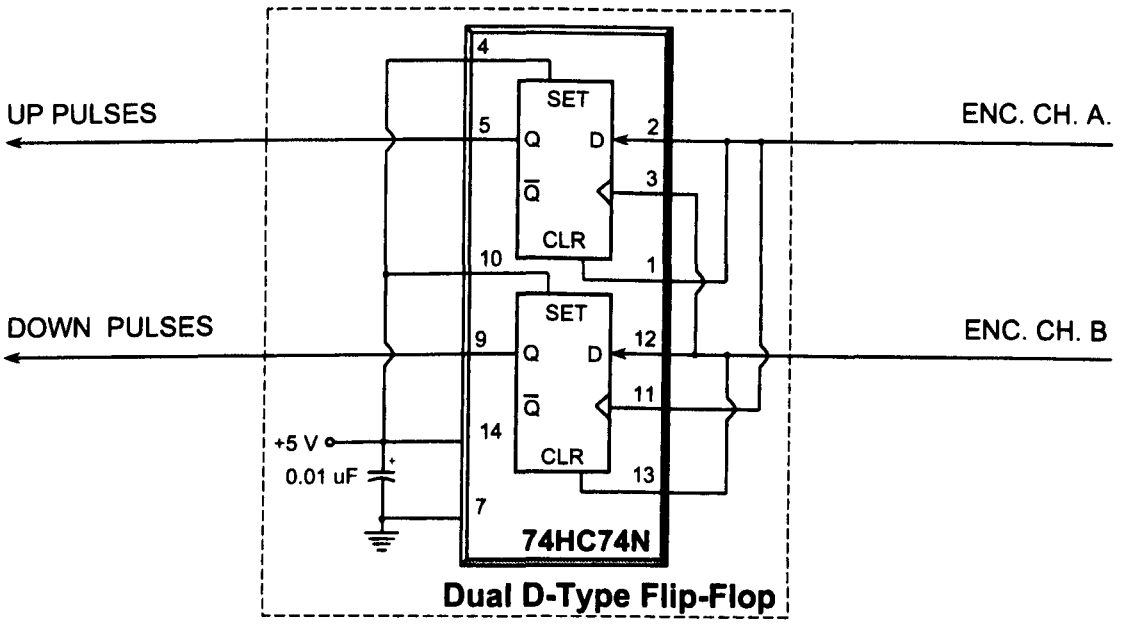


**Figure 4. Decoder circuit for the motor shaft encoder outputs.**

The interface between the circuit (EBox) and actuators was established via six RJ45 connectors. The pin outs of a single female RJ45 connector on the Ebox are provided in Table 2. A single 8 pin 'D' type female connector provided RS232 connection to the PC. The interface pin outs between the power stage board and the processing board are presented in Table 1.

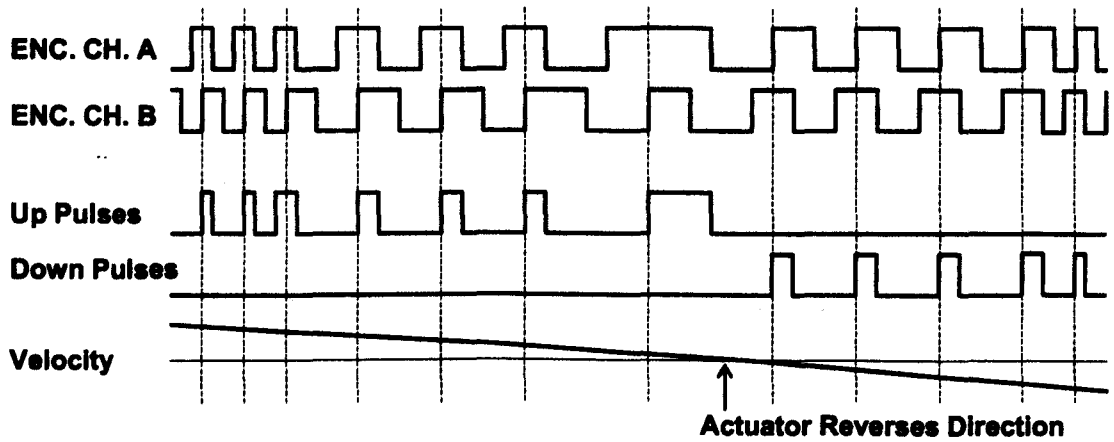


**Figure 5. Actuator feedback signals. ENC CH A & B are raw signals from the motor shaft encoder (pulse trains). Up and down pulses are raw signals after encoder signals are processed via D Type Flip-Flops.**

## 3. Control

The PID algorithm was utilised for the position control of the actuator. In addition, an integrator anti-windup logic was added, which disabled integral action when control signal was saturated.

| Pin no | Description | Pin no | Description |
|---|---|---|---|
| 1 | Ground | 5 | Trigger A of Actuator |
| 2 | + Power Line for Motor | 6 | – Power Line for Motor |
| 3 | Trigger B of Actuator | 7 | + 5V |
| 4 | Channel A of Encoder | 8 | Channel B of Encoder |

**Table 2. Pin outs of the female actuator RJ45 connector.**

The reference signal *u(k)* was passed through a motion control block, before entering the PID loop. Two types of motion control modes were implemented: pure PID and trajectory. In the pure PID mode, the incoming reference value was directly passed to the PID control loop. In the trajectory control mode, the speed and acceleration of the actuator were controlled in addition to the position. A linear piecewise velocity trajectory was implemented for this purpose. For an actuator position change, the velocity was incremented by a constant acceleration value until a specified maximum velocity was reached. The maximum velocity was then maintained for a required amount of time and then decremented by the same acceleration

(deceleration) value until zero velocity was attained. The velocity trajectory was therefore trapezoidal for a long move and triangular for a short move where maximum velocity was not reached, Figure 6.

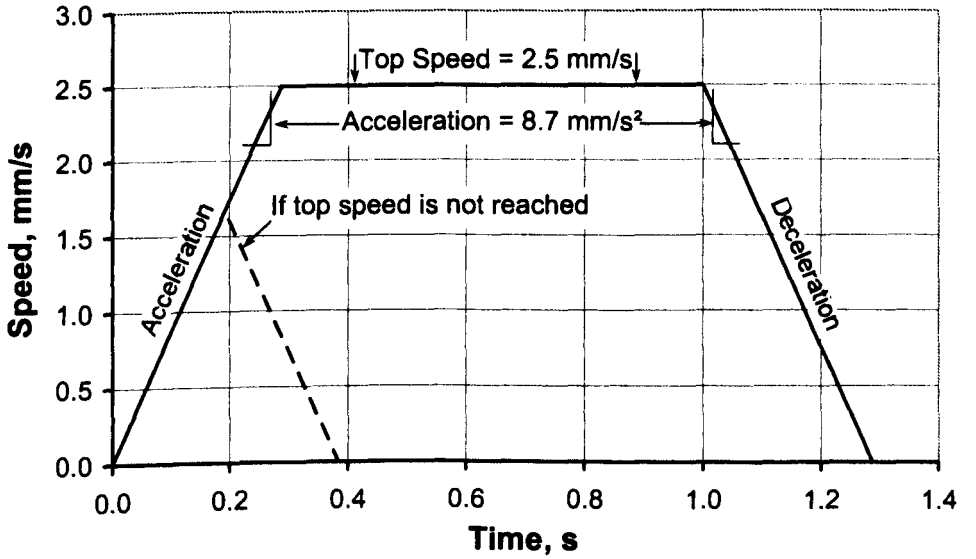


**Figure 6. Velocity profile for the trajectory controlled motion.**

The control loop turn around time was set to 0.8 ms. The PWM signal was clocked at 20 kHz and had 8 bit resolution. This allowed for 256 values of PWM in either actuator motion direction. The frequency of the PWM was chosen to be on the outside of the human hearing range and high enough to minimise the amount of a current ripple induced in the d.c. motor windings. Setting the PWM frequency any higher would only increased switching losses in the motor driver (DMOS Bridge).

More details on the PID algorithm implementation in the MCUs can be found in [94, 95].

## 4. Software

### 4.1 Master MCU

The master MCU was responsible for maintaining the communication link between the PC and slave MCUs. It was converting data between two types of communication buses: serial and $I^2C$. The code was written in assembler language for maximum efficiency. The $I^2C$ routines were interrupt-driven. The serial communication was implemented in the polling type routine. Serial commands are summarised in Table 3. The command and status byte structures are presented in Table 4.

| Comm-and | Description | TX Data | RX Data |
|---|---|---|---|
| 0x00 | Set EBox status: 0x00 – stand by, 0x80 – power on | 1 byte | Null |
| 0x?1 | Set control status | 1 byte | Null |
| 0x?2 | Recalibrate origin of the actuator | Null | Null |
| 0x?3 | Set PID control gains (kp, ki, kd) | 4 bytes | Null |
| 0x?4 | Set trajectory profile (max velocity, acceleration) | 4 bytes | Null |
| 0x?5 | Set max PWM | 1 byte | Null |
| 0x?6 | Set position of the actuator (reference value) | 3 bytes | Null |
| 0x?7 | Reserved for future use | N/A | N/A |
| 0x?8 | Report position of the actuators (1-6) | Null | 3 bytes |
| 0x?9 | Reserved for future use | Null | 4 bytes |
| 0x?A | Get PID gains (kp, ki, kd) | Null | 4 bytes |
| 0x?B | Get I2C command status | Null | 1 byte |
| 0x?C | Get current trajectory profile parameters | Null | 4 bytes |
| 0x?D | Get control status | Null | 1 byte |
| 0x?E | Get max PWM | Null | 1 byte |
| 0x0F | Get EBox status: 0x00 – stand by, 0x80 – power on | Null | 1 byte |

**Table3. RS232 command set for communication with the EBox. Commands are in hex and are one byte wide. ? – indicates that values 0-6 inclusively can be substituted. Values 1-6 address individual slaves 1-6. Value zero will address all slaves; note that the data sent and received will be 6 times larger with 1-6 slaves' data respectively.**

The commands can be passed to the EBox in two ways: addressing each slave individually, or all together. To address slave individually, the slave MCU number

(1-6) has to be inserted instead of the question mark in the command list, Table 3. To address all slaves with same command, zero instead of the question mark has to be substituted. The commands are in the hexadecimal (hex) format. The benefit of addressing all slaves together is that some RS232 bandwidth is saved since the command has to be sent only once. The command is then followed by six sets of data for slave MCUs 1-6.

| Control Status Byte | |
|---|---|
| Bit 7 | Motion direction is negative |
| Bit 6 | N. A. |
| Bit 5 | Synchronisation enabled |
| Bit 4 | Trajectory execution ended |
| Bit 3 | Maximum velocity reached |
| Bit 2 | Half of motion is reached |
| Bit 1 | N. A. |
| Bit 0 | Control signal is saturated |

| I2C Command Status Byte | |
|---|---|
| Bit 7 | N. A. |
| Bit 6 | N. A. |
| Bit 5 | Error |
| Bit 4 | Ready to receive |
| Bit 3 | Ready to transmit |
| Bit 2 | Command is cued |
| Bit 1 | Command is being executed |
| Bit 0 | Command received |

**Table 4. Control and command status byte bit structure. Bit 0 is the least significant bit in the byte. N. A. – not available.**

When transmitting data to the slave MCUs, handshaking is taking place. After the 'transmitting' command is sent (first eight commands in Table 3), the master MCU will acknowledge readiness to receive data by sending back a null byte (0x00). Only after receiving the null byte can the data be sent. This transmitting mechanism prevents command execution overlaps.

The MCUs only support integer math operations and therefore all variables are in the integer format. Some conversion is therefore necessary when receiving and passing data from and to the EBox. Any resulting numbers after conversion have to be rounded to integer. Equation 5 converts positional units (mm) to the EBox positional units (lines). A scaling factor of 700 is used since encoder produces 700 lines per one revolution of the shaft and hence 1 mm of motion.

$$x_{EBox} = 700 \cdot x \ \text{[lines]} \tag{5}$$

Equation 6 converts velocity units (mm/s) to the EBox velocity units (lines per iteration). The 1250 scaling factor is the PID execution frequency and 256 takes care of the least significant byte (more details in Section 8.3.4.3 of this chapter).

$$v_{EBox} = \frac{700 \cdot 256}{1250} \cdot v \ \text{[lines/iteration]} \qquad (6)$$

Equation 7 converts acceleration units (mm/s$^2$) to the EBox acceleration units (lines per interation$^2$).

$$a_{EBox} = \frac{700 \cdot 256}{1250 \cdot 1250} \cdot a \ \text{[lines/iteration}^2\text{]} \qquad (7)$$

Two types of command passing modes from the master to the slave MCUs were implemented: instantaneous and synchronised. In the instantaneous mode, the slave MCU executed a command immediately upon receipt of it. In the synchronised mode, the slave MCU waited for the master MCU to send the start event via a dedicated hardware synchronisation line upon receipt of the command. This enabled simultaneous execution of commands on all six slave MCUs.

The master MCU also controlled the EBox power state. Using a dedicated line connected to the reset line of all slave MCUs, it could control their power state. When the slave MCUs were placed in a reset mode, the power stage was powered down, thus saving power. The default state of the EBox after powering up is the suspend mode when slave MCUs are in a reset state.

## 4.4 Slave MCU

The slave MCU was responsible for execution of the commands received from the master MCU and actuator control. The PID and motion control were implemented in the slave MCU using assembler language as described in section 8.3.3 of the thesis. The I$^2$C communication was implemented on the polling basis, Figure 7. The PID control loop required uniform sampling times and therefore it was implemented using interrupt service routines (ISRs), Figure 8. Each time the slave MCU was

powered down, the position of the actuator together with other control variables were stored in the onboard non-volatile memory (EEPROM). Those values were retrieved every time the slave MCU was powered up. This reduced the need for actuator positional reference recalibration.

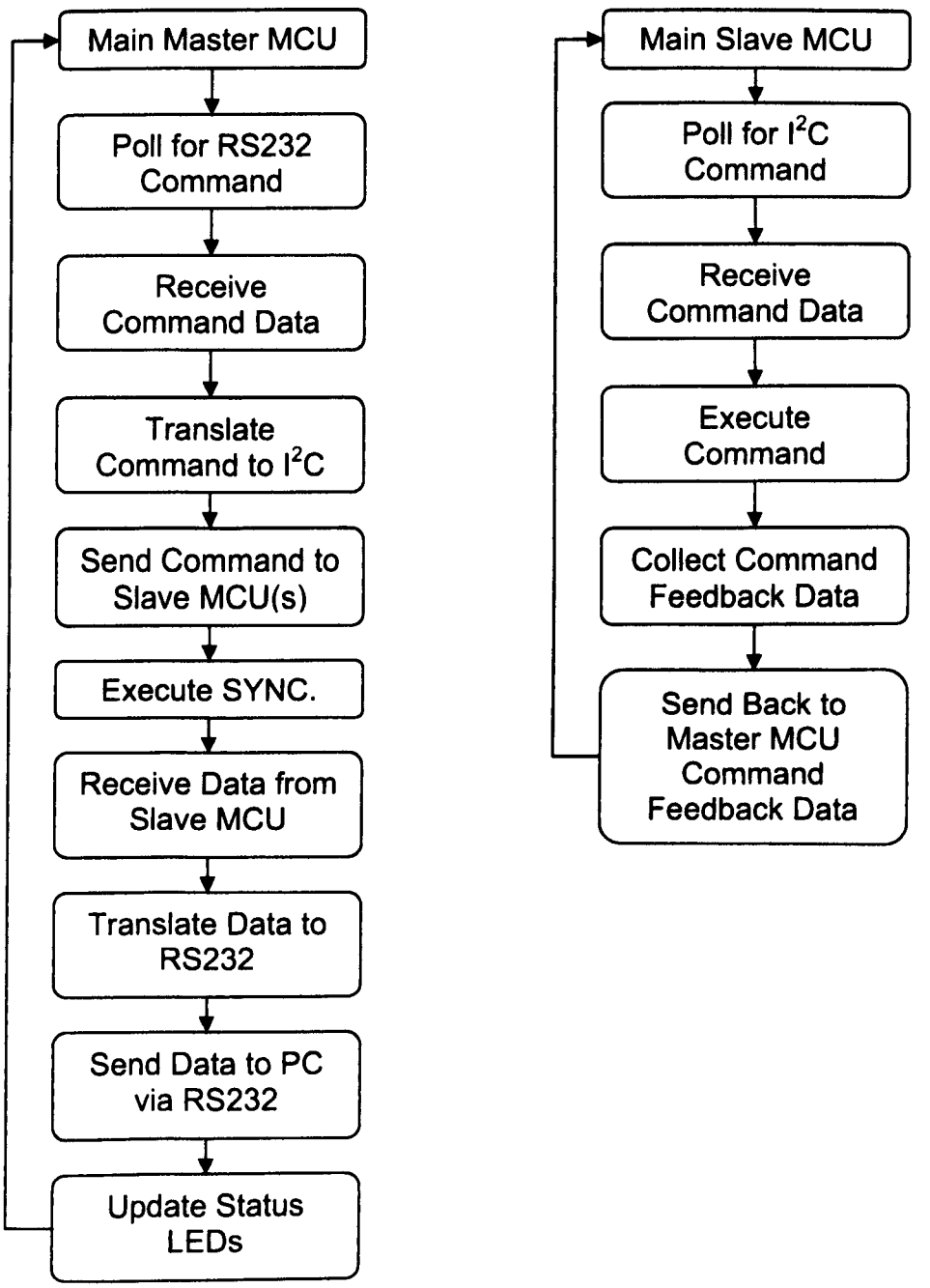


**Figure 7. Main poll routines of a) master and b) slave MCUs.**

The slave MCUs do not support floating point operations and do not have a maths coprocessor. Therefore, the control algorithm was implemented using integer

variables. Custom-written routines were used for division and multiplication, since the MCU was only capable of hardware-based addition and subtraction. Table 5 summarise the variables used and their sizes. The resolution of the position was extended with an additional least significance byte (LSB) for the trajectory control calculations. This allowed lower speeds and accelerations to be used. However, this byte was not taken into account for the PID calculations and only the first three most significant bytes (MSB) were used. The PID resulted in the four byte wide (32 bits) control signal value. The second lowest significant byte was used to determine the PWM value.

| Variable | | Byte | | | | |
|---|---|---|---|---|---|---|
| | | 4(MSB) | 3 | 2 | 1 | 0(LSB) |
| y | Control signal | + | + | [+] | + | |
| pos | Position | | + | + | + | |
| d_pos | Destination position | | + | + | + | (+) |
| kp | PID proportional gain | | | + | + | |
| ki | PID integral gain | | | | + | |
| kd | PID derivative gain | | | | + | |
| vel | Maximum velocity | | | | + | + |
| acc | Acceleration | | | | + | + |

**Table 5. Slave MCU variable table. [+] – this byte value is taken as PWM value. (+) – this byte is virtual one and is only used in for trajectory calculation purposes.**

The maximum PWM value (saturated value) can be modified. This can be useful when maximum power output of the active strut has to be limited.

Finally, details on the $I^2C$ bus implementation can be found in [96, 97].

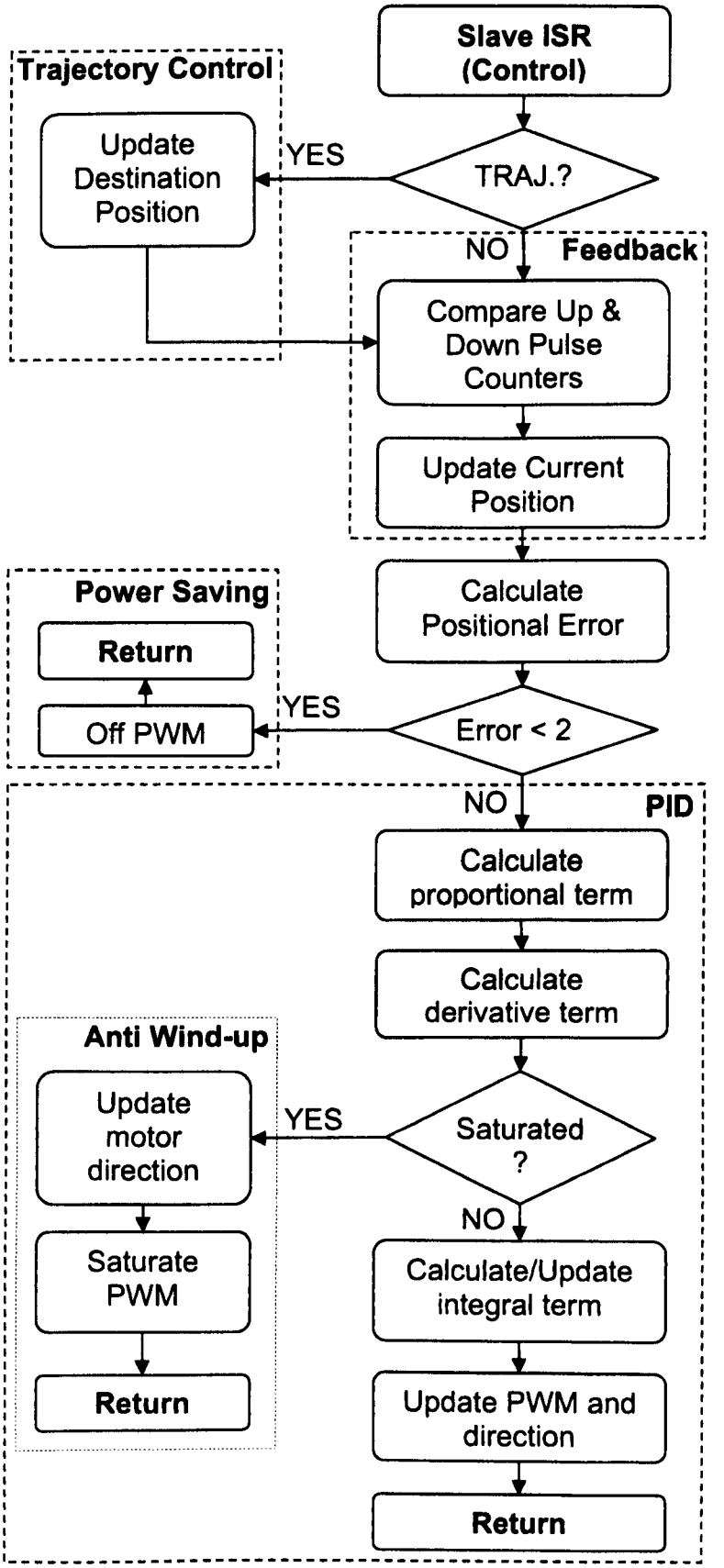


**Figure 8. Interrupt routine flowchart of the slave MCU.**

| RevNo | Revision note | Date | Signature | Checked |
|---|---|---|---|---|

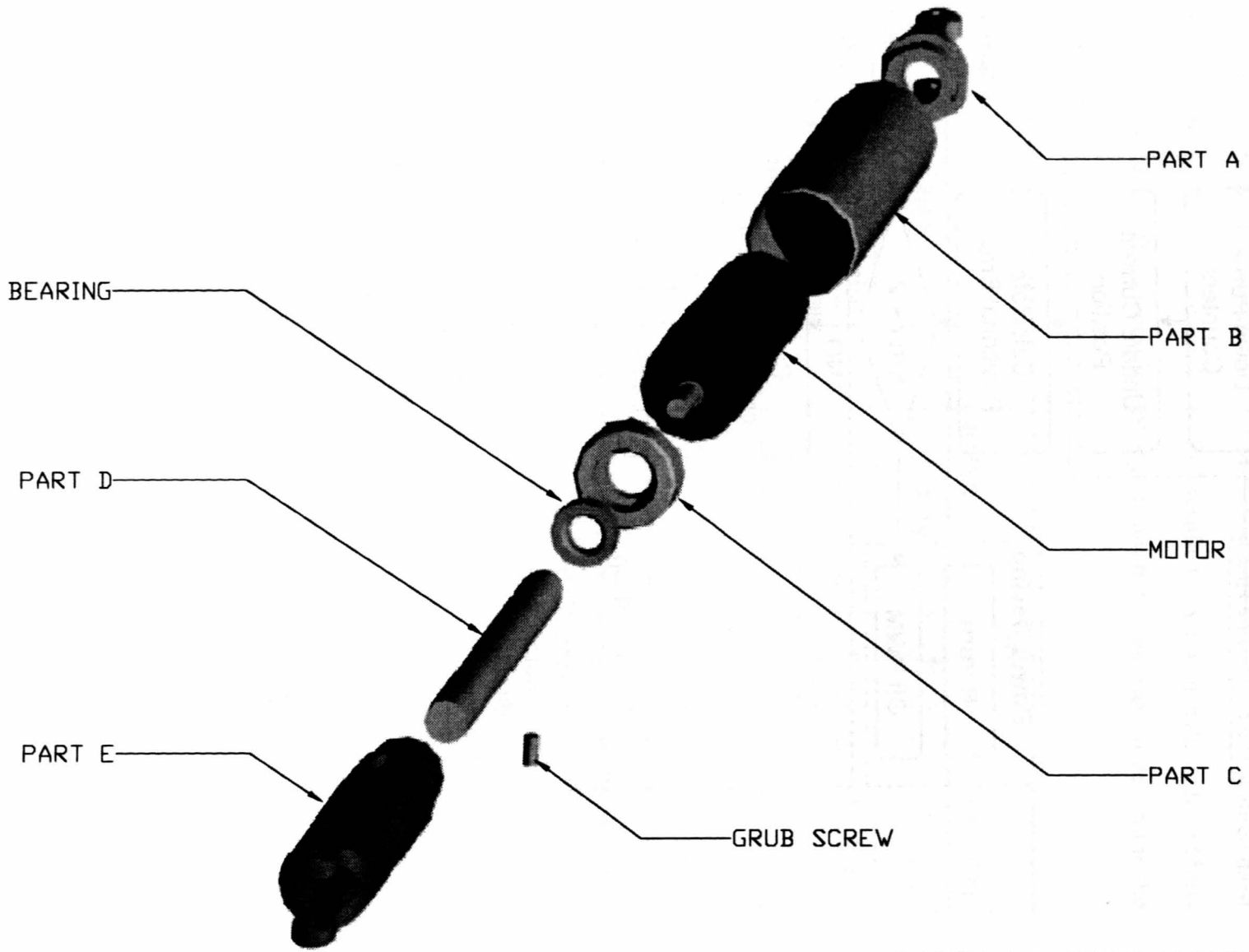


| Itemref | Quantity | Title/Name, designation, material, dimension etc | | | Article No./Reference | |
|---|---|---|---|---|---|---|
| Designed by A Nikonovas | | Checked by AN | Approved by - date 01/11/2044 | File name Motorised strut | Date 01/11/2004 | Scale -:- |
| AN | | Strut assembly diagram | | | | |
| | | 006 | | | Edition A | Sheet 1/1 |

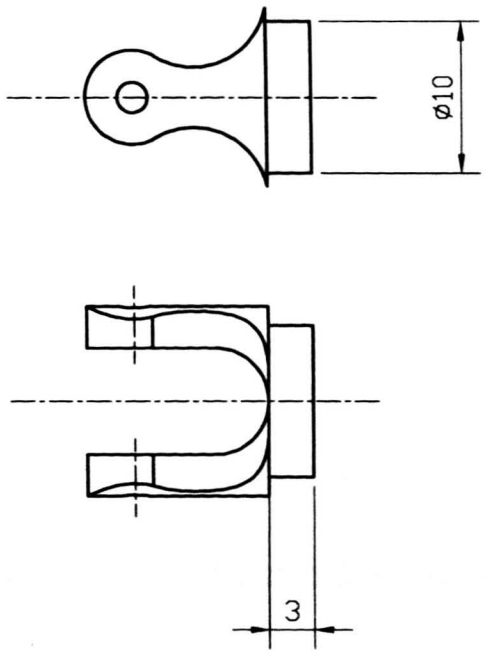


| Itemref | Quantity | Title/Name, designation, material, dimension etc | | | Article No./Reference | |
|---|---|---|---|---|---|---|
| Designed by A Nikonovas | | Checked by AN | Approved by - date 01/11/2004 | File name Part A | Date 01/11/2004 | Scale 2:1 |
| AN | | Part A | | | | |
| | | 001 | | | Edition A | Sheet 1/1 |

| RevNo | Revision note | Date | Signature | Checked |
|---|---|---|---|---|

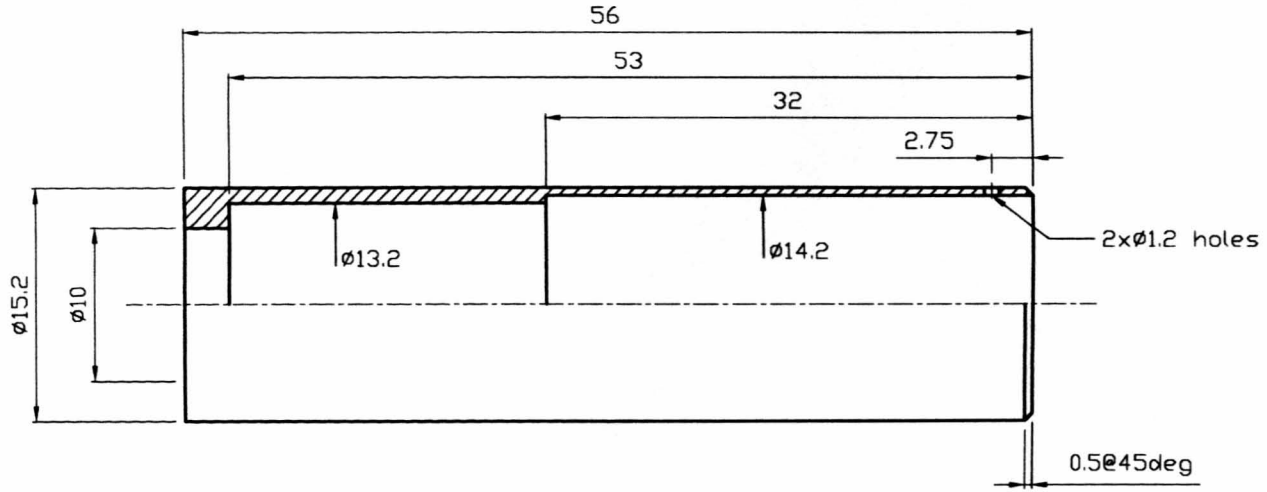


| Itemref | Quantity | Title/Name, designation, material, dimension etc | | | Article No./Reference | |
|---|---|---|---|---|---|---|
| Designed by<br>A Nikonovas | | Checked by<br>AN | Approved by - date<br>01/11/2004 | File name<br>Part B | Date<br>01/11/2004 | Scale<br>2:1 |
| AN | | Part B | | | | |
| | | 002 | | | Edition<br>A | Sheet<br>1/1 |

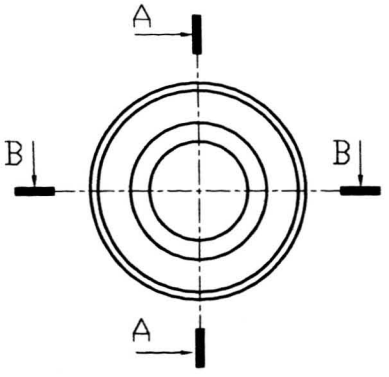


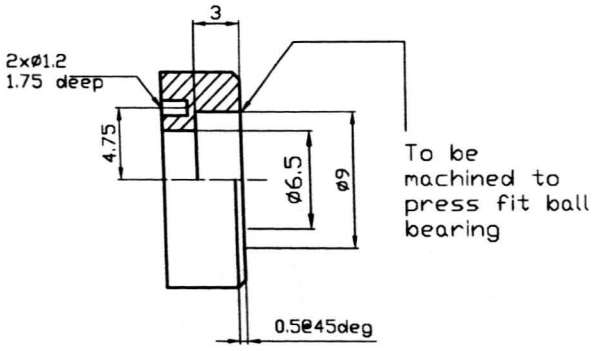


SECTION A-A

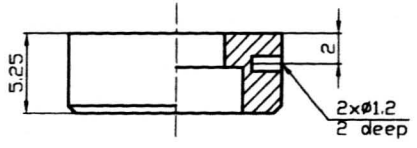


SECTION B-B

| Itemref | Quantity | Title/Name, designation, material, dimension etc | | | Article No./Reference | |
|---|---|---|---|---|---|---|
| Designed by A Nikonovas | | Checked by AN | Approved by - date 01/11/2004 | File name Part C | Date 01/11/2004 | Scale 2:1 |
| AN | | Part C | | | | |
| | | 003 | | | Edition A | Sheet 1/1 |

| RevNo | Revision note | Date | Signature | Checked |
|---|---|---|---|---|

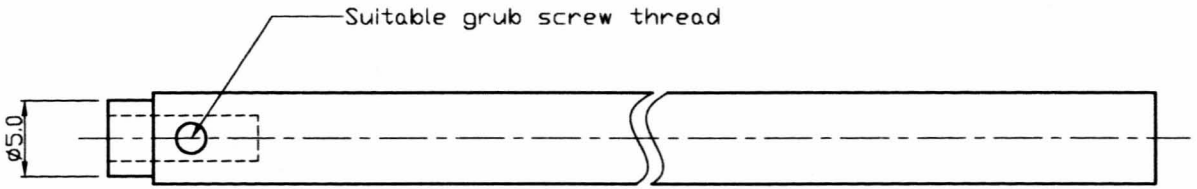


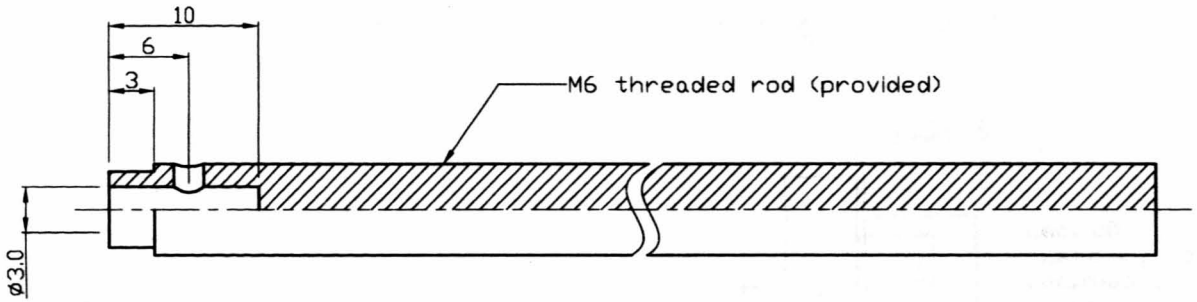


| Itemref | Quantity | Title/Name, designation, material, dimension etc | | | Article No./Reference | |
|---|---|---|---|---|---|---|
| Designed by<br>A Nikonovas | | Checked by<br>AN | Approved by - date<br>01/11/2004 | File name<br>Part D | Date<br>01/11/2004 | Scale<br>2:1 |
| AN | | Part D | | | | |
| | | 004 | | | Edition<br>A | Sheet<br>1/1 |

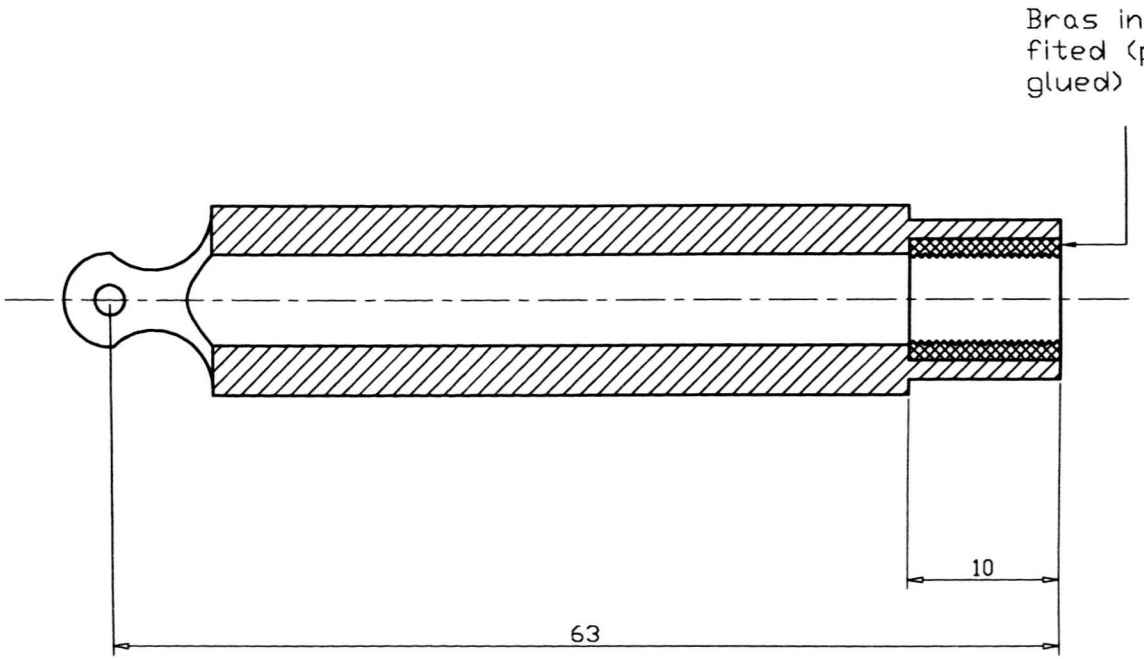


| Itemref | Quantity | Title/Name, designation, material, dimension etc | | | Article No./Reference | |
|---|---|---|---|---|---|---|
| Designed by A Nikonovas | | Checked by AN | Approved by - date 01/11/2004 | File name Part E | Date 01/11/2004 | Scale 2:1 |
| AN | | | | | Part E | |
| | | | | | 005 | Edition A / Sheet 1/1 |